



BLOOD FLOW ANALYSIS THROUGH AN INCLINED ARTERY HAVING MULTIPLE STENOSIS WITH VARIABLE NANOFLUID VISCOSITY USING SINGLE WALL CARBON NANOTUBE (SWCNT)

Syed Nisar Ahmed^{a,b},  Karanam Maruthi Prasad^{a*},  R. Sridevi^c

^aDepartment of Mathematics, School of Science, GITAM (Deemed to be University), Hyderabad, Telangana State, India-502329

^bDepartment of Mathematics, Global Institute of Engineering and Technology, Chilkur Road, Telangana State, India – 501504

^cCYIENT Ltd, Telangana State, India – 500032

*Corresponding Author e-mail: mkaranam@gitam.edu

Received December 16, 2024; revised January 25, 2025; accepted February 3, 2025

The steady flow of viscous fluid flow through an inclined tube of the non-uniform cross-section including multiple stenoses has been investigated under the influence of a single-wall carbon Nanotube (SWCNT). We linearized the flow equations and determined the flow resistance and wall shear stress expressions assuming mild stenoses. Studies have examined how parameters affect flow variables. It is found that the resistance of the flow increases with stenoses height. It is also interesting to notice that the wall shear stress decreases with the increase of the height of stenoses. It is also observed that the resistance to the flow ($\bar{\lambda}$) increases with inclination (α), source and sink parameter (β), Grashof number (B_r), dynamic viscosity (μ) and flux (q). The velocity profiles are presented in the form of streamlines.

Keywords: Stenosis; Resistance to the flow; Carbon Nanotube; Wall shear stress

PACS: 47.15.-x

1. INTRODUCTION

The narrowing of the atrial lumen, the inner open space or cavity of an artery, due to fatty deposits is one of the biggest health risks today. This can cause hypertension, myocardial infarction, etc., so stenosis, or abnormal and unnatural growth, disrupts normal blood flow. Hydrodynamical factors like wall shear stress, flow resistance, etc. can cause and progress this pathological condition. Knowledge of the flow condition in a stenosed tube may help understand and avoid vascular disorders.

Thus, several authors have investigated mathematical models for constricted duct flows (Young [1], LEE and Fung [2], Shukla et al. [3], Radhakrishnamacharya and Srinivasa Rao [4]).

All these mathematical investigations have described blood as a Newtonian fluid. Furthermore, when the diameters of the channel or tube are small and the rate of shearing is low, blood exhibits non-Newtonian behavior. The amount of red blood cells (RBCs) in erythrocytes influences this behavior. Numerous analytical research 5-9 have been conducted out to analyze the mathematical impacts of stenosis on arterial blood flow characteristics, flow resistance, and shear stress on the wall. Liu et al. [5] established a computational model for pulsating blood flow through stenotic and tapered arteries. Prasad K.M. and Yasa P.R.[6] have developed a mathematical model of a micro polar fluid flow in a tapering stenosed artery having permeable walls.

However, all these studies focused on the impact of individual stenosis, assuming a uniform cross-section of the tube. However, it is recognized that numerous blood vessels exhibit gradual changes in cross-section through their length and may present multiple stenoses at junctions and bends (Schneck et al. [7]). Maruthi Prasad and Radhakrishnamacharya [8] examined blood circulation in an artery characterized by multiple stenoses and a non-uniform cross-section, treating blood as a Herschel-Bulkley fluid.

Nano-fluids have generated significant interest from researchers because of their increased thermal conductivity, a concept first introduced by Choi [9]. Nadeem and Noreen Sher Akbar [10] investigated the flow of a micro-polar fluid containing nanoparticles in the small intestine. Maruthi Prasad and Prabhakar Reddy [11] studied the thermal effects of two immiscible fluids through a permeable stenosed artery having Nano-fluid in the core region and Newtonian fluid in the peripheral region. Many researchers have focused on Nano fluids because of their importance in the biomedical field [12-15]. The presence of nanoparticles suspended in the base fluid is insufficient to improve thermal conductivity, as this enhancement is contingent upon the particles' shape and size. Murshed et al. [16] demonstrated that Carbon Nanotubes (CNTs) exhibit thermal conductivity six times superior to other materials. Iijima and Ichihashi [17] discovered that Carbon Nanotubes are in the form of long and thin cylinders of Carbon. They have a wide range of applications in engineering and Science because of their chemical and physical properties. Carbon Nanotubes are used in medicine, gene, and drug delivery systems. The key features of CNT are three types 1) single-wall carbon nanotubes, ii) double-wall carbon nanotubes, and iii) multi-wall carbon nanotubes.

Nano-electronics is one of the most prospective submissions of single-walled nanotubes for their excellent conductivity. They are potential nanomaterials for anisotropic strengthening of thin composite films for balloon chattered

fabrication. Many authors have studied carbon Nano fluids. [18,19]. Many researchers have penned their studies presenting their applications in modern technology. Kim & Yoosuk presented their study of CNT in device applications (Kim & Kuljanishvili, [20]). Thermal outcomes relating to SWCNT and MWCNT were also presented by Majeed, Aaqib Majeed et al., [21]) and Wang, Mansir (Wang et al., [22]).

It is known that numerous ducts within physiological systems are not aligned horizontally but exhibit a certain inclination to the axis. Recently Maruthi Prasad and Sreekala [23] have studied the thermal effects on peristaltic transport in an inclined circular elastic tube.

Keeping this motivation and purpose a mathematical model is formulated to analyze blood flow through an inclined tube with a non-uniform cross-sectional and multiple stenoses, affected by a single wall carbon nanotube, while treating blood as a viscous fluid. Assuming mild stenoses, closed-form solutions have been derived. Resistance to flow and wall shear stress expressions have been developed, and the influence of different parameters on these fluid flow parameters has been examined.

2. MATHEMATICAL FORMATION

Considered is a steady, incompressible blood flow across a non-uniform cross-sectional tube with multiple stenoses. A cylindrical polar coordinate system ($z; r$) ensures that the tube's center line and z -axis coincide. Presumably, the tube is inclined at an angle of α concerning the parallel (see Fig. 1). The stenosis should be moderate and symmetrical in its development along the axis. The tube's radius is considered as: (Maruthi Prasad and Radhakrishnamacharya [2008] [8])

$$h = R(z) = \begin{cases} R_0 : 0 \leq z \leq d_1, \\ R_0 - \frac{\delta_1}{2} \left(1 + \cos \frac{2\pi}{L_1} \left(z - d_1 - \frac{L_1}{2} \right) \right) : d_1 \leq z \leq d_1 + L_1, \\ R_0 : d_1 + L_1 \leq z \leq B_1 - \frac{L_2}{2}, \\ R_0 - \frac{\delta_2}{2} \left(1 + \cos \frac{2\pi}{L_2} (z - B_1) \right) : B_1 - \frac{L_2}{2} \leq z \leq B_1, \\ R^*(z) - \frac{\delta_2}{2} \left(1 + \cos \frac{2\pi}{L_2} (z - B_1) \right) : B_1 \leq z \leq B_1 + \frac{L_2}{2} \\ R^*(z) : B_1 + \frac{L_2}{2} \leq z \leq B \end{cases} \quad (1)$$

where $R^*(z) = \exp[\beta B^2(z - B_1)^2]$.

Here δ_1, δ_2 and L_1, L_2 are the maximum heights and lengths of the two stenoses respectively.

Consequently, the fluid flow's governing equations are as follows: The following are the governing equations for a vertical artery's variable viscous Nano fluid that control the conservation of mass, momentum, and temperature:

$$\frac{\partial \bar{u}}{\partial \bar{r}} + \frac{\bar{u}}{\bar{r}} + \frac{\partial \bar{w}}{\partial \bar{z}} = 0 \quad (2)$$

$$\rho_{nf} \left(\bar{u} \frac{\partial \bar{u}}{\partial \bar{r}} + \bar{w} \frac{\partial \bar{u}}{\partial \bar{z}} \right) = -\frac{\partial \bar{p}}{\partial \bar{r}} + \frac{1}{\bar{r}} \frac{\partial}{\partial \bar{r}} \left(2\bar{r} \mu_{nf} \frac{\partial \bar{u}}{\partial \bar{r}} \right) + \frac{\partial}{\partial \bar{z}} \left(\mu_{nf} \left(\frac{\partial \bar{u}}{\partial \bar{z}} + \frac{\partial \bar{w}}{\partial \bar{r}} \right) \right) - 2\mu_{nf} \frac{\bar{u}}{\bar{r}^2} - \frac{\cos \alpha}{F} \quad (3)$$

$$\rho_{nf} \left(\bar{u} \frac{\partial \bar{w}}{\partial \bar{r}} + \bar{w} \frac{\partial \bar{w}}{\partial \bar{z}} \right) = -\frac{\partial \bar{p}}{\partial \bar{z}} + \frac{1}{\bar{r}} \frac{\partial}{\partial \bar{r}} \left(\bar{r} \mu_{nf} \left(\frac{\partial \bar{u}}{\partial \bar{z}} + \frac{\partial \bar{w}}{\partial \bar{r}} \right) \right) + \frac{\partial}{\partial \bar{z}} \left(2\mu_{nf} \frac{\partial \bar{w}}{\partial \bar{z}} \right) + g(\rho\gamma)_{nf} (\bar{T} - \bar{T}_0) - \frac{\sin \alpha}{F} \quad (4)$$

$$\left(\frac{\partial \bar{T}}{\partial \bar{t}} + \bar{u} \frac{\partial \bar{T}}{\partial \bar{r}} + \bar{w} \frac{\partial \bar{T}}{\partial \bar{z}} \right) = \frac{K_{nf}}{(\rho C_p)_{nf}} \left(\frac{\partial^2 \bar{T}}{\partial \bar{r}^2} + \frac{1}{\bar{r}} \frac{\partial \bar{T}}{\partial \bar{r}} + \frac{\partial^2 \bar{T}}{\partial \bar{z}^2} \right) + \frac{Q_0}{(\rho C_p)_{nf}} \quad (5)$$

In the given equations, \bar{u}, \bar{v} & \bar{w} represent the velocity components, \bar{T} denotes the fluid's temperature, and Q_0 represents the constant heat generation or absorption. In the suggested model for Nano fluids, μ_{nf} represents the variable viscosity of the fluid, γ_{nf} denotes thermal expansion coefficient, K_{nf} denotes thermal conductivity, ρ_{nf} denotes density, $(\rho C_p)_{nf}$ is the heat capacitance with the thermo-physical properties) [12] .

$$\mu_{nf} = \frac{\mu_0 e^{-\sigma \theta}}{(1-\phi)^{2.5}}, \alpha_{nf} = \frac{K_{nf}}{(\rho C_p)_{nf}}, \rho_{nf} = (1-\phi)\rho_f + \phi \rho_{SWCNT} \quad (6)$$

$$(\rho C_p)_{nf} = (1-\phi)(\rho C_p)_{nf} + \phi (\rho C_p)_{SWCNT}, (\gamma\rho)_{nf} = (1-\phi)(\gamma\rho)_f + \phi (\gamma\rho)_{SWCNT} \quad (7)$$

$$\frac{K_{nf}}{K_f} = \frac{(1-\phi) + 2\phi \frac{k_{SWCNT}}{k_{SWCNT} - k_F} \ln \frac{k_{SWCNT} + k_f}{2k}}{(1-\phi) + 2\phi \frac{k_f}{k_{SWCNT} - k_F} \ln \frac{k_{SWCNT} + k_f}{2K_f}} \quad (8)$$

Whereas for single wall carbon nanotubes, ρ_{SWCNT} is the density, $(\rho_{cp})_{SWCNT}$ is the heat capacitance, γ_{SWCNT} is the thermal expansion coefficient, k_{SWCNT} is the thermal conductivity and ϕ is the volume fraction. For the base fluid, μ_f is

the viscosity, ρ_f is the density, $(\rho_{cp})_f$ is the heat capacitance, γ_f is the thermal expansion coefficient, and k_f is the thermal conductivity.

The non-dimensional variables are

$$r = \frac{\bar{r}}{e_0}, w = \frac{\bar{w}}{u_0}, u = \frac{L\bar{u}}{u_0\delta}, p = \frac{e_0^2\bar{p}}{u_0s\mu_0}, \beta = \frac{Q_0e_0^2}{T_0K_f}, Re_n = \frac{e_0u_0\rho_f}{\mu_0}$$

$$Gr = \frac{g\gamma_f\rho_f e_0^2 T_0}{u_0\mu_0}, \theta = \frac{T-T_0}{T_0}, z = \frac{\bar{z}}{sl}, F = \frac{F}{\mu u\lambda}, \tau_{rz} = \frac{\tau_{rz}}{\mu(\frac{u}{R_0})}, \bar{\delta} = \frac{\delta}{R_0}, \bar{R} = \frac{R(z)}{R_0}$$

G_r constitutes the Grashof number, Re_n constitutes Reynold's number, β gives the non-dimensional heat source or sink parameter concerning the fluid and u_0 is the average velocity. Using mild stenosis approximation $\frac{\bar{\delta}}{e_0} \ll 1$ and using the condition, $\varepsilon = \frac{e_0}{sl} \ll O(1)$.

The constitutive equations (2) to (5) become

$$\frac{\partial p}{\partial r} = -\frac{\cos\alpha}{F} \quad (9)$$

$$\frac{\partial p}{\partial z} + \frac{\sin\alpha}{F} = \frac{1}{r} \frac{\partial}{\partial r} \left[\frac{\mu_1}{\mu_0} \left(r \frac{\partial w}{\partial r} \right) \right] + \frac{(\rho_r)_{nf}}{(\rho_r)_f} G_r \theta \quad (10)$$

$$\frac{\partial^2 \theta}{\partial r^2} + \frac{1}{r} \frac{\partial \theta}{\partial r} + \beta \frac{k_f}{k_{nf}} = 0 \quad (11)$$

The Nano fluid viscosity may be defined as

$$\frac{\mu_{nf}}{\mu_0} = \frac{1}{e^{\omega\theta(1-\varphi)^{2.5}}} \text{ and } e^{\omega\theta} = 1 + \omega\theta, \omega \ll 1$$

The problem's geometrical structure and dimensionless boundary conditions are presented below.

$$h = R(z) = \begin{cases} 1 : 0 \leq z \leq d_1, \\ 1 - \frac{\delta_1}{2} \left(1 + \cos \frac{2\pi}{L_1} \left(z - d_1 - \frac{L_1}{2} \right) \right) : d_1 \leq z \leq d_1 + L_1, \\ 1 : d_1 + L_1 \leq z \leq B_1 - \frac{L_2}{2}, \\ 1 - \frac{\delta_2}{2} \left(1 + \cos \frac{2\pi}{L_2} (z - B_1) \right) : B_1 - \frac{L_2}{2} \leq z \leq B_1, \\ R^*(z) - \frac{\delta_2}{2} \left(1 + \cos \frac{2\pi}{L_2} (z - B_1) \right) : B_1 \leq z \leq B_1 + \frac{L_2}{2} \\ R^*(z) : B_1 + \frac{L_2}{2} \leq z \leq B \end{cases} \quad (12)$$

Where $\frac{R^*(z)}{R_0} = \exp[\beta B^2(z - B_1)^2]$.

$$w = 0, \theta = 0 \text{ at } r = h(z) \quad (13)$$

$$\frac{\partial w}{\partial r} = 0, \frac{\partial \theta}{\partial r} = 0 \text{ at } r = 0 \quad (14)$$

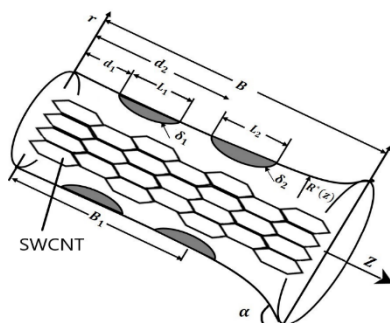


Figure 1. Schematic diagram of the inclined tube with multiple stenoses under the influence of SWCNT

The precise solutions of Eq. (10) & (11) using (13) to (14) are

$$\theta = \frac{\beta k_f}{4 k_{nf}} [h^2 - r^2] \quad (15)$$

$$w = \frac{(r^2 - h^2)}{4\mu} \left[\frac{dp}{dz} + \frac{\sin\alpha}{F} \right] - \frac{A\beta k}{8\mu} G_r \left[\frac{3h^4 - r^4}{8} + \frac{h^2 r^2}{2} \right] \quad (16)$$

The non-dimensional flux

$$q = \int_0^h 2rw dr. \quad (17)$$

Substituting Eq. (16) in Eq. (20), an expression is deduced for the pressure gradient as follows

$$\frac{dp}{dz} = \frac{-8\mu q}{h^4} - \frac{\sin\alpha}{F} + \frac{h^2}{6} A G_r \beta k \quad (18)$$

Where $A = \frac{(\rho_r)_{nf}}{(\rho_r)_f}$, $k = \frac{k_f}{k_{nf}}$, $\frac{\mu_1}{\mu_0} = \mu$

The pressure drop per wave length is

$$\Delta p = - \int_0^1 \frac{dp}{dz} dz \quad (19)$$

Substituting Eq. (18) in Eq. (19), we get

$$\Delta p = - \int_0^1 \left[\frac{-8\mu q}{h^4} - \frac{\sin\alpha}{F} + \frac{h^2}{6} A G_r \beta k \right] dz \quad (20)$$

The flow resistance

$$\lambda = \frac{\Delta p}{q} = - \frac{1}{q} \int_0^1 \left[\frac{-8\mu q}{h^4} - \frac{\sin\alpha}{F} + \frac{h^2}{6} A G_r \beta k \right] dz \quad (21)$$

The normalized flow resistance is

$$\bar{\lambda} = \frac{\lambda}{\lambda_N} = \frac{\int_0^1 \left[\frac{-8\mu q}{h^4} - \frac{\sin\alpha}{F} + \frac{h^2}{6} A G_r \beta k \right] dz}{\int_0^1 \left[\frac{-8\mu q}{1} - \frac{\sin\alpha}{F} + \frac{1}{6} A G_r \beta k \right] dz}. \quad (22)$$

The shear stress on the wall is

$$\tau_h = -\frac{h}{2} \left(\frac{\partial p}{\partial z} \right) \quad (23)$$

3. RESULT AND ANALYSIS

In this section, we analyze numerical measures of essential parameters to assess the dependability and accuracy of our exact solutions [Maruthi Prasad et al.33]

$$\frac{R^*(z)}{R_0} = \exp[\beta B^2(z - B_1)^2], \text{ and } d_1 = 0.2, L_1 = 0.2, B_1 = 0.8, B = 1, d_2 = 0.6,$$

which are illustrated through graphs. The graphs depict wall shear stress, and flow resistance as functions of the heat source or sink parameter (β), the inclination (α), and the heights of the stenosis (δ_1 and δ_2). We consider these graphs for cases involving pure blood and single-walled carbon nanotubes (SWCNT) at volume fractions of $\phi = 0.02$ and $\phi = 0.04$, while keeping certain parameters constant.

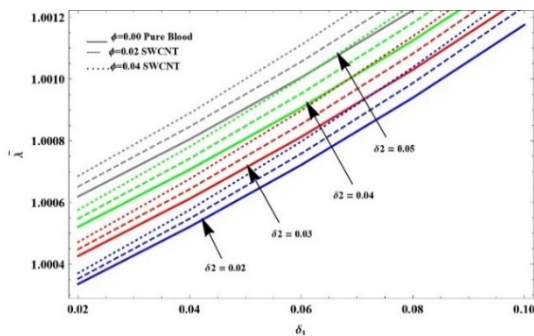


Figure 2. Effect of δ_1 on $\bar{\lambda}$, with δ_2 varying
($k_f = 0.2, k_s = 0.4, G_r = 0.2, q = 0.8, \beta = 0.01, \omega = 0.3, \mu = 0.01$)

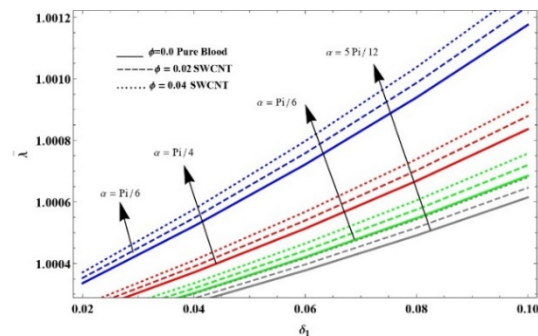


Figure 3. Effect of δ_1 on $\bar{\lambda}$, with α varying
($k_f = 0.2, k_s = 0.4, G_r = 0.2, q = 0.8, \beta = 0.01, \alpha = \frac{\pi}{6}, \omega = 0.3, \mu = 0.01$)

From Figures 2-6, it is observed that when the heights of the primary and secondary stenosis (δ_1 and δ_2) increase, the flow resistance also increases. As the height of the stenosis increases, it disturbs the flow pattern, the velocity of the fluid decreases, and the flow resistance increases. Interestingly, when comparing the SWCNT case to the pure blood instance, the flow resistance provides better results.

It is also noticed from Fig. 2-6, that the flow resistance ($\bar{\lambda}$) increases with inclination (α), source and sink parameter (β), dynamic viscosity (μ) and flux (q). It is interesting to note from the Fig. 5 that as the viscosity increases the resistance to the flow also increases, this resistance to more in SWCNT than the pure blood in the diseased artery.

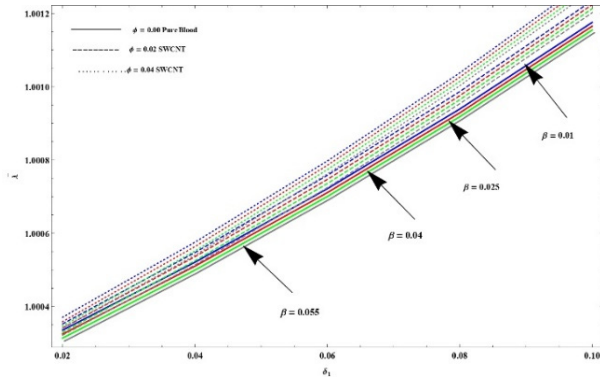


Figure 4. Effect of δ_1 on $\bar{\lambda}$, with β varying
($k_f = 0.2, k_s = 0.4, G_r = 0.2, q = 0.8, \omega = 0.3, \alpha = \frac{\pi}{6}, \mu = 0.01$)

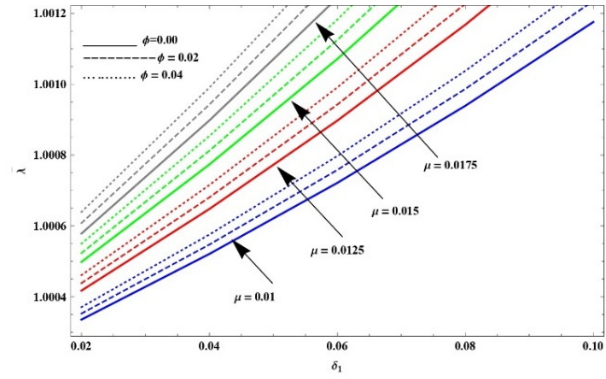


Figure 5. Effect of δ_1 on $\bar{\lambda}$, with μ varying
($k_f = 0.2, k_s = 0.4, G_r = 0.2, q = 0.8, \omega = 0.3, \beta = 0.01, \alpha = \frac{\pi}{6}$)

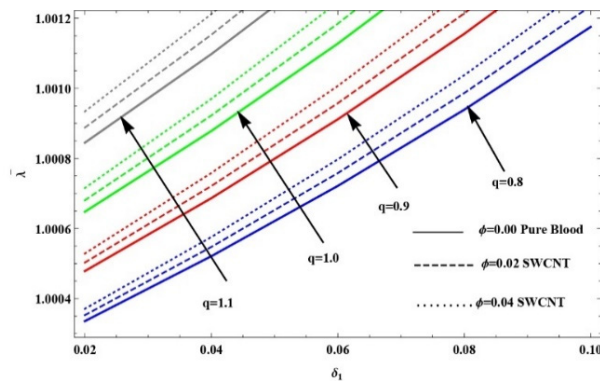


Figure 6. Effect of δ_1 on $\bar{\lambda}$, with q varying
($k_f = 0.2, k_s = 0.4, G_r = 0.2, q = 0.8, \omega = 0.3, \alpha = \frac{\pi}{6}, \beta = 0.01, \mu = 0.01$)

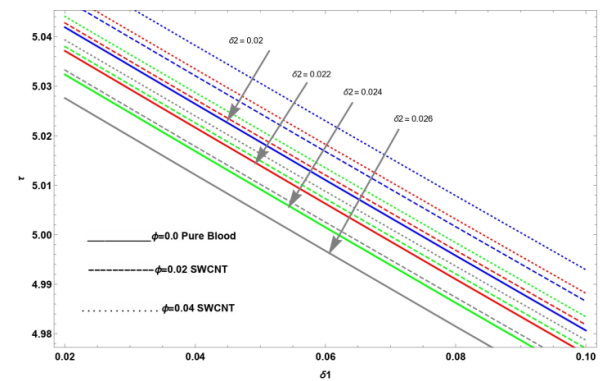


Figure 7. Effect of δ_2 on τ_h , with δ_2 varying
($k_f = 0.2, k_s = 0.4, G_r = 0.2, q = 0.8, \omega = 0.3, \alpha = \frac{\pi}{6}, \mu = 0.01$)

The graphs of shear stress on the wall along axial displacements are plotted in Fig. 7-11 for different cases. It is observed from these figures that the wall shear stress (τ) decreases with the heights of first and second stenosis (δ_1 and δ_2) i.e wall shear stress having stenosis (diseased artery) gives higher results for the pure blood case ($\phi = 0$) compared to the cases involving SWCNTs ($\phi = 0.02, 0.04$).

Figures 7-11 represents the graphs of shear stress on the wall as a function of axial displacements for various cases. Analysis of the figures indicates that wall shear stress (τ) decreases with increasing heights of the first and second stenosis (δ_1 and δ_2). Specifically, wall shear stress in the presence of stenosis (diseased artery) provides higher values for the pure blood case ($\phi = 0$) compared to the SWCNT cases ($\phi = 0.02, 0.04$).

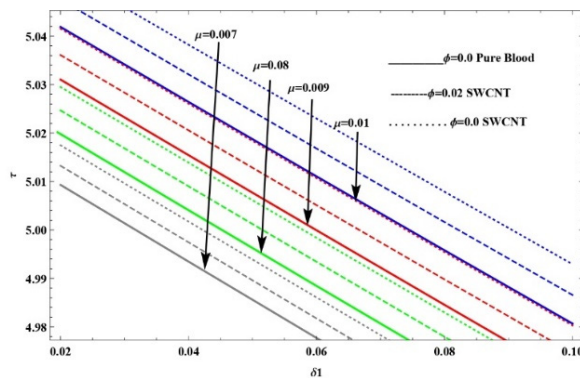


Figure 8. Effect of δ_2 on τ_h , with μ varying
($k_f = 0.2, k_s = 0.4, G_r = 0.2, q = 0.8, \omega = 0.3, \beta = 0.01, \alpha = \frac{\pi}{6}$)

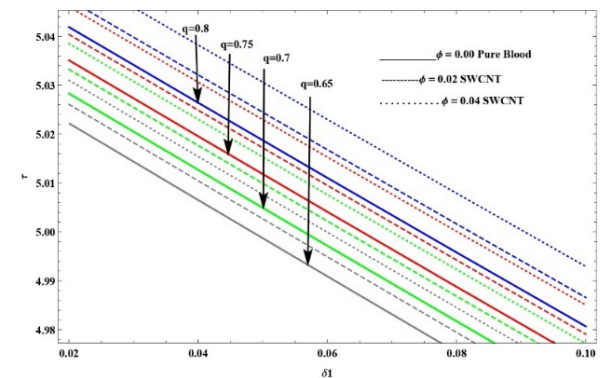


Figure 9. Effect of δ_2 on τ_h , with q varying
($k_f = 0.2, k_s = 0.4, G_r = 0.2, \omega = 0.3, \alpha = \frac{\pi}{6}, \beta = 0.01, \mu = 0.01$)

These results are observed in the region 0 to 0.1 only. When we apply SWCNT the wall shear stress reduces comparing with without SWCNT this indicates the thermal properties will reduce the frictional force and make the blood move freely. By controlling these parameters, blood flow can be optimized in the systems like drug delivery systems.

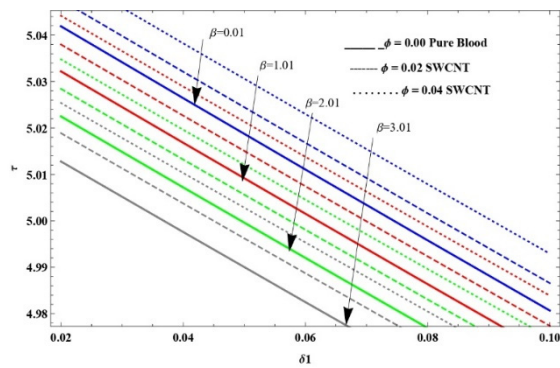


Figure 10. Effect of δ_2 on τ_h , with β varying
($k_f = 0.2, k_s = 0.4, G_r = 0.2, \omega = 0.3, \alpha = \frac{\pi}{6}, \mu = 0.01$)

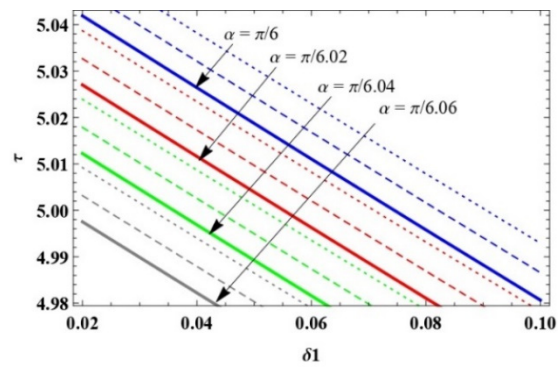


Figure 11. Effect of δ_2 on τ_h , with q varying
($k_f = 0.2, k_s = 0.4, G_r = 0.2, \omega = 0.3, \beta = 0.01, \mu = 0.01$)

It is also observed from the figures the wall shear stress decreases with the source and sink parameter (β), Viscosity Parameter (μ), and flux (q). Generally, the wall shear stress will damage the artery system. This analysis will help doctors, particularly in circulatory systems, and microfluidic devices, where the optimized shear stress prevents harm to the tissues and ensuring efficient fluid flow

Fig. 12-15 shows the streamlines for various values of Nanoparticle volume fraction (ϕ), Source and sink parameter (β), Grashof number G_r , and viscosity (μ). Here we discussed 3 different cases i.e. $\phi = 0, 0.02, 0.04$. It is observed from Fig. 12, the velocity of blood flow increases with an increase in the concentration of Nanoparticles as compared with the case of pure blood $\phi = 0$ i.e. the streamlines come closer in $\phi = 0.02, 0.04$ than $\phi = 0$. The streamlines for Grashof number G_r , Source, and sink parameter (β) are shown in Fig.13-14. It is interesting to note that, as G_r, β increases the streamline comes closer i.e. the middle part of the tube becomes wider so the velocity of the blood flow increases.

Fig. 15. shows the effect of viscosity parameter (μ) on the arteries. When the viscosity (μ) goes on increasing the velocity profiles are decreasing (i.e) the flow patterns have come very near.

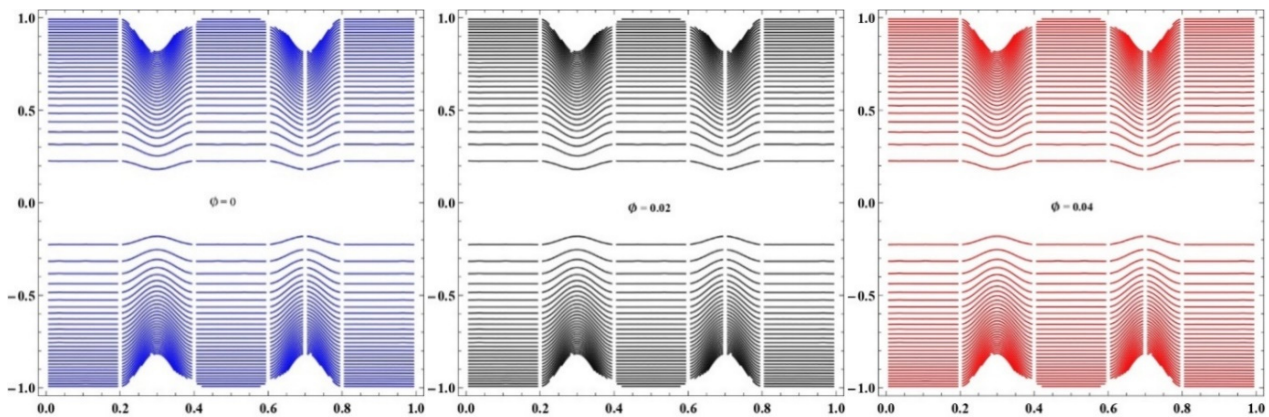


Figure 12. Streamlines for $\phi = 0.0, 0.02$ and 0.04

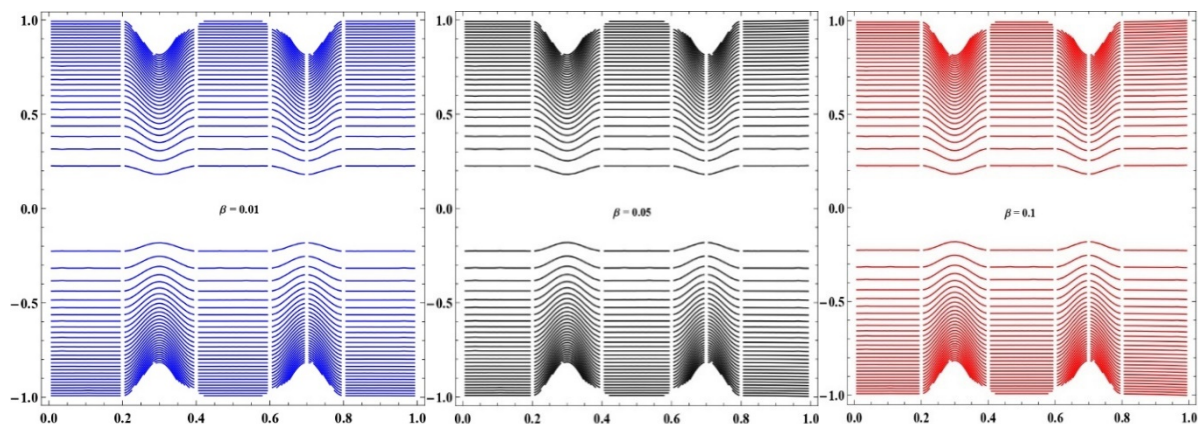


Figure 13. Streamlines for $\beta = 0.01, 0.05$ and 0.1

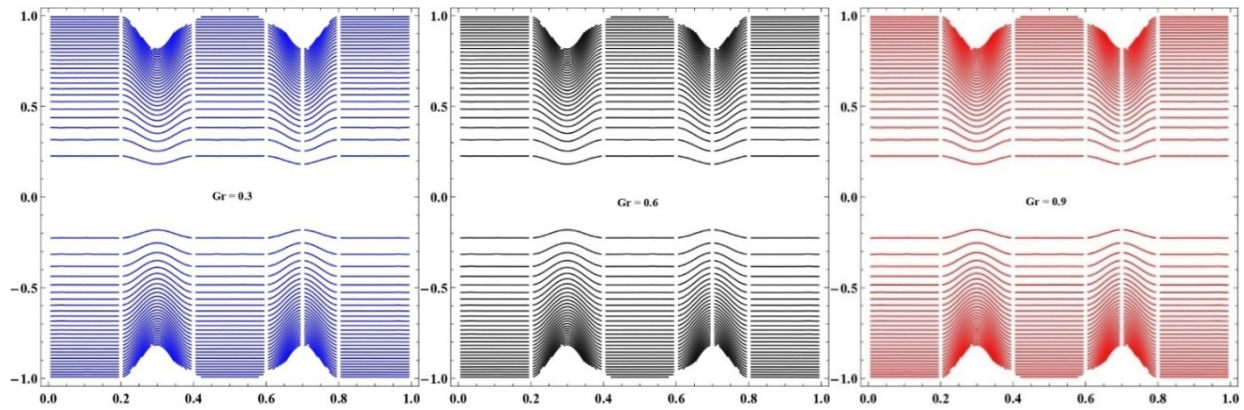
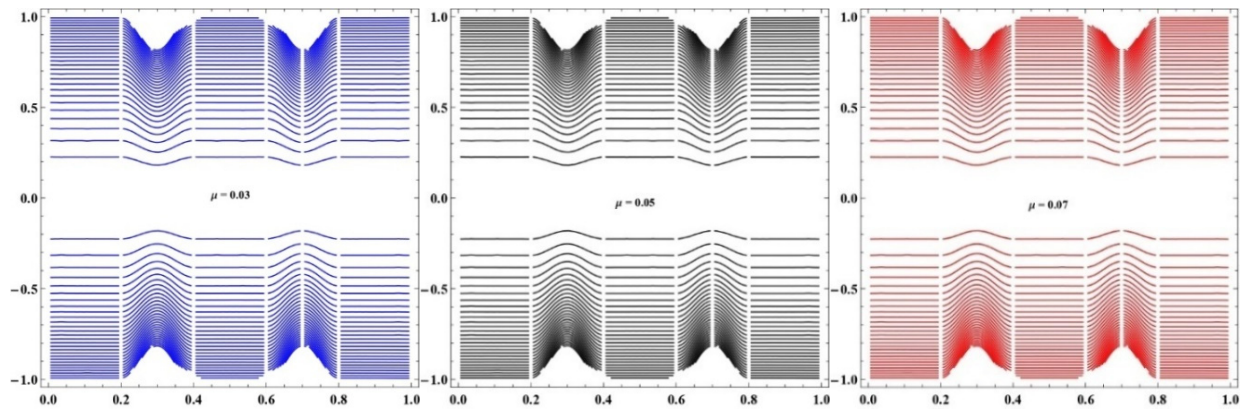
Figure 14. Streamlines for $Gr = 0.3, 0.6$ and 0.9 Figure 15. Streamlines for $\mu = 0.03, 0.05$ and 0.07

Table 1. Thermo-physical Properties of blood and SWCNT

Physical Properties	Blood	SWCNT
$C_p (J/Kg)K$	3594	425
$\rho (Kg/m^3)$	1063	2600
$K (W/mK)$	0.492	6600
$\gamma \times 10^{-5} (1/K)$	0.18	1.5

Table 2. Variations of $\bar{\lambda}$ for δ_1 & δ_2

δ_1	δ_2	(Resistance) $\bar{\lambda}$		
		$\phi = 0.00$	$\phi = 0.02$	$\phi = 0.04$
0.02	0.02	1.00034	1.00035	1.00037
0.04		1.00052	1.00055	1.00058
0.06		1.00072	1.00076	1.0008
0.08		1.00094	1.00099	1.00104
0.1		1.00118	1.00123	1.0013
0.02	0.04	1.00043	1.00045	1.00047
0.04		1.00061	1.00064	1.00068
0.06		1.00081	1.00085	1.0009
0.08		1.00103	1.00108	1.00114
0.1		1.00127	1.00133	1.0014
0.02	0.06	1.00052	1.00055	1.00058
0.04		1.00071	1.00074	1.00078
0.06		1.00091	1.00095	1.001
0.08		1.00112	1.00118	1.00124
0.1		1.00136	1.00143	1.0015
0.02	0.08	1.00062	1.00065	1.00069
0.04		1.0008	1.00085	1.00089
0.06		1.00101	1.00106	1.00111
0.08		1.00122	1.00128	1.00135
0.1		1.00146	1.00153	1.00161

Table 3. Variations of τ_h for $\delta 1$ & $\delta 2$

$\delta 1$	$\delta 2$	τ		
		$\phi = 0.00$	$\phi = 0.02$	$\phi = 0.04$
0.02	0.02	5.0419	5.04753	5.05358
0.04		5.02642	5.03212	5.03823
0.06		5.01105	5.01681	5.023
0.08		4.9958	5.00163	5.00789
0.1		4.98067	4.98658	4.99293
0.02	0.04	5.03713	5.04277	5.04883
0.04		5.02165	5.02736	5.03349
0.06		5.00628	5.01205	5.01825
0.08		4.99103	4.99687	5.00315
0.1		4.9759	4.98182	4.98818
0.02	0.06	5.03236	5.03802	5.04409
0.04		5.01689	5.0226	5.02874
0.06		5.00151	5.0073	5.01351
0.08		4.98626	4.99211	4.9984
0.1		4.97113	4.97707	4.98344
0.02	0.08	5.02759	5.03326	5.03935
0.04		5.01212	5.01785	5.024
0.06		4.99675	5.00254	5.00877
0.08		4.98149	4.98736	4.99366
0.1		4.96636	4.97231	4.9787

4. CONCLUSIONS

Effects of SWCNT characteristics on blood flow inclined artery with two symmetrical stenoses have been considered and solved analytically. This analysis will help the doctors particularly in circulatory system, microfluidic devices, where the optimized shear stress is preventing harm to the tissues and ensuring the efficient fluid flow. Based on the Mathematical analysis it is observed that:

- The resistance to the flow λ enhances with the stenoses height and with the addition of SWCNT compared to pure blood.
- The sink and source parameter of heat enhances the temperature & it gives better heat dissipation of the considered base fluid with the addition of SWCNT.
- The Wall shear stresses of arteries decrease with SWCNT stating that SWCNT base fluid give higher results compared to other base fluids.
- The various impacts of heights of multiple stenoses decrease for different Values of Nano fluid viscosity as correlate to constant Nano Fluid viscosity
- With the help of Stream Lines, blood velocity increases with an increase in the concentration of Nanoparticles as correlate with the case of pure blood ($\phi = 0$) i.e. by implementing the SWCNT we can reduce the stenosis height or decreases the resistance to the flow

ORCID

●Karanamu Maruthi Prasad, <https://orcid.org/0000-0002-9010-6452>; ●R. Sridevi, <https://orcid.org/0000-0002-8542-3197>

REFERENCES

- [1] D.F. Young, "Effects of time-dependent stenosis on flow through a tube," J. Engrg. Ind. Trans. ASME, **90**, 248-254 (1968). <https://doi.org/10.1115/1.3604621>
- [2] J.S. Lee, and Y.C. Fung, "Flow in Locally-Constricted Tubes and Low Reynolds Numbers," J. Appl. Mech., Trans. ASME, **37**, 9-16 (1970). <https://doi.org/10.1115/1.3408496>
- [3] J.B. Shukla, R.S. Parihar, and B.R.P. Rao, "Effects of stenosis on non-Newtonian flow through an artery with mild stenosis," Bull. Math. Biol. **42**, 283-294 (1980). <https://doi.org/10.1007/BF02460787>
- [4] G. Radhakrishnamacharya, and P.S. Rao, "Flow of magnetic fluid through a non-uniform wavy tube," in: *Proc. Nat. Acad. Sci. India*, 76(A), III 86, (2007).
- [5] G.-T. Liu, X.-J. Wang, B.-Q. Ai, and L.-G. Liu, "Numerical Study of Pulsating Flow Through a Tapered Artery with Stenosis," Chinese Journal of Physics, **42**(4), 401-409 (2004).
- [6] K.M. Prasad, P.R. Yasa, and J.C. Misra, "Characteristics of Blood Flow Through a Porous Tapered Artery Having Mild Stenoses under the Influence of an External Magnetic Field," Journal of Applied Science and Engineering, **24**(4), 661-671 (2021). [https://doi.org/10.6180/jase.202108_24\(4\).0022](https://doi.org/10.6180/jase.202108_24(4).0022)
- [7] D.J. Schneck, and S. Ostrach, "Pulsatile blood flow in a channel of small exponential Divergence-I. The linear approximation for low mean Reynolds number," J. Fluids Eng. **16**, 353-360 (1975). <https://doi.org/10.1115/1.3447314>
- [8] K.M. Prasad, and G. Radhakrishnamacharya, "Flow of Herschel-Bulkley fluid through an inclined tube of non-uniform cross-section with multiple stenoses," In. Arch. Mech. **60**(2), (2008). <https://am.ippt.pan.pl/am/article/view/v60p161/pdf>
- [9] S.U.S. Choi, "Enhancing thermal conductivity of fluids with nanoparticles," in: *Developments and applications of non-Newtonian flows*, edited by D.A. Signer, and H.P. Wang (ASME, NY, 1995), pp. 99-105.

- [10] N.S. Akbar, and S. Nadeem, "Peristaltic flow of a micro-polar fluid with nanoparticles in the small intestine," *Applied Nanoscience*, **3**(6), 461–468 (2012). <https://doi.org/10.1007/s13204-012-0160-2>
- [11] K.M. Prasad, P.R. Yasa, and R. Motahar, "Thermal effects of two immiscible fluids in a stenosed tube with nanoparticles in the core region," *International Journal of Ambient Energy*, **43**(1), 6651–6661 (2022). <https://doi.org/10.1080/01430750.2022.2037457>
- [12] S. Nadeem, and S. Ijaz, "Theoretical analysis of metallic nanoparticles on blood flow through stenosed artery with permeable walls," *Physics Letters A*, **379**(6), 542–554 (2015). <https://doi.org/10.1016/j.physleta.2014.12.013>
- [13] A.M. Abd-Alla, E.N. Thabet, and F.S. Bayones, "Numerical solution for MHD peristaltic transport in an inclined Nano fluid symmetric channel with porous medium," *Sci. Rep.* **12**(1), 1–11 (2022). <https://doi.org/10.1038/s41598-022-07193-5>
- [14] J. He, N.S. Elgazery, K. Elagamy, and A.N.Y. Elazem, "Efficacy of a modulated viscosity-dependent temperature/nanoparticles concentration parameter on a nonlinear radiative electromagnetic-Nano fluid flow along an elongated stretching sheet," *J. Appl. Comput. Mech.* **9**(3), 848–860 (2023). <https://doi.org/10.22055/jacm.2023.42294.3905>
- [15] J.-H. He, L. Verma, B. Pandit, A.K. Verma, R.P. Agarwal, "A new Taylor series-based numerical method: simple, reliable, and promising," *J. Appl. Comput. Mech.* **9**(4), 1122–1134 (2023). <https://doi.org/10.22055/jacm.2023.43228.4040>
- [16] S.M.S. Murshed, C.A.N. Castro, M.J.V. Lourenco, M.L.M. Lopes, and F.J.V. Santos, "A review of boiling and convective heat transfer with nanofluids," *Renew. Sustain. Energ. Rev.* **15**, 2342–2354 (2011). <https://doi.org/10.1016/j.rser.2011.02.016>
- [17] S. Iijima, and T. Ichihashi, "Single-shell carbon nanotubes of 1-nm diameter," *Nature*, **363**, 603–605 (1993). <https://doi.org/10.1038/363603a0>
- [18] N.S. Akbar, and A.W. Butt, "Carbon nanotubes analysis for the peristaltic flow in curved channel with heat transfer," *Applied mathematics and computation*, **259**, 231–241 (2015). <https://doi.org/10.1016/j.amc.2015.02.052>
- [19] N.S. Akbar, "Entropy generation analysis for a CNT suspension nanofluid in plumb ducts with peristalsis," *Entropy*, **17**, 1411–1424 (2015). <https://doi.org/10.3390/e17031411>
- [20] N. Turaeva, Y. Kima, and I. Kuljanishvili, "An extended model for chirality selection in single walled carbon nanotubes," *Nanoscale Adv.* **5**, 3684–3690 (2023). <https://doi.org/10.1039/d3na00192j>
- [21] A. Majeed, et al., "Thermally developed radiated flow of single and multiple carbon nanotubes (SWCNTs-MWCNTs) with variable thermal conductivity," *Journal of Radiation and Applied Sciences*, **18**(1), (2025). <https://doi.org/10.1016/j.jrras.2024.101244>
- [22] Y. Wang, et al., "Thermal outcomes for blood-based carbon nanotubes (SWCNT and MWCNTs) with Newtonian heating by using new Prabhakar fractional derivative simulations," *Case studies in Thermal Engineering*, **32**, (2022). <https://doi.org/10.1016/j.csite.2022.101904>
- [23] M. Prasad, and Sreekala, "Thermal Effects on Peristaltic Transport in an Inclined Circular Elastic Tube," *Eur. Chem. Bull.* **12**(Special Issue 1), 510–520 (2023). <https://doi.org/10.31838/ecb/2023.12.sa1.048>

АНАЛІЗ КРОВОТОКУ ЧЕРЕЗ НАХИЛЕНУ АРТЕРІЮ, ЯКА МАЄ ЧИСЛЕННИЙ СТЕНОЗ ЗІ ЗМІННОЮ В'ЯЗКІСТЮ НАНОРІДИНИ З ВИКОРИСТАННЯМ ОДНОСТІННОЇ ВУГЛЕЦЕВОЇ НАНОТРУБКИ (SWCNT)

Сайєд Нісар Ахмед^{a,b}, Каранаму Маруті Прасад^a, Р. Шрідеві^c

^aДепартамент математики, школа науки, GITAM (вважається університетом), Хайдарабад, штат Телангана, Індія–502329

^bДепартамент математики, Глобальний інститут інженерії та технології, Чілкур-роуд, штат Телангана, Індія – 501504

^cCYIENT Ltd, штат Телангана, Індія – 500032

Під впливом одностінної вуглецевої нанотрубки (ОСВНТ) досліджено стійкий потік потоку в'язкої рідини через похилу трубу неоднорідного поперечного перерізу з множинними стенозами. Ми лінеаризували рівняння течії та визначили вирази опору течії та напруги зсуву стінки, припускаючи легкі стенози. Дослідження показали, як параметри впливають на змінні потоку. Встановлено, що опір потоку зростає з висотою стенозу. Також цікаво відзначити, що напруга зсуву стінки зменшується зі збільшенням ступеня стенозу. Також спостерігається, що опір потоку (λ') збільшується з нахилом (α), параметром джерела та стоку (β), числом Грасгофа (Br), динамічною в'язкістю (μ) і потоком (q). Профілі швидкостей представлені у вигляді ліній струму.

Ключові слова: стеноз; стійкість до течії; вуглецева нанотрубка; напруга зсуву стінки

ANALYSIS OF THE PROPERTIES OF VACANCY MEDIATED METHYL AMMONIUM LEAD IODIDE PEROVSKITE: A DFT BASED STUDY

 **Md. Abdullah Al Asad^{a*}, Md. Abdul Alim^b, Mst. Halima Khatun^c, Abinash Chandro Sarker^d, Md. Arifur Rahman^e**

^a*Dept. of Electrical and Electronic Engineering, Bangabandhu Sheikh Mujibur Rahman Science and Technology University, Gopalganj, Bangladesh- 8100*

^b*Dept. of Chemistry, Bangabandhu Sheikh Mujibur Rahman Science and Technology University, Gopalganj, Bangladesh- 8100*

^c*Dept. of Physics, Bangabandhu Sheikh Mujibur Rahman Science and Technology University, Gopalganj, Bangladesh- 8100*

^d*Dept. of Chemistry, Begum Rokeya University, Rangpur 5404, Bangladesh*

^e*Dept. of Electrical and Electronic Engineering, First Capital University of Bangladesh, Chuadanga, Bangladesh- 7200*

*Corresponding Author e-mail: dr.asad.eee@gmail.com

Received August 18, 2024; revised October 16, 2024; accepted December 19, 2024

Intrinsic defects have a significant impact on carrier transport properties of Methyl Ammonium Lead Iodide (MAPI) Perovskite $\text{CH}_3\text{NH}_3\text{PbI}_3$. In this paper, we investigated how lead vacancies affect the photovoltaic properties of MAPI using density functional theory (DFT) studies. Lead vacancies in perovskite materials can significantly impact carrier dynamics and device efficiency. Our findings indicate that the lower energy configuration of the Pb vacancy does not create deep trap states that would otherwise reduce carrier lifetime. This suggests that Pb vacancies in MAPI might not be as detrimental to carrier dynamics as previously thought. Pb vacancies could potentially be compensated by other defects or dopants in the material, which might mitigate their negative effects on carrier dynamics. The introduction of a Pb vacancy leads to additional electronic states near the conduction band minimum (CBM) within the fundamental band gap. This indicates that the vacancy introduces localized electronic states that influence carrier behavior. The Highest Occupied Molecular Orbital (HOMO) becomes more localized around the vacant area, while the Least Unoccupied Molecular Orbitals (LUMOs) are only partially localized. This localization around the vacancy does not create strong trapping states that could hinder carrier movement. The presence of vacancies causes atomic movements that result in a more distorted optimized structure. This structural distortion can influence the overall material properties and potentially impact device performance. The HOMO and LUMO levels are primarily derived from the p orbitals of the atoms involved. This highlights the importance of p orbital interactions in determining the electronic properties of the material

Keywords: $\text{CH}_3\text{NH}_3\text{PbI}_3$; Density functional theory; Pb vacancy; Band gap energy; Structural distortion

PACS: 71.15.Mb, 71.20.-b, 61.72.-y

INTRODUCTION

Hybrid organic/inorganic perovskites (HOIPs) have drawn significant research interests due to the incomparable rapid rise in energy conversion efficiency seen in photovoltaic devices based on $\text{CH}_3\text{NH}_3\text{PbI}_3$. Current research attempts in this field have concentrated on searching for similar perovskites with better properties, manifested by good carrier mobility and long carrier lifetime with efficient transport properties. Defects play a vital role in carrier transport in semiconductors [1]. The carrier traps and nonradiative recombination center are basically created due to the presence of deep defect centers which are still detrimental for carrier transportation [1]. A great deal of studies has been examined a large number of native point defects under density functional theory (DFT) [2-5] that show the conflicted results regarding the positions of defect level in $\text{CH}_3\text{NH}_3\text{PbI}_3$. Indeed, a list of particular native defect can introduce deep charge transition in the band gap whenever other native defects have been shown a shallow level of transition. Due to the record of discrepancy outcome in the calculated defect level of $\text{CH}_3\text{NH}_3\text{PbI}_3$, it might be expeditious to reexamine the computational calculation of defected structure. Additionally, the point defects undergo a critical role in determining the electron hole diffusion length which are responsible for non-radiative recombination center [6]. A long electron hole diffusion length resumed the unusual defect properties of $\text{CH}_3\text{NH}_3\text{PbI}_3$. On the other hand, the thermodynamic stability under a humid condition and/or irradiation of $\text{CH}_3\text{NH}_3\text{PbI}_3$ and the formation mechanism of the dominant intrinsic defects are crucial for the efficiency improvement of halide perovskite based thin film solar cells [6]. Therefore, understanding defect properties is immensely important for optimizing the performance of halide perovskite solar cells.

In this letter, we discussed the electronic properties of intrinsic vacancy (Lead) defect of $\text{CH}_3\text{NH}_3\text{PbI}_3$ as the representative material for the methylammonium lead halide (MALHs). More importantly, the defect in $\text{CH}_3\text{NH}_3\text{PbI}_3$ with low formation energy creating only shallow levels can be ascribed to the unique electronic properties through DFT. The HOMO and LUMO level electronic charge distributions both of bulk and defected conditions and their corresponding optimized distorted structure are also considered under this discussion.

Computational Details: All calculations were performed with the Vienna ab initio simulation package (VASP, version 5.4.1), [7] based on DFT and the results were visualized by the VESTA (visualization for electronic and structural

analysis). The projector augmented wave (PAW) method [8] was used to describe the electron-ion interaction with the kinetic energy cutoff set to 600.0 eV. The Brillouin-zone was sampled with a gamma Γ centered k-point grid for structural relaxation. Spin-polarized calculations were performed, using the Perdew-Burke-Ernzerhof (PBE) [9] functional under electronic and ionic self-consistent, with convergence criteria of 10⁻⁸ eV and 10⁻⁷ eV/Å, respectively. In this study, the simple PBE calculation is performed for pristine CH₃NH₃PbI₃ and CH₃NH₃PbI₃ with Pb vacancy mediated defected structure without incorporating the effect of spin-orbit coupling (SOC). We have considered the following valence electrons for the atomic species involved: Pb (5d106s26p2), I (5s25p5), O (2s22p4), N (2s2 2p3), C (2s2 2p2) and H(1s1).

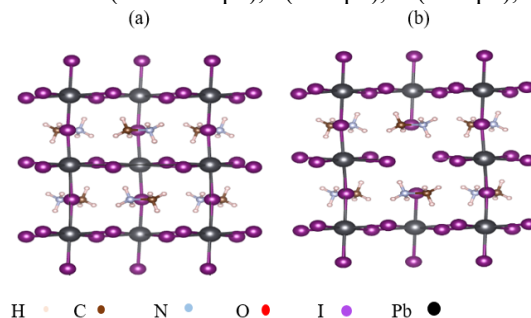


Figure 1. The structures of a) pristine super cell includes 48 atoms and b) defected structure after removing one Pb from the center of the bulk

We reproduced the experimentally verified simple orthorhombic CH₃NH₃PbI₃ super cell that consists of lattice parameter units ($a = 8.836\text{\AA}$, $b = 12.580\text{\AA}$, $c = 8.555\text{\AA}$) at low temperature [10]. The supercell of CH₃NH₃PbI₃ includes 48 atoms where the reference unit cell was fully relaxed until the atomic configuration converged to within convergence criteria. The orthorhombic phase [10] (space group Pm3m) of CH₃NH₃PbI₃ with the optimized supercell structure consisting the geometry of (a) 48-atoms ideal CH₃NH₃PbI₃ and (b) 47-atoms with Pb vacancy mediated defected CH₃NH₃PbI₃ structure as depicted in (Figure 1a,1b) respectively. Here, this elementary Pb vacancy leading structure shows the smallest formation energy, in excellent agreement to search the activation energies for diffusion processes that can be computed from the total energy difference between the diffusing species in their ground-state configuration and at the saddle point of the diffusion process. We found the smallest formation energy by the formula:

$$2\Delta E_{GB,n} = E_{GB,n} - E_{bulk} \quad (1)$$

Where, ΔE_{GB} = energy difference in GB structures, n = consecutive configuration number, E_{bulk} = energy of a bulk system

RESULT AND DISCUSSION

We have examined how Pb vacancies in CH₃NH₃PbI₃ perovskites affect their properties through simulations. The low formation energy of these defects means they are likely to occur and can significantly impact the material's electronic characteristics, which is crucial for optimizing the performance of devices like solar cells. In organic-inorganic MALH crystalline structure, we focus on the role of elemental defects in the perovskite structure, specifically in the context of methylammonium lead iodide (CH₃NH₃PbI₃). The general formula for a perovskite structure is ABX₃, where 'A' and 'B' are cations and 'X' is an anion. In CH₃NH₃PbI₃, 'A' is methylammonium (CH₃NH₃⁺), 'B' is lead (Pb²⁺), and 'X' is iodide (I⁻). Defects such as vacancies (missing atoms) in the perovskite structure can significantly impact its properties. In our case, we are focusing on lead (Pb) vacancies. The formation energy of defects refers to the energy required to create these defects within the crystal lattice. A low formation energy suggests that defects are more likely to occur under certain conditions. To study defects, simulations are often conducted in a supercell, which is a larger unit cell that can accommodate defects while still representing the material's bulk properties. Perovskite materials like CH₃NH₃PbI₃ typically have a low band gap and adjustable Fermi levels, the creation of charged defects is more feasible [4]. These defects can influence the electronic properties of the material, such as conductivity and optical properties.

To investigate the impacts of vacancy defect on electronic properties of CH₃NH₃PbI₃ perovskites, we calculate the density of states (DOS) of pristine crystalline structure as well as defect mediated supercell structure in relaxed conditions. DOS calculations provide valuable information about the electronic structure of both pristine and defected perovskite structures. By comparing the DOS of the ideal (pristine) structure with that of the defected supercell, we observed how the presence of vacancies affects the material's electronic properties. The reduction in the band gap energy for the defected structure indicates that the material's electronic properties are altered by the presence of vacancies. A smaller band gap generally suggests that the material may have increased optical absorption in the visible range, which is beneficial for applications like solar cells. However, this can also lead to increased recombination rates of charge carriers if not properly managed. The absence of new deep trap states within the band gap (as indicated by Figure 2) suggests that the vacancies do not introduce significant mid-gap states that could act as electron or hole traps.

This is a positive aspect, as deep trap states can negatively impact carrier mobility and recombination efficiency. The Valence Band Maximum (VBM) moving slightly downward indicates that the energy of the valence band has been

lowered. This could be due to the creation of localized states near the valence band edge, which can affect the material's ability to absorb light and participate in charge transfer. An additional peak near the Conduction Band Minimum (CBM) appears in defected cell due to the effect of surrounding atom near the vacancy and CBM coming closer to the Fermi level suggests that the conduction band is now more accessible to electrons. This can improve the material's electrical conductivity and make it easier for electrons to transition from the valence band to the conduction band. The extended CBM edges implies that the conduction band states are spread over a wider energy range. This can facilitate better electron transport because the smaller potential barriers and wider band edges allow for more efficient movement of charge carriers. This is beneficial for the overall performance of devices like solar cells, where efficient electron transport is crucial for high power conversion efficiencies.

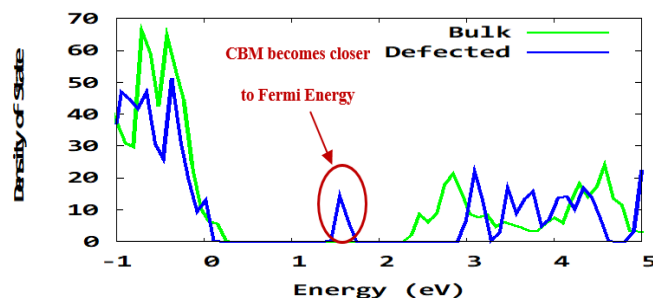


Figure 2. The total density of state (DOS) of bulk and detected structure

To clarify and enhance the accuracy of our findings, we conducted a detailed analysis comparing the Projected Density of States (PDOS) of a representative atom near the defect with that of a non-defective atom in the bulk structure (see Figure 3a and 3b). The additional density of State in Figure 3b is generated due to the charging contribution of surrounding atoms as indicated by red circle. This comparison clearly shows that an additional peak appears in the band gap region of the defected structure, whereas no such peak is present in the pristine material.

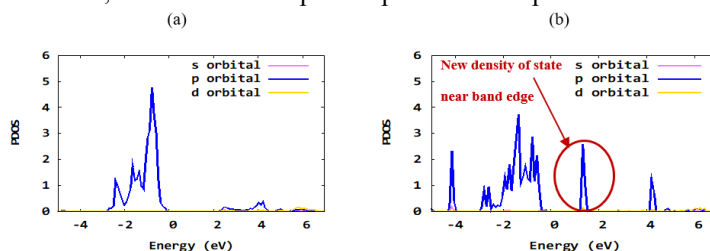


Figure 3. The partial density of state (PDOS) of one the representative atom (Iodine) nearer the vacant area of a) bulk and b) defected structure

We propose that the observed peak in the PDOS is responsible for generating the additional feature in the fundamental energy gap of the defected structure. This phenomenon is consistent with the behavior of shallow dopants [4], which are known to exhibit extended states within the band gap. Since the conduction and valence band edges are primarily contributed by the p orbitals of iodine (I) atoms, the additional charge introduced by vacancy defects creates a shallow level near the band edge that extends throughout the $\text{CH}_3\text{NH}_3\text{PbI}_3$ material. Consequently, it is important to note that vacancy defects are unlikely to act as non-radiative recombination centers.

Figure 4. represents the HOMO and LUMO level charge density distributions of ideal $\text{CH}_3\text{NH}_3\text{PbI}_3$ as well as defected structure, calculated at 0 K using the optimized structure.

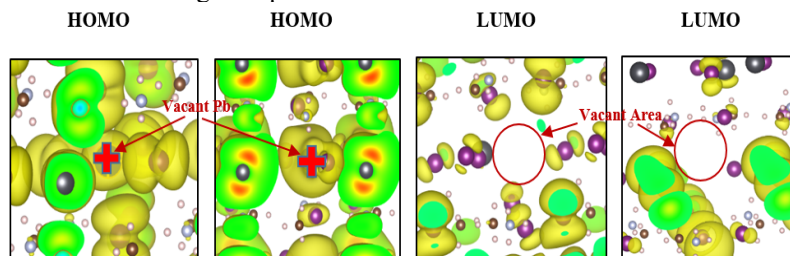


Figure 4. Iso-surface electronic charge distributions of crystalline (left two figures) and defect mediated condition (right two figures)

The charge distributions of both systems reveal the wave function of individuals has no overlapping each with others that mostly composed by orbitals of inorganic atoms. Consequently, the organic group do not show the favor of contribution on electron hole recombination and shows the disabilities to bring the electron and vibrational quanta closer

to resonance. In ideal structure, the HOMO is mostly localized on the iodine atoms with a slight contribution from the lead atoms, while the LUMO is primarily derived from the lead atoms, with some contribution from iodine atoms. This indicates a clear separation of the HOMO and LUMO contributions based on their respective atomic origins. In the presence of a Pb vacancy, both HOMO and LUMO become significantly influenced by the iodine atoms. This suggests that the absence of lead atoms alters the charge distribution, with the electronic charge becoming more concentrated around the vacancy. The HOMO is now more localized around the vacancy area, and while this could indicate a localized trapping site, it actually does not trap carriers dynamically, which is a favorable outcome for electronic and optical properties. The HOMO becomes more localized around the Pb vacancy. However, this localization does not negatively impact carrier dynamics as one might expect in other semiconductor materials with trap states. In fact, this is advantageous because it prevents the formation of detrimental trap states that could reduce solar conversion efficiency. The LUMO remains partially localized, but without the formation of bonding between adjacent atoms as observed in the bulk phase. This implies that the Pb vacancy does not introduce new bonding interactions that could disrupt carrier dynamics. Unlike $\text{CH}_3\text{NH}_3\text{PbI}_3$, conventional semiconductors such as silicon (Si) [11] and cadmium telluride (CdTe) [12] suffer from trap states due to structural defects, which decrease their solar conversion efficiency. The presence of the Pb vacancy in $\text{CH}_3\text{NH}_3\text{PbI}_3$ does not exhibit such detrimental effects, suggesting a superior performance in solar optoelectronic applications. [13]. The Pb vacancy in $\text{CH}_3\text{NH}_3\text{PbI}_3$ leads to significant changes in the charge density distribution of HOMO and LUMO, but these changes are beneficial for the material's performance in solar optoelectronic applications. Unlike traditional semiconductors, the Pb vacancy does not create harmful trap states, making $\text{CH}_3\text{NH}_3\text{PbI}_3$ an efficient material for these applications.

Figure 5. The structural distortions due to the Pb vacancy are compared with the bulk structure to show the changes in geometry. This helps visualize how the defect influences the overall structure and its implications for charge distribution and carrier dynamics. The optimized vacant area shrinks as surrounding atoms move toward the vacancy. This atomic movement is primarily demonstrated by lead atoms, although there are also some organic atoms, though they are relatively far from the inorganic ones. As a result of the vacancy-induced motion, the overall atomic positions are altered, leading to the formation of dangling bonds between unsaturated atoms. Consequently, the organized structure is distorted due to the presence of the vacancy. In this distorted structure, the representative atom indicated by the green arrow contributes to a new density of states near the edge of the Conduction Band Minimum (CBM), as shown in Figure 3(b). This new density of states is consistent with experimental evidence suggesting that intrinsic defects may be prevalent in the MALHs layer [4]. Our theoretical results align with the findings of Edri et al. [14], indicating that MALHs could achieve high-performance photovoltaic operation at a low fabrication cost. Further research on organic-inorganic hybrid materials is needed to identify additional potential candidates for photovoltaic applications.

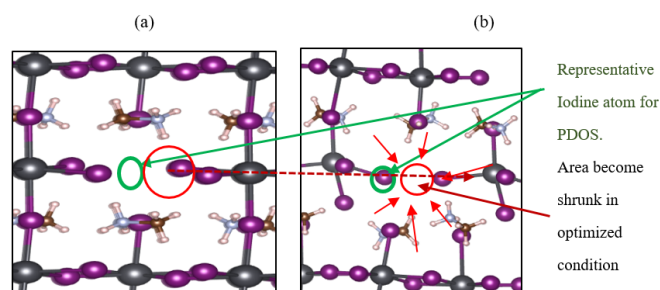


Figure 5. Structural distortion (Fig. 5a); vacancy-oriented movement of surrounding atoms in the optimized structure (Fig. 5b)

CONCLUSION

The Pb vacancy in $\text{CH}_3\text{NH}_3\text{PbI}_3$ does not create deep trap states that could severely impact carrier dynamics but instead introduces shallow states that could potentially influence doping characteristics. The localized nature of the HOMO and LUMO suggests that while there is some localization of electronic states around the vacancy, it does not lead to significant bonding or trapping issues. The structure's adaptation to the vacancy suggests that the material maintains some level of disorder while accommodating the defect.

Funding: No funding was received to assist with the preparation of this manuscript.

Declaration of competing interest:

The authors have no competing interests to declare that are relevant to the content of this article.

ORCID

© Mohammad Abdullah Al Asad, <https://orcid.org/0000-0002-9660-2860>

REFERENCES

- [1] H. Uratani, "Charge Carrier Trapping at Surface Defects of Perovskite Solar Cell Absorbers: A First-Principles Study," *J. Phys. Chem. Lett.* **8**, 4, 742–746 (2017). <https://doi.org/10.1021/acs.jpclett.7b00055>

- [2] X. Zeng, G. Niu, X. Wang, J. Jiang, L. Sui, Y. Zhang, A. Chen, *et al.*, Enhanced carrier transport in CsXSnBr_y perovskite by reducing electron-phonon coupling under compressive strain,” *Materials Today Physics*, **40**, 101296 (2024). <https://doi.org/10.1016/j.mtphys.2023.101296>
- [3] H. H. Otto, “Pyroelectric Bi_{1-x}(Bi₂S₃)₃₉I₁₂S: Fibonacci Superstructure, Synthesis Options and Solar Cell Potential,” *World Journal of Condensed Matter Physics*, **5**, 2, (2015). <https://www.scirp.org/journal/papercitationdetails?paperid=55984&JournalID=502>
- [4] J. Kim, S.H. Lee, J.H. Lee, and K.H. Hong, “The Role of Intrinsic Defects in Methylammonium Lead Iodide Perovskite,” *J. Phys. Chem. Lett.* **5**, 1312–1317 (2014), <https://doi.org/10.1021/jz500370k>
- [5] M.L. Ali, M. Khan, M.A.A. Asad, and M.Z. Rahaman, “Highly efficient and stable lead-free cesium copper halide perovskites for optoelectronic applications: A DFT based study,” *Heliyon*, **9**, e18816 (2023). <https://doi.org/10.1016/j.heliyon.2023.e18816>
- [6] I. Ullah, M.A. Hossain, A. Armghan, M.S. Rana, and M.A.A. Asad, “The optoelectronic enhancement in perovskite solar cells using plasmonic metal-dielectric core-shell and nanorod nanoparticles,” *Optical and Quantum Electronics*, **55**, 1018 (2023). <https://doi.org/10.1007/s11082-023-05252-3>
- [7] J. Hafner, “Ab-initio simulations of materials using VASP: Density-functional theory and beyond,” *J. Comput. Chem.* **29**, 2044–2078 (2008). <https://doi.org/10.1002/jcc.21057>
- [8] P.E. Blöchl, “Projector augmented-wave method,” *Physical Review B*, **50**, 17953–17979 (1994). <https://doi.org/10.1103/PhysRevB.50.17953>
- [9] J. Perdew, K. Burke, and M. Ernzerhof, Generalized Gradient Approximation Made Simple, *Phys. Rev. Lett.* **77**, 3865 (1996). <https://doi.org/10.1103/PhysRevLett.77.3865>
- [10] M.A.A. Asad, “Investigation of the Structural with Electronic Properties of Methylammonium Lead Iodide Perovskite Using Density Functional Theory,” *International Journal of Material and Mathematical Sciences*, **4**(6), 107–113 (2022). <https://doi.org/10.34104/ijmms.022.01070113>
- [11] R. Raghunathan, E. Johlin, and J. C. Grossman, “Grain Boundary Engineering for Improved Thin Silicon Photovoltaics,” *Nano Lett.* **14**, 4943–4950 (2014). <https://doi.org/10.1021/nl501020q>
- [12] T. Fiducia, A. Howkins, A. Abbas, B. Mendis, A. Munshi, K. Barth, W. Sampath, and John Walls, “Selenium passivates grain boundaries in alloyed CdTe solar cells,” *Solar Energy Materials and Solar Cells*, **238**, 111595 (2022). <https://doi.org/10.1016/j.solmat.2022.111595>
- [13] Y. Guo, Q. Wang, and W. A. Saidi, “Structural Stabilities and Electronic Properties of High-Angle Grain Boundaries in Perovskite Cesium Lead Halides,” *J. Phys. Chem. C*, **121**, 1715–1722 (2017). <https://doi.org/10.1021/acs.jpcc.6b11434>
- [14] Edri, E. Kirmayer, S. Henning, A. Mukhopadhyay, S. Gartsman, K. Rosenwaks, Y. Hodes, G.; Cahen, D. “Why Lead Methylammonium Tri-Iodide Perovskite-Based Solar Cells Require a Mesoporous Electron Transporting Scaffold (but Not Necessarily a Hole Conductor),” *Nano Lett.* **14**, 1000–1004. (2014), <https://doi.org/10.1021/nl404454h>

АНАЛІЗ ВЛАСТИВОСТЕЙ ПЕРОВСКІТУ МЕТИЛАММОНІЮ ЙОДИДУ СВИНЦЯ, ОПОСЕРЕДКОВАНОГО ВАКАНСІЯМИ: ДОСЛІДЖЕННЯ НА ОСНОВІ DFT

М. Абдулла Аль Асад^a, М. Абдул Алім^b, Мс. Халіма Хатун^c, Абінаш Чандро Саркер^d, М. Аріфур Рахман^e

^aДепартамент електротехніки та електронної інженерії, Науково-технічний університет імені шейха Муджибора Рахмана Бангабандху, Гопалгандж, Бангладеш

^bДепартамент хімії, Науково-технологічний університет імені шейха Муджибора Рахмана Бангабандху, Гопалгандж, Бангладеш

^cДепартамент фізики, Науково-технічний університет імені шейха Муджибура Рахмана Бангабандху, Гопалгандж, Бангладеш

^dДепартамент хімії, Університет Бежум Рокея, Рангпур, Бангладеш

^eДепартамент електротехніки та електронної інженерії, Перший столичний університет Бангладеш, Чуаданга, Бангладеш

Внутрішні дефекти мають значний вплив на транспортні властивості перовскіту CH₃NH₃PbI₃ метиламонію йодиду свинцю (МАРІ). У цій статті ми досліджували, як вакансії свинцю впливають на фотоелектричні властивості МАРІ, використовуючи дослідження теорії функціоналу густини (DFT). Вакансії свинцю в перовскітних матеріалах можуть суттєво впливати на динаміку носія та ефективність пристрою. Наші висновки показують, що нижча енергетична конфігурація вакансії Pb не створює станів глибокої пастки, які в іншому випадку зменшили б час життя носія. Це свідчить про те, що вакансії свинцю в МАРІ можуть бути не такими шкідливими для динаміки носія, як вважалося раніше. Вакансії Pb потенційно можуть бути компенсовані іншими дефектами або легуючими речовинами в матеріалі, що може пом'якшити їхній негативний вплив на динаміку носія. Введення вакансії Pb призводить до додаткових електронних станів поблизу мінімуму зони провідності (CBM) у фундаментальній забороненій зоні. Це вказує на те, що вакансія вводить локалізовані електронні стани, які впливають на поведінку носія. Найвища зайнята молекулярна орбіталь (НОМО) стає більш локалізованою навколо вакантної області, тоді як найменш незайняті молекулярні орбіталі (LUMO) локалізовані лише частково. Ця локалізація навколо вакансії не створює сильних станів захоплення, які могли б перешкоджати руху носія. Наявність вакансій викликає переміщення атомів, що призводить до більш спотвореної оптимізованої структури. Це структурне спотворення може вплинути на загальні властивості матеріалу та потенційно вплинути на продуктивність пристрою. Рівні НОМО і LUMO в основному походять від р-орбіталей залучених атомів. Це підкреслює важливість р-орбітальних взаємодій у визначенні електронних властивостей матеріалу.

Ключові слова: CH₃NH₃PbI₃; теорія функціоналу густини; вакансія Pb; енергія забороненої зони; структурне спотворення

A NEW FOURTH-ORDER COMPRESSION-DEPENDENT EQUATION OF STATE

Abhay P. Srivastava^a,  Brijesh K. Pandey^a,  Anod Kumar Singh^b, Reetesh Srivastava^c

^aDepartment of Physics & Material Science, Madan Mohan Malviya University of Technology, Gorakhpur (UP), India

^bDepartment of Humanities and Applied Science, School of Management Sciences, Lucknow, (UP), India

^cDepartment of Physics, Nandini Nagar P.G. College, Nawabganj, Gonda, (UP), India

Corresponding author e-mail: abhay.srivastava831@gmail.com

Received October 7, 2024; revised November 20, 2024; accepted December 16, 2024

This study introduces a new first- to fourth-order exponential equation of state (EOS) to enhance accuracy across varying compression levels. The proposed exponential EOS is compared to the widely used fourth-order Birch-Murnaghan EOS, and it not only matches but surpasses precision, especially at high compression. This comparison serves as a clear benchmark for the readers to understand the superiority of the new model. The findings of this study are crucial, as they reveal that the fourth-order exponential EOS provides an unmatched accuracy level at higher compression, notably for materials like HCP-iron and sodium halides. The Birch-Murnaghan EOS, though effective at low compression, deviates from experimental values at higher levels. Additionally, the study examines the Shanker EOS, in which M. Kumar et al. [Physica B: Condensed Matter, 239(3-4), 337-344 (1997)] suggest the requirement to improve at high compression and improve by fitting parameters that vary from material to material. This limitation is removed by developing the fourth-order exponential EOS, which is more versatile, offering reliable results across both low- and high-compression scenarios in high-pressure physics.

Keywords: Equation of state; Compression; Fourth-order exponential equation of state; Birch-Murnaghan fourth-order equation of state

PACS: 64.10.+h, 62.20.de

1. Introduction

Equations of state (EOS) play a crucial role in understanding how materials respond to changes in pressure and volume, particularly within materials science, condensed matter physics, geophysics, and planetary science. Our study aims to develop and compare different EOS models to better understand their effectiveness in high-pressure scenarios. These relationships are essential for delving into high-pressure physics, technological materials, and planetary interiors, as they allow scientists to predict and model how materials might behave under extreme conditions, such as compression, expansion, or phase changes [1-3].

Traditionally, the Birch-Murnaghan equation of state (BM-EOS) has been the go-to formula for characterizing the compressional behavior of solids. However, as experimental techniques have advanced and allowed for a broader range of pressure exploration, it has become evident that traditional EOS models like the BM-EOS have significant limitations. Calculated values deviate from experimental results at high pressures, particularly under exceptionally high compression [4-6].

A novel approach has been proposed to address the limitations of traditional EOS models: the fourth-order exponential equation of state. This innovative formulation, incorporating higher-order adjustments and an exponential element, aims to significantly enhance the accuracy and applicability of EOS under extreme conditions. It offers a more precise and versatile depiction of the pressure-volume relationship, marking a significant advancement in the field and providing researchers with a powerful tool for their studies [7-10].

Our upcoming study aims to develop exponential equations of state (EOS) from first to fourth order and assess their efficacy in calculating pressure under high compression. Our primary goal is to compare the effectiveness of the novel fourth-order exponential EOS with the widely used Birch-Murnaghan EOS and available experimental data. We seek to identify their respective advantages and limitations by comprehensively analyzing each model's mathematical framework, accuracy, parameter sensitivity, and applicability in high-pressure scenarios [11-12].

Our research is poised to have a significant impact, with potential applications in fields like shockwave physics and planetary science, as well as studying materials under ultrahigh pressure. By delving into the theoretical foundations of the fourth-order exponential EOS and the Birch-Murnaghan EOS, we aim to evaluate their performance across various materials and pressure ranges. Our findings could significantly enhance the precision of high-pressure material modelling and open up new avenues for exploration, thereby underlining the importance of our research in these fields [13-15]. This potential impact should make you feel the significance of our study in these fields.

Furthermore, we will explore the work of Kumar et al. [16], who proposed modifying the Shanker EOS [17] by introducing fitting parameters, as well as the efforts of Srivastava-Pandey [20], who increased accuracy by considering third-order compression and the anharmonic effect of solids. However, limitations in accuracy were identified at high compression. In our study, we have derived first-to-fourth-order exponential equations of state, observing an improvement in accuracy by increasing the order of compression in the equation of state. For the validity of the work, we have taken the sample ϵ -Fe, NaF, NaCl, NaBr, and NaI and tested up to the pressure range of 3595 kbar.

2. THEORY AND METHODOLOGY

The general equation by which we can derive the equation of state by the Gruneisen model is expressed as [17]:

$$P \left(\frac{V}{V_0} \right)^{4/3} = - \frac{B_0}{f_0 V_0} \int_{V_0}^V f dV,$$

$$P = - \left(\frac{V}{V_0} \right)^{-4/3} \frac{B_0}{f_0 V_0} \int_{V_0}^V f dV. \quad (1)$$

The equation (1) is the fundamental equation for deriving an EOS [17]. This formulation applies to all EOS for various types of solids and different potential functions. Shanker et al. [17] demonstrated that equation (1) produces the Born-Mie EOS [18] and the Brenan-Stacey EOS [19].

Let a potential function be given by

$$f = \frac{V_0}{V} \exp \alpha \left(1 - \frac{V}{V_0} \right).$$

Let $y = 1 - \frac{V}{V_0}$ then

$$f = (1-y)^{-1} \exp(\alpha y), \quad f = (1+y+y^2+y^3+\dots)\exp(\alpha y). \quad (2)$$

At $V = V_0$, $f = f_0 = 1$ and $P = 0$, Then equation (1) becomes:

$$P = B_0 \left(\frac{V}{V_0} \right)^{-4/3} \int_0^y (1+y+y^2+y^3+\dots)e^{\alpha y} dy. \quad (3)$$

2.1. First-order exponential equation of state:

For first order equation of state equation (3) can be written as:

$$P = B_0 \left(\frac{V}{V_0} \right)^{-4/3} \int_0^y (1+y)e^{\alpha y} dy. \quad (4)$$

On the integration of equation (4), we get the expression for pressure as a function of compression:

$$P = B_0 \left(\frac{V}{V_0} \right)^{-4/3} \left[\frac{(\alpha y + \alpha - 1)e^{\alpha y} - (\alpha - 1)}{\alpha^2} \right]. \quad (5)$$

Equation (5) represents first-order which is newly derived.

At $V = V_0$ then $P = 0$. Hence, equation (4) satisfies the condition of the equation of state and is valid according to the Stacey criterion [19].

The bulk modulus of the solid is given by:

$$B_T = -V \frac{dP}{dV} \quad (6)$$

Using equations (5) and (6), we can find bulk modulus corresponding to equation (5) as:

$$B_T = B_0 \left(\frac{V}{V_0} \right)^{-1/3} (1+y)\exp(\alpha y) + \frac{4}{3}P. \quad (7)$$

The first-order pressure derivative of bulk modulus $\left(\frac{dB_T}{dP} \right)$ Corresponding to equation (6) is given by:

$$B'_T = \left(1 - \frac{4P}{3B_T} \right) \left(\frac{1}{3} + \frac{V}{V_0} \left\{ \alpha + \frac{1}{(1+y)} \right\} \right) + \frac{4}{3} \quad (8)$$

The value of α is determined to form B'_0 , the zero-pressure value of $\frac{dB_T}{dP}$ at $V = V_0$. Using equation (8), we get:

$$\alpha = \frac{3B'_0 - 8}{3}. \quad (9)$$

2.2. Second-order exponential equation of state

For second order equation of state equation (3) can be written as:

$$P = B_0 \left(\frac{V}{V_0} \right)^{-4/3} \int_0^y (1 + y + y^2) e^{\alpha y} dy. \quad (10)$$

On integration equation (10), give Shanker equation of state [17]:

$$P = B_0 \left(\frac{V}{V_0} \right)^{-4/3} \left[\frac{\left\{ \alpha^2 y^2 + (\alpha^2 - 2\alpha)y + \alpha^2 - \alpha + 2 \right\} e^{\alpha y} - (\alpha^2 - \alpha + 2)}{\alpha^3} \right]. \quad (11)$$

Where $\alpha = \frac{3B'_0 - 8}{3}$. At $V = V_0$ then $P = 0$. Hence, equation (11) satisfies the condition of the equation of state and is valid according to the Stacey criterion. Equation (11) represents a second-order exponential equation of state (Shanker EOS) [17].

2.3. Third-order exponential equation of state

For third order equation of state equation (3) can be written as:

$$P = B_0 \left(\frac{V}{V_0} \right)^{-4/3} \int_0^y (1 + y + y^2 + y^3) e^{\alpha y} dy. \quad (12)$$

On integration equation (12), we can find Srivastava-Pandey EOS as [20]:

$$P = \frac{B_0}{\alpha^4} \left(\frac{V}{V_0} \right)^{-4/3} \left[\left\{ \alpha^3 (1 + y + y^2 + y^3) + \alpha^2 (-3y^2 - 2y - 1) + \alpha (6y + 2) - 6 \right\} e^{\alpha y} - (\alpha^3 - \alpha^2 + 2\alpha - 6) \right]. \quad (13)$$

Where $\alpha = \frac{3B'_0 - 8}{3}$. At $V = V_0$ then $P = 0$. Hence, equation (13) satisfies the condition of the equation of state and is valid according to the Stacey criterion. Equation (13) represents a third-order exponential equation of state (Srivastava-Pandey EOS) [20].

2.4. Fourth-order exponential equation of state

Due to complex integration, Shanker and Srivastava refused to solve the fourth-order equation of state, but due to including fourth-order compression, we include translators and vibrational, rotational and anharmonicity properties of solids; therefore, its accuracy increases than others. Now, further expand the equation (3) up to the fourth order to develop a new fourth-order equation of state. Thus, equation (3) can be written as:

$$P = B_0 \left(\frac{V}{V_0} \right)^{-4/3} \int_0^y (1 + y + y^2 + y^3 + y^4) e^{\alpha y} dy. \quad (14)$$

On integration equation (10), we can find EOS as follows:

$$P = \left[\frac{B_0}{\alpha^5} \left(\frac{V}{V_0} \right)^{-4/3} \right] \times \left[\left\{ \begin{aligned} &\alpha^4 y^4 + (\alpha^4 - 4\alpha^3)y^3 + (\alpha^4 - 3\alpha^3 + 12\alpha^2)y^2 + \\ &(\alpha^4 - 2\alpha^3 + 6\alpha^2 - 24\alpha)y + \\ &(\alpha^4 - \alpha^3 + 2\alpha^2 - 6\alpha + 24) \end{aligned} \right\} e^{\alpha y} - (\alpha^4 - \alpha^3 + 2\alpha^2 - 6\alpha + 24) \right]. \quad (15)$$

Where $\alpha = \frac{3B'_0 - 8}{3}$. At $V = V_0$ then $P = 0$. Hence, equation (15) satisfies the condition of the equation of state and is valid according to the Stacey criterion. Equation (15) represents the fourth-order exponential equation of state.

2.5. Birch-Murnaghan fourth order equation of state

The fourth-order Birch-Murnaghan equation of state extends the original model to include higher-order pressure-volume terms, improving accuracy for describing material behaviour under extreme compression. The fourth order Birch-Murnaghan EOS can be expressed as [21]:

$$P = \frac{3}{2} B_0 \left[x^{-7/3} - x^{-5/3} \right] \left[1 + \frac{3}{4} (B'_0 - 4) (x^{-2/3} - 1) + \frac{1}{24} \left\{ 9B_0'^2 - 63B'_0 - 9B_0 \left(\frac{1}{9B_0} (9B_0'^2 - 63B'_0 + 143) \right) (x^{-2/3} - 1)^2 \right\} \right]. \quad (16)$$

Where $x = \frac{V}{V_0}$.

Equations (5), (11), (13), (15), and (16) calculate the pressure of solids at different compressions.

In a past study, obtaining a fourth-order equation was described as impossible because it does not follow the general condition of the equation of state, and researchers derive the third-order compression-dependent equation. This statement was wrong. In this study, a fourth-order compression-dependent equation is derived, following the condition of the equation of state. By including fourth-order compression, the accuracy of the equation of state increases [22].

Table 1. Input parameters used in the present work.

Solids	K_0 (kbar)	K'_0
ϵ -Fe	1750 [23]	5.3 [23]
NaF	465 [24]	5.28 [24]
NaCl	240 [24]	5.39 [24]
NaBr	199 [24]	5.46 [24]
NaI	151 [24]	5.59 [24]

Table 2. Calculated values of pressure P(kbar) for (A) first-order exponential EOS, (B) second-order exponential EOS (Shanker EOS), (C) third-order exponential EOS (Srivastava-Pandey EOS), (D) fourth-order exponential EOS (present study) (E) fourth order Birch-Murnaghan EOS (B-M EOS) and with experimental data for ϵ -Fe.

V/V ₀	1 st order EOS	2 nd order EOS	3 rd order EOS	4 th order EOS	4 th Order B-M EOS	Experimental [25]
1.000	0.0	0.0	0.0	0.0	0.0	0.0
0.877	322.4	324.1	324.2	324.3	325.4	299.6
0.862	381.0	383.4	383.7	383.7	385.4	355.6
0.847	445.0	448.6	449.0	449.0	451.5	417.5
0.832	515.2	520.1	520.7	520.8	524.4	486.2
0.817	592.0	598.7	599.7	599.8	604.9	562.2
0.802	676.0	685.1	686.4	686.7	693.7	646.4
0.788	761.7	773.4	775.3	775.6	785.0	739.9
0.773	861.9	877.1	879.7	880.2	892.9	843.8
0.758	971.7	991.1	994.7	995.5	1012.3	959.2
0.743	1092.0	1116.6	1121.5	1122.5	1144.6	1087.6
0.728	1223.8	1254.7	1261.3	1262.7	1291.5	1230.5
0.713	1368.3	1406.9	1415.5	1417.5	1454.8	1390.0
0.698	1526.9	1574.5	1585.7	1590.5	1636.4	1568.0
0.684	1688.7	1746.5	1760.7	1792.4	1824.6	1767.1
0.669	1878.6	1949.1	1967.3	1998.2	2048.8	1989.9
0.654	2087.2	2172.8	2195.9	2229.5	2299.4	2239.8
0.639	2316.6	2419.9	2449.2	2496.8	2580.1	2520.6
0.624	2568.9	2693.3	2729.9	2798.3	2894.9	2836.5
0.609	2846.8	2995.8	3041.5	3168.3	3248.8	3192.6
0.594	3153.0	3330.9	3387.7	3496.8	3647.5	3595.0

Table 3. Calculated values of pressure P(kbar) for (A) first-order exponential EOS, (B) second-order exponential EOS (Shanker EOS), (C) third-order exponential EOS (Srivastava-Pandey EOS), (D) fourth-order exponential EOS (present study) (E) fourth order Birch-Murnaghan EOS (B-M EOS) and with experimental data for NaF.

V/V ₀	1 st order EOS	2 nd order EOS	3 rd order EOS	4 th order EOS	4 th Order B-M EOS	Experimental [26,27]
1.000	0.0	0.0	0.0	0.0	0.0	0.0
0.980	9.7	9.8	9.8	9.8	9.8	10.0
0.962	19.8	19.8	19.8	19.8	19.8	20.0
0.946	29.7	29.7	29.7	29.7	29.8	30.0
0.932	39.4	39.5	39.5	39.5	39.5	40.0
0.868	94.7	95.3	95.3	95.3	95.7	94.0
0.832	136.6	137.9	138.1	138.1	139.1	140.0
0.804	176.1	178.5	178.8	178.9	180.7	180.0
0.782	212.2	215.7	216.2	216.3	219.2	210.0
0.778	219.3	223.0	223.6	223.8	226.8	224.0

Table 4. Calculated values of pressure P(kbar) for (A) first-order exponential EOS, (B) second-order exponential EOS (Shanker EOS), (C) third-order exponential EOS (Srivastava-Pandey EOS), (D) fourth-order exponential EOS (present study) (E) fourth order Birch-Murnaghan EOS (B-M EOS) and with experimental data for NaCl.

V/V ₀	1 st order EOS	2 nd order EOS	3 rd order EOS	4 th order EOS	4 th Order B-M EOS	Experimental [26,27]
1.000	0.0	0.0	0.0	0.0	0.0	0.0
0.963	10.1	10.1	10.1	10.1	10.1	10.0
0.933	20.2	20.2	20.2	20.2	20.2	20.0
0.907	30.5	30.6	30.6	30.6	30.6	30.0
0.883	41.5	41.7	41.8	41.8	41.9	40.0
0.760	132.8	135.4	135.9	136.0	138.1	135.0
0.702	206.6	212.9	214.4	214.8	220.6	200.0
0.697	214.3	221.1	222.7	223.1	229.5	220.0
0.675	251.3	260.4	262.7	263.3	272.5	250.0
0.658	283.5	294.9	298.0	298.9	310.9	290.0

Table 5. Calculated values of pressure P(kbar) for (A) first-order exponential EOS, (B) second-order exponential EOS (Shanker EOS), (C) third-order exponential EOS (Srivastava-Pandey EOS), (D) fourth-order exponential EOS (present study) (E) fourth order Birch-Murnaghan EOS (B-M EOS) and with experimental data for NaBr.

V/V ₀	1 st order EOS	2 nd order EOS	3 rd order EOS	4 th order EOS	4 th Order B-M EOS	Experimental [25,26]
1.000	0.0	0.0	0.0	0.0	0.0	0.0
0.956	10.1	10.1	10.1	10.1	10.1	10.0
0.921	20.6	20.6	20.6	20.6	20.6	20.0
0.891	31.1	31.3	31.3	31.3	31.4	30.0
0.866	41.8	42.1	42.1	42.1	42.3	40.0
0.746	124.2	127.0	127.5	127.6	129.7	130.0
0.725	146.0	149.8	150.6	150.8	153.9	160.0
0.663	230.1	239.2	241.6	242.2	251.1	240.0
0.633	284.5	297.8	301.6	302.8	317.0	290.0
0.616	320.4	336.7	341.7	343.2	361.7	340.0

Table 6. Calculated values of pressure P(kbar) for (A) first-order exponential EOS, (B) second-order exponential EOS (Shanker EOS), (C) third-order exponential EOS (Srivastava-Pandey EOS), (D) fourth-order exponential EOS (present study) (E) fourth order Birch-Murnaghan EOS (B-M EOS) and with experimental data for NaI.

V/V ₀	1 st order EOS	2 nd order EOS	3 rd order EOS	4 th order EOS	4 th Order B-M EOS	Experimental [26,27]
1.000	0.0	0.0	0.0	0.0	0.0	0.0
0.942	10.6	10.6	10.6	10.6	10.6	10.0
0.899	21.5	21.6	21.6	21.6	21.6	20.0
0.865	32.4	32.6	32.7	32.7	32.8	30.0
0.836	43.7	44.1	44.2	44.2	44.4	40.0
0.694	142.9	147.6	148.7	149.0	152.6	150.0
0.648	199.7	208.4	210.7	211.4	219.2	210.0
0.641	210.0	219.4	222.1	222.9	231.5	230.0
0.609	263.3	277.4	281.7	283.1	297.6	280.0
0.599	282.5	298.4	303.4	305.1	322.0	310.0

3. RESULT AND DISCUSSION

In the past, researchers have noted that the accuracy of the equation of state improves with an increase in the order of compression. Birch-Murnaghan's fourth-order equation of state was a significant development in this regard. However, our study proposes a novel approach—a first—to the fourth-order exponential equation of state. This new equation promises to provide more precise insight into the results as we compare it with Birch-Murnaghan's equation and the available experimental values [24-26].

Our research is built on a foundation of thorough calculations. We have utilised equations (5), (11), (13), (15), and (16) to calculate the pressure at different compressions, which are listed in Tables 2-6, along with the associated experimental values and references. The input values employed in the calculation can also be found in Table 1, with corresponding references. To enhance clarity, we have plotted a graph showing the relationship between pressure at different compressions, as illustrated in Fig 1-5.

The HCP-iron is known for its exceptional strength and high binding energy per nucleon, indicated by its remarkably high bulk modulus at zero pressure. Regarding low compression, various equations of state (EOS) and the Birch-Murnaghan fourth-order equation tend to produce results that exceed experimental values. However, at higher compression, the fourth-order exponential EOS yields results that closely match experimental values, while the Birch-Murnaghan equation produces results that surpass experimental data. Essentially, the accuracy of the fourth-order

exponential equation of state is improved at high compression, while the accuracy of the Birch-Murnaghan equation decreases. At low compression, all EOS produce similar results.

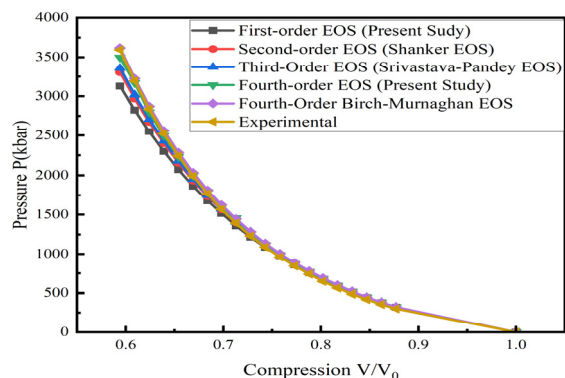


Figure 1. Variation of pressure with increasing compression of ϵ -Fe

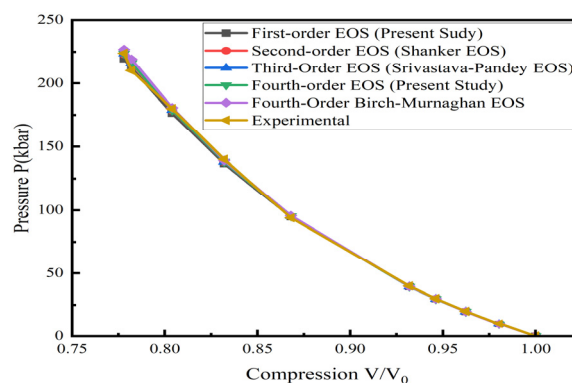


Figure 2. Variation of pressure with growing compression of NaF

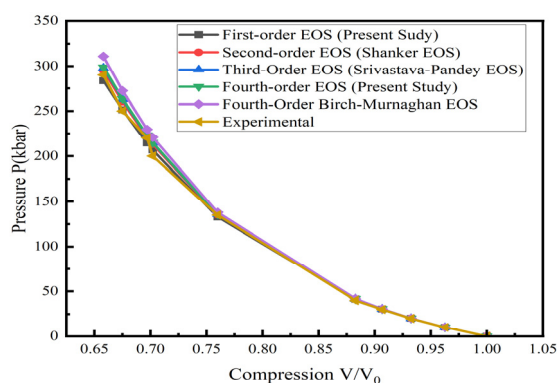


Figure 3. Variation of pressure with increasing compression of NaCl

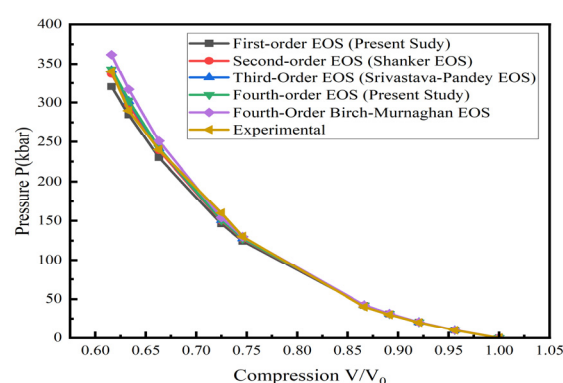


Figure 4. Variation of pressure with increasing compression of NaBr

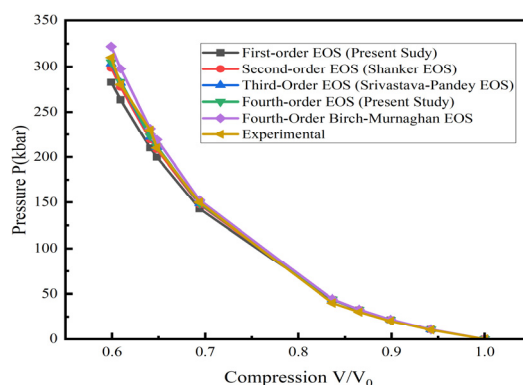


Figure 5. Variation of pressure with increasing compression of NaI

In the case of sodium halides, all EOS and Birch-Murnaghan EOS provide similar results. Still, when compression increases, deviation in Birch-Murnaghan EOS increases, whereas the fourth-order exponential equation of state goes towards better accuracy, as seen in Table 3-6 and Figure 2-5. From the above discussion, we conclude that first- and second-order exponential equations can be used to calculate compression-dependent pressure at low compression. Still, at high compression, the fourth-order exponential equation of state is better than other orders and Birch-Murnaghan EOS.

The Birch-Murnaghan equation of state (EOS) is suitable only for HCP-iron. However, at higher compression, it starts to deviate from experimental data. On the other hand, the fourth-order exponential EOS closely matches experimental results at higher compression, indicating its superior accuracy compared to other EOS models. It performs similarly at low compression but shows increased accuracy at high compression. Therefore, the fourth-order exponential equation of state can be utilised effectively at both low and high compression, highlighting its significance in high-pressure solid-state physics.

The second-order exponential equation of state is also known as the Shanker EOS. In a study by M. Kumar et al. [16], it was suggested that the accuracy of the Shanker EOS at high compression be enhanced by introducing a fitting parameter. The value of the fitting parameter varies for different solids. The Srivastava-Pandey EOS [20]

overcomes this limitation by incorporating higher-order compression and anharmonic vibrations of solids. However, accuracy is significantly improved by including fourth-order compression. The fourth-order EOS includes symmetric and asymmetric vibrations at high compressions, significantly increasing accuracy.

4. CONCLUSION

The study presents a first- to fourth-order exponential equation of state (EOS) to enhance the accuracy of pressure calculations under varying compressions, comparing it with the Birch-Murnaghan equation. At low compression, all EOS, including Birch-Murnaghan, produce similar results. However, the fourth-order exponential EOS shows better accuracy at higher compression, while the Birch-Murnaghan EOS deviates from experimental values. The fourth-order exponential EOS proves more reliable for HCP-iron and sodium halides, especially at high compressions. The study concludes that the fourth-order exponential EOS is suitable for both low and high compressions, offering improvements over existing models, such as Shanker and Srivastava-Pandey EOS, by incorporating higher-order compression and anharmonic vibrations for greater accuracy in high-pressure physics.

Ethical Approval:

The authors confidently declare that the manuscript is their original work and has not been published elsewhere.

Competing interests:

The authors of this paper explicitly confirm that they have no financial interests or personal relationships, such as employment, consultancies, stock ownership, honoraria, paid expert testimony, patent applications/registrations, and grants or other funding that could potentially influence the work presented in this report.

Author's Contribution:

All authors were engaged in developing the research outline, with Abhay P. Srivastava taking charge of all calculations and the initial draft of the manuscript. Meanwhile, Professor B. K. Pandey played a pivotal role by offering resources and providing guidance throughout the project.

Funding:

The authors have stated that they do not have any funding from an agency.

Availability of data and Materials:

You can rest assured that the study's conclusions are backed by information in the references and readily accessible to the public.

ORCID

©Brijesh K. Pandey, <https://orcid.org/0000-0002-7999-4743>; ©Anod Kumar Singh, <https://orcid.org/0000-0001-5934-923X>

REFERENCES

- [1] S.R. Baty, L. Burakovsky, and D. Errandonea, "Ab initio phase diagram of copper," *J. Phys. Condens. Matter*, **11**(48), 1–14 (2021). <https://doi.org/10.3390/cryst11050537>
- [2] P. Singh, B.K. Pandey, S. Mishra, and A.P. Srivastava, "Formulation for the melting temperature prediction of metallic solids using suitable equation of states," *Comput. Condens. Matter*, **35**, e00807 (2023). <https://doi.org/10.1016/j.cocom.2023.e00807>
- [3] J. Gal, "ab Initio DFT and MD Simulations Serving as an Anchor for Correcting Melting Curves Reported by DAC and SW Experiments—Some Transition Metals as Illustrative Examples," *Crystals*, **13**(8), (2023). <https://doi.org/10.3390/cryst13081263>
- [4] P. Parisiades, "A review of the melting curves of transition metals at high pressures using static compression techniques," *Crystals*, **11**(4), (2021). <https://doi.org/10.3390/cryst11040416>
- [5] J. Shanker, M.P. Sharma, and S.S. Kushwah, "Analysis of melting of ionic solids based on the thermal equation of state," *J. Phys. Chem. Solids*, **60**(5), 603–606 (1999). [https://doi.org/10.1016/S0022-3697\(98\)00323-0](https://doi.org/10.1016/S0022-3697(98)00323-0)
- [6] K. Kholiya, and J. Chandra, "A theoretical model to study the melting of metals under pressure," *Mod. Phys. Lett. B*, **29**(27), (2015). <https://doi.org/10.1142/S0217984915501614>
- [7] S. Kumar, A. Kumar, S. Abbas, M. Al Qurashi, and D. Baleanu, "A modified analytical approach with existence and uniqueness for fractional Cauchy reaction-diffusion equations," *Adv. Differ. Equations*, **2020**(1), (2020). <https://doi.org/10.1186/s13662-019-2488-3>
- [8] S. Kumar, K.S. Nisar, R. Kumar, C. Cattani, and B. Samet, "A new Rabotnov fractional-exponential function-based fractional derivative for diffusion equation under external force," *Math. Methods Appl. Sci.* **43**(7), 4460–4471 (2020). <https://doi.org/10.1002/mma.6208>
- [9] S. Kumar, R. Kumar, R.P. Agarwal, and B. Samet, "A study of fractional Lotka-Volterra population model using Haar wavelet and Adams-Bashforth-Moulton methods," *Math. Methods Appl. Sci.* **43**(8), 5564–5578 (2020). <https://doi.org/10.1002/mma.6297>
- [10] R.S. Chauhan, K. Lal, and C. P. Singh, "Pressure dependence of melting temperature in alkali halides," *Phys. B Condens. Matter*, **396**(1-2), 211–213 (2007). <https://doi.org/10.1016/j.physb.2007.04.006>
- [11] I.Y. Alkammash, "Evaluation of pressure and bulk modulus for alkali halides under high pressure and temperature using different EOS," *J. Assoc. Arab Univ. Basic Appl. Sci.* **14**(1), 38–45 (2013). <https://doi.org/10.1016/j.jaubas.2013.01.001>
- [12] Z. Wang, P. Lazor, and S.K. Saxena, "The analysis on high pressure melting temperature dependence of the thermodynamic parameters of solids," *Mater. Lett.* **49**(5), 287–293 (2001). [https://doi.org/10.1016/S0167-577X\(00\)00386-4](https://doi.org/10.1016/S0167-577X(00)00386-4)
- [13] C. Nie, "Pressure derivative of the melting temperature for some alkali halides," *Can. J. Phys.* **88**(3), 175–179 (2010). <https://doi.org/10.1139/P10-004>
- [14] J. Ma, et al., "Modeling the pressure-dependent melting temperature of metals," *Phys. Earth Planet. Inter.* **309**, (2020). <https://doi.org/10.1016/j.pepi.2020.106602>
- [15] R.S. Chauhan, and C.P. Singh, "Analysis of melting for alkali halides based on the potential energy curve," *Phys. B Condens.*

- Matter, **324**(1), 151–156 (2002). [https://doi.org/10.1016/S0921-4526\(02\)01289-9](https://doi.org/10.1016/S0921-4526(02)01289-9)
- [16] M. Kumar, and M. Kumar, “Shanker formulation needs modification at high pressures,” *Journal of Physics and Chemistry of Solids*, **68**(4), 670–672 (2007). <https://doi.org/10.1016/j.jpcs.2007.01.036>
- [17] J. Shanker, S.S. Kushwah, and P. Kumar, “Equation of state and pressure derivatives of bulk modulus for NaCl crystal,” *Physica B: Condensed Matter*, **239**(3–4), 337–344 (1997). [https://doi.org/10.1016/S0921-4526\(97\)00349-9](https://doi.org/10.1016/S0921-4526(97)00349-9)
- [18] O.L. Anderson, *Equation of State of Solids for Geophysics and Ceramic Science*, (Oxford Univ. Press, Oxford, 1995).
- [19] B.J. Brennan, and F.D. Stacey, “A thermodynamically based equation of state for the lower mantle,” *JGR Solid Earth*, **84**(B10), 5535–5539 (1979). <https://doi.org/10.1029/JB084iB10p05535>
- [20] A.P. Srivastava, B.K. Pandey, A.K. Gupta, *et al.*, “The Relevance of the New Exponential Equation of State for Semiconductors,” *Iran J. Sci.* **48**, 1067–1074 (2024). <https://doi.org/10.1007/s40995-024-01657-1>
- [21] T. Katsura, and Y. Tange, “A Simple Derivation of the Birch–Murnaghan Equations of State (EOSs) and Comparison with EOSs Derived from Other Definitions of Finite Strain,” *Minerals*, **9**(12), 745 (2019). <https://doi.org/10.3390/min9120745>
- [22] A.P. Srivastava, B.K. Pandey, A.K. Gupta, *et al.*, “Theoretical prediction of thermoelastic properties of bismuth ferrite by a new approach,” *J. Math. Chem.* **62**, 2253–2264 (2024). <https://doi.org/10.1007/s10910-024-01647-z>
- [23] F.D. Stacey, “Finite strain, thermodynamics and the earth’s core,” *Physics of the Earth and Planetary Interiors*, **128**(1–4), 179–193 (2001). [https://doi.org/10.1016/S0031-9201\(01\)00285-0](https://doi.org/10.1016/S0031-9201(01)00285-0)
- [24] A. Dhoble, and M. P. Verma, “Thermodynamic analysis of the Anderson–Grüneisen parameters,” *Physica Status Solidi b*, **133**(2), 491–497 (1986). <https://doi.org/10.1002/pssb.2221330207>
- [25] O.L. Anderson, L. Dubrovinsky, S.K. Saxena, and T. LeBihan, “Experimental vibrational Grüneisen ratio values for ϵ -iron up to 330 GPa at 300 K,” *Geophysical Research Letters*, **28**(12), 2359–2359 (2001). <https://doi.org/10.1029/2000GL008544>
- [26] S.N. Vaidya, and G.C. Kennedy, “Compressibility of 27 halides to 45 kbar,” *Journal of Physics and Chemistry of Solids*, **32**(5), 951–964 (1971). [https://doi.org/10.1016/S0022-3697\(71\)80340-2](https://doi.org/10.1016/S0022-3697(71)80340-2)
- [27] Y.S. Sorensen, “Phase transitions and equations of state for the sodium halides: NaF NaCl, NaBr, and NaI,” *JGR Solid Earth*, **88**(B4), 3543–3548 (1983). <https://doi.org/10.1029/JB088iB04p03543>

НОВЕ РІВНЯННЯ СТАНУ ЧЕТВЕРТОГО ПОРЯДКУ, ЗАЛЕЖНОГО ВІД СТИСНЕННЯ

Абхай П. Шривастава^a, Брієш К. Панді^a, Анод Кумар Сінгх^b, Рітеш Шривастава^c

^aФакультет фізики та матеріалознавства, Технологічний університет Мадана Мохана Малвія, Горакхпур (UP), Індія

^bДепартамент гуманітарних і прикладних наук, Школа менеджменту, Лакхнау, (UP), Індія

^cДепартамент фізики, Nandini Nagar P.G. Коледж, Навабгандж, Гонда, (UP), Індія

У цьому дослідженні представлено нове експоненціальне рівняння стану першого-четвертого порядку (EOS) для підвищення точності на різних рівнях стиснення. Запропонований експоненціальний EOS порівнюється з широко використовуваним EOS Берча-Мурнагана четвертого порядку, і він не тільки відповідає, але й перевершує точність, особливо при високому стисненні. Це порівняння служить чітким орієнтиром для читачів, щоб зрозуміти перевагу нової моделі. Висновки цього дослідження мають вирішальне значення, оскільки вони показують, що експоненціальний EOS четвертого порядку забезпечує неперевершений рівень точності при більш високому стисненні, особливо для таких матеріалів, як НСР-залізо та галогеніди натрію. EOS Берча-Мурнагана, хоча ефективний при низькому стисненні, відхиляється від експериментальних значень на вищих рівнях. Крім того, дослідження вивчає Shanker EOS, в якому M. Kumar et al. [*Physica B: Condensed Matter*, 239(3–4), 337–344 (1997)] висувають вимогу щодо покращення при високому стисненні та покращення шляхом підгонки параметрів, які відрізняються від матеріалу до матеріалу. Це обмеження усувається завдяки розробці експоненціального EOS четвертого порядку, який є більш універсальним, пропонуючи надійні результати в сценаріях як низького, так і високого стиснення у фізиці високого тиску.

Ключові слова: рівняння стану; стиснення; показникове рівняння стану четвертого порядку; рівняння стану Берча-Мурнагана четвертого порядку

ANALYSIS OF HIGHER OVERTONE VIBRATIONAL FREQUENCIES IN CYCLOHEXANE USING A LIE ALGEBRAIC APPROACH

M.V. Subba Rao^a, T. Sreenivas^{a,b},  J. Vijayasekhar^{c*}

^aDepartment of Mathematics, Anil Neerukonda Institute of Technology & Sciences (ANITS), Visakhapatnam, India

^bDepartment of Mathematics, Jawaharlal Nehru Technological University, Kakinada, India

^cDepartment of Mathematics, GITAM (Deemed to be University), Hyderabad, India

*Corresponding Author e-mail: vijayjaliparthi@gmail.com

Received September 30, 2024; revised December 24, 2024; accepted February 1, 2025

This study contains a sophisticated computational approach to predict cyclohexane while maintaining the D_{3d} point group symmetry higher overtone vibrational frequencies (C_6H_{12}), precisely, third, fourth, and fifth. We utilize a Lie algebraic approach within the context of the vibrational Hamiltonian. The method uses cyclohexane's carbon-hydrogen (C-H) and carbon-carbon (C-C) bonds as unitary Lie algebras, accurately modelling the molecular vibrational structure. Thus, the vibrational Hamiltonian takes Casimir and Majorana's invariant operators and parameters and successfully outlines the molecules' vibrational modes. This Lie algebraic approach clearly outlined cyclohexane's higher overtone vibrational dynamics and provided helpful information that can be applied in other fields of study and technology.

Keywords: Lie algebraic approach; Vibrational frequencies; Vibrational Hamiltonian; Cyclohexane

PACS: 02.20.Sv, 33.20.Tp, 31.15.Xv, 33.20.Ea

1. INTRODUCTION

One of the essential aspects of molecular spectroscopy is the determination of the vibrational and energy distribution characteristics of the molecules within a study and, therefore, the understanding of different structures, interactions and activities of such molecules. Vibrational spectroscopy methods deal with the so-called vibrational spectra, which correspond to discrete energy levels, each of which relates to molecular vibrations. Such frequencies are also considered molecular fingerprints, essential in understanding the types of chemical bonds, structures, and interactions and identifying different molecules. Cyclohexane (C_6H_{12}), with its simple D_{3d} point group symmetry, is ideally suited for such studies since it is known to have very complex vibrational interactions even at high overtone levels [1,2]. Many of the traditional approaches taken by researchers seeking to explain the vibration of molecules have been based on the so-called harmonic oscillator model, where it is assumed that the behaviour of a vibrating molecule can be appreciated within the limits of a symmetrical parabolic potential well-located about the equilibrium position of the molecule. Remember that this modelling of the fundamental vibrational modes works well. It is well known that the anharmonicity of molecular vibrations is most apparent at higher energy levels. The simple fact is that molecular bonds show non-linearities instead of a perfect harmonic oscillation due to the atoms' stretching in a molecule. This anharmonicity becomes much more significant as I work with higher vibrational overtones where the simple picture of the potential energy curve as a parabola fails all along the sides [3-9]. The Morse oscillator model improves and provides a better geometrical description of molecules than the diatomic oscillator model because it incorporates the concept of anharmonicity into the potential energy surface. The Morse potential extends bond lengths and allows bond breaking to be considered a refinement using spherical averages of molecular vibration models. Besides, describing and analyzing the data of vibrational spectra involves working with conventional models of molecules and applying the Morse oscillator, which is necessary to assess energy distributions and vibrational transitions adequately, particularly at high overtone levels. More detailed representations of present or future molecules, like cyclohexane, should extend classical models and consider more advanced mathematical frameworks. The significant relation in this case is the vibrational Hamiltonian, which summarizes all modes of molecular vibrations and enables any rationalization of the normal modes and their couplings. Tackling the many body problems and other Hamiltonian terms by reformulating the vibrational Hamiltonian in terms of Lie algebras pretty much exhausts within the amends of the harmonic approximation in polyatomic systems. The benefit of the Lie algebraic approach is the ability to model Hamiltonians elegantly; this is essential for the calculations of complex vibrational spectra in a Lie algebra-based model. This method is well suited for polyatomic molecules because the theoretical presumption is satisfied by this formulation of Hamiltonian designed using invariant operators, such as Casimir and Majorana operators. These operators are part of the Lie algebraic representation and are indispensable in a holistic sense of molecular vibrational interactions. For example, the Casimir operator determines the number of angular momenta in the system. In contrast, the contribution of Majorana operators includes enhancing the vibrational coupling of different molecular bonds. As described in the article, Lie algebraic methods are used to create a cyclohexane vibrational Hamiltonian, capable of reproducing the higher overtones vibrational frequencies (third, fourth and fifth overtone) with more accuracy than existing methods. We construct a Hamiltonian consistent with the D_{3d} symmetry of cyclohexane and include the nonharmonic couplings present in the molecule's vibrational spectrum by viewing the chemical

bonds C-H and C-C as unitary Lie algebras. To find the vibrational frequencies, for which the Hamiltonian matrix for the molecule will be constructed in such a way as to include all possible vibrational couplings in the account of cyclohexane. Each vibrational state corresponds to a matrix element of the Hamiltonian, and there is no need to solve the matrix directly; instead, the energy eigenvalues of the matrix through which the state associated with the vibrations is represented are evaluated [10-12]. This way of looking at matrices also aids in predicting higher overtone frequency levels. It gives a glimpse of the interaction between the various vibrational forms and the general motion of the molecule. The main conclusion of this research is that the Lie algebraic approach is a practical tool for estimating cyclohexane's higher overtone vibrational frequencies since it accounts for anharmonicity, and the interaction of active coordinates typically neglected within simple harmonic models. Regardless of the covalent bonding nature, when the kinetic energy operator is expressed as a linear combination of the Lie algebra generators, Casimir and Majorana operators, we systematically elucidate the vibrational properties of cyclohexane and other more complex polyatomic systems. One of the outcomes of this work is that these molecular vibrations are essential for spectroscopic studies and other related scientific activities. Experimentally, assigning vibrational frequencies accurately can be significant since it will help interpret experimental spectra and molecular reactivity and map out the potential energy surfaces of the molecules in question. The Lie algebraic approach provides a coherent and generalizable framework that can be applied to other polyatomic molecules to facilitate the examination of vibrational spectra for various chemical, physical, and engineering purposes [13,14]. It brings new insights into the molecular vibrations that are of great importance to material science, chemical engineering and molecular physics with respect to the design, application and enhancement of advanced spectroscopic techniques aimed at studying reaction pathways and constructing novel materials reaction mechanisms.

Concisely, this investigation proves the predictive capability of the Lie algebraic approach to extending higher overtone vibrational frequencies and confirms this method as a single-line weapon in molecular spectroscopy development. It is also worth mentioning that such a thorough incorporation of the Morse oscillator model, anharmonicity and, importantly, Lie algebraic operators within the vibrational Hamiltonian opens new technological opportunities for the polyatomic molecules vibration analysis and cyclohexane tasks.

2. LIE ALGEBRAIC APPROACH

The Lie algebraic approach has thus proved to be a very effective tool in representing the vibrational frequencies within a molecule being fashioned, such a treatment accommodating the interactions involved in both the fundamental and the overtone transitions. This approach differs in that instead of using potential energy surfaces or differential equations to outline framework, it employs the mathematical structures of Lie algebras, particularly the U(2) algebra wherein vibrational states are treated as vectors and transitions as operators acting on these states. With the aid of algebra, molecular vibrations can be described which has advantages because harmonic and non-harmonic behaviours can be dealt with in a single framework. Central to this system is the formulation of the vibrational Hamiltonian which determines the energy levels and vibrational frequencies of the molecule. The Hamiltonian is written in terms of U(2) Lie algebra generators that operate with raising, lowering and projection including projection operators, Casimir (C_i, C_{ij}) and Majorana (M_{ij}) operators bonding single vibrational mode and modes interaction. By adjusting parameters such as $A_i, A_{ij}, \lambda_{ij}$, the Hamiltonian accurately models the vibrational dynamics, capturing fundamental frequencies and overtone transitions observed in molecular spectra. This strategy is effective in the case of complex and multi-vibrational molecules as it allows the analysis of vibrational spectra systematically and flexibly for molecules of extensive diversity. The advantage of the Lie algebraic approach is that it makes it possible to describe molecular vibrations not only in harmonic systems but also in anharmonic ones, which is, to a great degree, essential in molecular spectroscopy and enables correlation with experimental [13, 14].

To determine the vibrational modes of the molecule, it is essential to have the C-H and C-C stretching leads to the so-called vibrational Hamiltonians in cyclohexane. These Hamiltonians account for stretching vibrational interactions and energy and provide an idea of how the energy levels of vibration are structured within the molecule. For the case of the C-H stretching vibrations, this Hamiltonian is prepared to describe how the C-H bonds behave when they are stretched. It includes the normal vibrational modes and other inclusions to model higher overtone frequencies. This Hamiltonian usually has terms about the harmonic oscillator basis; however, other terms are included regarding flexible coupling terms, which are more representative of the accurate molecular picture. Similarly, cyclohexane is modelled for the C-C stretching vibrations with a Hamiltonian considering the bond stretching between the carbon atoms. However, the picture is more complicated in this case because of the cyclohexane symmetry and the coupling of the neighbouring C-C bonds. It is designed to include interactions between individual C-C stretching modes and between C-H and C-C vibrations, providing a more holistic representation of the vibrational structure.

The Hamiltonian can be expressed in terms of Lie algebra generators, in particular, using the U(2) algebraic model. This method permits a thorough and systematic description of the fundamental and overtone vibrational frequencies, which ensures that the calculated frequencies are consistent with experimental data. These Hamiltonians include harmonic and anharmonic terms, which can be used in detail to analyze the vibrational dynamics of cyclohexane. The established Hamiltonian operator which keeps in view the D_{3d} symmetry of cyclohexane is given as [15]:

$$H^{C-H} = E_0 + \sum_{i=1}^{n=12} A_i^{C-H} C_i + \sum_{i<j}^{n=12} A_{ij}^{C-H} C_{ij} + \sum_{i<j}^{n=12} \lambda_{ij}^{C-H} M_{ij} \quad (1)$$

$$H^{C-C} = E_0 + \sum_{i=1}^{n=6} A_i^{C-C} C_i + \sum_{i < j}^{n=6} A_{ij}^{C-C} C_{ij} + \sum_{i < j}^{n=6} \lambda_{ij}^{C-C} M_{ij} \quad (2)$$

The algebraic operators and dimensionless Vibron number N can be defined from the following expressions,

$$\langle C_i \rangle = -4(N_i v_i - v_i^2) \quad (3)$$

$$\langle N_i, v_i; N_j, v_j | C_{ij} | N_i, v_i; N_j, v_j \rangle = 4(v_i + v_j)(v_i + v_j - N_i - N_j) \quad (4)$$

$$\left. \begin{aligned} \langle N_i, v_i; N_j, v_j | M_{ij} | N_i, v_i; N_j, v_j \rangle &= v_i N_j + v_j N_i - 2v_i v_j \\ \langle N_i, v_i + 1; N_j, v_j - 1 | M_{ij} | N_i, v_i; N_j, v_j \rangle &= -[v_j(v_i + 1)(N_i - v_i)(N_j - v_j + 1)]^{1/2} \\ \langle N_i, v_i - 1; N_j, v_j + 1 | M_{ij} | N_i, v_i; N_j, v_j \rangle &= -[v_i(v_j + 1)(N_j - v_j)(N_i - v_i + 1)]^{1/2} \end{aligned} \right\} \quad (5)$$

The vibrational quantum numbers for the different bonds i and j are denoted by v_i and v_j , respectively. .

$$N = \frac{\omega_e}{\omega_e x_e} - 1 \quad (6)$$

The initial guess for the parameters A_i is obtained from the energy expression for single-oscillator fundamental mode,

$$E_i^{C-H}(v = 1) = -4A_i^{C-H}(N^{C-H}-1) \quad (7)$$

$$E_i^{C-C}(v = 1) = -4A_i^{C-C}(N^{C-C}-1) \quad (8)$$

The initial guesses for λ_{ij} are obtained by the relations,

$$\lambda_{ij}^{C-H} = \frac{E_i^{C-H} - E_j^{C-H}}{12 N^{C-H}}, \quad \lambda_{ij}^{C-C} = \frac{E_i^{C-C} - E_j^{C-C}}{6 N^{C-C}} \quad (9)$$

Here, $E_i^{C-H}, E_j^{C-H}, E_i^{C-C}, E_j^{C-C}$ represent the different energies corresponding to the symmetric and antisymmetric combinations of the two local vibrational modes. The initial values for A_{ij} are assumed to be zero.

3. RESULTS AND DISCUSSIONS

To predict the third, fourth, and fifth overtone frequencies for cyclohexane using the U(2) Lie algebraic approach, we utilize the established vibrational Hamiltonian parameters as outlined in the methodology [15]. The Table below summarizes the third, fourth and fifth overtone vibrational frequencies, symmetry species, and associated vibrational modes within the cyclohexane molecule. These values are also presented graphically in the accompanying figure.

Table. Vibrational frequencies (in cm^{-1}) for cyclohexane

Vibrational Mode	Symmetry Species	III overtone	IV overtone	V overtone
ν_1 (CH ₂ a-str)	a _{1g}	10132	13293	15881
ν_2 (CH ₂ s-str)	a _{1g}	10180	12780	15186
ν_3 (CH ₂ scis)	a _{1g}	3975	6703	7959
ν_4 (CH ₂ rock)	a _{1g}	3511	4551	5741
ν_5 (CC str)	a _{1g}	2623	3297	3973
ν_9 (CC str)	a _{1u}	3662	4598	5536
ν_{12} (CH ₂ a-str)	a _{2u}	9945	13815	15114
ν_{13} ((CH ₂ s-str))	a _{2u}	10530	12871	15721
ν_{14} (CH ₂ scis)	a _{2u}	5120	6651	7786
ν_{15} (CH ₂ rock)	a _{2u}	2975	4798	5750
ν_{17} ((CH ₂ a-str))	e _g	9894	13112	15210
ν_{18} ((CH ₂ s-str))	e _g	10604	13876	16107
ν_{19} (CH ₂ scis)	e _g	5040	6783	8285
ν_{22} (CC Str)	e _g	3869	4703	5835
ν_{23} (CH ₂ rock)	e _g	2775	3388	4082
ν_{25} (CH ₂ a-str)	e _u	10602	13596	15865
ν_{26} (CH ₂ s-str)	e _u	10759	12842	15904
ν_{27} (CH ₂ scis)	e _u	5023	6693	8101
ν_{30} (CH ₂ rock)	e _u	3012	4209	5197
ν_{31} (CC str)	e _u	3156	3878	4630

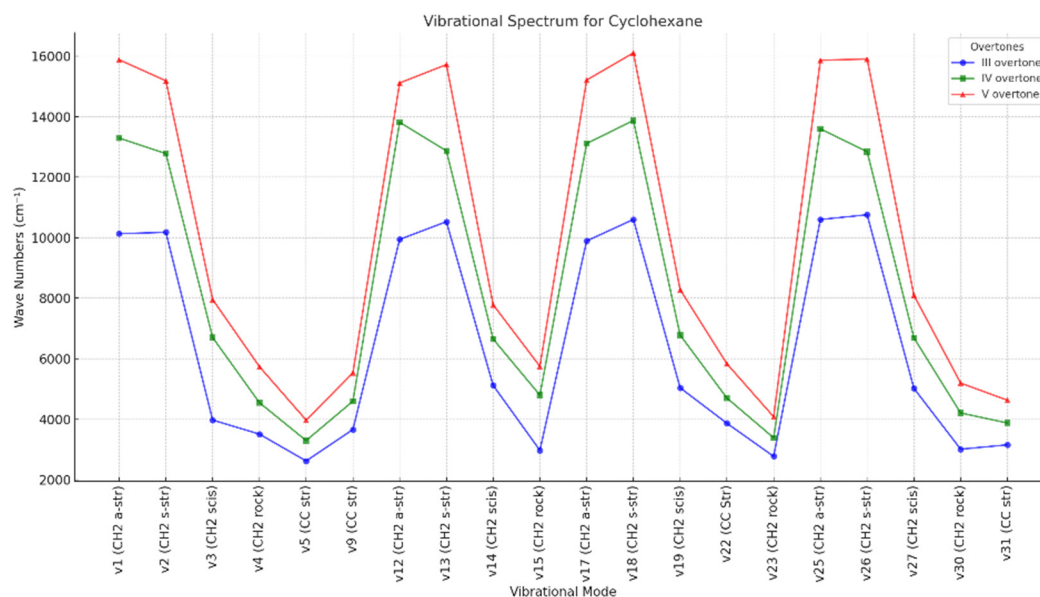


Figure. Vibrational Frequencies Representation for Cyclohexane - III, IV, and V Overtones

4. CONCLUSIONS

In this study, cyclohexane's third, fourth, and fifth overtone vibrational frequencies are predicted and analyzed using the U(2) Lie algebraic method for symmetric D_{3d} point group configurations. Applying a vibrational Hamiltonian with incorporated Casimir and Majorana operators enables one to correctly reproduce the anharmonic couplings and interactions between C–H and C–C bonds. The results prove that this method significantly gives better insight into the vibrational dynamics than the modelled systems in terms of overtones high order transitions. The results confirm the practical usefulness of the so-called Lie algebraic method for solving problems of the vibrational spectra of complex polyatomic molecules and indicate its good prospects for various studies of molecular vibrations in various other systems. The assignment of the vibration spectra is important for interpreting the experimental spectra, understanding the molecular reactivity and mapping the potential energy surfaces. This general strategy is systematic and flexible. It will help develop complex analyses with a scope that can be expanded to other molecules and provide valuable information regarding their vibrational characteristics for use in spectroscopy, materials and molecular design. In general, the findings of this research support the idea that the Lie algebraic model can predict overtone frequencies with precision while appreciably enhancing the knowledge of molecular vibrations, especially in molecules with high anharmonicity. Other studies may investigate applying this method to other polyatomic molecules and apply it to vibrational spectra of more complicated molecular systems.

Acknowledgments

On behalf of Vijayasekhar, special thanks are rendered regarding the Research Seed Grants (RSG) of GITAM Deemed to be University, Hyderabad, India, as mentioned in the Sanction Letter Ref: F.No. 2021/0114, dated 26-09-2022. Also, the authors thank the NIST Standard Reference Database 69: NIST Chemistry WebBook [webbook.nist.gov] for providing the experimental database utilized in this research.

ORCID

© J. Vijayasekhar, <https://orcid.org/0000-0002-2745-7401>

REFERENCES

- [1] I.S. Butler, R.P. Kengne-Momo, G. Jaouen, C. Policar, and A. Vessières, "Recent Analytical Applications of Molecular Spectroscopy in Bioorganometallic Chemistry—Part I: Metal Carbonyls," *Appl. Spectrosc. Rev.* **47**(7), 531–549 (2012). <https://doi.org/10.1080/05704928.2012.673189>
- [2] I.S. Butler, R.P. Kengne-Momo, A. Vessières, G. Jaouen, and C. Policar, "Recent Applications of Molecular Spectroscopy in Bioorganometallic Chemistry—Part 2: Ferrocenes and Other Organometallic Complexes," *Appl. Spectrosc. Rev.* **47**(8), 620–632 (2012). <https://doi.org/10.1080/05704928.2012.697088>
- [3] S. Brodersen, and J.-E. Lolck, "Calculation of rotation-vibrational energies directly from an anharmonic potential function," *J. Mol. Spectrosc.* **126**(2), 405–426 (1987). [https://doi.org/10.1016/0022-2852\(87\)90246-3](https://doi.org/10.1016/0022-2852(87)90246-3)
- [4] P.T. Panek, A.A. Hoeske, and C.R. Jacob, "On the choice of coordinates in anharmonic theoretical vibrational spectroscopy: Harmonic vs. anharmonic coupling in vibrational configuration interaction," *J. Chem. Phys.* **150**(5), 054107 (2019). <https://doi.org/10.1063/1.5083186>
- [5] K.B. Beć, J. Grabska, and C.W. Huck, "Current and future research directions in computer-aided near-infrared spectroscopy: A perspective," *Spectrochim. Acta A.* **254**, 119625 (2021). <https://doi.org/10.1016/j.saa.2021.119625>

- [6] G. Pitsevich, and A. Malevich, "Symmetry properties, tunneling splittings of some vibrational energy levels and torsional IR spectra of the trans- and cis-conformers of hydroquinone molecule," J. Mol. Spectrosc. **404**, 111937 (2024). <https://doi.org/10.1016/j.jms.2024.111937>
- [7] G. Pandimeena, T. Mathavan, E.J.J. Samuel, and A.M.F. Benial, "Quantum chemical, spectroscopic and molecular docking studies on methyl 2-chloro-6-methyl pyridine-4-carboxylate: A potential inhibitor for irritable bowel syndrome," Spectrochim. Acta Part A: Mol. Biomol. Spectrosc. **294**, 122544 (2023). <https://doi.org/10.1016/j.saa.2023.122544>
- [8] A.V. Nikitin, A. Campargue, A.E. Protasevich, M. Rey, K. Sung, and V.I.G. Tyuterev, "Analysis of experimental spectra of phosphine in the Tetradecead range near 2.3 μm using ab initio calculations," Spectrochim. Acta Part A: Mol. Biomol. Spectrosc. **302**, 122896 (2023). <https://doi.org/10.1016/j.saa.2023.122896>
- [9] I.M. Chandramalar, and V.P. Subhasini, "Vibrational spectroscopic analysis of 2,3:4,5-Bis-O-(1-methylethylidene)beta-D-fructopyranose Sulfamate (Topiramate) by density functional method," Spectrochim. Acta Part A: Mol. Biomol. Spectrosc. **302**, 122997 (2023). <https://doi.org/10.1016/j.saa.2023.122997>
- [10] V. Jaliparthi, "Vibrational Energies of Silylene, Difluorosilylene and Dichlorosilylene, Using U(2) Lie Algebraic Model," Ukr. J. Phys. Opt. **23**(3), 126-132 (2022). <https://doi.org/10.3116/16091833/23/3/126/2022>
- [11] A.G. Rao, K. Lavanya, and J. Vijayasekhar, "Higher Overtone Vibrational Frequencies of Cyclobutane-D8 Using Lie Algebraic Framework," East Eur. J. Phys. (2), 411-415 (2024). <https://doi.org/10.26565/2312-4334-2024-2-53>
- [12] J. Vijayasekhar, P. Sunetha, and K. Lavanya, "Vibrational spectra of cyclobutane-d8 using symmetry-adapted one-dimensional Lie algebraic framework," Ukr. J. Phys. Opt. **24**, 193-199 (2023). <https://doi.org/10.3116/16091833/24/3/193/2023>
- [13] F. Iachello, and R.D. Levine, *Algebraic theory of molecules*, (Oxford University Press, Oxford, 1995).
- [14] S. Oss, "Algebraic models in molecular spectroscopy," Adv. Chem. Phys. **93**, 455-649 (1996).
- [15] T. Sreenivas, and J. Vijayasekhar, "Exploring Cyclohexane Vibrational Dynamics Through a Lie Algebraic Hamiltonian Framework," Ukr. J. Phys. Opt. **25**(3), 03093-03100 (2024). <https://doi.org/10.3116/16091833/Ukr.J.Phys.Opt.2024.03093>

АНАЛІЗ ВИЩИХ ОБЕРТОННИХ КОЛИВАЛЬНИХ ЧАСТОТ В ЦИКЛОГЕКСАНІ ЗА ДОПОМОГОЮ АЛГЕБРАЇЧНОГО ПІДХОДУ ЛІ

М.В. Субба Рао^a, Т. Срінівас^{a,b}, Дж. Віджаясекар^c

^aДепартамент математики, Інститут технологій і наук Аніла Ніруконди (ANITS), Вісакхапатнам, Індія

^bФакультет математики, Технологічний університет Джавахарлала Неру, Какінада, Індія

^cДепартамент математики, GITAM (вважається університетом), Хайдарабад, Індія

У цьому дослідженні представлено складний обчислювальний підхід до прогнозування вищих обертонних коливальних частот D3d точкової групи циклогексану (C₆H₁₂), зокрема третьої, четвертої та п'ятої. Ми використовуємо алгебраїчний метод Лі в рамках коливального гамільтоніана. У цьому підході використовуються вуглець-водневі (C-H) і вуглець-вуглецеві (C-C) зв'язки циклогексану як унітарні алгебри Лі, точно моделюючи молекулярну коливальну структуру. Як наслідок, коливальний гамільтоніан включає інваріантні оператори та параметри Казимира та Майорани, ефективно окреслюючи коливальні режими молекули. Цей алгебраїчний метод Лі пояснює вібраційну динаміку циклогексану з вищими обертонами та дає цінну інформацію для застосування в різних галузях досліджень та технологій.

Ключові слова: алгебраїчний підхід Лі; коливальні частоти; коливальний гамільтоніан; циклогексан

ON THE INFLUENCE OF VACUUM CONDITIONS ON THE POWER LEVEL OF ELECTROMAGNETIC WAVES GENERATED BY A RELATIVISTIC MAGNETRON

 A.B. Batrakov*,  S.I. Fedotov,  O.M. Lebedenko,  I.N. Onishchenko,  O.L. Rak,  M.V. Volovenko,  Yu.N. Volkov

National Science Center «Kharkiv Institute of Physics and Technology», Kharkiv, Ukraine

*Corresponding Author e-mail: a.batrakov67@gmail.com

Received October 12, 2024; revised January 3, 2025; accepted February 4, 2025

The high-power microwave radiation, generated in a relativistic high-voltage pulsed magnetron with the range of 8 mm, was experimentally investigated. The factors that negatively affect the generation of microwave radiation were experimentally studied and analyzed. It was determined that the low pressure in the vacuum diode of the magnetron also was associated with the processes reducing the efficiency and duration of the pulse generation. The air components are known to be the major residual gases in the magnetron vacuum diode. During the magnetron operation, a significant increase in the pressure of the residual atmosphere of hydrocarbons, water vapor, and hydrogen is to be observed. A vacuum system was composed to pump them out, thus ensuring the magnetron optimal operation. A cryogenic condensation-adsorption pump was developed and applied for the new vacuum system allowing to increase the evacuation rate of the main residual gases. The peculiarity of the developed pump is that the pumping element with the adsorbent has a double working surface due to the use of a corrugated form of the sorption cartridge. Another feature of the pump is its efficiency, which is achieved due to the use of nitrogen vapors for cooling the space between the walls. Due to the use of the cryogenic means of pumping, it became possible to obtain the pressure at the level of $1 \cdot 10^{-6}$ Torr, thus achieving an increase in the microwave radiation of the relativistic magnetron by 25 percent.

Keywords: Relativistic magnetron; Microwave radiation; Vacuum system; Adsorption pump

PACS: 52.30.q, 50.80.Vp

INTRODUCTION

The use of high-energy microwave radiation is necessary in a variety of applications including plasma physics and many fields of applied research [1]. When operating in the millimeter wavelength range the relativistic magnetron researchers face the problems associated with the efficiency of microwave energy extraction both in the radial direction of the cylindrical structure and in the axial one [2]. Such undesirable effects as an increase of the voltage action duration in the electrodynamic structure (EDS), the pressure at the level of $1 \cdot 10^{-4}$ Torr resulted in a rapid deterioration of the EMF [3-6]. Therefore, the problem to improve the method of removing high-frequency power from the EMF of the magnetron arose [7-9]. One of the steps that contribute to this result is to obtain the residual gases pressure at the level of $1 \cdot 10^{-6}$ Torr. The air components are the major residual gases to be known in the magnetron vacuum diode. During operation of the magnetron, a significant increase in the residual atmosphere of hydrocarbons, water vapor, and hydrogen is observed. Before the reconstruction, the vacuum pumping system included a forevacuum pump for obtaining a low vacuum and a magnet discharge pump for obtaining a high vacuum ($1 \cdot 10^{-4}$ - $6 \cdot 10^{-5}$ Torr). This configuration of the vacuum evacuation facilities did not cope well with pumping-out of hydrocarbons, hydrogen and water vapor. This was one of the reasons why the magnetron operation efficiency was low. At the same time, the working surfaces of the magnet discharge pump used to fail, what caused the work stoppages. To generate microwave radiation in the magnetron, it is necessary to maintain a certain pressure in the vacuum system, which should be $1 \cdot 10^{-6}$ Torr. This is the objective of the work. Achieving the highest vacuum provides the optimal conditions for the formation and stable maintenance of the electron flow, which interacts with the electromagnetic field. This paper presents the results of the microwave radiation increase by 25% due to obtaining the working vacuum at the level of $1 \cdot 10^{-6}$ Torr.

MAGNETRON VACUUM SYSTEM

The developed vacuum circuit provides optimal conditions for the formation and stable maintenance of the electron flow, which interacts with the electromagnetic field. It is proposed to increase the microwave radiation owing to generation of the pressure in the magnetron vacuum system at the level of $P = 1 \cdot 10^{-6}$ Torr. An increase in the microwave radiation is proposed owing to generation of the pressure in the magnetron vacuum system at the level of $P = 1 \cdot 10^{-6}$ Torr. The research was carried out on the installation, whose schematic is presented in Fig. 1.

The experiments with the PM-48 magnetron revealed microwave generation at the frequency from 36 to 4 GHz with the magnetic induction magnitude from $B_0 = 0.35$ to 0.8 T and the anode voltage from $U_0 = 190$ kV to 250 kV. The diameters of the anode and cathode were $d_a = 25$ mm and $d_c = 14$ mm, respectively, and the gap between the cathode and

anode d_{ca} was in the range of 3-5mm. The observed oscillations can be defined as $\pi/2$; π or $(2/3)\pi$ modes. However, the result of the horn-supported axial microwave power feed-out experiments is to be still classified as unsatisfactory one.

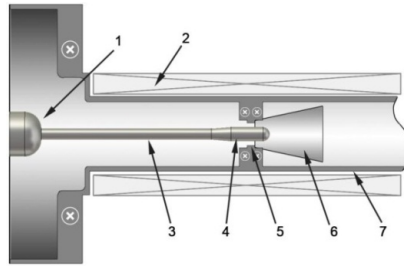


Figure 1. Schematic of a relativistic magnetron

1. Vacuum resonator. 2. Solenoid. 3. Cathode holder. 4. Cathode. 5. Anode. 6. Output horn. 7. Oversized waveguide.

One of the reasons of this problem is the impact of the anode-cathode plasma on the discharge. The worse is the vacuum conditions in the magnetron, the greater is the effect of the anode-cathode plasma on the discharge. If the vacuum level in the magnetron is not properly maintained, several problems can occur:

1. Instability of the electron flow: Insufficient vacuum can cause some fluctuations and instability of the electron flow, thus negatively affecting the generation of microwave radiation.

2. Increased gas pressure: When the gas pressure in the vacuum chamber is increased, some unwanted collisions of electrons with gas molecules can occur, thus reducing the magnetron efficiency.

3. Overheating of the elements: Low vacuum can cause overheating of the magnetron and other system components, which can result in their being damaged or fail.

4. Reduced lifetime: Constant fluctuations in the vacuum level can shorten the lifetime of the magnetron and other system components.

5. Breakdown between the cathode and anode: In the literature, the data are provided that in this case the pressure in the vacuum chamber of the magnetron deteriorates by an order of magnitude [10].

The carried-out studies allow assuming that a pre-breakdown in the anode-cathode gap can occur on a relativistic magnetron. The current that appears in this case is 50-100 μA . Here we see significant destruction of the anode, which has the appearance of hollows. The condition of the anode and cathode surface is shown in Fig. 2.

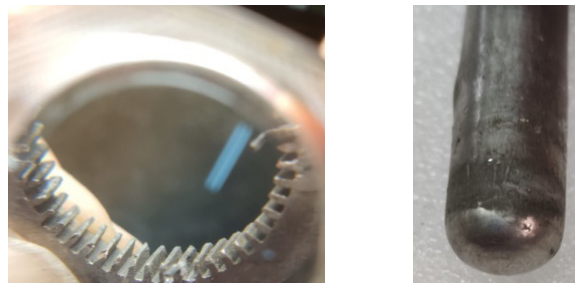


Fig. 2. The condition of the damaged surface of the anode and cathode of the relativistic magnetron

The destruction on the anode indicates the electronic nature of the current. Also, the transfer of metal from the cathode to the anode can be seen. On the anode, in this case, the metal is destroyed and some soot appears. This happens owing to the inability to achieve the required level of vacuum with the existing means of pumping. Therefore, the problem of improving the magnetron vacuum system arose

The new vacuum system was composed basing on the requirements to ensure optimal operation of the relativistic magnetron. The vacuum pumping system includes a pre-vacuum pumping line and a high vacuum pumping line. Fig. 3 shows the schematic diagram of the vacuum pumping system of the relativistic magnetron chamber.

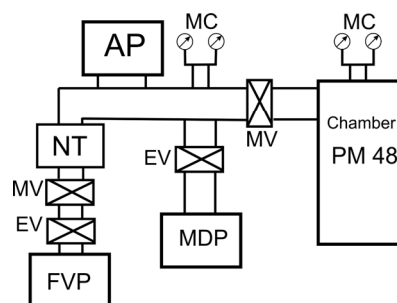


Figure 3. Schematic diagram of the vacuum pumping system of the relativistic magnetron chamber

FVP – forevacuum pump; AP – adsorption pump; MDP – magnet discharge pump; MV – manually operated valves; EAV - electric-actuated valves; Chamber PM48 – magnetron chamber; MC – manometric converters, NT – nitrogen trap, EV - emergency air inlet valve

The vacuum chamber system, presented in Fig. 3, has a forevacuum pumping line, which is designed to pump out Chamber PM48 from the current atmospheric pressure to $\sim 7 \cdot 10^{-2}$ Torr. The forevacuum pumping is carried out by a forevacuum pump (FVP) through an open electric-actuated valve (EAV) and a nitrogen-filled nitrogen trap NT-LAF-32. The pressure in the line and working chamber is measured by manometric converters (MC). The high vacuum pumping line consists of an adsorption pump (AP) with the manometric converter (MC), connected to the magnetron chamber PM48 through the manually operated valve (MV), and the magnet discharge pump (MDP), which is connected to the relativistic magnetron chamber through the electric-actuated valve (EAV). In addition, the vacuum system includes an emergency air inlet valve (EV), which is activated when the light is turned off.

To obtain the working pressure in the relativistic magnetron at the level of $1 \cdot 10^{-6}$ Torr, it is proposed to use cryogenic means of pumping [11, 12]. For this purpose, a design of a high-vacuum cryogenic condensation-adsorption pump was developed, which works on one refrigerant with efficient use of the outgoing vapors. The use of nitrogen vapors will increase the service life of the pump without increasing the refrigerant consumption. The schematic of the developed cryogenic condensation-adsorption pump is shown in Fig. 4.

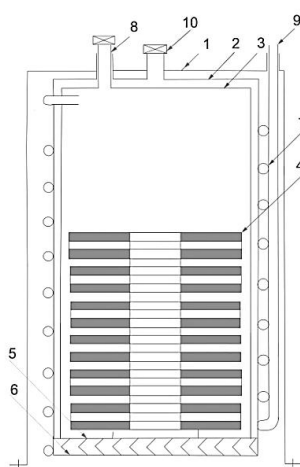


Figure 4. Schematic of the condensation-adsorption pump

The pump consists of an outer casing 1, in which the pumping element is placed, in the form of an inner casing 3 with the refrigerant, and a screen 2. Cassettes with adsorbent 4 (birch activated carbon – BAC) are placed in the lower part of the inner casing 3. The evacuation of the main mass of gas is carried out by condensation on the condensing surface 6 of the inner casing 3. The non-condensed part of the gas, as a consequence of the repeated contact with the surfaces having the temperature of the refrigerant, is absorbed by the adsorbent. Screen 2 with chevron 6 is designed to protect inner casing 3 from external radiation and other thermal flows. Screen 2 is cooled by the vapor flowing through coil 7. The components condensed from the pumped volume are also frozen here. The surfaces of inner housing 3 with the refrigerant and the elements of screen 2 are wrapped in mylar to minimize the heat inflow to them. Screen 2 and inner casing 3 with the refrigerant are suspended in outer housing 2 of the pump on two pipes 8 and 9, so that it would be possible to fill in the refrigerant through pipe 8, and to let the refrigerant vapors out through pipe 9. To reduce the thermal load on the inner casing, the volume between inner casing 3 and screen 2 is pumped out through pipe 10.

The vacuum system operates in the following way:

1. When MV1, MV2, MV3, EAV valves are open, we pump the accelerator chamber out using the EVP AVZ-20 forevacuum pump through the NT LAF-32 nitrogen trap filled with liquid nitrogen to the pressure of $7 \cdot 10^{-2}$ Torr which is the transitional mode between viscous and molecular gas flow mode. Then we close the MV1 valve and turn off the forevacuum pump.

2. We close the MV3 valve and fill in the adsorption pump (AP) with nitrogen, after starting the AP open MV3 and pump the system up to $3 \cdot 10^{-4}$ Torr.

3. We close the valves EAV and start the magnet discharge pump (MDP) "toward itself". Reaching the pressure of $2 \cdot 10^{-4}$ Tor, we open the pump MDP to the magnetron chamber. This allows obtaining the pressure of $1 \cdot 10^{-6}$ Torr.

The updated vacuum system allows operating the relativistic magnetron in a cyclic mode without failure of the pumping elements.

EXPERIMENTAL PART

After updating the relativistic magnetron vacuum system, the experiments were conducted to obtain the microwave radiation at different pressures of the residual atmosphere in the magnetron vacuum volume. The value of the magnetic induction was $B_0 = 0.75$ T, the anode voltage was $U_0 = 250$ kV. The output microwave radiation of the

magnetron passed through a round waveguide with the diameter of 80 mm and the length of 775 mm, and was ejected into free space through a window made of organic glass. The output power of the emitted microwaves was estimated by measuring the magnetron microwave spatial distribution. As a receiving antenna, a pyramidal horn with an open end ($4 \times 3.2 \text{ cm}^2$) was used, which was placed in the azimuthal direction at the distance of 1.35 m from the window. The envelope curve of the output microwave signal was obtained using a diode D 404 and recorded by a digital oscilloscope with the bandwidth of 200 MHz. The first experiment was conducted at the pressure in the magnetron vacuum volume $P = 3 \cdot 10^{-4}$ Torr, the second – at the pressure $P = 1 \cdot 10^{-6}$ Torr. The oscillograms of voltage, current and microwave radiation are shown in Fig. 5.

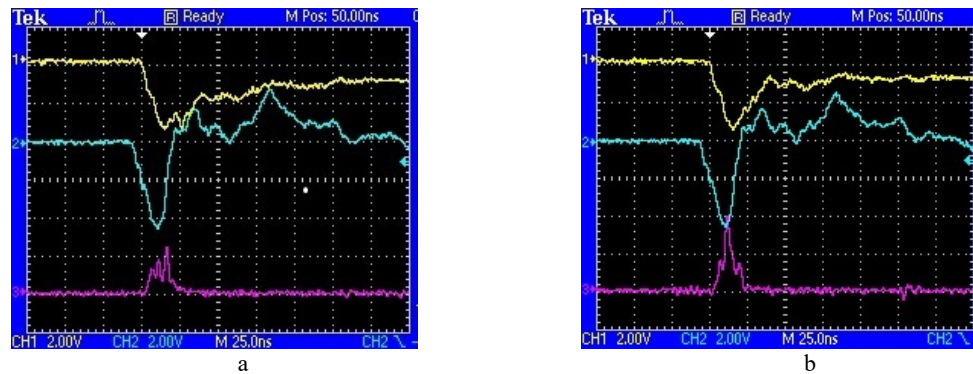


Figure 5. Oscillograms of voltage, current and microwave radiation
a – oscillogram at the pressure in the magnetron vacuum volume $P = 3 \cdot 10^{-4}$ Torr; b – oscillogram at the pressure in the magnetron vacuum volume $P = 1 \cdot 10^{-6}$ Torr

On the oscillograms, the first line is the anode voltage, the second line is the current, and the third line is the microwave radiation.

The calculated microwave radiation power in the first case was 650 kW, in the second – 875 kW. The obtained pressure of the residual gases in the relativistic magnetron at the level of $P = 1 \cdot 10^{-6}$ Torr gives an increase in the microwave radiation power by 25 percent.

CONCLUSIONS

The vacuum system presented in the paper allows obtaining the oil-free vacuum. It provides optimal conditions for the formation and stable maintenance of the electron flow, which interacts with the electromagnetic field. The vacuum pumping system allows to reach the operating pressure of $1 \cdot 10^{-6}$ Torr quickly, maintain the device in a pumped state for a long time, and reduce the time of the vacuum chamber preparation between the pulses. Obtaining the residual gases pressure in the relativistic magnetron at the level of $P = 1 \cdot 10^{-6}$ Torr gives an increase in microwave radiation power by 25 percent.

ORCID

©A.B. Batrakov, <https://orcid.org/0000-0001-6158-2129>; ©S.I. Fedotov, <https://orcid.org/0000-0002-7216-0615>
©M.V. Volovenko, <https://orcid.org/0000-0001-7216-2058>; ©O.M. Lebedenko, <https://orcid.org/0009-0004-2243-8393>
©I.N. Onishchenko, <https://orcid.org/0000-0002-8025-5825>; ©Yu.N. Volkov, <https://orcid.org/0009-0002-0557-8090>
©O.L. Rak, <https://orcid.org/0009-0000-6683-1235>

REFERENCES

- [1] R.J. Barker, and E. Schamiloglu, editors, *High Power Microwave Sources and Technologies*, (New York: Wiley-IEEE Press, 2001).
- [2] T. Nakamura, et al., “Output Evaluation of Microwave Pulse Emitted from Axially-Extracted Vircator with Resonance Cavity,” in: *Recent developments of pulsed power technology and plasma application research*, edited by J. Hasegawa, and O. Tetsuo, (Tokyo Institute of Technology, Tokyo, Japan, 2018), p. 55-60
- [3] N.P. Gadetski, E.I. Kravtsova, I.I. Magda, V.D. Naumenko, S.S. Pushkaryov, S.N. Terekhin, and A.S. Tischenko, “Relativistic magnetron of 8 mm waveband,” *Problems of Atomic Science and Technology, Series “Plasma Electronics”*, (4), 18-20 (2008).
- [4] A. Kuskov, A. Elfrgani, and E. Schamiloglu, “Relativistic magnetron with diffraction output (MDO) with a permanent magnet anode block configuration,” in: *IEEE International Vacuum Electronics Conference (IVEC)*, 2018.
- [5] S. Xu, L. Lei, F. Qin, and D. Wang, “Compact, high power and high efficiency relativistic magnetron with L-band all cavity axial extraction,” *Physics of Plasmas*, **8**, 22-29 (2018). <https://doi.org/10.1063/1.5041860>
- [6] N.P. Gadetskiy, A.N. Lebedenko, I.I. Magda, O.G. Melezhik, A.A. Shtanko, and M.V. Volovenko, “A relativistic magnetron-type source of nanosecond-length pulsed radiation in the 8 mm waveband,” *Problems of Atomic Science and Technology, Series “Plasma Electronics”*, (6), 40-42 (2017). https://vant.kipt.kharkov.ua/ARTICLE/VANT_2017_6/article_2017_6_40.pdf
- [7] A. Sayapin, and A. Shlapakovski, “Transient operation of the relativistic S-band magnetron with radial output,” *Journal of Applied Physics*, (6), 61-67 (2011). <https://doi.org/10.1063/1.3553839>
- [8] N.P. Gadetski, V.G. Korenev, A.N. Lebedenko, I.I. Magda, O.G. Melezhik, V.G. Sinitsin, A.A. Shtanko, and N.V. Volovenko. “Millimeter-wavelength relativistic magnetron: problems of microwave power extraction,” *Problems of Atomic Science and*

- Technology, Series: Nuclear Physical Investigations, (6), 80-84 (2021).
https://vant.kipt.kharkov.ua/ARTICLE/VANT_2021_6/article_2021_6_80.pdf
- [9] V.A. Markov, and V.D. Naumenko, "On the influence of the shape of anode voltage pulse on the operation stability of spatial-harmonic magnetron with cold secondary emission cathode," *Radiofiz. elektron.* **23**(1), 53-60 (2018).
<https://doi.org/10.15407/rej2018.01.053>
- [10] E.S. Borovik, and B.P. Batrakov, "Study of breakdown in vacuum," *Journal of Technical Physics*, **28**(9), (1958). (in Russian)
- [11] A.B. Batrakov, V.A. Kravchenko, *et al.*, "Cryogenic adsorption pumps for obtaining pure vacuum," in: *Kharkiv Scientific Assembly ICVTE-6*, 2003, p. 226-228.
- [12] A.B. Batrakov, Yu.N. Volkov, Yu.F. Lonin, and A.G. Ponomaryov, "Neon cryovacuum system for life testing of electric jet," *Problems of Atomic Science and Technology. Series "Plasma Physics"*, (1), 213-215 (2015).
https://vant.kipt.kharkov.ua/ARTICLE/VANT_2015_1/article_2015_1_213.pdf

ПРО ВПЛИВ ВАКУУМНИХ УМОВ НА РІВЕНЬ ПОТУЖНОСТІ ЕЛЕКТРОМАГНІТНИХ ХВИЛЬ, ЩО ГЕНЕРУЮТЬСЯ РЕЛЯТИВІСТСЬКИМ МАГНЕТРОНОМ

А.Б. Батраков, С.І. Федотов, О.М. Лебеденко, І.Н. Онищенко, О.Л. Рак, М.В. Воловенко, Ю.Н. Волков

Національний науковий центр «Харківський фізико-технічний інститут», Харків, Україна

Експериментально досліджено потужне НВЧ-випромінювання, що генерується в релятивістському високовольтному імпульсному магнетроні діапазону 8 мм. Експериментально досліджено та проведено аналіз факторів, що негативно впливають на генерацію НВЧ випромінювання. Визначено, що до процесів, котрі зменшують ефективність та тривалість імпульсу генерації, відноситься також низький тиск у вакуумному діоді магнетрону. Відомо, що в вакуумному діоді магнетрону головними залишковими газами є компоненти повітря. При роботі магнетрону спостерігається значне збільшення тиску залишкової атмосфери: вуглеводнів, водяної пари і водню. Для їх відкачування була скомпонована вакуумна система, що забезпечує оптимальну роботу магнетрону. Для нової вакуумної системи було розроблено та застосовано криогенний конденсаційно-адсорбційний насос, який дозволив збільшити швидкість відкачування основних залишкових газів. Особливість розробленого насоса полягає в тому, що відкачувальний елемент з адсорбентом має збільшену в два рази робочу поверхню-за рахунок використання гофрованої форми сорбційного патрона. Іншою особливістю насоса є його економічність, вона досягнута за рахунок використання парів азоту для охолодження між стінного проміжку. За рахунок використання криогенних засобів відкачування вдалося отримати тиск на рівні $1 \cdot 10^{-6}$ Тор, що призвело до збільшення випромінювання НВЧ релятивістського магнетрону на рівні 25 відсотків.

Ключові слова: *релятивістський магнетрон; мікрохвильове випромінювання; вакуумна система; адсорбційний насос*

ULTRASOUND DOPPLER SYSTEM'S RESOLUTION USING COHERENT PLANE-WAVE COMPOUNDING TECHNIQUE

✉ Evgen A. Barannik, ✉ Mykhailo O. Hrytsenko*

*Department of Medical Physics and Biomedical Nanotechnologies, V.N. Karazin Kharkiv National University
4 Svobody Sq., 61022, Kharkiv, Ukraine*

**Corresponding Author: mykhailo.hrytsenko@student.karazin.ua*

Received November 14, 2024; revised January 5, accepted February 12, 2025

Among modern ultrasound technologies for medical diagnostics, a special place is held by the technology of compounding plane waves with different propagation directions, which form synthesized images. In this work, based on the previously developed theory of Doppler response formation, the resolution of a system that uses plane wave compounding is investigated. In this case, small nonlinear components in the angle of inclination of the wave vectors of different plane waves were taken into account for the phase of the synthesized response and for the envelope of the radiation pulses. As a result of the study, it was found that the dimensions of the measuring volume in the longitudinal and transverse directions do not change. Taking into account small components leads to a slight change in the shape of the measuring volume, which ceases to be exactly spherical. This is explained by the fact that the resolution is determined not only by the interference of plane waves, but also by the area of their intersection at a certain point in space. The results obtained indicate that neglecting small inclination angles in the envelope is fully justified and allows simplifying the process of obtaining Doppler signal spectra in plane wave compounding technology.

Keywords: *Ultrasound; Doppler spectrum; Plane wave compounding; Sensitivity function; Spatial resolution; Envelope*

PACS: 43.28.Py, 43.35.Yb, 43.60.-c, 87.63.D-, 87.63.dk

INTRODUCTION

Due to the advancement of technology and the significant increase in the capabilities of computer systems, methods of ultrasound diagnostics requiring extensive computations are actively evolving. To achieve high-resolution imaging in every point of the entire analyzed area, synthetic aperture (SA) methods using ultrasound waves with various spatial configurations are increasingly employed compared to traditional imaging methods [1,2]. A distinctive feature of this method is that ultrasound echo signals from each spatial point are coherently accumulated for different wavefront propagation angles. Since the SA method enables focusing in each spatial point and constructing high-frame-rate images, it has found applications in various medical areas, including Doppler imaging [3-6,9], elastography [8], and more. Enhancing and analyzing the quality of the obtained images and integrating these methods into existing ultrasound diagnostic systems are important challenges [9-12].

Technologies based on this method are advancing rapidly, particularly ultrasound probing using plane ultrasonic waves [13,14,9] with various propagation directions [15,16,9]. For example, through the technology of plane-wave compounding (PWC), improvements in Doppler evaluations, especially for slow blood flows, have been achieved compared to conventional methods [4,19-21]. Additionally, experimental studies using this technology have investigated velocity vector estimation [17,18], visualized vessel walls, implemented color and 3D ultrafast Doppler imaging, brain functional imaging, and elasticity visualization using shear waves [22-24,4,5,9].

Each emission of single ultrasonic plane waves produces only low-quality images. However, coherent accumulation of echo signals from waves propagating at different angles yields high-quality images with frame rates of several kilohertz, increasingly utilized in medicine today [25,26]. PWC simultaneously provides high-quality B-mode images [27-30] and a continuous data stream for Doppler analysis methods [31-34,22].

Various approaches to improving PWC resolution are actively being developed, including novel adaptive compounding techniques [35], the use of artificial intelligence [36,37], beamforming strategies [38,39], motion correction schemes based on multi-angle vector Doppler velocity estimates [40], employing multiple transducer arrays for plane-wave compounding [41], multiperspective imaging with curved arrays [42], and methods for increasing frame rates [43], among others.

Improving the quality of ultrasound and Doppler diagnostics using coherent plane-wave compounding technology remains a pressing issue. Based on the original developed theory of Doppler response formation [44-46], theoretical resolution estimates for systems applying PWC were previously obtained [47]. These studies considered only linear phase components of plane waves with small deviations in wave vectors. The aim of this work is to investigate the resolution of ultrasound systems utilizing PWC, accounting for nonlinear components in both the response signal phase and the envelopes of transmitted plane-wave pulses.

THEORETICAL MODEL

Previously [46-48], in theoretical studies of the spectral characteristics of ultrasound Doppler response signals in systems utilizing PWC, the complex amplitude of the transmitted field $G_t(\vec{r}, t)$ and the complex sensitivity function of the receiver to scattered waves $G_r(\vec{r}, t)$ were used. Physically, these functions describe the ultrasound fields of transmission and receiving, taking into account their deviation from a plane wave with a constant wave vector \vec{k} , aligned with the x' axis of the ultrasonic fields shown in Fig. 1.

This approach is particularly convenient when describing traditional ultrasound diagnostic systems [44,45], as they utilize stationary ultrasound fields. The time dependence of these functions arises specifically with PWC, where the probing direction changes over time according to a defined wave vector $\vec{k}(t)$. In this case, it is more convenient to use an approach based on the direct wave fields of transmission $P_t(\vec{r}, t)$ and receiving $P_r(\vec{r}, t)$, represented as plane waves with the wave vector $\vec{k}(t)$. Here, the vector \vec{k} represents the time-averaged wave vector directed along the x' axis.

From this point forward, we assume that both the acquisition of ultrasound Doppler response signals and the emission with plane wavefronts occur at the same angle Φ , as illustrated in Fig. 1. Thus, the resulting transmission-receiving field can be expressed as follows

$$\begin{aligned} P(\vec{r}, t) &= G_t(\vec{r}, t)G_r(\vec{r}, t)e^{2i\vec{k}\vec{r}}b\left(T_1 - \frac{2x''}{c_0}\right)g(z) = P_t(\vec{r}, t)P_r(\vec{r}, t)b\left(T_1 - \frac{2x''}{c_0}\right)g(z) = \\ &P_tP_re^{2i\vec{k}(t)\vec{r}}b\left(T_1 - \frac{2x''}{c_0}\right)g(z) \equiv P_0e^{2i\vec{k}(t)\vec{r}}b\left(T_1 - \frac{2x''}{c_0}\right)g(z). \end{aligned} \quad (1)$$

Where P_t and P_r are, respectively, the real amplitudes of the transmitted and received plane waves; $b\left(T_1 - \frac{2x''}{c_0}\right)$ is the envelope of the ultrasonic transmitted pulses; and $g(z)$ represents the field distribution along the z axis.

The pulse envelope describes their spatial length in the direction $x'' = x''(x', y')$, i.e., in the direction of the emission and receiving of plane waves for a given wave vector $\vec{k}(t)$ and corresponding angle Φ . As shown in Fig. 1, the distance l_0'' to a given target point, i.e., the probing depth, is determined by the strobing time delay T_1 .

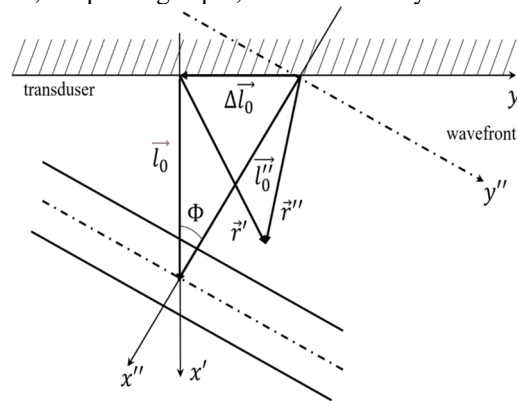


Figure 1. Coordinate system (x', y') associated with the ultrasonic transducer and coordinate system (x'', y'') , where the x'' axis is directed along the propagation direction of the plane wavefront

According to the continuous model of ultrasound wave scattering on density inhomogeneities $\rho(\vec{r}, t)$ and compressibility $\tilde{\beta}(\vec{r}, t)$ the ultrasound Doppler response signal can now be expressed in a simplified form as:

$$e_d(t) = k^2 \int_R P_p'(\vec{r}, t) \{ \tilde{\beta}(\vec{r}, t) - \rho(\vec{r}, t) \} d\vec{r}. \quad (2)$$

The power spectral density of the response signal is determined through the temporal and spatial Fourier transform of the autocorrelation function of the response signal (2):

$$R(\tau) = k^4 \iint_R \overline{P(\vec{r}_1, t_1)P^*(\vec{r}_0, t_0)} C(\vec{r}_1 - \vec{r}_0, \tau) d\vec{r}_0 d\vec{r}_1,$$

The overline indicates averaging over the initial moment of time t_0 , and $C(\vec{r}_1 - \vec{r}_0, \tau)$ is the correlation function of fluctuations of density and compressibility inhomogeneities, which depends only on the difference in coordinates and the time difference $\tau = t_1 - t_0$ for any type of scatterer motion after averaging over the statistical ensemble [48].

The Doppler spectrum is derived in full analogy with the method in [48] and, in the absence of signal accumulation from different directions, can be represented as:

$$S(\omega_p) = \frac{k^4}{(2\pi)^3} \sum_{\omega_j} \int d\vec{q} C(\vec{q}, \omega_p - \omega_j) |P(\vec{q}, \omega_j)|^2.$$

where $C(\vec{q}, \omega_p - \omega_j)$ and $P(\vec{q}, \omega_j)$ are the Fourier transforms of the fluctuation correlator and the transmission-receiving field, respectively. When compounding responses from different plane waves, which is a widely accepted algorithm in all variations of the synthetic aperture method, the Doppler response takes the form:

$$S(\omega_p) = \frac{k^4}{(2\pi)^3} \int d\vec{q} C(\vec{q}, \omega_p) |P(\vec{q}, 0)|^2. \quad (3)$$

Here, $\omega_p = \frac{2\pi}{T}p$ is the discrete frequency of the Fourier transform of the function $P(\vec{r}, t)$, which is periodically extended with a period T . The value T represents the data acquisition period of response signals required for wave compounding.

RESULTS

Directly from expression (3), it follows that in the case of compounding plane waves, the quantity $P(\vec{r}, 0)$ serves as the transmission-receiving field. Furthermore, following [48], the envelope of the emitted pulses will be chosen in the form of a Gaussian function. In this approximation, the transmission-receiving field (1) can be written as:

$$P(\vec{r}, t) = P_0 e^{-2ik((l_0-x')\cos\Phi+y'\sin\Phi)} e^{-\frac{2((l_0-x')\cos\Phi+y'\sin\Phi)^2}{a^2}} g(z), \quad (4)$$

where $2a$ is the spatial length of the pulses along the x'' axis at the e^{-1} level. In formula (4), the relationship between the coordinate system (x', y') and the coordinate systems (x'', y'') and (x, y) is taken into account. Assuming the angles $\Phi(t) = \Omega t$ are small for all plane waves, in the expansion of the transmission-receiving field in terms of Φ , we will retain small terms, including quadratic ones. To estimate the Fourier transforms in this approximation, we will apply a Gaussian weighting window in time, which allows extending the integration limits to infinity:

$$\begin{aligned} P(\vec{r}, \omega_j) &= P_0 g(z) T^{-1} e^{-\frac{2(l_0-x')^2}{a^2}} \int_{-\frac{T}{2}}^{\frac{T}{2}} e^{-2ik\left(\frac{-\Omega^2 t^2}{2}(x'-l_0)+\Omega t y'\right)+i\omega_j t} e^{-\frac{2(y'^2 \Omega^2 t^2 + 2(l_0-x')y'\Omega t - (l_0-x')^2 \Omega^2 t^2)}{a^2}} dt \cong \\ &\cong P_0 g(z) T^{-1} e^{-\frac{2(l_0-x')^2}{a^2}} \int_{-\infty}^{+\infty} e^{-2ik\left(\frac{-\Omega^2 t^2}{2}(x'-l_0)+\Omega t y'\right)+i\omega_j t} e^{-\frac{2(y'^2 \Omega^2 t^2 + 2(l_0-x')y'\Omega t - (l_0-x')^2 \Omega^2 t^2)}{a^2}} e^{-\frac{t^2}{T_W^2}} dt, \end{aligned} \quad (5)$$

where the parameter $T_W \sim T$ in practice describes the effective length of the response signal obtained when applying signal compounding from plane wave responses.

The asymptotic estimate of the integral in (5) can be obtained using the saddle point method, which gives:

$$\begin{aligned} P(\vec{r}, \omega_j) &= P_0 g(z) T^{-1} e^{-\frac{2(l_0-x')^2}{a^2} - 2ik(x'-l_0)} \times \\ &\times \frac{\pi}{\sqrt{-ik\Omega^2(x'-l_0) + \frac{2y'^2 \Omega^2}{a^2} - \frac{2(l_0-x')^2 \Omega^2}{a^2} + \frac{1}{T_W^2}}} e^{\frac{\left(2ik\Omega y' - i\omega_j + \frac{4(l_0-x')y'\Omega}{a^2}\right)^2}{4\left(-ik\Omega^2(x'-l_0) + \frac{2y'^2 \Omega^2}{a^2} - \frac{2(l_0-x')^2 \Omega^2}{a^2} + \frac{1}{T_W^2}\right)}} \end{aligned} \quad (6)$$

The small parameter in formulas (5) and (6) is represented by the value $\Omega T_W \sim \Phi_{\max} \ll 1$, where Φ_{\max} is the maximum angle of inclination of the wave vector $\vec{k}(t)$ from its mean value \vec{k} . It is easy to see that for $\omega_j = 0$, the numerator of the exponent in the second exponential term in (6) is of the second order of smallness. Therefore, in the denominator of this exponent the small terms can be neglected:

$$\begin{aligned} P(\vec{r}, 0) &= P_0 g(z) T^{-1} e^{-\frac{2(l_0-x')^2}{a^2} - 2ik(x'-l_0)} \times \\ &\times \frac{\pi}{\sqrt{-ik\Omega^2(x'-l_0) + \frac{2y'^2 \Omega^2}{a^2} - \frac{2(l_0-x')^2 \Omega^2}{a^2} + \frac{1}{T_W^2}}} e^{(\Omega T_W y')^2 \left(ik + \frac{2(l_0-x')^2}{a^2}\right)}. \end{aligned}$$

Furthermore, the primary dependence of $P(\vec{r}, 0)$ on the coordinates is evidently described by exponential factors, which allows us to neglect small quadratic terms in the denominator of the fraction under the square root. As a result, we obtain:

$$P(\vec{r}, 0) = P_0 T^{-1} \sqrt{\pi T_W^2} g(z) e^{-\frac{2(l_0-x')^2}{a^2} - 2ik(x'-l_0)} e^{(\Omega T_W y')^2 \left(ik + \frac{2(l_0-x')^2}{a^2}\right)}.$$

Finally, for the modulus of this quantity, we have:

$$|P(\vec{r}, 0)| = P_0 g(z) e^{-\frac{2(l_0 - x')^2}{a^2}} T^{-1} \sqrt{\pi T_W^2} e^{-(\Omega T_W y')^2 \left(k^2 - \frac{4(l_0 - x')^2}{a^4} \right)} \quad (7)$$

The parameters in synthetic aperture technologies should be chosen such that the resolution along the y' axis is no worse than in other directions. Therefore, we will assume that the equality $T_W \Omega = \sqrt{2}(ka)^{-1}$ holds. Taking this into account, formula (7) takes its final form:

$$|P(\vec{r}, 0)| = P_0 T^{-1} \sqrt{\pi T_W^2} e^{-\frac{2(l_0 - x')^2}{a^2} - 2z^2} e^{-\frac{2y'^2}{a^2} \left(1 - \frac{4(l_0 - x')^2}{k^2 a^4} \right)} g(z). \quad (8)$$

DISCUSSION

The size and shape of the measuring volume are directly described by formula (8), from which, in particular, the equation for the boundary of the measuring volume at the e^{-1} level follows:

$$\frac{2(l_0 - x')^2}{a^2} + \frac{2y'^2}{a^2} - \frac{8(l_0 - x')^2 y'^2}{a^6 k^2} = 1. \quad (9)$$

From this, we find:

$$l_0 - x' = \pm \frac{a^2 k}{2} \sqrt{\frac{\frac{a^2}{2} - y'^2}{\frac{a^4 k^2}{4} - y'^2}}. \quad (10)$$

This function has zeros at $y' = \pm a/\sqrt{2}$, which describe the boundaries of the measuring volume along the y' axis at $x' = l_0$. It is easy to see that for $y' = 0$, equation (10) gives the same boundary values for the x' axis: $x' = l_0 \pm a/\sqrt{2}$. The obtained solution is valid in the case where the inequality holds:

$$\frac{a^2}{2} < \frac{a^4 k^2}{4}, \quad (11)$$

in which the denominator of the fraction under the square root remains positive as the numerator approaches zero. Formally, equation (10) has additional real solutions in the region where both the numerator and the denominator become negative. However, such solutions are physically invalid, as the measuring volume would acquire additional infinite boundaries, as illustrated in Fig. 2.

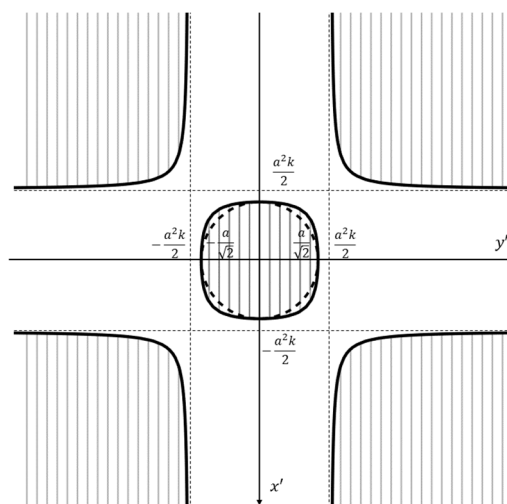


Figure 2. The measuring volume at the center (horizontally shaded) and its boundaries, which are symmetric with respect to x' and y' , along with additional non-physical solutions—branches (vertically shaded) and their asymptotes.

The zeros of the denominator in (10) define the asymptotes of these non-physical regions. Without accounting for the dependence of the pulse envelope on small terms, i.e., without the third term on the left-hand side of equation (9), the measuring volume in the (x', y') plane represents a circle with a radius of $a/\sqrt{2}$, shown in Fig. 2 as a horizontal dashed line. This shape is determined by the chosen value of Ω . Considering the dependence of the pulse envelope on

small linear and quadratic terms results in the resolution along the y' and x' axes remaining unchanged, but the shape of the measuring volume changes along with an increase in its area, as shown in Fig. 2 by the horizontal dashed line. This phenomenon is related to the fact that resolution is determined not only by the interference of responses from plane waves but also by the shape of the region of their intersection around the point l_0 . When the inverse inequality to (11) is satisfied, an increase in the value of y'^2 causes the denominator of the fraction in (10) to first reach zero. Such a solution is also non-physical because, in this case, the measuring volume has no boundaries, as illustrated in Fig. 3.

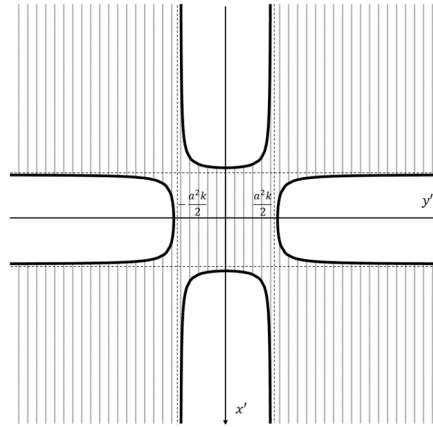


Figure 3. Non-physical infinite measurement volume and its symmetric asymptotes in the case of the inverse of inequality (11) being satisfied

The inequality (11) can be rewritten as $a > \lambda/\sqrt{2}\pi$, which holds well for real ultrasound systems. Specifically, for a frequency of 3.5 MHz, the wavelength is 0.42 mm and the characteristic value of a is 1 mm. This condition becomes even more intuitive from a physical perspective when expressed in terms of the maximum angle of inclination $\Phi_{max} \cong T_w \Omega < 1$. In fact, this is the condition for the smallness of the maximum angle of inclination, for which the obtained solutions are still valid. In the considered approximation, when $\Phi_{max} \cong T_w \Omega = 1$, the measurement volume in the (x', y') plane becomes a square.

CONCLUSIONS

In this work, based on the continuum model of ultrasound wave scattering on inhomogeneities in the medium, the resolution of the PWC system is analyzed. The consideration is carried out taking into account the linear and quadratic terms in the expansion of the small deviations of the wave vector of the current viewpoint from the wave vector of a plane wave without inclination. The condition of smallness of the inclination angles of the plane waves ensures the physicality and correctness of the obtained solutions. The results show that accounting for linear and quadratic angle Φ deviations in the directions of wave transmission and receiving only leads to changes in the shape and volume of the measured volume, which, without accounting for small components, has a spherical shape. At the same time, the dimensions of the measurement volume in the longitudinal and transverse directions do not change.

The noted change in the shape of the measurement volume for realistic values of the maximum inclination angle Φ_{max} is not significant. As is known, the size of the measured volume only affects the time of flight of scatterers through it, which also does not change significantly. This means that the contribution to the Doppler spectrum width, determined by the flight time, cannot change significantly either. Therefore, it can be concluded that when evaluating the spectral characteristics of the ultrasound Doppler response signals, it is quite justified to neglect the dependence of the envelope of the plane wave pulses on the inclination angles if they are small. This circumstance opens the possibility for simplifying spectral Doppler estimates.

ORCID

©Evgen A. Barannik, <https://orcid.org/0000-0002-3962-9960>; ©Mykhailo O. Hrytsenko, <https://orcid.org/0009-0002-5670-5686>

REFERENCES

- [1] I. Trots, A. Nowicki, M. Lewandowski, and Y. Tasinkevych, *Synthetic Aperture Method in Ultrasound Imaging*, (IntechOpen, London, UK, 2011). <http://dx.doi.org/10.5772/15986>
- [2] M.H. Pedersen, K.L. Gammelmark, and J.A. Jensen, *Ultrasound Med. Biol.* **33**(1), 37-47 (2007). <https://doi.org/10.1016/j.ultrasmedbio.2006.07.041>
- [3] J. Bercoff, G. Montaldo, T. Loupas, D. Savery, F. Meziere, M. Fink, and M. Tanter, *IEEE Trans. Ultrason. Ferroelec. Freq. Contr.* **58**(1), 134 (2011). <https://doi.org/10.1109/TUFFC.2011.1780>
- [4] J. Provost, C. Papadacci, C. Demene, J. Gennisson, M. Tanter, and M. Pernot, *IEEE Trans. Ultrason. Ferroelec. Freq. Contr.* **62**(8), 1467 (2015). <https://doi.org/10.1109/TUFFC.2015.007032>
- [5] J. Udesen, F. Gran, K.L. Hansen, J.A. Jensen, C. Thomsen and M.B. Nielsen, *IEEE Trans. Ultrason. Ferroelec. Freq. Contr.* **55**(8), 1729 (2008). <https://doi.org/10.1109/TUFFC.2008.858>

- [6] B. Osmanski, M. Pernot, G. Montaldo, A. Bel, E. Messas, and M. Tanter, *IEEE Trans. Med. Imag.* **31**(8), 1661 (2012). <http://doi.org/10.1109/TMI.2012.2203316>
- [7] C. Papadacci, M. Pernot, M. Couade, M. Fink and M. Tanter, *IEEE Trans. Ultrason. Ferroelec. Freq. Contr.* **61**(2), 288 (2014). <https://doi.org/10.1109/TUFFC.2014.6722614>
- [8] G. Montaldo, M. Tanter, J. Bercoff, N. Benez, and M. Fink, *IEEE Trans. Ultrason. Ferroelectr. Freq. Contr.* **56**(3), 489 (2009). <https://doi.org/10.1109/TUFFC.2009.1067>
- [9] J. Jensen, M.B. Stuart, and J.A. Jensen, *IEEE Trans. Ultrason. Ferroelec. Freq. Contr.* **63**(11), 1922 (2016). <https://doi.org/10.1109/TUFFC.2016.2591980>
- [10] B. Denarietal, *IEEE Trans. Med. Imaging*, **32**(7), 1265 (2013). <https://doi.org/10.1109/TMI.2013.2255310>
- [11] R. Moshavegh, J. Jensen, C.A. Villagómez-Hoyos, M.B. Stuart, M.C. Hemmsenand, and J.A. Jensen, in: *Proceedings of SPIE Medical Imaging*, (SanDiego, California, United States, 2016), pp. 97900Z-97900Z-9. <https://doi.org/10.1117/12.2216506>
- [12] J.-l. Gennisson, et al., *IEEE Trans. Ultrason. Ferroelec. Freq. Contr.* **62**(6), 1059 (2015). <https://doi.org/10.1109/TUFFC.2014.006936>
- [13] J.A. Jensen, S.I. Nikolov, K.L. Gammelmarkand, and M.H. Pedersen, *Ultrasonics*, **44**(1), e5 (2006). <https://doi.org/10.1016/j.ultras.2006.07.017>
- [14] M. Tanter, J. Bercoff, L. Sandrin, and M. Fink, *IEEE Trans. Ultrason. Ferroelectr. Freq. Contr.* **49**(10), 1363 (2002). <https://doi.org/10.1109/TUFFC.2002.1041078>
- [15] J.Y. Lu, *IEEE Trans. Ultrason., Ferroelec. Freq. Contr.* **44**(4), 839 (1997). <https://doi.org/10.1109/58.655200>
- [16] S. Ricci, L. Bassi and P. Tortoli, *IEEE Trans. Ultrason. Ferroelec. Freq. Contr.* **61**(2), 314 (2014). <https://doi.org/10.1109/TUFFC.2014.6722616>
- [17] N. Oddershedeand J.A. Jensen, *IEEE Trans. Ultrason. Ferroelec. Freq. Contr.* **54**(9), 1811 (2007). <https://doi.org/10.1109/TUFFC.2007.465>
- [18] Y. L. Li, D. Hyun, L. Abou-Elkacem, J. K. Willmann, J.J. Dahl, *IEEE Trans. Ultrason. Ferroelec. Freq. Contr.* **63**(11), 1878 (2016), <https://doi.org/10.1109/TUFFC.2016.2616112>
- [19] Y.L. Li, J.J. Dahl, *IEEE Trans. Ultrason. Ferroelec. Freq. Contr.* **62**(6), 1022 (2015). <https://doi.org/10.1109/TUFFC.2014.006793>
- [20] I. K. Ekroll, A. Swillens, P. Segers, T. Dahl, H. Torp and L. Lovstakken, *IEEE Trans. Ultrason. Ferroelec. Freq. Contr.* **60**(4), 727 (2013). <https://doi.org/10.1109/TUFFC.2013.2621>
- [21] S. Salles, H. Liebgott, O. Basset, C. Cachard, D. Vray, and R. Lavarello, *IEEE Trans. Ultrason. Ferroelectr. Freq. Control*, **61**, 1824–1834 (2014). <https://doi.org/10.1109/TUFFC.2014.006543>
- [22] C.-C. Shen, and and C.-L. Huang, *Sensors*, **24**, 262 (2024). <https://doi.org/10.3390/s24010262>
- [23] J. Viti, H.J. Vos, N.D. Jong, F. Guidi, and P. Tortoli, “Contrast detection efficacy for plane vs. focused wave transmission,” in: *2014 IEEE International Ultrasonics Symposium*, (Chicago, 2014), pp. 1750–1753.
- [24] J. Bercoff, “Ultrafast ultrasound imaging,” in: *Ultrasound Imaging-Medical applications*, edited by I.V. Minin, and O.V. Minin, pp. 3-24, (2011). <https://doi.org/10.5772/19729>
- [25] C. Dmené et al., "Spatiotemporal clutter filtering of ultrafast ultrasound data highly increases Doppler and fUltrasound sensitivity," *IEEE transactions on medical imaging*, vol. 34, no. 11, pp. 2271-2285, 2015.
- [26] S. Salles, F. Varray, Y. Bénane and O. Basset, 2016 IEEE International Ultrasonics Symposium (IUS), 2016, pp. 1-4, <https://doi.org/10.1109/ULTSYM.2016.7728751>
- [27] C. Zheng, Q. Zha, L. Zhang and H. Peng, *IEEE Access* **6**, 495 (2018), <https://doi.org/10.1109/ACCESS.2017.2768387>
- [28] Y.M. Benane et al., 2017 IEEE International Ultrasonics Symposium (IUS), 2017, pp. 1-4, <https://doi.org/10.1109/ULTSYM.2017.8091880>
- [29] X. Yan, Y. Qi, Y. Wang, Y. Wang, *Sensors* **21**, 394 (2021), <https://doi.org/10.3390/s21020394>
- [30] C. Golfetto, I. K. Ekroll, H. Torp, L. Løvstakken and J. Avdal, *IEEE Trans. Ultrason. Ferroelec. Freq. Contr.* **68**(4), 1105 (2021), <https://doi.org/10.1109/TUFFC.2020.3033719>
- [31] C.-C. Shen, Y.-C. Chu, *Sensors* **21**, 4856 (2021), <https://doi.org/10.3390/s21144856>
- [32] J. Baranger, B. Arnal, F. Perren, O. Baud, M. Tanter, and C. Dmené, *IEEE transactions on medical imaging*, **37**(7), 1574 (2018). <https://doi.org/10.1109/TMI.2018.2789499>
- [33] A. Daae, M. Wigen, M. Halvorsrød, L. Løvstakken, A. Støylen, S. Fadnes, *Ultrasound i Medicine & Biology*, **49**(9), 1970 (2023), <https://doi.org/10.1016/j.ultrasmedbio.2023.04.019>
- [34] M. Hashemseresht, S. Afrakhteh, and H. Behnam, *Biomedical Signal Processing and Control*, **73**, 103446 (2022). <https://doi.org/10.1016/j.bspc.2021.103446>
- [35] K. Miura, H. Shidara, T. Ishii, K. Ito, T. Aoki, Y. Saijo, and J. Ohmiya, *Ultrasonics*, **145**, 107479 (2025). <https://doi.org/10.1016/j.ultras.2024.107479>
- [36] N. Chennakeshava, B. Luijten, O. Drori, M. Misch, Y.C. Eldarand and R.J.G. van Sloun, “High ResolutionPlane Wave CompoundingThrough Deep Proximal Learning,” in: *2020 IEEE International UltrasonicsSymposium (IUS)*, (Las Vegas, USA, 2020), pp. 1-4, <https://doi.org/10.1109/IUS46767.2020.9251399>
- [37] J. Zhao, Y. Wang, X. Zeng, J. Yu, B.Y.S. Yiu, and A.C.H. Yu, *Ferroelectrics, and Frequency Control*, **62**(8), 1440 (2015). <https://doi.org/10.1109/tuffc.2014.006934>
- [38] Y. Xu, B. Li, J. Luo, X. Liu, and D. Ta, *AIP Advances*, **14**(6), 065001 (2024). <https://doi.org/10.1063/5.0201371>
- [39] I.K. Ekroll, M.M. Voormolen, O.K.-V. Standal, J.M. Rau, and L. Lovstakken, *IEEE Trans. Ultrason. Ferroelec. Freq. Contr.* **62**(9), 1634 (2015). <https://doi.org/10.1109/TUFFC.2015.007010>
- [40] J. Foiret, X. Cai, H. Bendjador, et al., *Sci. Rep.* **12**, 13386 (2022). <https://doi.org/10.1038/s41598-022-16961-2>
- [41] S. Afrakhteh, and H. Behnam, *IEEE Transactions on Ultrasonics, Ferroelectrics, and Frequency Control*, **68**(10), 3094 (2021). <https://doi.org/10.1109/tuffc.2021.3087504>
- [42] R. Paridar, and B.M. Asl, *Ultrasonics*, **135**, 107136 (2023). <https://doi.org/10.1016/j.ultras.2023.107136>
- [43] E.A. Barannik, *Ultrasonics*, **39**(2), 311 (2001). [https://doi.org/10.1016/S0041-624X\(01\)00059-2](https://doi.org/10.1016/S0041-624X(01)00059-2)

- [44] I.V. Skresanova, and E.A. Barannik, *Ultrasonics*, **52**(5), 676 (2012). <https://doi.org/10.1016/j.ultras.2012.01.014>
- [45] I.V. Sheina, O.B. Kiselov, and E.A. Barannik, *East Eur. J. Phys.* (4), 5 (2020), <https://doi.org/10.26565/2312-4334-2020-4-01>
- [46] I.V. Sheina, and E.A. Barannik, *East European Journal of Physics*, (1), 116-122. <https://doi.org/10.26565/2312-4334-2022-1-16>
- [47] E.A. Barannik, and O.S. Matchenko, *East Eur. J. Phys.* **3**(2) 61 (2016). <https://doi.org/10.26565/2312-4334-2016-2-08>. (in Russian)
- [48] E.A. Barannik, and M.O. Hrytsenko, *East Eur. J. Phys.* (1), 476 (2024). <https://doi.org/10.26565/2312-4334-2024-1-52>

РОЗДІЛЬНА ЗДАТНІСТЬ УЛЬТРАЗВУКОВОЇ ДОПЛЕРІВСЬКОЇ СИСТЕМИ З ВИКОРИСТАННЯМ ТЕХНОЛОГІЇ КОГЕРЕНТНОГО КОМПАУНДИНГУ ПЛОСКИХ ХВИЛЬ

Євген О. Баранник, Михайло О. Гриценко

Кафедра медичної фізики та біомедичних нанотехнологій, Харківський національний університет ім. В.Н. Каразіна, 61022, пл. Свободи, 4, м. Харків, Україна

Серед сучасних ультразвукових технологій медичної діагностики особливе місце посідає технологія компаундингу плоских хвиль з різними напрямками поширення, які формують синтезовані зображення. В роботі на базі розвинутої раніше теорії формування доплерівського відгуку досліджена роздільна здатність системи, в якій використовується компаундинг плоских хвиль. При цьому для фази синтезованого відгуку і огинаючої імпульсів випромінювання враховувались малі нелінійні складові по куту відхилення хвильових векторів різних плоских хвиль. В результаті дослідження винайдено, що розміри вимірювального об'єму у поздовжньому та поперечному напрямках не змінюються. Урахування малих складових приводить до незначної зміни форми вимірювального об'єму, який перестає бути точно сферичним. Це пояснюється тим, що роздільна здатність визначається не тільки інтерференцією плоских хвиль, але й областю їх перетину у визначеній точці простору. Отримані результати свідчать про те, що нехтування малими кутами відхилення у огинаючій є повністю виправданим і дозволяє спростити процес отримання спектрів доплерівських сигналів в технології компаундингу плоских хвиль.

Ключові слова: *ультразвук; доплерівський спектр; компаундування плоских хвиль; просторова роздільна здатність; огинаюча імпульсів*

ANISOTROPIC COSMOLOGICAL MODEL IN A MODIFIED THEORY OF GRAVITATION

 G. Satyanarayana^a,  T. Vinutha^b,  Y. Sobhanbabu^c,  B. Srinivasu^c,  P. Jnana Prasuna^d,
 M. Pruthvi Raju^e

^aSasi Institute of Technology and Engineering College (A), Tadepalligudem, India

^bDepartment of Applied Mathematics, Andhra University-530003, India

^cDepartment of Engineering Mathematics and Humanities, SRKR Engineering College (A), Bhimavaram-534204, India

^dDepartment of Science and Humanities, Swarnandhra College of Engineering and Technology (A), Narsapur-534280, India

^eDepartment of Meteorology and Oceanography, Andhra University-530003, India

*Corresponding Author e-mail: sobhan.maths@gmail.com

Received November 11, 2025; revised January 28, 2025; accepted February 18, 2025

In this research, spatially homogeneous and anisotropic LRS Bianchi type-I cosmological model in $f(R, T)$ theory is discussed by choosing the specific form as $f(R, T) = R + \mu e^{-\gamma R} + \lambda T$, here R is the Ricci scalar, T is the trace of the energy-momentum tensor, μ , γ , and λ are constants. In this research the functional form consists of an exponential function which is more generalised than linear, quadratic and other polynomials. The solutions of the field equations are derived by considering the following two conditions (i) the scale factor ($a(t)$) is considered as a hybrid expansion law. By assumption of this scale factor, we can obtain the deceleration parameter as a function of the time dependent variable (ii) $\sigma \propto \theta$ (the proportionality of shear scalar with expansion scalar). For the obtained model, the physical and geometrical properties like as Hubble parameter (H), expansion scalar (θ), volume (V), pressure (p), the energy density (ρ), equation of state (ω) parameter, state-finder parameter (r, s), deceleration parameter (q), jerk parameter (j) are discussed. The graphical behavior of all the parameters of the model is examined with respect to redshift (z) by taking two different values of $\mu = -2.985, -2.902$. In the discussion of all energy conditions, it is noticed that DEC is satisfied for both the values of μ , whereas NEC is satisfied in past ($z > 0$), present ($z = 0$), and violated in future ($z < 0$) for $\mu = -2.985, -2.902$. For both values of μ , the SEC is violated. The violation of SEC represents the accelerating expansion of the cosmos. The obtained results in the model match with recent observational data.

Keywords: LRS Bianchi Type-I; $f(R, T)$ Theory; Exponential Functional Form; Perfect Fluid

PACS: 98.80.-k, 95.36.+x

1. INTRODUCTION

The dynamics of macro-objects such as galaxies, clusters, stars, and planets are described by gravity, the concept of gravity aids in visualizing the stretching and twisting of space-time. The formulation of gravity in curvature has modified our perspective of the cosmos, which comprises two fundamental components: dark energy and dark matter [1, 2, 3]. Dark energy (DE) and dark matter (DM) are two important components and which plays a main role in expanding universe. The rapid behaviour of the universe is thought to be due to a mysterious force that has a negative pressure called DE. Analytical research arises in this space to determine whether DE is the only candidate for the universe's acceleration or other universe resources can accelerate. Such uncertainties have created a hunt for an alternative perspective on general relativity (GR) [4].

In general, GR has forecasted the production of singularities, which is a significant issue in cosmology's big bang theory. Without a singularity, models could predict how much pressure would build up during the decelerating and accelerating phases of the cosmos expansion. The foundation of GR is extraordinary, and has long been regarded as the mathematical sound theory of gravity [5, 6]. The GR cannot adequately explain DE and DM, which leads researchers to divert their attention towards its modification. These modifications have been proposed in two different ways. Firstly, Einstein's field equations have been modified [7, 8, 9, 10]. Secondly, modified theories of gravity, scalar-tensor theories etc., came into existence to change the left-hand side part of the Einstein equation. Different modifications to the GR give different theories of gravitation. Various modified theories such as $f(R)$ gravity, $f(T)$ gravity, $f(G)$ gravity and $f(R, G)$ gravity, where R , T and G are scalar curvature, torsion scalar and Gauss-Bonnet scalar, have emerged. Among all the modified theories of gravity, the $f(R)$ theory is the first and most popular gravitational field theory derived from Einstein's Hilbert action, and $f(R)$ is a function of the Ricci scalar. The $f(R)$ theory reveals many aspects that help to explain the DE problem and also this theory has received the most incredible attention in the previous decade. Chiba et al. [11] have discussed the modified theories of gravity have been shown to be equivalent to scalar-tensor theories of gravity that are incompatible with solar system tests of general relativity, as long as the scalar field propagates over solar system scales. The unification of early-time inflation and late-time acceleration has been established using viable $f(R)$ gravity models

Cite as: G. Satyanarayana, T. Vinutha, Y. Sobhanbabu, B. Srinivasu, P.J. Prasuna, M.P. Raju, East Eur. J. Phys. 1, 357 (2025), <https://doi.org/10.26565/2312-4334-2025-1-44>

© G. Satyanarayana, T. Vinutha, Y. Sobhanbabu, B. Srinivasu, P.J. Prasuna, M.P. Raju, 2025; CC BY 4.0 license

[12]. Within the framework of $f(R)$ gravity, Starobinsky [13] have introduced the DE model. For instance, Buchdahl [14] has looked into modified gravity concepts. Also, the inflationary epoch and dark matter are discussed in this theory [15, 16]. Harko *et al.* [17] have suggest a current improved theory of gravity, in this theory the gravitational Lagrangian is given by an arbitrary Ricci scalar R and trace of the stress-energy tensor T . The $f(R, T)$ gravity field equations are obtained from action principle. In this research, we are considering the following functional form given by

$$f(R, T) = f_1(R) + f_2(T). \quad (1)$$

Also, we take specific choice for functional form as

$$f(R, T) = f_1(R) + f_2(T) = R + \mu e^{-\gamma R} + \lambda T, \quad (2)$$

where μ , γ and λ are constants.

By taking the functional form $f_1(R) = R + me^{-sR}$, Paul et al. [18] have discussed the flat FRW cosmological model in $f(R)$ theory, and also Sahoo et al. [19] have discussed the flat FRW cosmological model in the presence of $f(R, T)$ theory with the functional form $f(R, T) = R + me^{-sR} + \lambda T$. The authors have shown that this functional form exhibits the current accelerating expansion of the universe. By using $f(R, T)$ theory, Moraes and Sahoo [19] have studied traversable wormholes with the function $f(R, T) = R + \gamma e^{\lambda T}$ and by using the same functional form Moraes et al. [20] have obtained FRW cosmological model in the same theory. Noureen and Zubair [21], Moraes et al. [22] and Yousaf et al. [23] have investigated various aspects of the $f(R, T)$ theory.

In today's cosmos, Bianchi space time is essential for examining and understanding the early phases of the universe's evolution. Stephani et al. [24] have a complete list of all solutions of Einstein field equations for all Bianchi type cosmological models (i.e., from I to IX) with perfect fluid. Many authors have been concentrating on this topic in recent days. Sobhanbabu et al. [25] have investigated Kantowski-Sachs interacting and non-interacting Barrow holographic dark energy (BHDE) models in the Saez-Ballester (SB) theory of gravitation. Luciano [26] has investigated SB gravity in the kantowski-sachs universe: a new reconstruction paradigm for BHDE. The authors in the references [27, 28, 29] have worked on Bianchi universe with various theories. Gudekli and Caliskan [30] and Sahoo and Siva kumar [31] have studied the perfect fluid LRS Bianchi type $-I$ universe model in $f(R, T)$. Sahoo and Raghavender [32], Kumar and Archana [33], and Tiwari *et al.* [34] have discussed the LRS Bianchi type- I cosmological model in $f(R, T)$ theory of gravity by choosing various functional forms. Sobhanbabu et al. [35] have analyzed anisotropic BHDE models in the scalar-tensor theory of gravitation. Very recently, Gupta et al. [36] have investigated observational constraints for BHDE with Hubble and Granda-Oliveros cut-off in the modified theory of gravity. Myrzakulov et al. [37] have discussed the probing DE properties with BHDE model in the $f(Q, C)$ gravity.

This paper organized as follows: In section 2, the formulation of field equations for $f(R, T)$ theory is introduced, the metric is given and solutions to the field equations are derived in section 3, in section 4, we have the discussed the physical and geometric properties of the model obtained, and provides the conclusion in last section.

2. METRIC AND FIELD EQUATIONS OF THE MODEL

Now, we consider the LRS Bianchi type- I homogeneous and anisotropic metric of the form

$$ds^2 = -M^2 dx^2 - N^2(dy^2 + dz^2) + dt^2, \quad (3)$$

where M and N are metric potentials and functions of cosmic time t only and (x, y, z) are the co-moving coordinates.

Sharif and Zubair [38], Sahoo and Reddy [39], Tiwari et al. [40], Bishi et al. [41], Shamir and Raza [42], and Rodrigues et al. [43] are some of the authors who have worked with the above metric in various theories of gravity.

The field equations for the metric (3) with help of (2) and (1) are obtained as follows:

$$\left. \begin{aligned} \frac{2\dot{N}}{N} + \frac{\dot{N}^2}{N^2} &= \frac{(8\pi + \frac{3\lambda}{2})p}{1 - \mu\gamma e^{-\gamma R}} - \frac{\lambda\rho}{2(1 - \mu\gamma e^{-\gamma R})} \\ &- \frac{(\mu e^{-\gamma R})(1 + \gamma R)}{2(1 - \mu\gamma e^{-\gamma R})} + \frac{\mu\gamma^2 e^{-\gamma R}\dot{R}}{1 - \mu\gamma e^{-\gamma R}} \left(\frac{2\dot{N}}{N} \right) \\ &+ \frac{\mu\gamma^2 e^{-\gamma R}\ddot{R}}{1 - \mu\gamma e^{-\gamma R}} - \frac{\mu\gamma^3 e^{-\gamma R}\dot{R}^2}{1 - \mu\gamma e^{-\gamma R}} \end{aligned} \right\} \quad (4)$$

$$\left. \begin{aligned} \frac{\dot{N}}{N} + \frac{\dot{M}}{M} + \frac{\dot{M}\dot{N}}{MN} &= \frac{(8\pi + \frac{3\lambda}{2})p}{1 - \mu\gamma e^{-\gamma R}} - \frac{\lambda\rho}{2(1 - \mu\gamma e^{-\gamma R})} \\ &- \frac{(\mu e^{-\gamma R})(1 + \gamma R)}{2(1 - \mu\gamma e^{-\gamma R})} + \frac{\mu\gamma^2 e^{-\gamma R}\dot{R}}{1 - \mu\gamma e^{-\gamma R}} \left(\frac{\dot{M}}{M} + \frac{\dot{N}}{N} \right) \\ &+ \frac{\mu\gamma^2 e^{-\gamma R}\ddot{R}}{1 - \mu\gamma e^{-\gamma R}} - \frac{\mu\gamma^3 e^{-\gamma R}\dot{R}^2}{1 - \mu\gamma e^{-\gamma R}} \end{aligned} \right\} \quad (5)$$

$$\left. \begin{aligned} \frac{\dot{M}\dot{N}}{MN} + \frac{\dot{N}^2}{N^2} &= \frac{(\frac{1}{2})p}{1 - \mu\gamma e^{-\gamma R}} - \frac{(8\pi + \frac{3\lambda}{2})\rho}{1 - \mu\gamma e^{-\gamma R}} \\ &- \frac{(\mu e^{-\gamma R})(1 + \gamma R)}{2(1 - \mu\gamma e^{-\gamma R})} + \frac{\mu\gamma^2 e^{-\gamma R}\dot{R}}{1 - \mu\gamma e^{-\gamma R}} \left(\frac{\dot{M}}{M} + \frac{2\dot{N}}{N} \right) \\ &+ \frac{\mu\gamma^2 e^{-\gamma R}\dot{R}}{1 - \mu\gamma e^{-\gamma R}} \end{aligned} \right\} \quad (6)$$

Here dot denotes the derivative with respect to cosmic time t .

3. SOLUTIONS OF THE FIELD EQUATIONS

The three field equations (4) to (6) contains four unknowns namely p, ρ, M, N , also these field equations are highly non-linear, so in order to find deterministic solution we need to assume two physically valid conditions,

- (i) The shear scalar σ of the model is proportional to the expansion scalar θ of the model, it builds a relation between the metric potentials as given below (Thorne [44], Collins *et al.*, [45]).

$$M = N^n, \quad (7)$$

where n is an arbitrary constant. If $n = 1$, the model is isotropic model otherwise it is anisotropic.

- (ii) Secondly, we take a cosmological scale factor in the form of the hybrid expansion law (Saha *et al.*, [46])

$$a(t) = e^{lt} t^m, \quad (8)$$

here $l > 0, m > 0$ are constants. Any other values of l and m will have new directions to explore cosmology in the context of the hybrid expansion, and this scale factor is first proposed by Akarsu *et al.* [47]. The average scale factor $a(t)$ is defined as

$$a(t) = v^{\frac{1}{3}} = (MN^2)^{\frac{1}{3}}. \quad (9)$$

From equations (7), (8) and (9) we get metric potentials as

$$M = (e^{lt} t^m)^{\frac{3n}{n+2}} \text{ and } N = (e^{lt} t^m)^{\frac{3}{n+2}}. \quad (10)$$

Now the metric (3) with the help of equation (10) gives LRS Bianchi type - I homogeneous and anisotropic cosmological model as

$$ds^2 = -(e^{lt} t^m)^{\frac{6n}{n+2}} dx^2 - (e^{lt} t^m)^{\frac{6}{n+2}} (dy^2 + dz^2) + dt^2. \quad (11)$$

4. COSMOLOGICAL PARAMETERS OF THE MODEL

Equation (11) gives the LRS Bianchi type - I homogeneous and anisotropic cosmological model with a perfect fluid matter source in the $f(R, T)$ theory of gravity, along with the physical and geometrical parameters are discussed. This model is useful for discussing the early stages of the evolution of the universe.

With the help of equations (10) and (8), we get the Hubble parameter (H) of the model as

$$H = l + \frac{m}{t}.$$

The expansion scalar (θ) of the model is obtained as

$$\theta = 3 \left(l + \frac{m}{t} \right).$$

The shear scalar (σ) of the model is given by

$$\sigma^2 = \frac{3(lt + m)^2(n-1)^2}{t^2(n+2)^2}; n \neq -2.$$

The average anisotropic parameter (A_h) for the model is given by

$$A_h = \frac{2(n-1)^2}{(n+2)^2}; n \neq -2.$$

In the present model $A_h = 0$ for $n = 1$ and $A_h \neq 0$ for $n \neq 1$ indicates isotropic and anisotropic nature of the model respectively. The spatial volume (V) of the model is obtained as

$$V = a^3 = e^{3lt} t^{3m}.$$

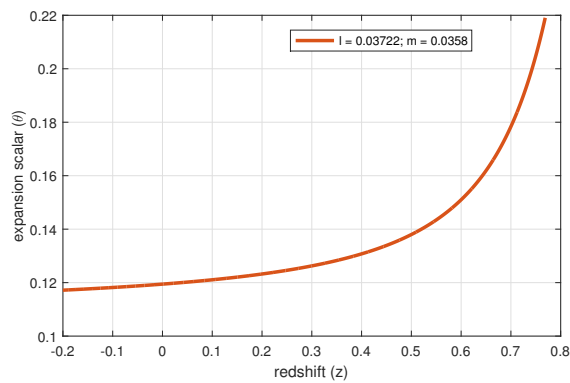


Figure 1. Plot of expansion scalar (θ) versus redshift(z).

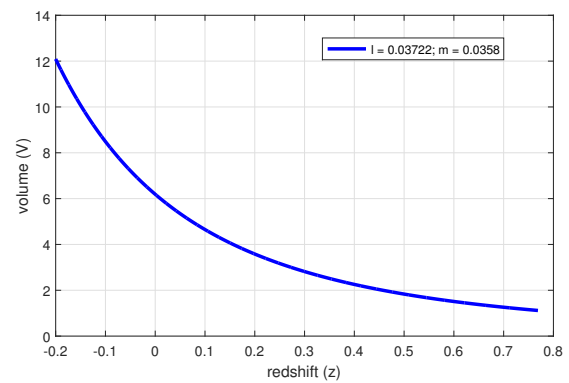


Figure 2. Plot of volume (V) versus redshift(z).

In order to study the behavior of physical parameters, we have plotted them in terms of cosmological redshift. We used the relation between the redshift and the average scale factor $a(t)$ as $1 + z = \frac{a_0}{a}$. We consider the present value of average scale factor a_0 which has been normalized to one.

The graphical behavior of expansion scalar (θ) and volume (V) corresponding to redshift (z) is shown in the Figures 1 and 2. Figure 1 shows that expansion scalar is a positive increasing function of redshift (z). Similarly, the volume is a positive increasing function of redshift (z) which is depicted in Figure 2.

Deceleration parameter (q): The deceleration parameter describes whether the current model is accelerating or not. Recent observational data reveal that the positive sign of q indicates a decelerating mode, whereas the negative sign of q indicates an accelerating phase and q shows expansion at a constant rate if $q = 0$. From equation (12) the deceleration parameter of the model is obtained as

$$q = -1 + \frac{m}{(lt + m)^2}.$$

The behavior of the deceleration parameter (q) with respect to redshift (z) is shown in Figure 3. From Figure 3, it is observed that q exhibits a transition from decelerating phase to accelerating phase at transition redshift (z_t). The transition redshift point (z_t) in the obtained model is observed at $z_t = 0.5$ for $l = 0.3722, m = 0.0358$ which match with recent observational data. The value of q in our model is observed to be negative at present, i. e., $q = -0.8814$, which results the current universe is accelerating and expanding.

Jerk parameter (j): The cosmic jerk parameter $j(t)$ is essential for describing DE and Λ CDM models. When $j = 1$, the model is referred to as a Λ CDM model. The jerk parameter of the model is given by

$$j = \frac{\ddot{a}}{aH^3} = \frac{m^3 + (3lt - 3)m^2 + (3t^2l^2 - 3lt + 2)m + t^3l^3}{(lt + m)^3}.$$

The graphical behavior of jerk parameter (j) corresponding to redshift (z) is shown in Figure 4. For all values of l , m and z , the jerk parameter is positive and reaches the Λ CDM model ($j = 1$).

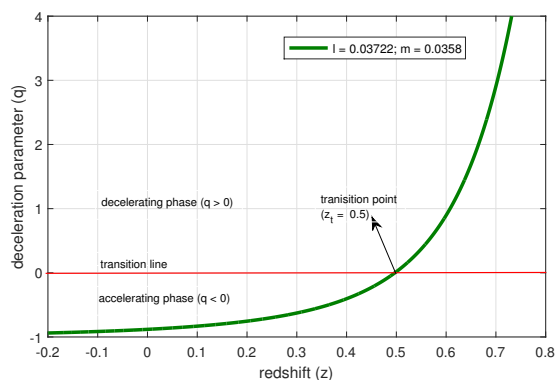


Figure 3. Plot of deceleration parameter (q) versus redshift(z).

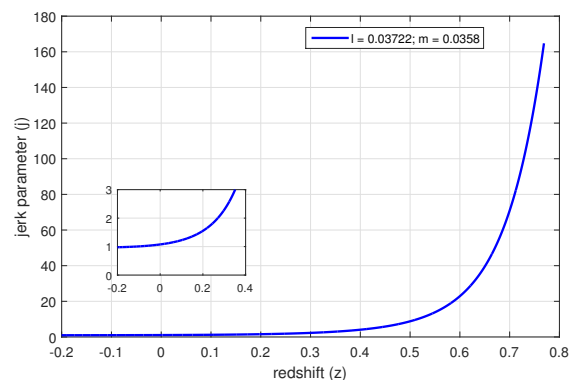


Figure 4. Plot of jerk parameter (j) versus redshift(z).

Pressure and Energy Density: In relativity, pressure, and energy density are two crucial parameters, and they play an essential role in establishing the DE and DM. Another cosmic acceleration known as inflation is predicted to have started in the cosmos before the radiation-dominated epoch in the twenty-first century. Inflation solves many fundamental problems. It gave a lot of evidences for an inflationary phase and DE. By solving the system of equations (4) - (6) with help of equation (10) for the current model pressure and energy density expressions are given as follows:

$$p = \frac{1}{4} \left(\frac{\chi + \phi - 2\psi + \xi_4 - 2\xi_5 - 2\xi_6 + \xi_7}{\xi_1 - \xi_2} + \frac{\chi + \phi + 2\psi + 4\xi_3 - 7\xi_4 - 2\xi_5 - 2\xi_6 - 3\xi_7}{\xi_1 + \xi_2} \right) \quad (12)$$

and

$$\rho = \frac{1}{4} \left(\frac{\chi + \phi - 2\psi - \xi_4 - \xi_5 + 2\xi_6 + 2\xi_7}{\xi_1 - \xi_2} - \frac{\chi + \phi + 2\psi + 4\xi_3 - 7\xi_4 - 2\xi_5 - 2\xi_6 - 3\xi_7}{\xi_1 + \xi_2} \right) \quad (13)$$

$$\chi = \frac{27m^2 + (54lt - 6n - 12)m + 27l^2t^2}{t^2(n+2)^2}$$

$$\phi = \frac{1}{t^2(n+2)^2} \left(n^2 + n + 1 \right) 9m^2 + \left((18lt - 3)n^2 + (18lt - 9)n + 18lt - 6 \right) m$$

$$\psi = \frac{1}{(n+2)^2t^2} \left(9(lt+m)^2(2n+1) \right)$$

$$\xi_1 = \frac{16\pi + 3\lambda}{2(1 - \mu\gamma e^{-\gamma\eta})}$$

$$\xi_2 = \frac{\lambda}{2(1 - \mu\gamma e^{-\gamma\eta})}$$

$$\xi_3 = \frac{\mu e^{-\gamma\eta}(1 + \gamma\eta)}{2(1 - \mu\gamma e^{-\gamma\eta})}$$

$$\xi_4 = \frac{3\mu\gamma^2 e^{-\gamma\eta}(lt+m)}{(1 - \mu\gamma e^{-\gamma\eta})(n+2)t} \left(\frac{36m}{t^3(n+2)^2} \right) \left(\left(lt + m - \frac{1}{3} \right) n^2 + \left(2lt + 2m - \frac{4}{3} \right) n + 3lt + 3m - \frac{4}{3} \right)$$

$$\xi_5 = \frac{\mu\gamma^2 e^{-\gamma\eta}}{(1 - \mu\gamma e^{-\gamma\eta})} \left(\frac{72m}{t^4(n+2)^2} \right) \left(\left(lt + m - \frac{3m}{2} \right) n^2 + 3lt + (2lt + 3m - 2)n + \frac{9m}{2} - 2 \right)$$

$$\xi_6 = (-\mu\gamma^3 e^{-\gamma\eta}) \left(\frac{36m}{t^3(n+2)^2} \right) \left(\left(lt + m - \frac{1}{3} \right) n^2 + 3lt + \left(2lt + 2m - \frac{4}{3} \right) n + 3m - \frac{4}{3} \right)^2$$

$$\xi_7 = \frac{3n\mu\gamma^2 e^{-\gamma\eta}(lt+m)}{(1 - \mu\gamma e^{-\gamma\eta})(n+2)t} \left(\frac{36m}{t^3(n+2)^2} \right) \left(\left(lt + m - \frac{1}{3} \right) n^2 + \left(2lt + 2m - \frac{4}{3} \right) n + 3lt + 3m - \frac{4}{3} \right)$$

here

$$\eta = \frac{1}{t^2(n+2)^2} \left((n^2 + 2n + 3)18m^2 + \left((6lt - 1)6n^2 + (3lt - 1)24n + 108lt - 24 \right) m + 18l^2t^2(n^2 + 2n + 3) \right)$$

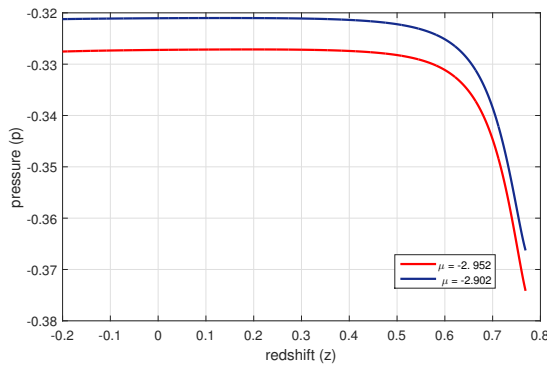


Figure 5. Plot of pressure (p) versus redshift(z) for $l = 0.03722$, $m = 0.0358$, $\gamma = 2.1535$, $\lambda = 7.5562$ and $n = 5$

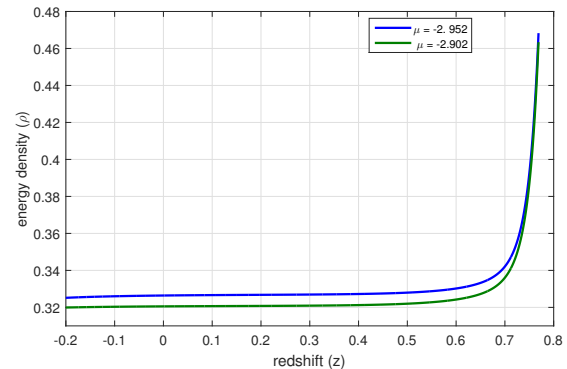


Figure 6. Plot of energy density (ρ) versus redshift(z) for $l = 0.03722$, $m = 0.0358$, $\gamma = 2.1535$, $\lambda = 7.5562$ and $n = 5$

The pressure (p) and energy density (ρ) are plotted against redshift (z) for two different values $\mu = -2.958, -2.902$, which is shown in the Figures 5 and 6. Figure 5, indicates that pressure (p) is negative, increasing function of redshift (z) for both the values of μ . Similarly, the energy density (ρ) is a positive and decreasing function of redshift (z) for both the values of $\mu = -2.985$ and $\mu = -2.902$, which is shown in Figure 6.

Diagnostic Parameters: Many astrophysicists have explored dark energy models to explain the behavior of the universe, even then some geometric parameters cannot classify DE models. As a result, a device that provides reliable information about the universe's accelerating expansion is necessary. Due to this reason, a new pair of state-finder parameters, named $\{r, s\}$ are introduced by Sahni *et al.* (2003) [48]. These parameters represent well-known DE regions of the universe as follows: $(r, s) = (1, 0)$ and $(1, 1)$ corresponds to the Λ CDM and CDM limits, respectively. $s < 0$ and $r > 1$ represent the Chaplygin gas, whereas $s > 0$ and $r < 1$ describe the DE regions of the phantom and quintessence eras.

For the current model, the statefinder parameters are obtained as

$$r = \frac{\ddot{a}}{aH^3} = \frac{m^3 + (3lt - 3)m^2 + (3t^2l^2 - 3lt + 2)m + t^3l^3}{(lt + m)^3},$$

$$s = \frac{r - 1}{3(q - \frac{1}{2})} = \frac{2m(lt + m - \frac{2}{3})}{(3t^2l^2 + 6lmt + 3m^2 - 2m)(lt + m)}.$$

From Figure 7 it is observed that initially it lies in the chaplygin gas region ($r > 1, s < 0$) and moves towards the Λ CDM model ($r = 1, s = 0$), finally it approaches the quintessence region ($r < 1, s > 0$) at late-times.

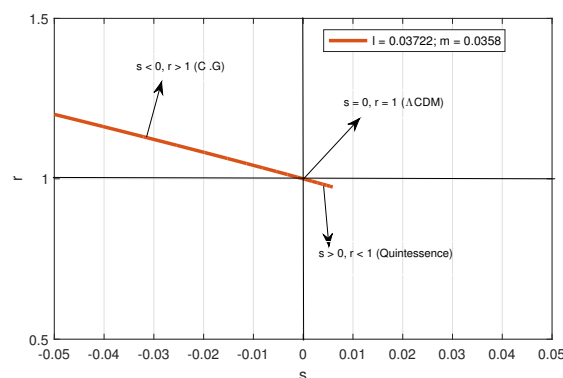


Figure 7. Plot of statefinder parameters (r, s) versus redshift(z).

Equation of State Parameter: The EoS parameter, illustrated by the ratio of pressure and energy density (i.e., $\omega = \frac{p}{\rho}$), is one of the most vital aspects in describing the dark energy phenomenon $\omega = 1$, $\omega = \frac{1}{3}$ and $\omega = 0$, for stiff fluid, dust (radiation matter-dominated) and decelerating phase respectively and also $\omega = -1$ indicates Λ CDM, $-1 < \omega < -\frac{1}{3}$ represents the quintessence region and $\omega < -1$ indicates the phantom region. The equation of state (ω) parameter is

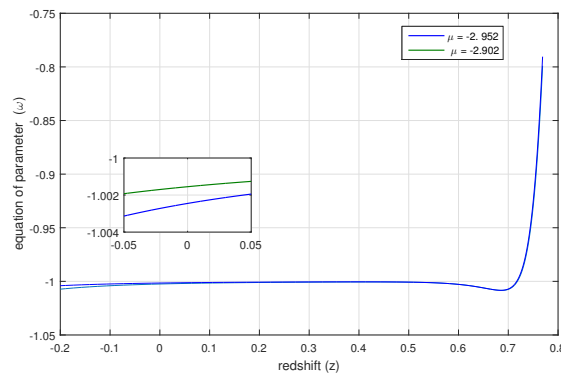


Figure 8. Plot of equation of state (ω) parameter versus redshift(z) for $l = 0.03722$, $m = 0.0358$, $\gamma = 2.1535$ and $\lambda = 7.5562$, $n = 5$.

plotted against redshift (z) and is shown in Figure 8. From Figure 8, it is observed that it exhibits quintom-like behavior, i.e., initially, it lies in the quintessence region ($\omega > -1$) and later on reaches the phantom region ($\omega < -1$) by crossing the phantom divide line ($\omega = -1$).

Energy Conditions: To understand the behavior of light-like, or spacelike, timelike curve compatibility, energy conditions are usually necessary. Null energy conditions (NEC), weak energy conditions (WEC), dominant energy conditions (DEC), and strong energy conditions (SEC) are the four types of energy conditions used in current cosmology. Energy conditions are also significant in theoretical applications, such as verifying the positive mass theorem using DEC and discovering the second law of black hole thermodynamics with NEC. Capozziello et al. [49] used the contraction of time-like and null vectors for the energy-momentum, Ricci, and Einstein tensors to explain energy conditions. Capozziello et al. [50] have explained the energy conditions in modified gravities in a very clear way.

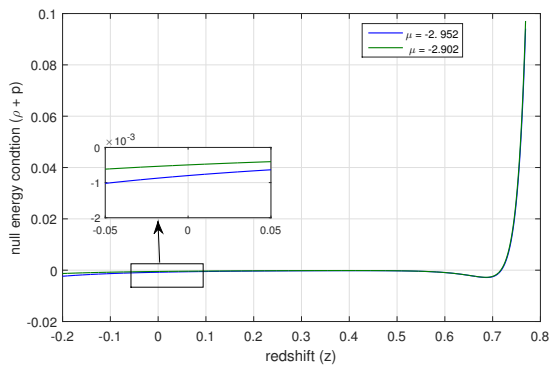


Figure 9. Plot of null energy condition ($\rho + p$) versus redshift(z) for $l = 0.03722$, $m = 0.0358$, $\gamma = 2.1535$, $\lambda = 7.5562$ and $n = 5$.

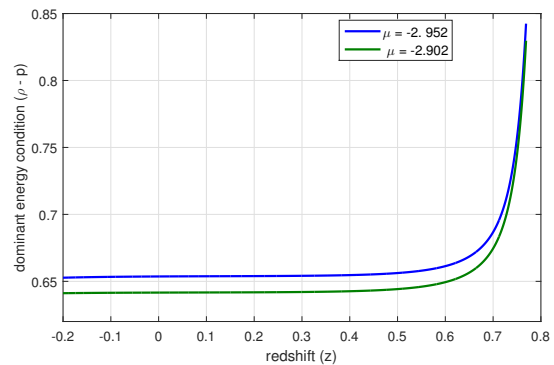


Figure 10. Plot of dominant energy condition ($\rho - p$) versus redshift(z) for $l = 0.03722$, $m = 0.0358$, $\gamma = 2.1535$, $\lambda = 7.5562$ and $n = 5$.

Many authors have investigated these energy conditions in the context of modified gravity and discovered intriguing results (Santos et al. [51, 52]). The energy conditions can be used to impose constraints on these functions consistent with those observed in the cosmological arena. These energy conditions have been recently discussed in the $f(T)$ (Liu and Reboucas [53]) and $f(R, T)$ (Sharif and Zubair [54]) theories. The energy conditions are derived from a well-known purely geometric relationship known as the [55] Raychaudhuri equation in conjunction with the gravitational attractiveness feature. An anomaly and a singularity are crucial in understanding the universe's evolution.

The behavior of the null energy condition (NEC) corresponding to redshift(z) is shown in the Figure 9. It is observed that for both values of μ , the NEC is positive at present and past whereas it is negative in future. At present $z = 0$ the NEC is satisfied and in future NEC is violated. Violation of NEC leads to the formation of big rip. Same phenomenon we may observe in EoS parameter.

The dominant energy condition and strong energy condition are plotted with respect to redshift (z) and these are shown in the Figures 10, 11 for both the values of μ . The strong energy condition is violated throughout the universe's expansion for both the values of μ . The violation of strong energy condition leads to the accelerating expansion of the cosmos.

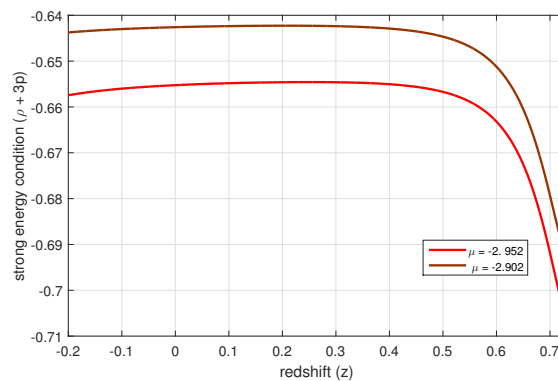


Figure 11. Plot of strong energy condition ($\rho + 3p$) versus redshift(z) for $l = 0.03722$, $m = 0.0358$, $\gamma = 2.1535$, $\lambda = 7.5562$ and $n = 5$.

5. CONCLUSIONS







In this paper, we have discussed the $f(R, T)$ gravity by considering the spatially homogeneous and anisotropic LRS Bianchi type- I cosmological model with $f(R, T) = R + \mu e^{-\gamma R} + \lambda T$ as a functional form by assuming perfect fluid as a matter source. We have obtained the solutions from the field equations by using two conditions i.e., hybrid expansion law ($a(t) = e^{lt} t^m$) and another condition is $\sigma \propto \theta$ (which leads to the relationship between the metric potentials). The graphical behavior of the geometrical parameters like Hubble parameter (H), expansion scalar (θ) and volume (V), deceleration parameter (q), state-finder parameters (r, s) and jerk parameter (j) are done with respect to redshift (z), by considering the parameters $l = 0.03722$ and $m = 0.0358$. Meanwhile, the graphical behavior of physical parameters like pressure (p), energy density (ρ), EoS parameter (ω) and energy conditions with respect to redshift (z) is done by considering two different values of $\mu = -2.958, -2.902$ and observed the following interesting results.

- The behavior of the expansion scalar (θ) with respect to redshift (z) is a positive function which represents the universe's accelerating expansion.
- From figure 2, it is observed that volume is a positive and increasing function of redshift (z), and at late-times it approaches to large value.
- The deceleration parameter (q) exhibits transition from decelerating phase ($q > 0$) to accelerating phase ($q < 0$) at $z_t = 0.5$, which match with the observational data. The theoretical value of q obtained in the present model is $q = -0.8814$ for $z = 0$ and at late-times ($z < 0$) the value of q approaches to -1 (de-Sitter model). The jerk parameter is positive throughout the evolution of the universe. Akarsu *et al.* (2014) [47] assessed the jerk parameter value as $j = 1$ for the Λ CDM model.
- Figures 5 and 6 represent the behavior of energy density ρ and pressure p against redshift (z) for different values of $\mu = -2.958, -2.902$. It is observed that ρ is positive for both the values of μ throughout the universe's evolution and approaches zero as $z \rightarrow -1$. The pressure (p) stays in the negative region for both the values of μ throughout the universe's expansion. The negative value of pressure may be responsible for cosmic acceleration.
- The graphical behavior of EoS parameter (ω) initially it is in quintessence region ($\omega > -1$) and reaches the phantom region ($\omega < -1$) by passing the phantom divide line ($\omega = -1$) for both the values of μ (i.e., it exhibits quintom like behavior).
- The behavior of the null energy condition (NEC) corresponding to redshift(z) is shown in the figure 9. From figure 9 it is observed that for both values of μ , the NEC is positive at present and past whereas it is negative in future. At present $z = 0$ the NEC is satisfied and in future NEC is violated. Violation of NEC leads to the formation of big rip and the same phenomenon we have observe in EoS parameter.
- Similarly the study of dominant energy condition ($\rho - p$) and strong energy condition ($\rho + 3p$) corresponding to redshift (z) were illustrated in the figures 10 and 11. Clearly it is observed that the dominant energy condition is satisfied for both the values of μ while the strong energy condition is violated throughout the evolution of cosmos. The violation of strong energy condition leads to the accelerating expansion of the universe. Finally in the obtained model, the study on the LRS Bianchi type - I space-time with the form $f(R, T) = R + \mu e^{-\gamma R} + \lambda T$ is carried out. The behavior of various cosmological parameters illustrated here represents accelerating expansion of universe. The interesting point in this article is without including any exotic fluid the present model represents accelerating and expanding.

Acknowledgments

The authors express their sincere thanks to the anonymous reviewers for their constructive comments and suggestions which have improved the presentation and quality of the manuscript.

ORCID

 **G. Satyanarayana**, <https://orcid.org/0000-0003-3452-1675>;  **T. Vinutha**, <https://orcid.org/0000-0002-9968-3686>;
 **Y. Sobhanbabu**, <https://orcid.org/0000-0003-0717-1323>;  **B. Srinivasu**, <https://orcid.org/0009-0004-8305-9688>;
 **P. Jnana Prasuna**, <https://orcid.org/0009-0000-2369-7339>;  **M. Pruthvi Raju**, <https://orcid.org/0000-0002-3620-4545>

REFERENCES

- [1] K. Bamba, *et al.*, *Astrophys. Space Sci.* **342**, 155 (2012). <https://doi.org/10.1007/s10509-012-1181-8>
- [2] E. J. Copeland, *et al.*, *Int. J. Mod. Phys. D*, **15**, 1753 (2006). <http://dx.doi.org/10.1142/S021827180600942X>
- [3] L. Amendola, and S. Tsujikawa, (Cambridge University Press, 2010).
- [4] A. G. Riess, *et al.*, *Astron. J.* **116**, 1009 (1998). <https://doi.org/10.1086/300499>
- [5] S. Nojiri, and S. D. Odintsov, *Phys. Rep.* **505**, 59 (2011). <https://doi.org/10.1016/j.physrep.2011.04.001>
- [6] S. Nojiri, *et al.*, *Phys. Rept.* **692**, 1 (2017). <https://doi.org/10.1016/j.physrep.2017.06.001>
- [7] A. Kamenshchik, *et al.*, *Phys. Lett. B*, **511**, 265 (2001). [https://doi.org/10.1016/S0370-2693\(01\)00571-8](https://doi.org/10.1016/S0370-2693(01)00571-8)
- [8] V. Gorini, *et al.*, *Phys. Rev. D*, **67**, 063509 (2003). <https://doi.org/10.1103/PhysRevD.67.063509>
- [9] B. Ratra, and P. J. E. Peebles, *Phys. Rev. D*, **37**, 3406 (1988). <https://doi.org/10.1103/PhysRevD.37.3406>
- [10] R. R. Caldwell, *Phys. Lett. B*, **545**, 23 (2002). [https://doi.org/10.1016/S0370-2693\(02\)02589-3](https://doi.org/10.1016/S0370-2693(02)02589-3)
- [11] T. Chiba, T.L. Smith, and A. L. Erickcek, *Phys. Rev. D*, **75**, 124014 (2007). <https://doi.org/10.1103/PhysRevD.75.124014>
- [12] S. Nojiri, S. D. Odintsov, in: *Problems of Modern Theoretical Physics. A Volume in Honour of Prof. Buchbinder, I.L. in the Occasion of his 60th Birthday*, pp. 266-285. (HTSPU Publishing, Tomsk, 2010).
- [13] A. A. Starobinsky, *Phys. Lett. B*, **91**, 99 (1980). [https://doi.org/10.1016/0370-2693\(80\)90670-X](https://doi.org/10.1016/0370-2693(80)90670-X)
- [14] H. A. Buchdahl, *Monthly Notices of the Royal Astronomical Society*, **150**, 1 (1970). <https://doi.org/10.1093/mnras/150.1.1>
- [15] R. Myrzakulov, *et al.*, *Eur. Phys. J. C*, **75**, 444 (2015). <https://doi.org/10.1140/epjc/s10052-015-3672-6>
- [16] A. O. Barvinsky, *et al.*, *Eur. Phys. J. C*, **75**, 584 (2015). <https://doi.org/10.1140/epjc/s10052-015-3817-7>
- [17] T. Harko, *et al.*, *Phys. Rev. D*, **84**, 024020 (2011). <https://doi.org/10.1103/PhysRevD.84.024020>
- [18] B. C. Paul, *et al.*, *Phys. Rev. D*, **79**, 083534 (2009). <https://doi.org/10.1103/PhysRevD.79.083534>
- [19] P. K. Sahoo, *et al.*, *Eur. Phys. J. C*, **78**, 46 (2018). <https://doi.org/10.1140/epjc/s10052-018-5538-1>
- [20] P. H. R. S. Moraes, *et al.*, *Gen. Relativ. Gravit.* **52**, 32 (2020). <https://doi.org/10.1007/s10714-020-02681-3>
- [21] I. Noureen, and M. Zubair, *Eur. Phys. J. C*, **75**, 62 (2015). <https://doi.org/10.1140/epjc/s10052-015-3289-9>
- [22] P. H. R. S. Moraes, and P.K. Sahoo, *Eur. Phys. J. C*, **79**, 677 (2019). <https://doi.org/10.1140/epjc/s10052-019-7206-5>
- [23] Z. Yousaf, *et al.*, *Eur. Phys. J. Plus*, **132**, 268 (2017). <https://doi.org/10.1140/epjp/i2017-11541-6>
- [24] H. Stephani, *et al.*, *Exact solutions of Einstein's field equations*, (Deutscher Verlag Der Wissenschaften, Berlin, 1980).
- [25] Y. Sobhanbabu, *et al.*, *New Astronomy*, **104**, 102066 (2023). <https://doi.org/10.1016/j.newast.2023.102066>
- [26] G. G. Luciano, arXiv:2301.12488 [gr-qc], <https://doi.org/10.48550/arXiv.2301.12488>
- [27] E. N. Saridakis, *Phys. Review D*, 2020, **102**, 123525 (2020). <https://doi.org/10.1103/PhysRevD.102.123525>
- [28] G. P. Singh, *et al.*, *Chin. J. Phys.* **54**, 895 (2016). <https://doi.org/10.1016/j.cjph.2016.10.005>
- [29] E. A. Hegazy, and F. Rahaman, *Indian J. Phys.* **93**, 1643 (2019). <https://doi.org/10.1007/s12648-019-01424-8>
- [30] E. Gudekli, and A. Caliskan, *AIP Conf. Proc.* **2042**, 020052(2018). <https://doi.org/10.1063/1.5078924>
- [31] P. K. Sahoo, and M. Sivakumar, *Astrophys. Space Sci.* **357**, 60 (2015). <https://doi.org/10.1007/s10509-015-2264-0>
- [32] P. Sahoo, and R. Reddy, *Astrophys.* **2**, 61 (2017). <https://doi.org/10.1007/s10511-018-9522-0>
- [33] B. V. Kumar, and D. Archana, *Int. J. Geom. Methods Mod. Phys.* **17**, 2050203 (2020). <https://doi.org/10.1142/S0219887820502035>
- [34] R. K. Tiwari, *et al.*, *Int. J. Geom. Methods Mod. Phys.* **17**, 2050187 (2020). <https://doi.org/10.1142/S021988782050187X>
- [35] Y. Sobhanbabu, *et al.*, *East Eur. J. Phys.* (2), 48-63 (2024). <https://doi.org/10.26565/2312-4334-2024-2-04>
- [36] S. Gupta, *et al.*, *Physica Scripta*, **100**, 015035 (2024). <https://doi.org/10.1088/1402-4896/ad9e51>
- [37] N. Myrzakulov, *et al.*, *Phys. Dark Universe*, **47**, 101790 (2024). <https://doi.org/10.1016/j.dark.2024.101768>
- [38] M. Sharif, and M. Zubair, *J. Phys. Soc. Jpn.* **82**, 014002 (2013). <https://doi.org/10.7566/JPSJ.82.014002>
- [39] P. Sahoo, and R. Reddy, *Astrophys.* **61**, 134 (2018). <https://doi.org/10.1007/s10511-018-9522-0>
- [40] R. K. Tiwari, *et al.*, *Int. J. Geom. Methods Mod. Phys.* **17**, 2050187 (2020). <https://doi.org/10.1142/S021988782050187X>

- [41] B. K. Bishi, *et al.*, Int. J. Geom. Methods Mod. Phys. **14**, 1750158 (2017). <https://doi.org/10.1142/S0219887817501584>
- [42] M. F. Shamir, and Z. Raza, Can. J. Phys. **93**, 37 (2015). <https://doi.org/10.1139/cjp-2014-0338>
- [43] M. E. Rodrigues, *et al.*, Int. J. Mod. Phys. D, **23**, 1450004 (2014). <https://doi.org/10.1142/S0218271814500047>
- [44] K. S. Thorne, Astrophys. J. **148**, 51 (1967). <https://doi.org/10.1086/149127>
- [45] C. B. Collins, J. Math. Phys. **18**, 2116 (1977). <https://doi.org/10.1063/1.523191>
- [46] B. Saha, *et al.*, Astrophys. Space Sci. **342**, 257 (2012). <https://doi.org/10.1007/s10509-012-1155-x>
- [47] O. Akarsu, *et al.*, J. Cosmol. Astropart. Phys. **01**, 022 (2014). <https://doi.org/10.1088/1475-7516/2014/01/022>
- [48] V. Sahni, *et al.*, J. Exp. Theor. Phys. Lett. **77**, 201 (2003). <https://doi.org/10.1134/1.1574831>
- [49] S. Capozziello, *et al.*, Phys. Rept. **509**, 167 (2011). <https://doi.org/10.1016/j.physrep.2011.09.003>
- [50] S. Capozziello, *et al.*, Phys. Rev. D, **91**, 124019 (2015). <https://doi.org/10.1103/PhysRevD.91.124019>
- [51] J. Santos, *et al.*, Phys. Rev. D, **76**, 083513 (2007). <https://doi.org/10.1103/PhysRevD.76.083513>
- [52] J. Santos, *et al.*, Int. J. Mod. Phys. D, **19**, 1315 (2010). <https://doi.org/10.1142/S0218271810017639>
- [53] D. Liu, and M. J. Reboucas, Phys. Rev. D, **86**, 083515 (2012). <https://doi.org/10.1103/PhysRevD.86.083515>
- [54] M. Sharif, and M. Zubair, J. High Energy Phys. **2013**, 79 (2013). [https://doi.org/10.1007/JHEP12\(2013\)079](https://doi.org/10.1007/JHEP12(2013)079)
- [55] A. Raychaudhuri, Phys. Rev. **98**, 1123 (1955). <https://doi.org/10.1103/PhysRev.98.1123>

Анізотропна космологічна модель у модифікованій теорії гравітації

Г. Сат'янараяна^a, Т. Вінута^b, Й. Собханбабу^c, Б. Срінівасу^c, П. Джнана Прасуна^d, М. Прутві Раджуе^e

^aІнститут технології та інженерний коледж Сасі (А), Тадепаллігудем, Індія

^bКафедра прикладної математики, Університет Андхра-530003, Індія

^cКафедра інженерної математики та гуманітарних наук, Інженерний коледж SRKR (А), Бхімаварам-534204, Індія

^dВідділ науки та гуманітарних наук, коледж інженерії та технологій Сварнандхра (А), Нарсапур-534280, Індія

^eВідділ метеорології та океанографії, Університет Андхра-530003, Індія

У цьому дослідженні обговорюється просторово однорідна та анізотропна космологічна модель LRS Bianchi типу I в теорії $f(R, T)$ шляхом вибору конкретної форми як $f(R, T) = R + \mu e^{-\gamma R} + \lambda T$, тут R — скаляр Річчі, T — слід тензора енергії-імпульсу, μ , γ і λ є константами. У цьому дослідженні функціональна форма складається з експоненціальної функції, яка є більш узагальненою, ніж лінійні, квадратичні та інші поліноми. Розв'язки рівнянь поля виводяться з урахуванням наступних двох умов (i) масштабний коефіцієнт ($a(t)$) розглядається як гібридний закон розширення. Припускаючи цей масштабний коефіцієнт, ми можемо отримати параметр уповільнення як функцію змінної, що залежить від часу (ii) $\sigma \propto \theta$ (пропорційність скаляра зсуву зі скаляром розширення). Для отриманої моделі обговорюються такі фізичні та геометричні властивості, як параметр Хаббла (H), скаляр розширення (θ), об'єм (V), тиск (p), густина енергії (ρ), параметр рівняння стану (ω), параметр пошуку стану (r, s), параметр уповільнення (q), параметр ривка (j). Графічну поведінку всіх параметрів моделі досліджено щодо червоного зсуву (z), взявши два різних значення $\mu = -2, 985, -2, 902$. Під час обговорення всіх енергетичних умов помічено, що DEC задовольняється для обох значень μ , тоді як NEC задовольняється в минулому ($z > 0$), теперішньому ($z = 0$) і порушується в майбутньому ($z < 0$) для $\mu = -2, 985, -2, 902$. Для обох значень μ SEC порушується. Порушення SEC являє собою прискорене розширення космосу. Отримані результати в моделі збігаються з останніми даними спостережень.

Ключові слова: LRS Б'янчі-I; $f(R, T)$ теорія; експоненціальна функціональна форма; ідеальна рідина

MODULATING EFFECTS OF POLYPHENOLS ON THE INTERACTIONS BETWEEN FUNCTIONAL PROTEINS AND AMYLOID FIBRILS

 U. Malovytsia^a,  V. Trusova^{a*},  M.H. Thomsen^b,  G. Gorbenko^a

^a*Department of Medical Physics and Biomedical Nanotechnologies, V.N. Karazin Kharkiv National University
4 Svobody Sq., Kharkiv, 61022, Ukraine*

^b*AAU Energy, Aalborg University, Niels Bohrs Vej 8, 6700 Esbjerg, Denmark*

**Corresponding Author e-mail: valerija.trusova@karazin.ua*

Received December 1, 2024, revised January 15, 2025; accepted February 1, 2025

The present study was focused on the investigation of the binary and ternary systems containing the functional proteins, polyphenols and amyloid fibrils using the differential absorption spectroscopy, intrinsic protein fluorescence and fluorescent probe techniques. The group of polyphenols (PF) included the representatives of four different classes: flavonoid quercetin (QR), phenolic acid (salicylic acid, SA), curcuminoid curcumin (CR) and tannin gallic acid (GA). The functionally important proteins were represented by hemoglobin (Hb), cytochrome c (Ct) and serum albumin (BSA). The amyloid fibrils were prepared from the N-terminal (1-83) fragment of apolipoprotein A-I with amyloidogenic mutation G26R (ApoA-IF). It was demonstrated that the spectral markers such as the position and intensity of the bands in differential absorption spectra, fluorescence intensity and emission maxima of the intrinsic (Trp) and extrinsic (TDV) fluorophores can be regarded as sensitive indicators of the protein structural modifications induced by amyloid fibrils and polyphenols. The observed changes in the Trp and TDV fluorescence were interpreted in terms of several processes: i) PF-induced conformational changes of the protein molecules accompanied by the alterations in microenvironment of Trp residues; ii) competition between PF and TDV for the protein binding sites; iii) non-resonance quenching of Trp or TDV fluorescence by PF; iv) resonance quenching (Forster resonance energy transfer) between Trp or TDV and PF. Taken together, the results obtained suggest that polyphenolic compounds can modulate the interactions between functional proteins and amyloid fibrils and can be considered as perspective agents for reducing the amyloid toxicity.

Key words: Amyloid fibrils; Functional proteins; Polyphenols; Differential absorption spectroscopy; Fluorescence

PACS: 87.14.C++c, 87.16.Dg

Amyloid fibrils, the ordered aggregates with a core β -sheet structure, are currently associated with a variety of human diseases, including neurodegenerative disorders, systemic amyloidosis, type-II diabetes, cancer, etc. [1-3]. Among the proposed mechanisms of amyloid cytotoxicity are disruption of plasma and intracellular cell membranes [4-7], suppression of proteasomal degradation [7], mitochondrial dysfunction [8] and generation of reactive oxygen species [9]. It was also demonstrated that amyloid fibrils can form complexes with endogenous proteins, thereby affecting their structural and functional properties. For instance, A β peptide are capable of interacting with human serum albumin [10], while islet amyloid polypeptide, β -amyloid and insulin amyloid fibrils directly interact with the receptor protein NLRP3 resulting in NLRP3 inflammasome activation and pyroptotic cell death [11-13]. In view of this, the aim of the present study was to explore the interactions between functionally important proteins differing in their structure and physicochemical properties such as serum albumin, hemoglobin and cytochrome c. with the amyloid fibrils from N-terminal fragment of apolipoprotein A-I and a series of polyphenols including quercetin (QR), curcumin (CR), gallic acid (GA) and salicylic acid (SA). The choice of the endogenous proteins for experimental study was governed by their availability and significant physiological roles. Albumin, the major protein in human plasma, is responsible for maintaining the osmotic pressure, transport of various small molecules, regulation of the immune response, etc. [14]. Hemoglobin accounts for transport of oxygen and carbon dioxide, modulation of erythrocyte metabolism, heat transduction via oxygation-deoxygenation reactions [15], while cytochrome c functions as a component of the electron transport chain in the inner mitochondrial membrane and displays pro-apoptotic activity [16]. Polyphenols (PF), which are abundant in various fruits and vegetables, have garnered attention for their potential to modulate different types of biomolecular interactions [17]. These compounds can interact with both amyloid fibrils and functional proteins, but the implications of these interactions are not yet fully understood.

MATERIALS AND METHODS

The bovine serum albumin (BSA), horse hemoglobin (Hb), cytochrome c from bovine heart (Ct) and polyphenols were purchased from Sigma. The phosphonium dye TDV was kindly provided by Prof. Todor Deligeorgiev (Faculty of Chemistry, University of Sofia, Bulgaria). The N-terminal (1-83) fragment of apolipoprotein A-I with amyloidogenic mutation G26R was kindly provided by Professor Hiroyuki Saito (Kyoto Pharmaceutical University, Japan). All other reagents were of analytical grade and used without further purification.

The fibrillization of N-terminal (1-83) fragment of apolipoprotein A-I with mutations G26R, W50F and W72F was conducted at 37 °C with constant agitation on an orbital shaker after the protein dialysis from 6M guanidine hydrochloride

solution into 10mM Tris-HCl buffer, 150 mM NaCl, 0.01% NaN₃, pH 7.4. The fibril growth was monitored through measuring the intensity of Thioflavin T fluorescence at excitation and emission wavelengths of 440 and 484 nm, respectively. Hereafter, the fibrillar form N-terminal fragment of apolipoprotein A-I is referred to as ApoA-IF. The stock solutions of polyphenols, viz. quercetin, curcumin, salicylic and gallic acids, were prepared in dimethylsulfoxide (DMSO) in the concentration 620 μ M. The absorption measurements were performed in 10 mM Tris-HCl buffer (pH 7.4) with a Shimadzu UV-Visible spectrophotometer UV-2600 (Shimadzu, Japan) using the 10 mm path-length quartz cuvettes. The protein concentrations were determined spectrophotometrically using the following extinction coefficients $\epsilon_{406}^{Hb} = 1.415 \cdot 10^5 \text{ M}^{-1}\text{cm}^{-1}$, $\epsilon_{406}^{Ct} = 1.05 \cdot 10^5 \text{ M}^{-1}\text{cm}^{-1}$, $\epsilon_{280}^{BSA} = 4.25 \cdot 10^4 \text{ M}^{-1}\text{cm}^{-1}$ for hemoglobin (per heme), cytochrome c and albumin, respectively. The fluorescence measurements were carried out in 10 mM Tris-HCl buffer (pH 7.4) with a Shimadzu RF-6000 spectrofluorimeter (Shimadzu, Japan) using the 10 mm path-length quartz cuvettes. The protein fluorescence spectra were recorded from 300 to 500 nm with the excitation wavelength 280 nm, while TDV emission spectra were measured from 490 to 700 nm with the excitation wavelength 470 nm. The excitation and emission slit widths were set at 10 nm.

RESULTS AND DISCUSSION

The first series of experiments was aimed at exploring the influence of polyphenols on the protein absorbance in the absence in presence of amyloid fibrils. Shown in Fig. 1 are the differential absorption spectra of the binary (Hb + PF) and ternary (Hb + PF + ApoA-IF) mixtures of Hb with PF and ApoA-IF, calculated as ((Hb+PF)-Hb-PF, red line) and ((Hb+PF+ApoA-IF)-(Hb+ApoA-IF)-PF, black line). The effects produced by ApoA-IF in the systems Hb+QR included slight intensity decrease of the peaks ~ 340 nm and ~ 418 nm, accompanied by the hypsochromic shift of the peak around 400 nm. At the same time, in the systems containing GA and SA, the addition of ApoA-IF led to reduction in the intensity of PF-induced peaks observed at ~ 340 , 400 nm (GA) and ~ 340 , 425 nm (SA). Notably, the most pronounced effects of amyloid fibrils were observed in the system Hb+CR+ApoA-IF where the peaks at ~ 340 , 400, 420 nm undergo greater changes compared to the other polyphenols. Overall, the comparison of the differential absorption spectra indicates that the binding of all examined polyphenols to hemoglobin is followed by appearance of the peaks around 340, 400 and 420 nm. These peaks turned out to be sensitive to Hb-fibril complexation, suggesting that both PF and fibrillar ApoA-I modify the protein structural state trough affecting the intramolecular interactions of the heme group.

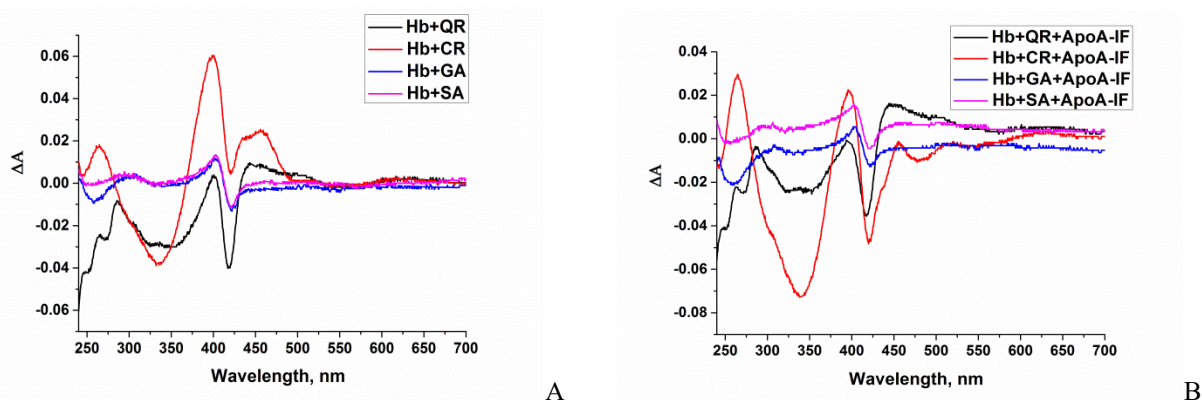


Figure 1. The differential absorption spectra of Hb in the systems Hb + PF and Hb + PF + ApoA-IF. Hb concentration was 1.4 μ M, polyphenol concentration was 27 μ M, ApoA-IF concentration was 5.3 μ M.

Shown in Fig. 2 are the differential absorption spectra of Ct calculated as ((Ct+PF)-Ct-PF, red line) and ((Ct+PF+ApoA-IF)-(Ct+ApoA-IF)-PF, black line).

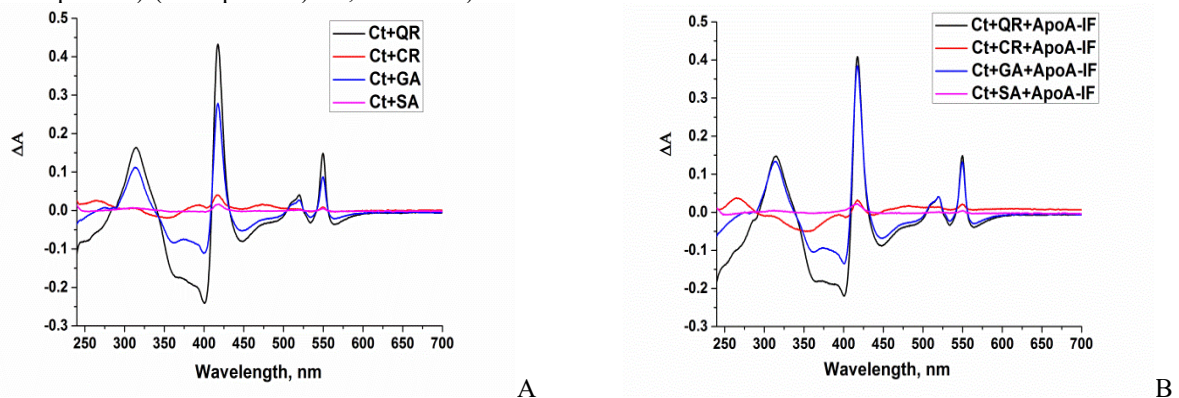


Figure 2. The differential absorption spectra of Ct in the systems Ct + PF and Ct + PF + ApoA-IF. Ct concentration was 9.8 μ M, polyphenol concentration was 27 μ M, ApoA-IF concentration was 5.3 μ M

As can be seen, Ct-QR binding is followed by the emergence of the intense peaks at 314 nm, 417 nm, 520 nm and 550 nm. The appearance of the peaks at 520 and 550 nm instead of the broad band centered at ~ 530 nm indicates that quercetin causes the transition of cytochrome c from the ferric to ferrous form. The oxidation state of heme group in Ct is known to change between + 3 (ferric form) and + 2 (ferrous form), thereby accounting for Ct ability to transfer electrons in the inner mitochondrial membrane [18]. Our findings indicate that quercetin can serve as an effective reducing agent for cytochrome c. Among the other investigated polyphenol's similar ability was revealed for GA, whereas CR and SA did not display any reducing ability (Fig. 2, A).

It appeared that in the system Ct+QR ApoA-IF does not significantly perturb the structure of cytochrome c (Fig. 2, B). In the presence of GA ApoA-I fibrils produced the decrease of the peaks at 314 nm, 417 nm, 520 nm and 550 nm, with the magnitude of this effect being greatest at 417 nm peak. The spectral changes caused by ApoA-IF in the system Ct+CR turned out to be rather pronounced, especially in the differential peaks at ~ 350 nm and ~ 400 nm. Thus, the influence of QR and GA on the structural state of cytochrome c is much stronger than that of CR and SA, whereas the effects of amyloid fibrils manifest themselves most strongly in the CR-containing systems.

The formation of BSA-PF complexes resulted in the appearance of characteristic differential peaks centered around 280 nm, 360 nm, 425 nm (QR), 350 nm, 480 nm (CR), 300 nm (GA), 310 nm (SA) (Fig. 3).

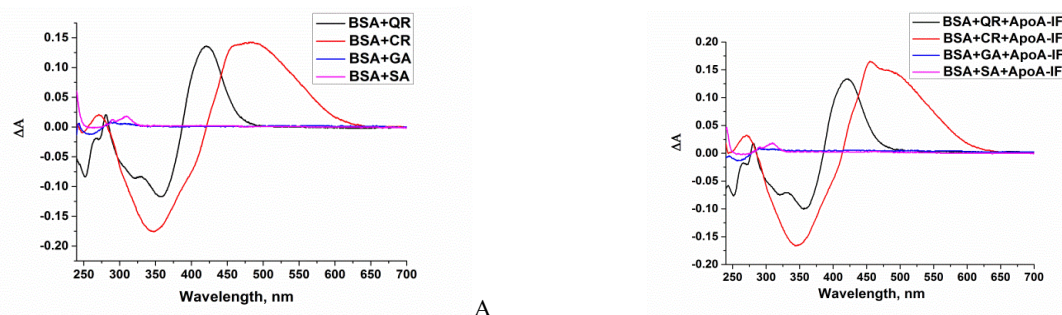


Figure 3. The differential absorption spectra of BSA in the systems BSA + PF and BSA + PF + ApoA-IF. BSA concentration was 15.4 μ M, polyphenol concentration was 27 μ M, ApoA-IF concentration was 5.3 μ M.

In contrast to Hb and Ct, the differential absorption spectra of BSA showed very weak changes on the addition of ApoA-IF. Taken together, the absorption measurements provided evidence for the ability of polyphenols to modify the structural and physicochemical properties of the examined proteins, thereby affecting their responsiveness to amyloid fibrils.

The second series of experiments was aimed at obtaining information on the interactions between functional proteins, polyphenols and amyloid fibrils using the methods of intrinsic protein fluorescence and fluorescent probes. As illustrated in Fig. 4, A, Hb fluorescence spectrum has a maximum at 333 nm. Hb is known to contain different types of intrinsic fluorophores, such as tryptophan, tyrosine and phenylalanine.

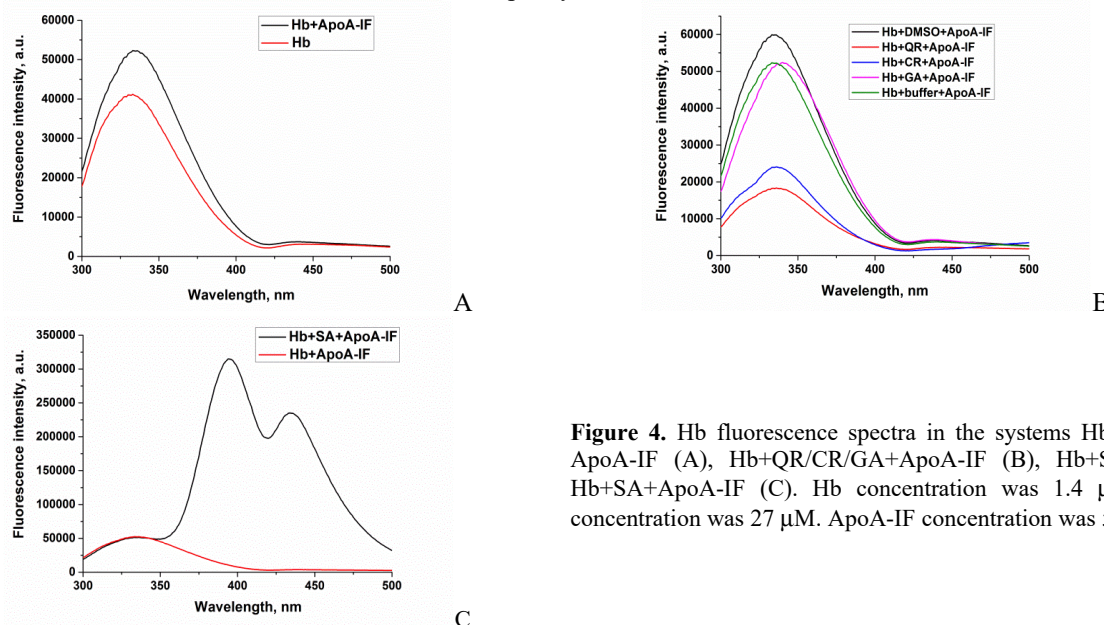


Figure 4. Hb fluorescence spectra in the systems Hb, Hb + ApoA-IF (A), Hb+QR/CR/GA+ApoA-IF (B), Hb+SA and Hb+SA+ApoA-IF (C). Hb concentration was 1.4 μ M, PF concentration was 27 μ M. ApoA-IF concentration was 5.3 μ M.

Among the six tryptophan residues, two $\alpha\beta$ dimers of Hb molecule have three Trp residues, α -Trp14, β -Trp15 and β -Trp37. Likewise, there are five tyrosine residues in each $\alpha\beta$ dimer, viz. α -Tyr24, α -Tyr42, α -Tyr140, β -Tyr34 and β -Tyr144. It was found that Hb fluorescence originates predominantly from the β -Trp37 residue residing at the $\alpha\beta$ 2 interface [19]. The addition of amyloid fibrils from ApoA-I was followed by the red shift of the emission maximum by ~ 3 nm and increase of fluorescence intensity (Fig. 4, A).

The complexation of Hb with polyphenols prior to addition of ApoA-IF resulted in the following changes in Hb fluorescence spectra: i) significant decrease of fluorescence intensity in the presence of QR and CR without any marked shift of emission maximum; ii) a red shift of emission maximum by ~ 5 nm in the presence of GA, without the changes in fluorescence intensity. At the same time, in the SA-containing system Hb emission spectrum was superimposed with the strong fluorescence signal from SA (Fig. 4).

As shown in Fig. 5, in the absence of PF ApoA-IF gives rise to fluorescence increase of a phosphonium probe TDV and blue shift of its emission maximum by ~ 3 nm.

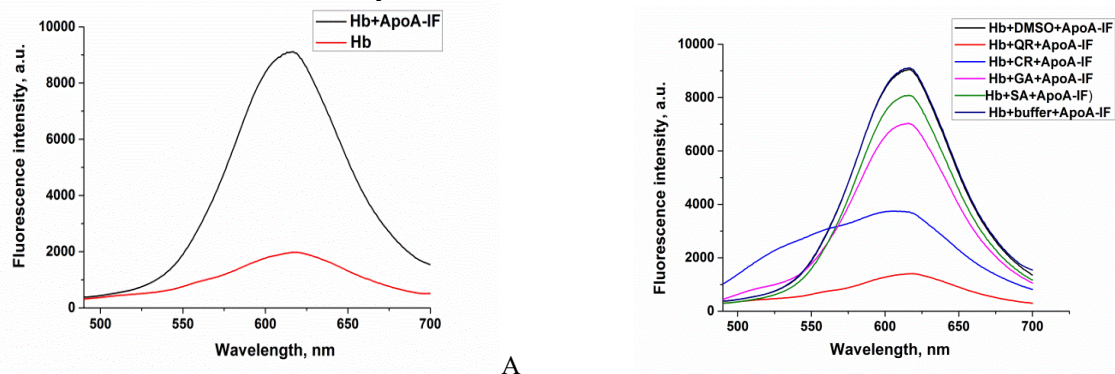


Figure 5. TDV fluorescence spectra in the systems Hb and Hb + ApoA-IF (A) and Hb + DMSO/PF + ApoA-IF (B). Hb concentration was $1.4 \mu\text{M}$, TDV concentration was $0.4 \mu\text{M}$, PF concentration was $27 \mu\text{M}$, ApoA-IF concentration was $5.3 \mu\text{M}$.

The analysis of the TDV fluorescence spectra in the systems Hb+PF+ApoA-IF revealed that: i) the maximum of TDV fluorescence (~ 616 nm) remains virtually unchanged in the presence of GA and SA, while fluorescence intensity shows a decrease by about 22% and 12%, respectively; ii) QR and CR provoke a decrease in TDV fluorescence by 84% and 59%, respectively; iii) CR produces a blue shift in emission maximum ~ 10 nm. The results obtained indicate that polyphenols are capable of modulating the effects of amyloid fibrils on the structural state of hemoglobin molecule. The observed decrease in the fluorescence of intrinsic hemoglobin fluorophore Trp37 and extrinsic fluorophore TDV can be interpreted in terms of several processes which require further investigation: i) PF-induced conformational changes of Hb accompanied by the alterations in microenvironment of Trp37; ii) competitive binding of PF and TDV to Hb; iii) non-resonance quenching of Trp or TDV fluorescence by PF; iv) resonance quenching (Forster resonance energy transfer) between Trp or TDV and PF.

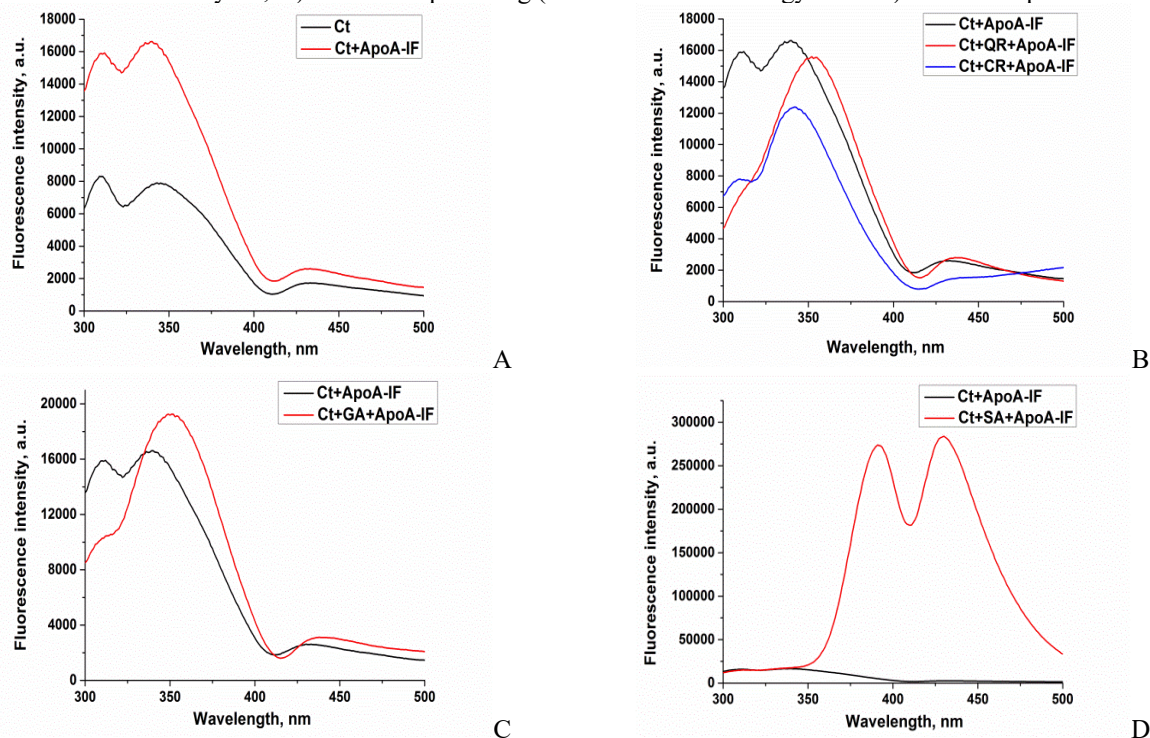


Figure 6. Ct fluorescence spectra in the systems Ct + ApoA-IF (A), Ct+PF+ApoA-IF (B-D). Ct concentration was $9.8 \mu\text{M}$, PF concentration was $27 \mu\text{M}$, ApoA-IF concentration was $5.3 \mu\text{M}$.

Shown in Fig. 6, are Ct fluorescence spectrum measured in the absence and presence of polyphenols and fibrillar ApoA-I. Cytochrome c has a single tryptophan residue at position 59 whose fluorescence is significantly quenched by the heme group of the protein. The Ct emission spectrum has a maximum at 342 nm and is distorted by the Raman scattering

peak centered around 309 nm. In the system Ct+ ApoA-IF the emission maximum shifted by ~2 nm towards shorter wavelengths, to ~340 nm, whereas the fluorescence intensity showed about 2-fold increase (Fig. 6, A).

The changes in Ct fluorescence spectra upon the formation of Ct-PF complexes involved: i) slight decrease of fluorescence intensity and a bathochromic shift of emission maximum by ~10 nm in the presence of QR (Fig. 6, B; ii) fluorescence decrease by 25% without any shift of emission maximum in the presence of CR (Fig. 6, B; iii) fluorescence increase by 16% and a red shift of emission maximum by ~10 nm upon addition of GA (Fig. 6, C). Similar to Hb, fluorescence of SA was significantly stronger than that of Ct, thereby masking the effects of this polyphenol on Ct structure (Fig. 6, D).

The spectral behavior of TDV in Ct+ApoA-IF mixture was similar to that in the mixture Hb + ApoA-IF – the addition of amyloid fibrils resulted in the fluorescence increase and blue shift of TDV emission maximum by ~6 nm. However, in the Ct-containing systems the fibril-induced rise of TDV fluorescence was about twofold smaller compared to Hb (Figs. 7, A, 5, A). In the systems Ct+PF+ApoA-IF the maximum of TDV emission (~615 nm) did not undergo any marked change for QR, GA and SA, while in the presence of CR a blue shift (~3 nm) of emission maximum was observed. The fluorescence intensity decreased by ~25% for QR, and showed only slight alterations for CR, GA and SA (Fig. 7, B, C).

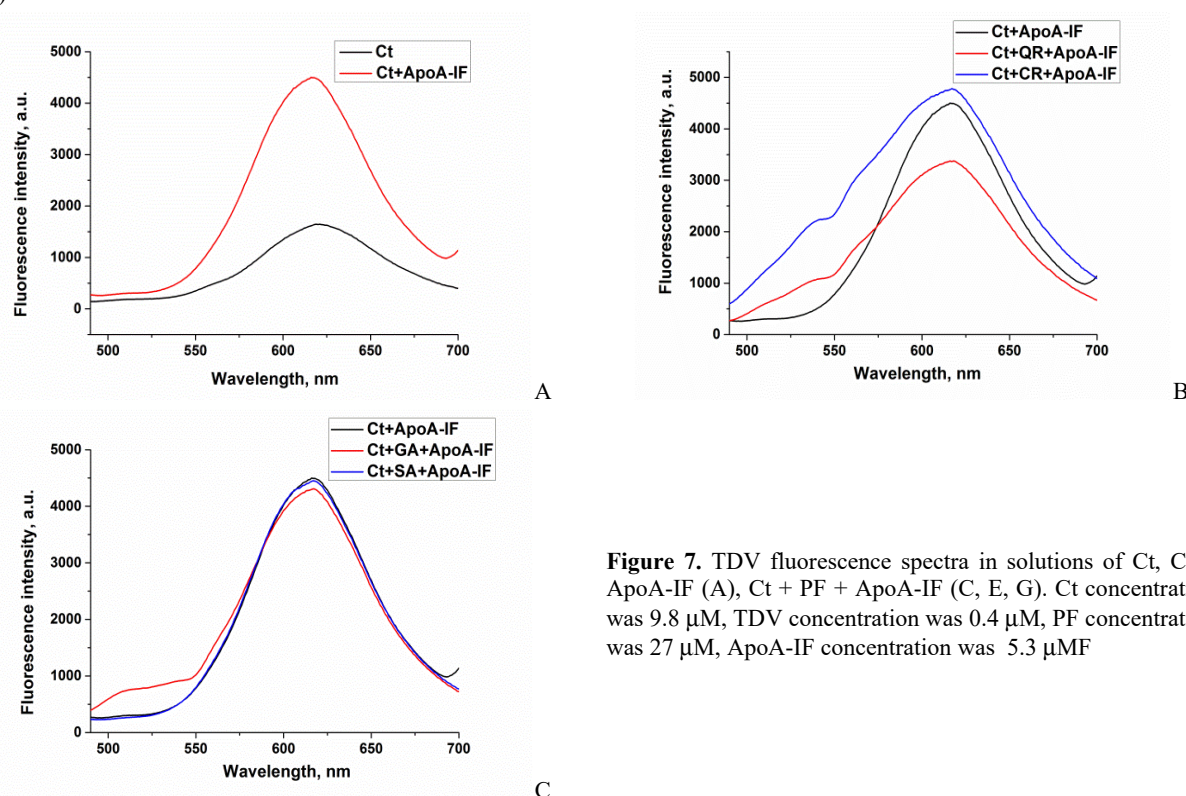


Figure 7. TDV fluorescence spectra in solutions of Ct, Ct + ApoA-IF (A), Ct + PF + ApoA-IF (C, E, G). Ct concentration was 9.8 μM , TDV concentration was 0.4 μM , PF concentration was 27 μM , ApoA-IF concentration was 5.3 μM

In a separate series of experiments, we measured the intrinsic fluorescence of BSA upon varying concentrations of polyphenols, QR/CR – from 0 to 3.9 μM , GA/SA – from 0 to 39 μM . The molecule of BSA consists of three homologous domains (I, II, III) divided into nine loops (L1-L9) by 17 disulfide bonds. The intrinsic fluorescence of BSA originates from two tryptophan residues: Trp-134 from the first domain and Trp-212 from the second domain. Of these, Trp-212 resides within a hydrophobic binding pocket, while Trp-134 is located on the surface of the molecule [20]. As shown in Fig. 8, all examined polyphenols are capable of quenching the BSA fluorescence, with the magnitude of this effect being the greatest for quercetin.

To describe the BSA-PF complexation quantitatively, the decrease in fluorescence intensity observed in the presence of polyphenols (ΔF), was assumed to be proportional to the concentration of bound dye (B) defined in terms of the Langmuir adsorption model:

$$\Delta F_i = F_0 - F_{Z_i} = aB = 0.5a \left[Z_i + nP + K_a^{-1} - \sqrt{(Z_i + nP + K_a^{-1})^2 - 4Z_i nP} \right] \quad (1)$$

where F_0 , F_{Z_i} are the protein fluorescence intensities in the absence and presence of polyphenol, respectively; a is the coefficient of proportionality between the fluorescence changes and concentration of bound polyphenol; P and Z are the concentrations of the protein and polyphenol, respectively; K_a is the association constant; n is the binding stoichiometry (in mole of PF per mole of protein).

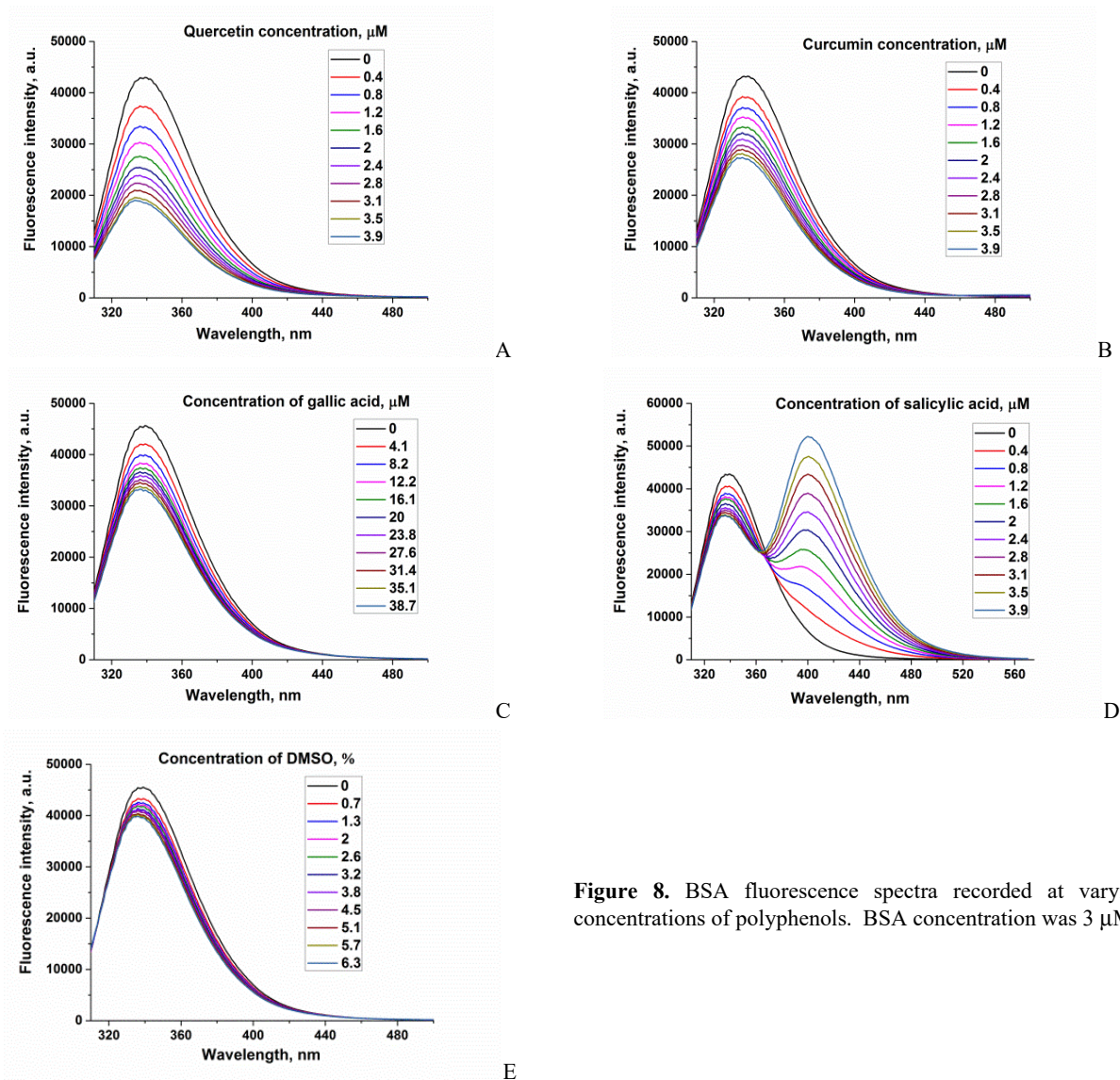


Figure 8. BSA fluorescence spectra recorded at varying concentrations of polyphenols. BSA concentration was 3 μM .

To determine the quantitative parameters of the BSA-PF complexation (K_a , n , a) the $\Delta F_i^{\text{theor}}(Z_i)$ values calculated from the Eq. (1), were fitted to the experimental ΔF values ($\Delta F_i^{\text{exp}}(Z_i)$) through minimization of the function:

$$f = \frac{1}{N} \sum_{i=1}^N (\Delta F_i^{\text{theor}} - \Delta F_i^{\text{exp}}) \quad (2)$$

where N is the number of the experimental points ($N = 10$).

Table 1. Quantitative parameters of polyphenol binding to BSA

Polyphenol	K_a , M^{-1}	n	a , M^{-1}
Quercetin	$3.3 \times 10^6 \pm 4.3 \times 10^5$	1.02 ± 0.2	$1.1 \times 10^{10} \pm 1.7 \times 10^9$
Curcumin	$3.2 \times 10^6 \pm 4.1 \times 10^5$	1.01 ± 0.3	$7.7 \times 10^9 \pm 8.2 \times 10^8$
Gallic acid	$1.7 \times 10^5 \pm 3.3 \times 10^4$	1.7 ± 0.3	$2.7 \times 10^9 \pm 3.7 \times 10^8$
Salicylic acid	$2.7 \times 10^6 \pm 3.6 \times 10^5$	0.78 ± 0.4	$5.6 \times 10^9 \pm 4.6 \times 10^8$

As seen in Table 1, quercetin, curcumin and salicylic acid have comparable high affinities for BSA, while the affinity of gallic acid was found to be ~ 20 -fold lower. In contrast to Hb and Ct, fibrillar ApoA-I did not cause any marked changes of BSA fluorescence in the control sample (when DMSO was added instead of PF, (Fig. 9, E)), while in the presence of polyphenols amyloid fibrils induced the increase of BSA fluorescence (Fig. 9, A-D). One possible explanation for this effect is the competition between ApoA-IF and PF for the protein binding sites and lowering the extent of the BSA fluorescence quenching by polyphenols.

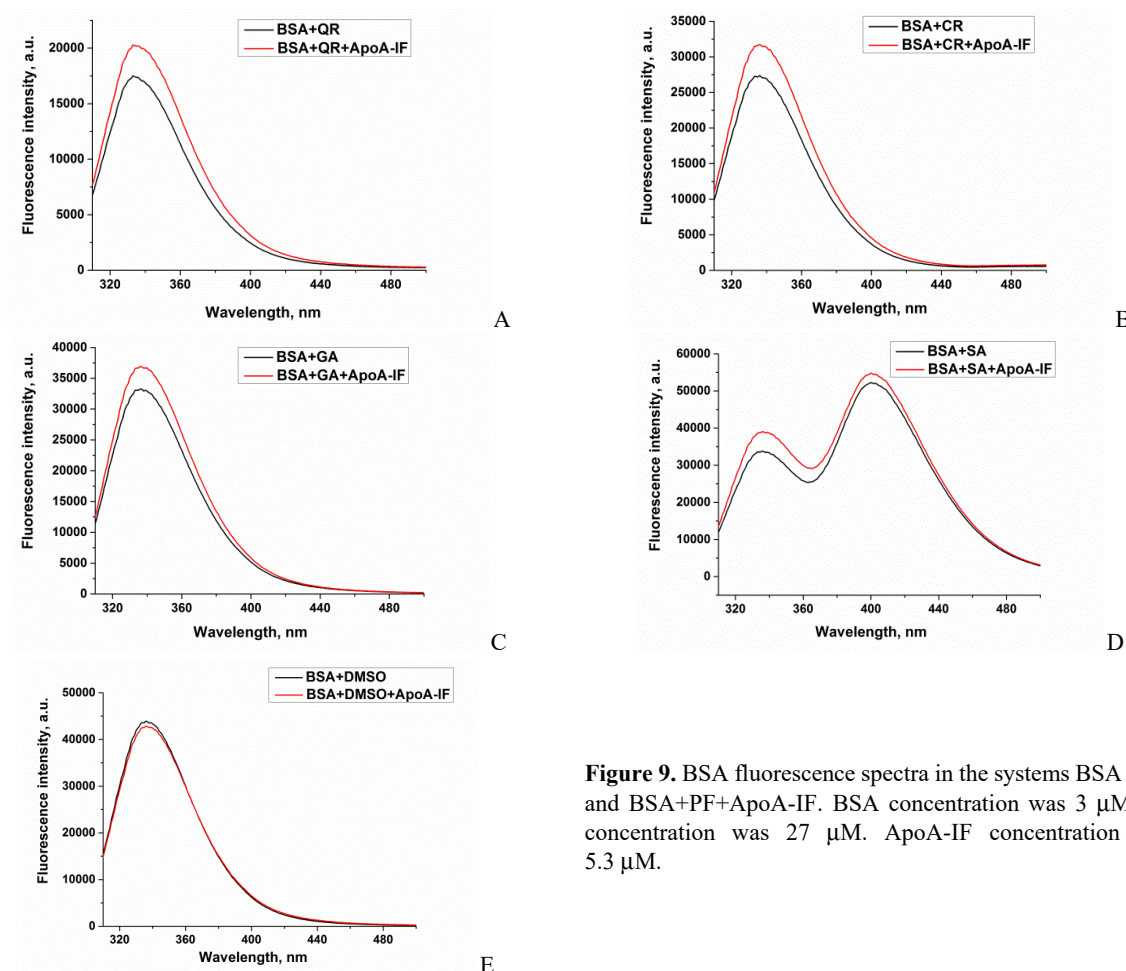


Figure 9. BSA fluorescence spectra in the systems BSA + PF and BSA+PF+ApoA-IF. BSA concentration was 3 μ M, PF concentration was 27 μ M. ApoA-IF concentration was 5.3 μ M.

The measurements of TDV fluorescence in the BSA-containing systems revealed the effects differing from those observed for Hb and Ct. As shown in Fig. 10, A, B, amyloid fibrils brought about significant red shift of the TDV emission maximum (from 592 nm to 604 nm) without marked changes of fluorescence intensity.

Quercetin induced further shift of TDV emission maximum towards 606 nm and slight decrease of fluorescence intensity, while in the presence of curcumin emission maximum of TDV was close to that in BSA solution (593 nm), but fluorescence intensity showed about 5-fold increase (Fig. 10, B). In the systems with gallic and salicylic acids the longest wavelength emission maximum of TDV (~609 nm) and insignificant decrease of fluorescence intensity were observed.

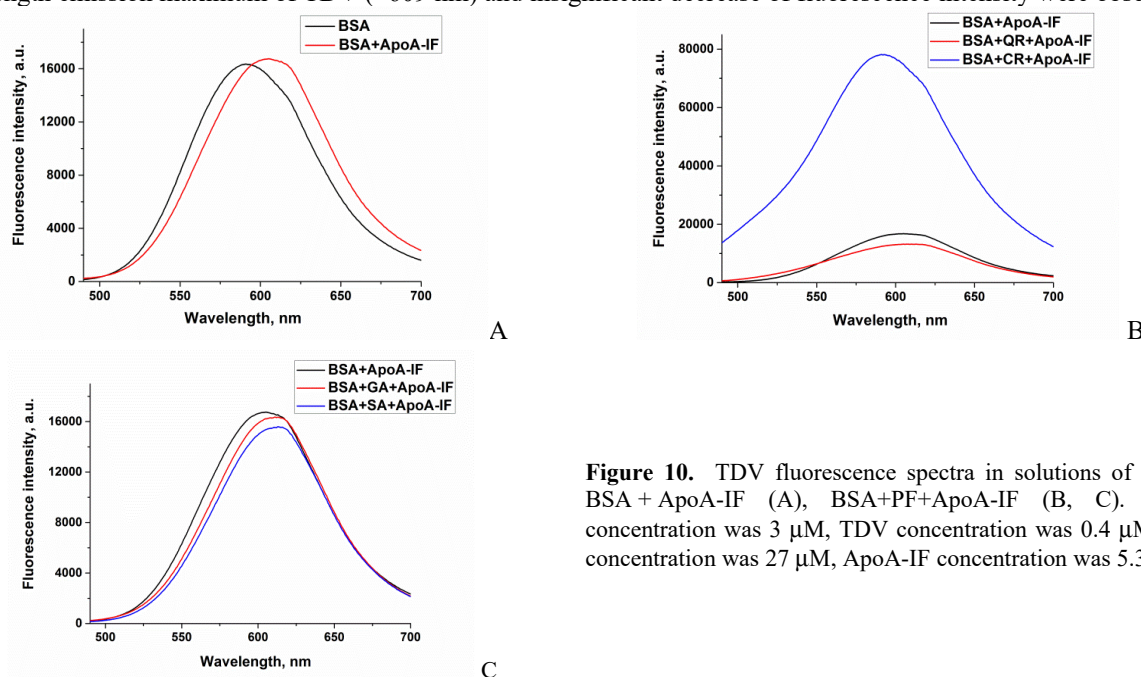


Figure 10. TDV fluorescence spectra in solutions of BSA, BSA + ApoA-IF (A), BSA+PF+ApoA-IF (B, C). BSA concentration was 3 μ M, TDV concentration was 0.4 μ M, PF concentration was 27 μ M, ApoA-IF concentration was 5.3 μ M

CONCLUSIONS

In summary, the present study provided new information on the interactions of quercetin, curcumin, gallic and salicylic acids with functionally important proteins such as hemoglobin, cytochrome c and serum albumin, and modulating effects of polyphenols on the binding of amyloid fibrils from N-terminal fragment of apolipoprotein A-I to the proteins. Using several spectroscopic techniques including the differential absorption spectroscopy, intrinsic protein fluorescence and fluorescent probes, the spectral markers of polyphenol modulating abilities have been identified. The analysis of the differential absorption spectra revealed that: i) in the systems Hb+PF+ApoA-IF the peaks around 340, 400 and 420 nm are sensitive to Hb-fibril complexation; ii) quercetin gives rise to the transition of cytochrome c from the ferric to ferrous form as judged from the appearance of the peaks at 520 and 550 nm; iii) the effects of amyloid fibrils are the strongest in the system Ct+CR+ApoA-IF; iv) the formation of BSA-PF complexes resulted in the appearance of characteristic differential peaks depending on PF structure, while amyloid fibrils ApoA-IF did not affect the BSA absorbance. The measurements of the intrinsic protein fluorescence showed that: i) amyloid fibrils bring about the fluorescence increase of Hb and Ct, accompanied by the bathochromic (Hb) or hypsochromic (Ct) shifts of emission maximum; ii) QR and CR produce significant decrease of Hb fluorescence intensity, while the main effect of GA involves a bathochromic shift of Hb emission maximum; iii) the most pronounced changes in Ct fluorescence spectra (bathochromic shift of emission maximum by ~10 nm) were induced by QR and GA; iv) the quantitative interpretation of the data on BSA fluorescence quenching by PF gives the following order for the affinities of polyphenols for BSA: QR ≥ CR > SA >> GA. The spectral alterations of a phosphonium fluorescent probe TDV involved; i) fluorescence increase and hypsochromic shift of emission maximum on the binding of ApoA-IF to Hb and Ct; ii) significant decrease in TDV fluorescence in the systems containing Hb and QR/CR; iii) a hypsochromic shift in TDV emission maximum (10 nm for Hb + CR and 3 nm for Ct + CR); iv) considerable (12 nm) bathochromic shift of TDV emission maximum upon BSA complexation of BSA with ApoA-IF, that was enhanced in the presence of QR, GA and SA. Overall, the above findings show that the spectral parameters such as the position and intensity of the bands in differential absorption spectra, the intensity and emission maxima of the intrinsic (Trp) and extrinsic (TDV) fluorophores can serve as sensitive indicators of the protein structural changes produced by amyloid fibrils and polyphenols.

Acknowledgements

This project has received funding through the EURIZON project, which is funded by the European Union under grant agreement No. 871072.

ORCID

● Uliana Malovytsia, <https://orcid.org/0000-0002-7677-0779>; ● Valeriya Trusova, <https://orcid.org/0000-0002-7087-071X>
● Mette Hedegaard Thomsen, <https://orcid.org/0000-0001-6805-7247>; ● Galyna Gorbenko, <https://orcid.org/0000-0002-0954-5053>

REFERENCES

- [1] G.J. Cooper, A.C. Willis, A. Clark, R.C. Turner, R.B. Sim, K.B. Reid, *Proc. Natl. Acad. Sci. USA* **84**, 8628 (1987). <https://www.ncbi.nlm.nih.gov/pubmed/3317417>
- [2] A.P. Ano Bom, L.P. Rangel, D.C. Costa, G.A. de Oliveira, D. Sanches, C.A. Braga, L.M. Gava, *et al.*, *J. Biol. Chem.* **287**, 28152 (2012). <http://dx.doi.org/10.1074/jbc.M112.340638>
- [3] M. G. Spillantini, M. L. Schmidt, V. M.-Y. Lee, J. Q. Trojanowski, R. Jakes, M. Goedert, *Nature* **388**, 839-840 (1997). <https://doi.org/10.1038/42166>
- [4] F. J. Bauerlein, I. Saha, A. Mishra, M. Kalemánov, A. Martínez-Sánchez, R. Klein, I. Dudanova, M. S. Hipp, F. U. Hartl, W. Baumeister, R. Fernández-Busnadiego, *Cell* **171**, 179 (2017). <https://doi.org/10.1016/j.cell.2017.08.009>
- [5] H. Olzscha, S. M. Schermann, A. C. Woerner, S. Pinkert, M. H. Hecht, G. G. Tartaglia, M. Vendruscolo, M. Hayer-Hartl, F. U. Hartl, R. Martin Vabulas, *Cell* **144**, 67 (2011). <https://doi.org/10.1016/j.cell.2010.11.050>
- [6] S. C. Goodchild, T. Sheynis, R. Thompson, K. W. Tipping, W. F. Xue, N. A. Ranson, P. A. Beales, E. W. Hewitt, S. E. Radford, *PLOS One* **9**, e104492 (2014). <https://doi.org/10.1371/journal.pone.0104492>
- [7] M. P. Jackson, E. W. Hewitt, *Essays Biochem.* **60**, 173 (2016). <https://doi.org/10.1042/EBC20160005>
- [8] K. F. Winklhofer, C. Haass, *Biochim. Biophys. Acta* **1802**, 29 (2010). <https://doi.org/10.1016/j.bbadis.2009.08.013>
- [9] B. Uttara, A.V. Singh, P. Zamboni, R.T. Mahajan, *Curr. Neuropharmacol.* **7**, 65 (2009). <https://doi.org/10.2174/157015909787602823>
- [10] H. Xie, C. Guo, *Front. Mol. Biosci.* **7**, 629520 (2021). <https://doi.org/10.3389/fmolb.2020.629520>
- [11] S. Morikawa, N. Kaneko, C. Okumura, H. Taguchi, M. Kurata, T. Yamamoto, H. Osawa, A. Nakanishi, T. Zako, J. Masumoto, *Int. J. Immunopathol. Pharmacol.* **32**, 2058738 (2018). <https://doi.org/10.1177/2058738418788749>
- [12] A. Nakanishi, N. Kaneko, H. Takeda, T. Sawasaki, S. Morikawa, W. Zhou, M. Kurata, T. Yamamoto, S. M. F. Akbar, T. Zako, J. Masumoto, *Inflamm. Regen.* **38**, 27 (2018). <https://doi.org/10.1186/s41232-018-0085-6>
- [13] W. Mori, N. Kaneko, A. Nakanishi, T. Zako, and J. Masumoto, *Int. J. Immunopathol. Pharmacol.* **35**, 1–7 (2021). <https://doi.org/10.1177/20587384211038357>
- [14] N. Wu, T. Liu, M. Tian, C. Liu, S. Ma, H. Cao, and J. Qi, *Mol. Med. Rep.* **29**, 24 (2024). <https://doi.org/10.3892/mmr.2023.13147>
- [15] M.H. Ahmed, M. S. Ghatge, M. K. Safo, *Subcellular Biochemistry*, **94**, (2020). https://doi.org/10.1007/978-3-030-41769-7_14
- [16] Y.L. Ow, D. Green, Z. Hao, and T.W. Mak, *Nat. Rev. Mol. Cell. Biol.* **9**, 532 (2008). <https://doi.org/10.1038/nrm2434>
- [17] A. Rana, M. Samtiya, T. Dhewa, V. Mishra, and R.E. Aluko, *J. Food Biochem.* **46**, e14264 (2022). <https://doi.org/10.1111/jfbc.14264>
- [18] G. Zazeri, A.P.R. Povinelli, N. M. Pavan, D.R. de Carvalho, C.L. Cardoso, V.F. Ximenes, *J. Mol. Struct.* **1244**, 130995 (2021). <https://doi.org/10.1016/j.molstruc.2021.130995>
- [19] S. Chaudhuri, S. Chakraborty, P. K. Sengupta, *Biophys. Chem.* **154**, 26 (2011). <https://doi.org/10.1016/j.bpc.2010.12.003>

[20] A. Papadopoulou, R.J. Green, R.A. Frazier, J. Agric. Food Chem. **53**, 158 (2005). <https://doi.org/10.1021/jf048693g>

МОДУЛЮЮЧИЙ ВПЛИВ ПОЛІФЕНОЛІВ НА ВЗАЄМОДІЇ МІЖ ФУНКЦІОНАЛЬНИМИ БІЛКАМИ ТА АМІЛОЇДНИМИ ФІБРИЛАМИ

У. Маловиця^а, В. Трусова^а, М.Х. Томсен^б, Г. Горбенко^а

*^аКафедра медичної фізики та біомедичних нанотехнологій, Харківський національний університет імені В.Н. Каразіна
м. Свободи 4, Харків, 61022, Україна*

^бУніверситет Аалборг, вул. Нільса Бора 8, 6700 Есб'єрг, Данія

В даній роботі з використанням методів диференційної абсорбційної спектроскопії, власної флуоресценції білків та флуоресцентних зондів були досліджені подвійні та потрійні системи, що містили функціональні білки, поліфеноли та амілоїдні фібрили. Група поліфенолів включала представників чотирьох різних класів: флавоноїд кверцетин (QR), фенольну кислоту (саліцилова кислота (SA)), куркуміноїд куркумін (CR) і таннін галова кислота (GA). Функціонально важливі білки були представлені гемоглобіном (Hb), цитохромом с (Ct) та сироватковим альбуміном (BSA). Амілоїдні фібрили були отримані із N-термінального (1-83) фрагменту аполіпопротеїну A-I з амілоїдогенною мутацією G26R (ApoA-IF). Було продемонстровано, що спектральні маркери, такі як положення та інтенсивність смуг в диференційних спектрах поглинання, інтенсивність флуоресценції та максимуми емісії внутрішніх (Trp) та зовнішніх (TDV) флуорофорів можуть слугувати чутливими індикаторами структурних модифікацій білків під впливом амілоїдних фібрил та поліфенолів. Спостережувані зміни флуоресценції Trp та TDV були інтерпретовані в рамках наступних процесів: i) PF-індукованих конформаційних змін білкових молекул, що супроводжуються змінами мікрооточення залишків Trp; ii) конкуренцією між PF та TDV за білкові сайти зв'язування; iii) нерезонансне гасіння флуоресценції Trp та TDV поліфенолами; iv) резонансне гасіння (Фьорстерівський резонансний перенос енергії) між Trp чи TDV та PF. В цілому, отримані результати дозволяють припустити, що поліфенольні сполуки здатні модулювати взаємодії між функціональними білками та амілоїдними фібрилами, та можуть розглядатись як перспективні агенти для зниження токсичності амілоїдів.

Ключові слова: *амілоїдні фібрили; функціональні білки; поліфеноли; диференційна абсорбційна спектроскопія; флуоресценція*

COMPUTATIONAL STUDY OF DRUG DELIVERY SYSTEMS WITH RADIONUCLIDE AND FLUORESCENCE IMAGING MODALITIES. II. DOXORUBICIN DELIVERY SYSTEMS BASED ON ALBUMIN AND TRANSFERRIN

 V. Trusova^{a*},  U. Malovytsia^a,  P. Kuznietsov^b, I. Karnaukhov^c,  A. Zelinsky^c,  B. Borts^c,
I. Ushakov^c, L. Sidenko^c,  G. Gorbenko^a

^aDepartment of Medical Physics and Biomedical Nanotechnologies, V.N. Karazin Kharkiv National University
4 Svobody Sq., Kharkiv, 61022, Ukraine

^bO.I. Akhiezer Department for Nuclear Physics and High Energy Physics, V.N. Karazin Kharkiv National University
4 Svobody Sq., Kharkiv, 61022, Ukraine

^cNational Science Center "Kharkov Institute of Physics and Technology", Kharkiv, Ukraine

*Corresponding Author e-mail: valerija.trusova@karazin.ua

Received December 12, 2025, revised January 20, 2025; accepted February 15, 2025

This study explores the development of advanced protein-based drug delivery systems for doxorubicin (DOX), an anticancer agent, incorporating both radionuclide (technetium-99m complexes) and fluorescence (Methylene Blue (MB), Indocyanine Green (IG), cyanine AK7-5 and squaraine SQ1) imaging modalities. Building upon previous research on albumin-based carriers, this work expands the scope by introducing transferrin (TRF) as a complementary protein component to create a more sophisticated and targeted delivery platform. Molecular docking technique was employed to design and characterize the multimodal delivery systems that incorporate radiopharmaceuticals and near-infrared fluorescent dyes. The results demonstrate that technetium-99m-based radiopharmaceuticals are capable of strong noncovalent binding to human serum albumin (HSA) and its complexes with transferrin. A comprehensive analysis of docking scores and interacting amino acid residues reveals that HSA-TRF-TcHyn/TcMEB/TcDIS-DOX-IG/SQ1 systems show the highest potential for experimental testing and further development. These findings support the potential of HSA-TRF complexes as nanocarriers with dual imaging capabilities for DOX delivery, offering an approach to enhance therapeutic efficacy while reducing systemic toxicity in anticancer treatment.

Keywords: Drug delivery nanosystems; Human serum albumin; Transferrin; Doxorubicin; Technetium complexes; Fluorescent dyes; Molecular docking

PACS: 87.14.C++c, 87.16.Dg

Protein-based drug delivery systems have emerged as a promising strategy for enhancing the therapeutic efficacy of anticancer agents while mitigating their systemic toxicity [1,2]. These systems offer exceptional biocompatibility, biodegradability, and the ability to accumulate in tumor tissues via the enhanced permeability and retention effect (EPR). Proteins, as drug delivery cargos, provide unique advantages such as natural abundance, renewable sources, and the presence of multiple functional groups for drug loading and targeting modifications [3,4]. In our previous paper we explored albumin-based drug delivery systems for doxorubicin (DOX) [5]. Accordingly, the study employed computational tools to design multimodal delivery systems incorporating radiopharmaceuticals and near-infrared fluorescent dyes, and the results obtained provided strong support for the ability of human serum albumin (HSA) as DOX delivery systems. Currently, the ongoing research in this field is focused on developing more sophisticated and efficient protein-based nanocarriers [6]. Motivated by these rationales, in the present paper we extend the scope of our research by introducing transferrin (TRF) as a complementary protein component to create a more sophisticated and targeted delivery platform. The combination of HSA and transferrin in a single delivery system aims to leverage the advantages of both proteins. While albumin provides excellent biocompatibility and drug-binding capabilities [7], transferrin adds an active targeting mechanism to cancer cells overexpressing transferrin receptors [8]. This dual-protein approach may result in improved drug accumulation in tumor tissues, not only through the EPR effect but also via receptor-mediated endocytosis.

METHODS

Human serum albumin (HSA) in its dimeric form (PDB ID: 1A06) was used as a main component of the designed PDDS. A therapeutic component of the examined drug delivery systems was represented by one of the most widespread antitumor drug doxorubicin (DOX), anthracycline antibiotic whose antineoplastic properties arise mainly from its abilities to intercalate into DNA, inhibit topoisomerase II, disrupt gene expression, generate reactive oxygen species and produce damage of cell membranes [9]. To design the PDDS, in the present study we used 12 ^{99m}Tc-based radiopharmaceuticals [5]: [^{99m}Tc]Tc-Sestamibi (TcSES), [^{99m}Tc]Tc-Tetrofosmin (TcTET), [^{99m}Tc]Tc-Medronate (TcMED), [^{99m}Tc]Tc-

Cite as: V. Trusova, U. Malovytsia, P. Kuznietsov, I. Karnaukhov, A. Zelinsky, B. Borts, I. Ushakov, L. Sidenko, G. Gorbenko, East Eur. J. Phys. 1, 376 (2025), <https://doi.org/10.26565/2312-4334-2025-1-46>

© V. Trusova, U. Malovytsia, P. Kuznietsov, I. Karnaukhov, A. Zelinsky, B. Borts, I. Ushakov, L. Sidenko, G. Gorbenko, 2025; CC BY 4.0 license

dimercaptosuccinic acid (TcDMSA), [^{99m}Tc]Tc-diethylenetriaminepentaacetate (Tc-DTPA), [^{99m}Tc]Tc-mercaptoacetyltriglycine (TcMAG), Pertechnetate [^{99m}Tc]TcO $_4^-$ (TcPER), [^{99m}Tc]Tc-Exametazime (TcEXA), [^{99m}Tc]Tc-diisopropyl iminodiacetic acid (TcDIS), [^{99m}Tc]Tc-ethylene cysteine dimer (TcECD), [^{99m}Tc]Tc- hydrazinonicotinic acid-H6F (TcHYN), [^{99m}Tc]Tc-Mebrofenin (TcMEB). To create the dual-labelled PDDS with both nuclear and optical imaging modalities, the examined protein systems were loaded by the binary combinations of the above ^{99m}Tc complexes and four NIR fluorescent dyes (FD), Methylene Blue (MB), Indocyanine Green (IG), cyanine AK7-5 and squaraine SQ1 [5]. To identify the most energetically favorable binding sites for TCC, DOX, FD in the HSA-TRF protein systems the molecular docking studies were performed using the HDock server. Prior to the docking procedure, the structures of HSA dimers and its complexes with TRF were relaxed through 1 ns MD simulations. The structures of ligands were built in MarvinSketch (version 18.10.0) and the geometries were further optimized in Avogadro (version 1.1.0). The selected docking poses were visualized with the UCSF Chimera software (version 1.14) and analyzed with Protein-Ligand Interaction Profiler [10].

RESULTS AND DISCUSSION

In our previous paper we conducted sophisticated molecular docking studies to design the albumin-based drug delivery systems for DOX with dual imaging modalities, including the complexes of the radionuclide technetium-99m (TCC) and near-infrared (NIR) fluorescent dyes [5]. In brief, our computational analysis revealed that among the compounds studied, the technetium complexes TcDIS, TcHYN, and TcMEB exhibited the strongest binding affinities to the protein. Furthermore, molecular docking analysis indicated that the majority of TCCs preferentially bound to domain I of HSA, with some exceptions showing affinity for both domains I and III or exclusively for domain III.

In the present paper we aimed at answering the question of whether HSA association with other functional proteins, such as transferrin (TRF), can affect the TCC binding properties. Fig. 1 represents the best score complexes of TCC with HSA-TRF complexes.

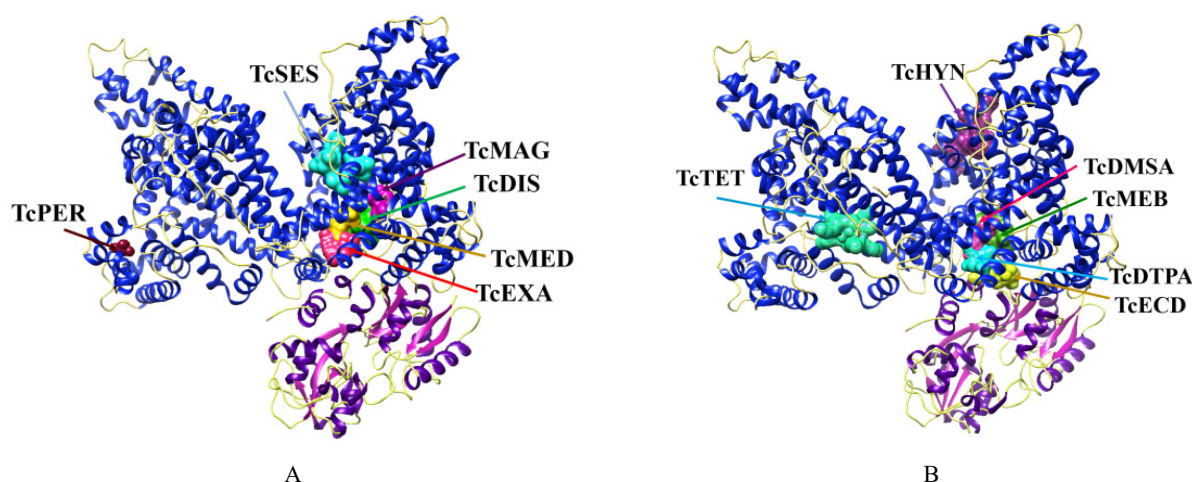


Figure 1. The most energetically favorable complexes of TCC with HSA-TRF complexes

In the hybrid protein systems, the best docking score (BDS) values were found to decrease in the row HSA + TRF - TcHYN > TcDIS > TcDTPA > TcMEB > TcDMSA > TcSES > TcTET ~ TcECD ~ TcMAG ~ TcMED ~ TcEXA > TcPER (Fig. 2). in all these systems the highest affinity was observed for TcHYN.

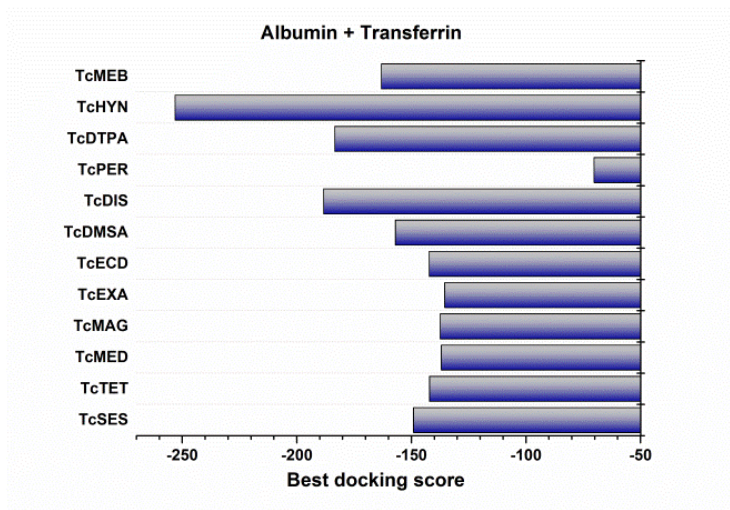


Figure 2. The best docking score values obtained for the TCC complexes with HSA and its associates with TRF

Notably, the BDS value for the neat HSA-TRF complexes (without TCC) was estimated to be -200.2, with the number of interface residues being equal to 62 (Table 1).

Table 1. The interface amino acid residues and the types of interactions involved in the binding of technetium-99m complexes (TCC) to the albumin-transferrin (TRF) associates

TCC	HSA-TRF-TCC interface residues		Type of interactions
	HSA	TRF	
TcSES	TYR _{150A} *, GLU _{153A} , PHE _{156A} , PHE _{157A} , ARG _{160A} , GLU _{188A} , ALA _{191A} , SER _{192A} , LYS _{195A} , GLN _{196A} , LYS _{199A} , ARG _{218A} , ARG _{222A} , HSD _{288A} , GLU _{292A} , VAL _{293A} , LYS _{436A} , HSD _{440A} , TYR _{452A}		Hydrophobic interactions, hydrogen bonds
TcTET	LEU _{115B} , ARG _{114B} , ARG _{145B} , LYS _{190B} , SER _{419B} , ARG _{428B} , ILE _{523B} , GLU _{540B}		Hydrophobic interactions, hydrogen bonds
TcMED	LEU _{115A} , ARG _{117A} , TYR _{138A} , ILE _{142A} , HSD _{146A} , PHE _{149A} , LEU _{154A} , PHE _{157A} , TYR _{161A} , LEU _{182A} , ASP _{183A} , LEU _{185A} , ARG _{186A} , ASP _{187A} , GLY _{189A} , LYS _{190A}		Hydrogen bonds
TcMAG	ASP _{107A} , ASP _{108A} , ASN _{109A} , ARG _{145A} , HSD _{146A} , PRO _{147A} , TYR _{148A} , GLY _{189A} , LYS _{190A} , ALA _{191A} , SER _{193A} , ALA _{194A} , ARG _{197A} , GLU _{425A} , ASN _{458A} , GLN _{459A}		Hydrogen bonds, salt bridges
TcEXA	LEU _{115A} , VAL _{116A} , ARG _{117A} , PRO _{118A} , MET _{123A} , PHE _{134A} , LYS _{137A} , TYR _{138A} , LEU _{139A} , GLU _{141A} , ILE _{142A} , ARG _{145A} , TYR _{161A} , PHE _{165A} , LEU _{182A} , ARG _{186A}		Hydrophobic interactions, hydrogen bonds
TcECD	GLN _{33A} , LEU _{112A} , PRO _{113A} , ARG _{114A} , LEU _{115A} , VAL _{116A} , ARG _{117A} , PRO _{118A} , TYR _{140A} , GLU _{141A} , ARG _{144A} , ARG _{145A}	TYR ₇₁ , LEU ₇₂ , ALA ₇₃ , ASN ₇₆ , LEU ₇₇ , LYS ₇₈ , PRO ₇₉ , SER ₂₅₅ , MET ₃₀₉ , ASP ₃₁₀	Hydrophobic interactions, hydrogen bonds, salt bridges
TcDMSA	LEU _{115A} , VAL _{116A} , ARG _{117A} , PRO _{118A} , MET _{123A} , TYR _{138A} , ILE _{142A} , HSD _{146A} , PHE _{149A} , LEU _{154A} , PHE _{157A} , TYR _{161A} , LEU _{182A} , LEU _{185A} , ARG _{186A} , ASP _{187A} , GLU _{188A} , GLY _{189A} , LYS _{190A}		Hydrogen bonds, salt bridges
TcDIS	ASN _{109A} , ARG _{145A} , HSD _{146A} , ARG _{186A} , LYS _{190A} , PRO _{421A} , GLU _{425A} , GLU _{520A}	ARG ₃₀₈	Hydrophobic interactions, hydrogen bonds, salt bridges
TcPER	TYR _{30B} , HSD _{67B} , THR _{68B} , PHE _{70B} , GLY _{71B} , LEU _{74B} , GLU _{95B} , ARG _{98B} , ASN _{99B} , PHE _{102B}		Hydrogen bonds
TcDTPA	LEU _{115A} , VAL _{116A} , ARG _{117A} , PRO _{118A} , MET _{123A} , PHE _{134A} , LEU _{135A} , LYS _{137A} , TYR _{138A} , GLU _{141A} , ILE _{142A} , TYR _{161A} , LEU _{182A} , ARG _{186A}		Hydrogen bonds, salt bridges
TcHYN	GLU _{383A} , LEU _{387A} , ASN _{391A} , LEU _{394A} , ALA _{406A} , LEU _{407A} , VAL _{409A} , ARG _{410A} , TYR _{411A} , LEU _{430A} , LEU _{453A} , SER _{489A} , GLU _{492A} , GLU _{542A} , LYS _{545A}		Hydrogen bonds, π -stacking, salt bridges
TcMEB	ASP _{108A} , ASN _{109A} , PRO _{110A} , ASN _{111A} , LEU _{112A} , PRO _{113A} , ARG _{114A} , LEU _{115A} , ARG _{145A} , HSD _{146A} , ARG _{186A} , LYS _{190A} , PRO _{421A} , THR _{422A} , VAL _{424A} , GLU _{425A} , ILE _{523A} , LYS _{524A} , THR _{527A}	ARG ₃₀₈	Hydrophobic interactions, hydrogen bonds, salt bridges

The modification of the ligand binding landscape upon HSA complexation with TRF resulted in the changes of the binding affinity for some TCC. As illustrated in Fig. 3, the most pronounced affinity increase was observed for TcDIS and less pronounced – for TcMED.

In the HSA-TRF systems the binding sites most TCC reside solely on the albumin molecule, only TcECD, TcMEB and TcDIS interact with both proteins, HSA and TRF (Fig. 1, Table 1). Interestingly, despite TcDIS makes contacts with

only one TRF residue, ARG308, this seems to play a role in the increase of TcDIS affinity in the presence of transferrin compared to HSA alone.

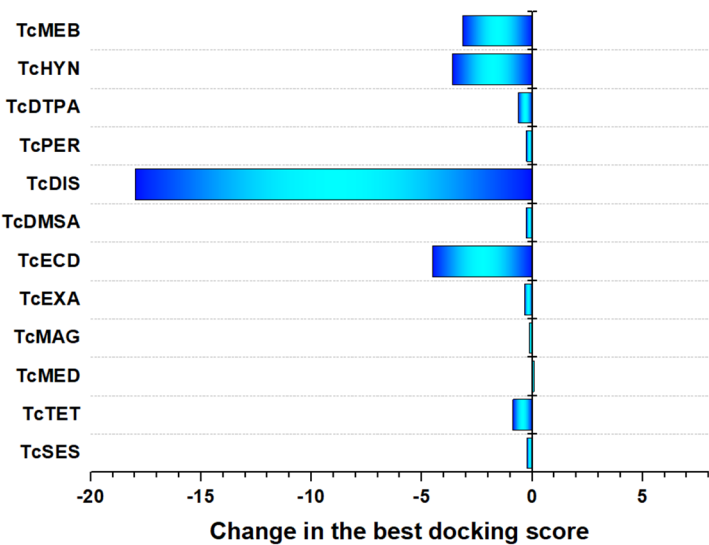


Figure 3. The changes in the best docking score values calculated for HSA-TRF-TCC systems relative to HSA alone

Next, we employed the multiple ligands docking approach to explore the ternary protein-ligand systems (HSA-TRF-TCC-DOX). The ternary systems were obtained by the docking of doxorubicin to the best score complexes of TCC with HSA-TRF (Fig. 4).

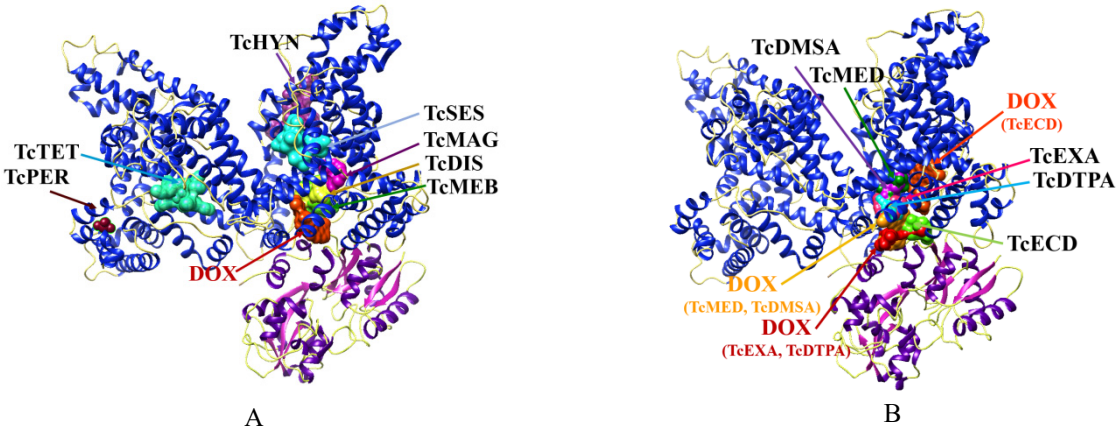


Figure 4. The most energetically favorable complexes of TCC with HSA-TRF complexes

The following features of the ternary systems are worthy of mention: i) in most HSA-TRF-TCC-DOX systems (except TcECD), the DOX protein affinities are higher than those for the HSA-TCC-DOX systems, ii) all DOX binding sites constitute the residues from both HSA (most residues from the site HSA₁₁₃₋₁₈₆) and TRF (predominantly TYR₇₁, LEU₇₂, ALA₇₃ and ASN₇₆) (Table 2).

Table 2. The interface amino acid residues and the types of interactions involved in the binding of DOX to HSA-TRF-TCC complexes

Complex	HSA-TRF-TCC-DOX- interface residues		Type of interactions
	HSA	TRF	
HSA-TRF-DOX	LEU _{112A} *, PRO _{113A} , ARG _{114A} , LEU _{115A} , VAL _{116A} , ARG _{117A} , PRO _{118A} , MET _{123A} , PHE _{134A} , LYS _{137A} , TYR _{138A} , GLU _{141A} , ARG _{145A} , TYR _{161A} , LEU _{182A} , ARG _{186A}	TYR ₇₁ , LEU ₇₂ , ALA ₇₃ , ASN ₇₆	Hydrophobic interactions, hydrogen bonds, π -stacking, π -cation interactions, salt bridges
HSA-TRF-TcSES-DOX	LEU _{112A} , PRO _{113A} , ARG _{114A} , LEU _{115A} , VAL _{116A} , ARG _{117A} , PRO _{118A} , MET _{123A} , PHE _{134A} , LYS _{137A} , TYR _{138A} , GLU _{141A} ,	TYR ₇₁ , LEU ₇₂ , ALA ₇₃ , ASN ₇₆	Hydrophobic interactions, hydrogen bonds, π -stacking, π -cation

Complex	HSA-TRF-TCC-DOX- interface residues		Type of interactions
	HSA	TRF	
	ARG _{145A} , TYR _{161A} , LEU _{182A} , ARG _{186A}		interactions, salt bridges
HSA-TRF-TcTET-DOX	LEU _{112A} , PRO _{113A} , ARG _{114A} , LEU _{115A} , VAL _{116A} , ARG _{117A} , PRO _{118A} , MET _{123A} , PHE _{134A} , LYS _{137A} , TYR _{138A} , GLU _{141A} , ARG _{145A} , TYR _{161A} , LEU _{182A} , ARG _{186A}	TYR ₇₁ , LEU ₇₂ , ALA ₇₃ , ASN ₇₆	Hydrophobic interactions, hydrogen bonds, π -stacking, π -cation interactions, salt bridges
HSA-TRF-TcMED-DOX	PRO _{113A} , ARG _{114A} , LEU _{115A} , VAL _{116A} , ARG _{117A} , PRO _{118A} , MET _{123A} , ALA _{126A} , PHE _{134A} , LYS _{137A} , TYR _{138A} , GLU _{141A} , ILE _{142A} , ARG _{145A} , TYR _{161A}	TYR ₆₈ , TYR ₇₁ , LEU ₇₂ , ALA ₇₃ , ASP ₃₁₀ , ALA ₃₁₁ , LYS ₃₁₂ , VAL ₃₂₀ , ARG ₃₂₄	Hydrophobic interactions, hydrogen bonds, π -cation interactions, salt bridges
HSA-TRF-TcMAG-DOX	LEU _{112A} , PRO _{113A} , ARG _{114A} , LEU _{115A} , VAL _{116A} , ARG _{117A} , PRO _{118A} , MET _{123A} , PHE _{134A} , LYS _{137A} , TYR _{138A} , GLU _{141A} , ARG _{145A} , TYR _{161A} , LEU _{182A} , ARG _{186A}	TYR ₇₁ , LEU ₇₂ , ALA ₇₃ , ASN ₇₆	Hydrophobic interactions, hydrogen bonds, π -stacking, π -cation interactions, salt bridges
HSA-TRF-TcEXA-DOX	LEU _{112A} , PRO _{113A} , ARG _{114A} , LEU _{115A} , VAL _{116A} , ARG _{117A} , PRO _{118A} , VAL _{122A} , LYS _{137A} , GLU _{141A} , ARG _{144A} , ARG _{145A}	TYR ₆₈ , TYR ₇₁ , LEU ₇₂ , ALA ₇₃ , ASN ₇₆ , ASP ₃₁₀ , ALA ₃₁₁ , LYS ₃₁₂ , VAL ₃₂₀ , ARG ₃₂₄ , GLU ₃₂₈	Hydrophobic interactions, hydrogen bonds, π -cation interactions, salt bridges
HSA-TRF-TcECD-DOX	ASP _{107A} , ASP _{108A} , ASN _{109A} , PRO _{110A} , ASN _{111A} , LEU _{112A} , PRO _{113A} , ARG _{114A} , ARG _{145A} , HSD _{146A} , PRO _{147A} , TYR _{148A} , LYS _{190A} , SER _{193A} , ALA _{194A} , ARG _{197A} , PRO _{421A} , THR _{422A} , GLU _{425A} , GLN _{459A}	ARG ₃₀₈	Hydrophobic interactions, hydrogen bonds
HSA-TRF-TcDMSA-DOX	PRO _{113A} , ARG _{114A} , LEU _{115A} , VAL _{116A} , ARG _{117A} , PRO _{118A} , MET _{123A} , ALA _{126A} , PHE _{134A} , LYS _{137A} , TYR _{138A} , GLU _{141A} , ILE _{142A} , ARG _{145A} , TYR _{161A}	TYR ₆₈ , TYR ₇₁ , LEU ₇₂ , ASP ₃₁₀ , ALA ₃₁₁ , LYS ₃₁₂ , VAL ₃₂₀ , ARG ₃₂₄	Hydrophobic interactions, hydrogen bonds, π -cation interactions, salt bridges
HSA-TRF-TcDIS-DOX	LEU _{112A} , PRO _{113A} , ARG _{114A} , LEU _{115A} , VAL _{116A} , ARG _{117A} , PRO _{118A} , MET _{123A} , PHE _{134A} , LYS _{137A} , TYR _{138A} , GLU _{141A} , ARG _{145A} , TYR _{161A} , LEU _{182A} , ARG _{186A}	TYR ₇₁ , LEU ₇₂ , ALA ₇₃ , ASN ₇₆	Hydrophobic interactions, hydrogen bonds, π -stacking, π -cation interactions, salt bridges
HSA-TRF-TcPER-DOX	LEU _{112A} , PRO _{113A} , ARG _{114A} , LEU _{115A} , VAL _{116A} , ARG _{117A} , PRO _{118A} , MET _{123A} , PHE _{134A} , LYS _{137A} , TYR _{138A} , GLU _{141A} , ARG _{145A} , TYR _{161A} , LEU _{182A} , ARG _{186A}	TYR ₇₁ , LEU ₇₂ , ALA ₇₃ , ASN ₇₆	Hydrophobic interactions, hydrogen bonds, π -stacking, π -cation interactions, salt bridges
HSA-TRF-TcDTPA-DOX	LEU _{112A} , PRO _{113A} , ARG _{114A} , LEU _{115A} , VAL _{116A} , ARG _{117A} , PRO _{118A} , VAL _{122A} , LYS _{137A} , GLU _{141A} , ARG _{144A} , ARG _{145A}	TYR ₆₈ , TYR ₇₁ , LEU ₇₂ , ALA ₇₃ , ASN ₇₆ , ASP ₃₁₀ , ALA ₃₁₁ , LYS ₃₁₂ , VAL ₃₂₀ , ARG ₃₂₄ , GLU ₃₂₈	Hydrophobic interactions, hydrogen bonds, π -cation interactions, salt bridges
HSA-TRF-TcHYN-DOX	LEU _{112A} , PRO _{113A} , ARG _{114A} , LEU _{115A} , VAL _{116A} , ARG _{117A} , PRO _{118A} , MET _{123A} , PHE _{134A} , LYS _{137A} , TYR _{138A} , GLU _{141A} , ARG _{145A} , TYR _{161A} , LEU _{182A} , ARG _{186A}	TYR ₇₁ , LEU ₇₂ , ALA ₇₃ , ASN ₇₆	Hydrophobic interactions, hydrogen bonds, π -stacking, π -cation interactions, salt bridges
HSA-TRF-TcMEB-DOX	LEU _{112A} , PRO _{113A} , ARG _{114A} , LEU _{115A} , VAL _{116A} , ARG _{117A} , PRO _{118A} , MET _{123A} , PHE _{134A} , LYS _{137A} , TYR _{138A} , GLU _{141A} , ARG _{145A} , TYR _{161A} , LEU _{182A} , ARG _{186A}	TYR ₇₁ , LEU ₇₂ , ALA ₇₃ , ASN ₇₆	Hydrophobic interactions, hydrogen bonds, π -stacking, π -cation interactions, salt bridges

*-A and B denote monomer subunits of the HSA dimer

In the following, to develop systems with dual imaging capabilities, we expanded our computational analysis by incorporating near-infrared (NIR) fluorophores into the highest-scoring protein-TCC-DOX complexes. This approach involved docking four distinct NIR fluorescent dyes to these complexes. We selected two conventional fluorophores, methylene blue and indocyanine green, along with two novel fluorescent agents, heptamethine cyanine dye AK7-5 and squaraine dye SQ1.

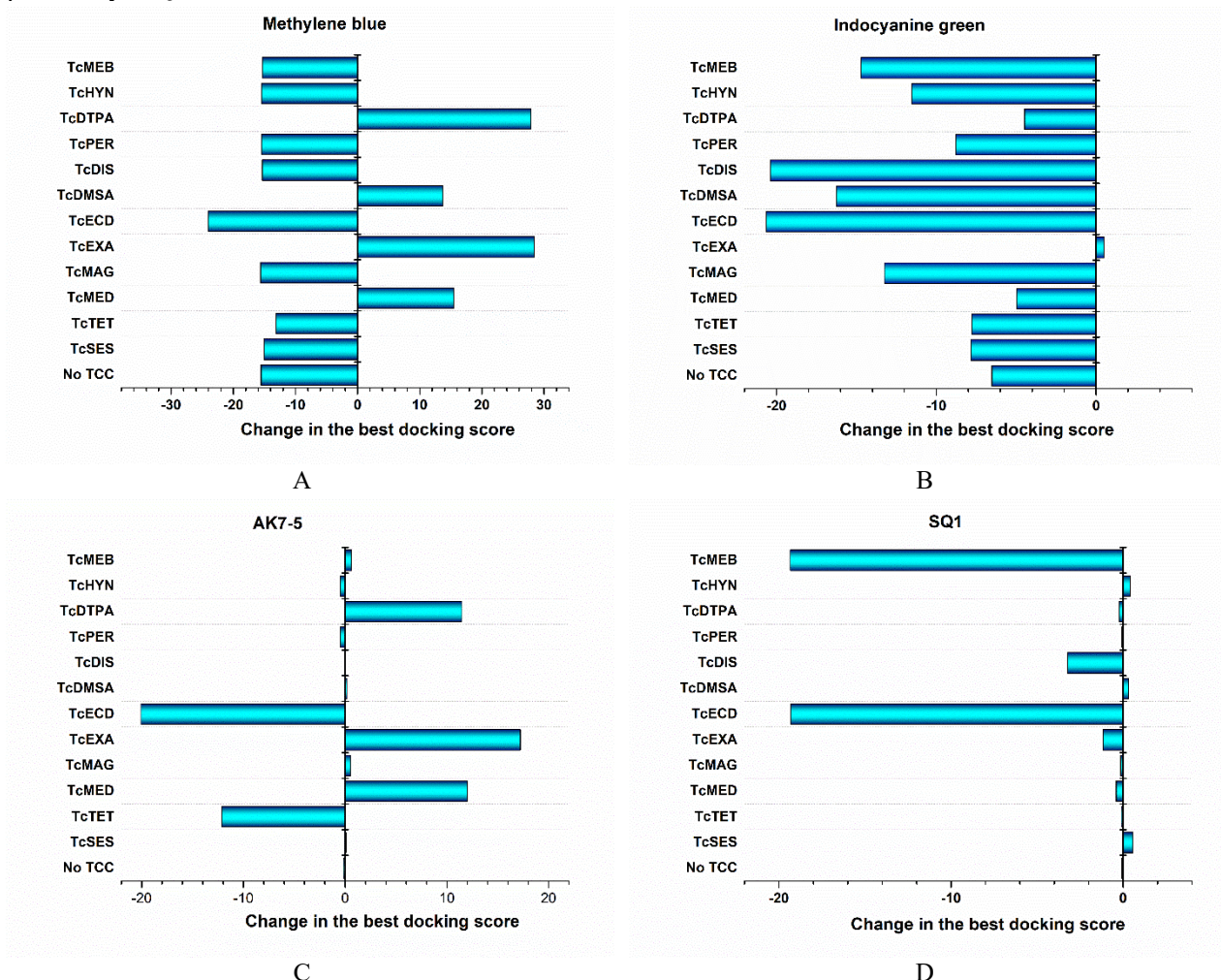


Figure 5. The changes in the best docking score values calculated for HSA-TRF-TCC-DOX-FD systems relative to the systems HSA-TCC-DOX-FD

By integrating these NIR fluorophores, we aimed to create multimodal imaging systems that combine the advantages of radionuclide-based imaging (via technetium complexes) with the high sensitivity and spatial resolution of NIR fluorescence imaging. A comprehensive evaluation of the docking results for the quaternary systems (protein + TCC + DOX + FD) reveals a clear trend in the binding affinities of the examined fluorescent dyes to HSA and HSA-DOX complexes [5]. The affinity decreases in the following order: indocyanine green (IG) > squaraine dye (SQ1) > heptamethine cyanine dye (AK7-5) > methylene blue (MB). This trend is evidenced by their respective BDS. While the specific amino acid residues involved in FD binding sites vary across different TCC and protein components, certain patterns emerge for each system. Notably, a consistent binding site for MB was identified in HSA-DOX, HSA-TCC-DOX, and HSA-TRF-DOX complexes. This site, designated as HSA₁₁₅₋₁₈₆, comprises 12 amino acid residues between LEU₁₁₅ and ARG₁₈₆ of albumin. Interestingly, in most HSA-TRF-TCC-DOX systems, the MB binding sites are composed of residues from both proteins in the complex. This suggests a cooperative binding mechanism involving multiple protein components. Furthermore, the addition of TRF to the HSA systems generally enhances MB binding affinity compared to HSA alone (Fig. 5, A).

The analysis of HSA binding sites for IG in HSA-TRF-TCC-DOX systems reveals the existence of three amino acid residues - ARG_{114A}, PRO_{421A}, and ILE_{523A} that are present in IG binding sites on HSA. The fluorescent dye AK7-5 interacts with HSA through sites composed of 18 (site HSA₁₁₅₋₅₂₃) or 12 amino acid residues from albumin domains I and III. Significant increases in binding affinity were observed in HSA-Lz-TcTET-DOX systems (Fig. 5, C) where AK7-5 binds either to the HSA₁₁₅₋₅₂₃ site or to hybrid sites of varying composition. Interestingly, in HSA-Lz/TRF complexes SQ1 binds to a site on HSA (HSA₁₁₅₋₅₂₃) supplemented by an additional residue (ASP_{173A}) from another albumin monomer. Overall, addition of TRF as second protein component gave rise to the substantial changes in BDS for MB and

IG as compared to the systems where protein was represented only by HSA (Fig. 5). In the case of AK7-5 and SQ1, the most pronounced changes in BDS were observed for TcECD.

CONCLUSIONS

In conclusion, the present study has been undertaken to verify the idea that the human serum albumin and its complexes with transferrin can be employed to create the nanocarriers with dual imaging capabilities for the antitumor drug doxorubicin. The results obtained showed that TcHYN, TcDIS, TcMEB and TcDTPA are capable of strong noncovalent binding to HSA and HSA-Lz/TRF/Hb complexes. Comprehensive analysis of best docking score values along with the interacting amino acid residues allows recommending HSA-TRF-TcHyn/TcMEB/TcDIS-DOX-IG/SQ1 systems as the most promising for experimental testing and further development of the protein-based nanoscale systems for DOX delivery with dual imaging functionalities.

Acknowledgements

This work was supported by the Ministry of Education and Science of Ukraine (the project № 0119U002525 “Development of novel ultrasonic and fluorescence techniques for medical micro- and macrodiagnostics”).

ORCID

Valeriya Trusova, <https://orcid.org/0000-0002-7087-071X>; Uliana Malovytsia, <https://orcid.org/0000-0002-7677-0779>
Galyna Gorbenko, <https://orcid.org/0000-0002-0954-5053>; Andrey Zelinsky, <https://orcid.org/0000-0002-4110-8523>
Borys Borts, <https://orcid.org/0000-0002-1492-4066>; Pylyp Kuznietsov, <https://orcid.org/0000-0001-8477-1395>

REFERENCES

- [1] C. Ferraro, M. Dattilo, F. Patitucci, S. Prete, G. Scopelliti, O. Parisi, and F. Puoci, *Pharmaceutics*. **16**, 1172 (2024). <https://doi.org/10.3390/pharmaceutics16091172>
- [2] S. Hong, D. Choi, H. Kim, C. Park, W. Lee, and H. Park, *Pharmaceutics*. **12**, 604 (2020). <https://doi.org/10.3390/pharmaceutics12070604>
- [3] A. Gorantla, J. Hall, A. Troidle, and J. Janjic, *Micromachines* **15**, 533 (2024). <https://doi.org/10.3390/mi15040533>
- [4] M. Larsen, M. Kuhlmann, M. Hvam, and K. Howard, *Mol. Cell Ther.* **4**, 3 (2016). <https://doi.org/10.1186/s40591-016-0048-8>
- [5] V. Trusova, U. Tarabara, I. Karnaukhov, A. Zelinsky, B. Borts, I. Ushakov, L. Sidenko, and G. Gorbenko, *East Eur. J. Phys.* (4), 447 (2024). <https://doi.org/10.26565/2312-4334-2024-4-54>
- [6] M. Puccetti, M. Pariano, A. Schoubben, S. Giovagnoli, and M. Ricci, *Pharmacol Res.* **201**, 107086 (2024). <https://doi.org/10.1016/j.phrs.2024.107086>
- [7] N. Qu, K. Song, Y. Ji, M. Liu, L. Chen, R. Lee, and L. Teng, *Int. J. Nanomedicine*. **19**, 6945 (2024). <https://doi.org/10.2147/IJN.S467876>
- [8] H. Choudhury, M. Pandey, P. Chin, Y. Phang, J. Cheah, S. Ooi, K. Mak, *et al.*, *Drug Deliv Transl Res.* **8**, 1545 (2018). <https://doi.org/10.1007/s13346-018-0552-2>
- [9] M. Kciuk, A. Gielecinska, S. Mujwar, D. Kołat, Z. Kałuzinska-Kołat, I. Celik, and R. Kontek, *Cells*. **12**, 659 (2023). <https://doi.org/10.3390/cells12040659>
- [10] M. F. Adasme, K. L. Linnemann, S. N. Bolz, F. Kaiser, S. Salentin, V. J. Haupt, and M. Schroeder, *Nucl. Acids Res.* **49**, W530-W534 (2021). <https://doi.org/10.1093/nar/gkab294>

КОМП'ЮТЕРНЕ ДОСЛІДЖЕННЯ СИСТЕМ ДОСТАВКИ ЛІКІВ З РАДІОНУКЛІДНИМИ ТА ФЛУОРЕСЦЕНТНИМИ МОДАЛЬНОСТЯМИ ВІЗУАЛІЗАЦІЇ. II. СИСТЕМИ НА ОСНОВІ АЛЬБУМІНУ ТА ТРАНСФЕРИНУ ДЛЯ ДОСТАВКИ ДОКСОРУБІЦИНУ В. Трусова^a, У. Маловиця^a, П. Кузнєцов^b, І. Карнаухов^c, А. Зелінський^c, Б. Борц^c, І. Ушаков^c, Л. Сіденко^c, Г. Горбенко^a

^aКафедра медичної фізики та біомедичних нанотехнологій, Харківський національний університет імені В.Н. Каразіна
м. Свободи 4, Харків, 61022, Україна

^bКафедра фізики ядра та високих енергій імені О.І. Ахієзера, Харківський національний університет імені В.Н. Каразіна
м. Свободи 4, Харків, 61022, Україна

^cНаціональний науковий центр «Харківський фізико - технічний інститут», Харків, вул. Академічна, 1, 61108, Україна

Дослідження присвячене розробці вдосконалених систем на основі білків для доставки лікарських засобів, зокрема, доксорубіцину (DOX) - протипухлинного агента, з інтеграцією радіонуклідних (комплексів технецію-99m) та флуоресцентних (метиленовий блакитний (МВ), індоціанін зелений (ІЗ), ціаніновий барвник AK7-5 та скварайновий барвник SQ1) модальностей. Базуючись на наших попередніх дослідженнях, в яких білкова компонента нанопереносників була представлена альбуміном, в даній роботі трансферин (TRF) було застосовано як комплементарну білкову складову для створення більш складної та таргет-специфічної платформи доставки. Метод молекулярного докінгу було застосовано для дизайну та характеристики мультимодальних систем доставки, що включають радіофармпрепарати та флуоресцентні барвники ближнього інфрачервоного спектру. Отримані результати показали, що радіофармпрепарати на основі технецію-99m зв'язуються за допомогою нековалентних зв'язків з людським сироватковим альбуміном (HSA) та його комплексами з трансферином. Комплексний аналіз даних докінгу та амінокислотних залишків, що беруть участь у взаємодії, виявив, що системи HSA-TRF-TcHyn/TcMEB/TcDIS-DOX-IG/SQ1 демонструють найбільш високий потенціал для експериментальної верифікації та подальшої розробки. Ці дані свідчать, що комплекси HSA-TRF є перспективними наноносійми з подвійною візуалізацією для доставки DOX, які характеризуються підвищенням терапевтичної ефективності при одночасній мінімізації системної токсичності в онкотерапії.

Ключові слова: наносистеми доставки ліків; людський сироватковий альбумін; трансферин; доксорубіцин; комплекси технецію; флуоресцентні барвники; молекулярний докінг

SLOW SURFACE ELECTROMAGNETIC WAVES ON A MU-NEGATIVE CYLINDER

 Victor Galaydych,  Mykola Azarenkov

National Science Center Kharkiv Institute of Physics and Technology, 1 Akademichna St., Kharkiv, Ukraine

*Corresponding Author e-mail: viktor.galaydych@gmail.com

Received December 20, 2024; revised February 2, 2025; accepted February 15, 2025

This paper presents the theoretical study of metamaterials with negative magnetic permeability. The electrodynamics phenomenological description has been chosen. The dispersion properties of slow surface electromagnetic waves propagating along a circular cylinder made of mu-negative metamaterial are studied. We neglect energy losses in the metamaterial. Negativity of permeability occurs in relatively bounded frequency intervals, and for all modes, a normal dispersion occurs, regardless of parameter values. The values of phase velocities of these waves lie between c and $0.3c$. The phase velocity dependencies of the studied modes versus their frequency have a diverse appearance. The directions of group and phase velocities coincide. The values of group velocity are less than $0.002c$. The wave fields are the superposition of transverse-electric and transverse-magnetic parts and decay exponentially in a radial direction away from the separating boundary. The wave fields penetrate mu-negative metamaterial much weaker than into a vacuum. Wave propagation in the structure does not require an external magnetic field. The variety of these wave features on the cylinder parameters can be used for different applications.

Keywords: Metamaterial; Negative permeability; Cylinder; Surface electromagnetic wave

PACS: 04.50.Kd, 04.20.Jb

1. INTRODUCTION

Metamaterials are artificially engineered materials consisting of special identical cells. These ones play role as artificial atoms for electromagnetic waves of wavelength much larger than cell size. The phenomenological description gives values of effective electric permittivity and magnetic permeability. Metamaterials may possess unique combinations of properties, that do not exist in natural materials [1]–[3].

Most of the articles are devoted to the study of metamaterials in which both these characteristics are negative. Meanwhile, it is easier to create a metamaterial with single negative magnetic permeability [4]. Such metamaterials have been studied much less (see, for example [5],[6])

Consider the slow surface electromagnetic eigenwaves on a mu-negative cylinder. Here, the term "slow" means that we consider waves with phase velocities less than the speed of light in vacuum (in the diagram on the right-hand of a light's line). Structure considered consists of an infinitely long circular cylinder of the ideal (lossless) homogeneous, isotropic and frequency dependent mu-negative medium ($r < R_c$) embedded in a vacuum ($r > R_c$) with permittivity $\epsilon_1 = 1$ and permeability $\mu_1 = 1$. Assume that the coordinate axis OZ and the cylinder axis coincide.

This mu-negative medium possesses such parameters: the constant permittivity $\epsilon_2 = 1$ and the frequency dependent permeability $\mu_2(\omega) = 1 - a\omega^2/(\omega^2 - \omega_0^2)$, $\omega_0/2\pi = 4GHz$ - resonant frequency, $a = 0.56$ - geometric factor (for example, [4]). Parameters a, ω_0 are uniquely determined by the specific design of a particular metamaterial. Throughout this communication our study was limited by such values of frequency $\omega_0 < \omega < \omega_0/\sqrt{1-a}$, that inequality $\mu_2(\omega) < 0$ is fulfilled.

2. RESULTS

We want to search the possibility of propagation (along OZ) the surface electromagnetic waves of angular frequency ω , wavenumber β and azimuthal number n . In what follows we assume the ansatz

$$A_j^n(r, \phi, z) = A_{0j}^n(r) \Psi^n, j = 1, 2 \quad (1)$$

where $\Psi^n = \exp i(\beta z - \omega t + n\phi)$.

As is a well-known, the cylindrical eigenwave fields are the superpositions of transverse-electric and transverse-magnetic modes [7]

$$E_{r,j}^n = \left[\frac{i\beta}{\kappa_j} F_n'(\kappa_j r) a_j^n - \frac{n\mu_j(\omega)\omega}{\kappa_j^2 r} F_n(\kappa_j r) b_j^n \right] \Psi^n \quad (2)$$

$$E_{\phi,j}^n = - \left[\frac{n\beta}{\kappa_j^2 r} F_n(\kappa_j r) a_j^n + i \frac{\mu_j(\omega)\omega}{\kappa_j} F_n'(\kappa_j r) b_j^n \right] \Psi^n \quad (3)$$

$$E_{z,j}^n = F_n(\kappa_j r) a_j^n \Psi^n \quad (4)$$

$$H_{r,j}^n = \left[\frac{nk_j^2}{\mu_j(\omega)\omega\kappa_j^2 r} F_n(\kappa_j r) a_j^n + i \frac{\beta}{\kappa_j} F_n'(\kappa_j r) b_j^n \right] \Psi^n \quad (5)$$

$$H_{\phi,j}^n = \left[\frac{ik_j^2}{\mu_j(\omega)\omega\kappa_j} F_n'(\kappa_j r) a_j^n - \frac{n\beta}{\kappa_j^2 r} F_n(\kappa_j r) b_j^n \right] \Psi^n \quad (6)$$

$$H_{z,j}^n = F_n(\kappa_j r) b_j^n \Psi^n \quad (7)$$

here $\kappa_j = \sqrt{k_j^2 - \beta^2}$, $k_j^2 = k^2 \epsilon_j \mu_j$, $k = \omega/c$, c - the speed of light in vacuum. In equations (2)-(7) the wave fields are presented in a compact form both for the vacuum ($j = 1$, $F_n = H_n^{(1)}$) and for mu-negative cylinder ($j = 2$, $F_n = J_n$). Sign ' denotes the derivative of cylindrical functions by the argument.

Satisfying of the boundary conditions for tangential wave field components at $r = R_c$

$$H_{z,1}^n = H_{z,2}^n, H_{\phi,1}^n = H_{\phi,2}^n, E_{z,1}^n = E_{z,2}^n, E_{\phi,1}^n = E_{\phi,2}^n \quad (8)$$

and the condition for solvability of the homogeneous system of equations for four coefficients $a_1^n, a_2^n, b_1^n, b_2^n$ give rise the dispersion equation for such wave disturbances

$$\left[\frac{\mu_2(\omega)}{u} \frac{J_n'(u)}{J_n(u)} - \frac{\mu_1}{v} \frac{H_n'(v)}{H_n(v)} \right] \left[\frac{\epsilon_2}{u} \frac{J_n'(u)}{J_n(u)} - \frac{\epsilon_1}{v} \frac{H_n'(v)}{H_n(v)} \right] \left[\frac{\omega}{c} \right]^2 - n^2 \beta^2 \left[\frac{1}{v^2} - \frac{1}{u^2} \right]^2 = 0 \quad (9)$$

$v = \kappa_1 R_c$, $u = \kappa_2 R_c$.

The solution of (9) at a given n gives rise to a pair (ω, β) , so we get the dispersion curve $\omega(\beta)$ for n th mode. We introduce the dimensionless wave frequency $\Omega = \omega/\omega_0$, wavenumber $K = \beta c/\omega_0$ and the dimensionless radius $R = R_c \omega_0/c$.

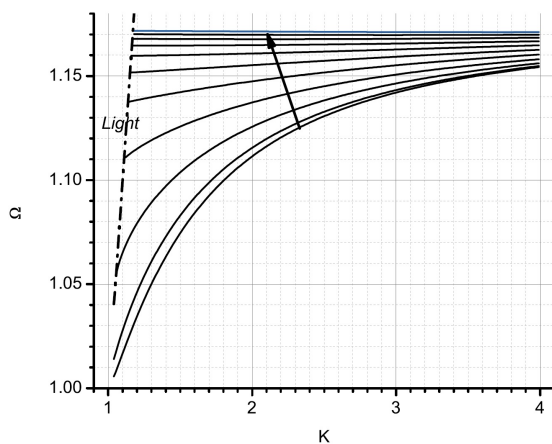


Figure 1. Dispersion curves for modes with different azimuthal number values $n=0,1...10$ (along in the direction of arrows) with $R=2$

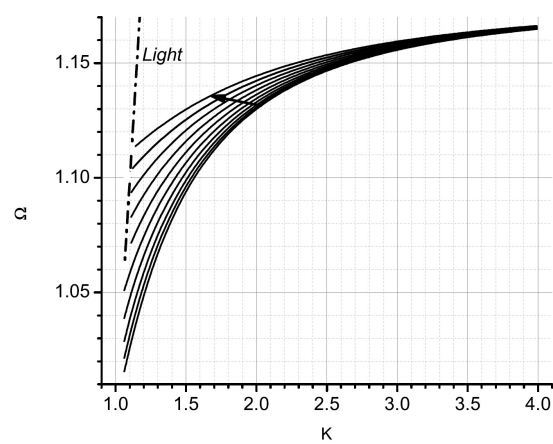


Figure 2. Dispersion curves for modes with different azimuthal number values $n=0,1...10$ (along in the direction of arrows) with $R=8$

In Fig.1,2 it has been shown the dispersion curves for modes with azimuthal number $n = 0, 1...10$ for cylinder with the dimensionless radius $R = 2$ and $R = 8$. The dash-dotted line correspond with the light dispersion. For all modes take

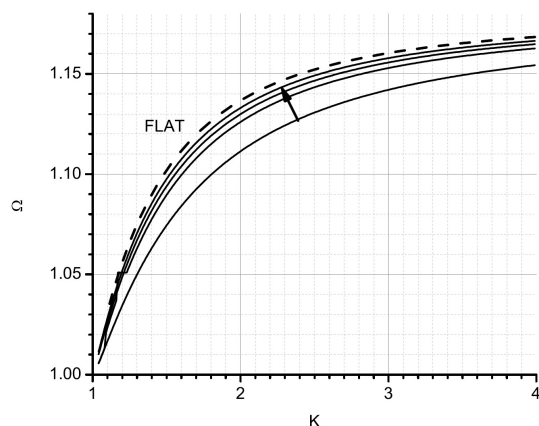


Figure 3. Dispersion curves for mode with azimuthal number $n=0$ for various values $R=2,5,8,15$ (along in the direction of arrows) and for planar surface mode [5] (dashed line)

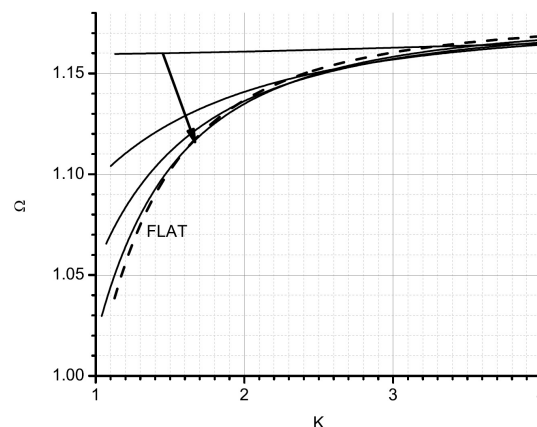


Figure 4. Dispersion curves for mode with azimuthal number $n=6$ for various values $R=2,5,8,15$ (along in the direction of arrows) and for planar surface mode [5] (dashed line)

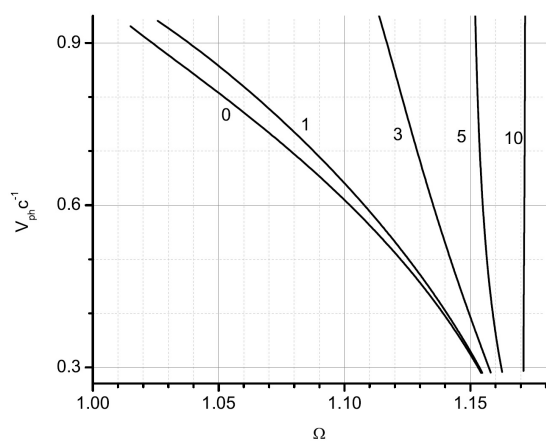


Figure 5. Phase velocity versus frequency for modes with azimuthal numbers $n=0, 1, 3, 5, 10$ for cylinder radius value $R=2$

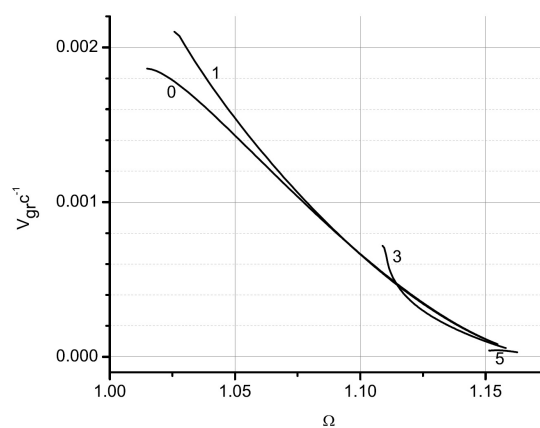


Figure 6. Group velocity versus frequency for modes with azimuthal numbers $n = 0, 1, 3, 5$ for cylinder radius value $R=2$

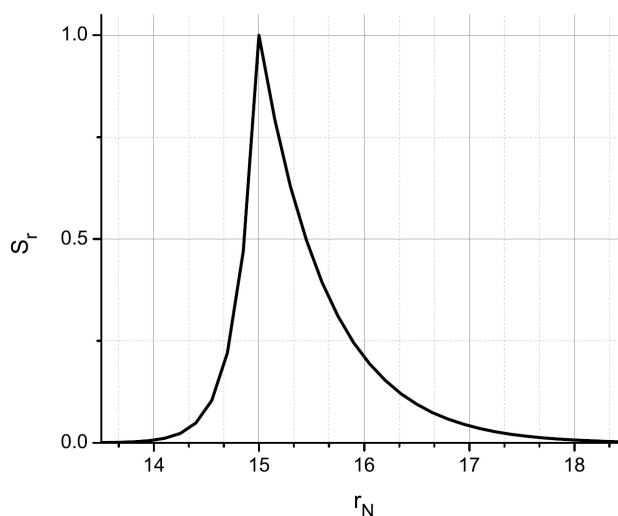


Figure 7. Radial Poynting vector S_r versus r_N for modes with azimuthal number $n=6$ at cylinder radius $R=15$ and wave frequency $\omega=1.054729$

place a normal dispersion. The modes with higher value n have higher frequencies and exist in a narrower bandwidths. The transverse wave numbers $\kappa_{1,2}$ are purely imaginary values. Therefore the wave fields decays exponentially with distance from the cylinder surface in the radial direction. Similar dispersion curves were obtained for an epsilon-negative circular cylinder [8]).

In Figs.3,4 we present the dispersion curves evolution with increasing cylinder radius R for modes with $n = 0$ and $n = 6$. The dispersion curves for larger cylinder radii asymptotically approach the dispersion curve of a surface wave in the planar geometry obtained in [5] (dashed line). The dispersion curves of the symmetric mode ($n = 0$) change little with increasing radius R .

The phase velocities of these modes vary by an order of magnitude within the frequency intervals considered (Fig.5). Variety of types the dependency phase velocity of the mode versus its frequency may be used in different devices. As an example, an almost linear dependence will certainly come in handy for broadband pulse amplification [9], etc.

The directions of group and phase velocities coincide, so these modes are forward waves (Fig.6). The values of group velocities no more $0.002c$. The group velocities for modes with angular wavenumber $n > 5$ are less by several orders.

The electromagnetic fields of surface modes on a mu-negative cylinder are attenuated in the radial direction away from the interface 'metamaterial/vacuum'. In Fig.7 it presents the radial component of the Poynting vector $S_r \sim \text{Re}(E_z H_\phi^*)$ versus the dimensionless radial coordinate $r_N = r\omega_0/c$. It can be seen that the wave fields penetrate not as deeply into the mu-negative cylinder as into the vacuum. This difference becomes more noticeable with a larger cylinder radius. This property makes these modes with promising for interacting with charged particle beams [?] that do not must to move very close to the cylinder.

The distribution of energy flux over the angle ϕ is symmetric for $n = 0$, but consists of $2n$ identical narrow radiant sectors for $n > 0$. For higher n , the total number of these sectors increases, they become narrower and have a higher energy flux density.

3. CONCLUSIONS

We found that surface electromagnetic modes can propagate along a mu-negative cylinder. These waves are slow and forward, consisting of a superposition of transverse-electric and transverse-magnetic modes. Modes with higher azimuthal numbers occur at higher frequencies. A significant practical advantage of these waves—especially for controlling the movement of charged particles—is their ability to function without an external magnetic field. We hope that these surface electromagnetic waves will enhance the existing range of modes used for generating electromagnetic waves and managing the motion of charged particles, as well as for receiving and transmitting signals and other applications.

Declarations

Conflict of interest. None declared.

Ethical approval. Not required.

ORCID

 Victor Galaydych, <https://orcid.org/0000-0002-2255-9716>;  Mykola Azarenkov, <https://orcid.org/0000-0002-4019-4933>

REFERENCES

- [1] N. Engheta, and R.W. Ziolkowski, *Electromagnetic Metamaterials: Physics and Engineering Explorations*, (Wiley and IEEE Press, 2006).
- [2] T. Cui, S. Zhang, A. Alù, et al., "Roadmap on electromagnetic metamaterials and metasurfaces," *Journal of Physics: Photonics*, **6**, 032502 (2024). <https://dx.doi.org/10.1088/2515-7647/ad1a3b>
- [3] I. Shadrivov, M. Lapine, and Y. Kivshar, *Nonlinear, tunable and active metamaterial*, (Springer, 2015). <https://link.springer.com/book/10.1007/978-3-319-08386-5>
- [4] J.B. Pendry, A.J. Holden, D.J. Robbins, and W.J. Stewart, "Magnetism from conductors and enhanced nonlinear phenomena," *IEEE Transactions on Microwave Theory and Techniques*, **47**, 2075-2084 (1999). <https://doi.org/10.1109/22.798002>
- [5] V. Galaydych, and M. Azarenkov, *Applied Physics B*, "Slow surface electromagnetic waves on a mu-negative medium," **128**(7), 132 (2022). <https://doi.org/10.1007/s00340-022-07854-3>
- [6] V. Galaydych, and M. Azarenkov, "Surface polaritons in a vacuum gap inside mu-negative medium," *Applied Physics A: Materials Science and Processing*, **129**(7), 466 (2023). <https://doi.org/10.1007/s00339-023-06751-6>
- [7] J.A. Stratton, *Electromagnetic Theory*, (John Wiley & Sons, LTD, 2007).
- [8] J. Ashley, and L. Emerson, "Dispersion relations for non-radiative surface plasmons on cylinders," *Surface Science*, **41**(2), 615-618 (1974). [https://doi.org/10.1016/0039-6028\(74\)90080-6](https://doi.org/10.1016/0039-6028(74)90080-6)
- [9] K. Galaidych, P. Markov, and G. Sotnikov, "Amplification of the Multifrequency Signal in the Coaxial Slow-Wave Structure," *Telecommunications and Radio Engineering*, **67**(2), 177-189 (2008). <https://doi.org/10.1615/TelecomRadEng.v67.i2.70>
- [10] K.E. Zayed, "Surface wave-beam interaction in cylindrical geometry," *Physica*, **58**(2), 177 (1972). [https://doi.org/10.1016/0031-8914\(72\)90285-6](https://doi.org/10.1016/0031-8914(72)90285-6)

- [11] A. Zayats, I. Smolyaninov, and A. Maradudin, "Nano-optics of surface plasmon polaritons," *Physics Reports*, **408**, 131-314 (2005). <http://dx.doi.org/10.1016/j.physrep.2004.11.001>
- [12] F. Zhang, W. Wang, and Z. Zhang, "Simulation Study of a High-Order Mode BWO with Multiple Inclined Rectangular Electron Beams," *Progress In Electromagnetics Research C*, **110**, 213-227 (2021). <http://dx.doi.org/10.2528/PIERC21010401>

ПОВІЛЬНІ ПОВЕРХНЕВІ ЕЛЕКТРОМАГНІТНІ ХВИЛІ НА МЮ-НЕГАТИВНОМУ ЦИЛІНДРІ

Віктор Галайдиш, Микола Азаренков

Національний науковий центр «Харківський фізико-технічний інститут», вул. Академічна, 1, м. Харків, Україна

У цій статті ми представляємо теоретичні дослідження метаматеріалів з негативною магнітною проникністю. Вибрано феноменологічний опис електродинаміки. Досліджено дисперсійні властивості повільних поверхневих електромагнітних хвиль, які можуть поширюватися вздовж круглого циліндра з мю-негативного метаматеріалу. Ми нехтуємо втратами енергії в метаматеріалі. Негативність проникності має місце в досить обмеженому інтервалі частот. Для всіх режимів має місце нормальна дисперсія, незалежно від значень параметрів. Значення фазових швидкостей цих хвиль лежать між c і $0,3c$. Залежності фазових швидкостей досліджуваних мод від їх частоти мають різноманітний вигляд. Напрями групових і фазових швидкостей збігаються. Значення групової швидкості менше $0,002c$. Хвильові поля являють собою суперпозицію поперечно-електричної та поперечно-магнітної частин і експоненціально спадають у радіальному напрямку від межі розділення. Хвильові поля проникають в мю-негативний метаматеріал набагато слабше, ніж у вакуум. Для поширення хвиль в структурі не потрібне зовнішнє магнітне поле. Різноманітність цих хвильових характеристик параметрів циліндра можна використовувати для різних застосувань.

Ключові слова: метаматеріал; негативна магнітна проникність; циліндр; поверхнева електромагнітна хвиля

INTERACTION BETWEEN A SPHERICAL PARTICLE AND ATMOSPHERIC PRESSURE CURRENTLESS ARGON PLASMA

 **Shiyi Gao**^{a,*},  **Andrii Momot**^{b,c},  **Igor Krivtsun**^b,  **Danylo Antoniv**^{b,c},  **Oksana Momot**^c

^aChina-Ukraine Institute of Welding Guangdong Academy of Sciences, Guangdong Provincial Key Laboratory of Advanced Welding Technology, 363 Changxing Road, Tianhe, Guangzhou, 510650, China

^bE.O. Paton Electric Welding Institute NAS of Ukraine, 11, Kazymyr Malevych St., Kyiv, 03150, Ukraine

^cTaras Shevchenko National University of Kyiv, 64/13, Volodymyrs'ka St., Kyiv 01601, Ukraine

*Corresponding Author e-mail: meshiyigao@163.com

Received December 21, 2024; revised January 31, 2025; accepted February 17, 2025

The interaction between a spherical particle of radius $10^{-5} - 10^{-3}$ m and atmospheric pressure currentless argon plasma was studied numerically within the hydrodynamic approach. The nonlinear problem was solved taking into account the temperature dependencies of transport and kinetic coefficients. A two-temperature model, which considers plasma thermal and ionization non-equilibrium near the particle, was used. The boundary condition for electron heat flux on the outer boundary of the space charge sheath is discussed in detail. The spatial distributions of plasma characteristics, such as temperature and number density, near the particle were determined and analyzed. The heat flux from plasma to the particle was calculated over a wide temperature range of singly ionized argon plasma.

Keywords: Atmospheric pressure argon plasma; Currentless argon plasma; Plasma numerical modeling; Spherical particle in plasma; Plasma-particle interaction

PACS: 52.27.Lw, 52.77.Fv

1. INTRODUCTION

The interaction between fine condensed matter particles and plasma has been of interest in plasma physics for many years. Low-pressure plasma containing fine particles is commonly referred to as dusty or complex plasma [1, 2, 3]. The study of dusty plasma often focuses on particle charge, potential, and interactions between particles [4, 5, 6, 7], as well as the propagation of various types of waves and solitons [8, 9, 10, 11].

Atmospheric-pressure thermal plasma [12, 13] containing fine metal particles occurs in many technical plasma processes, such as plasma spraying, plasma transferred arc (PTA) surfacing [14, 15, 16], spheroidization of metal powders [17, 18], and gas metal arc welding (GMAW) [19]. For the research and development of these processes, it is important to understand both the thermal effect of plasma on the particles and the influence of particles on plasma characteristics.

In the present study, we consider currentless plasma, which corresponds to the conditions of plasma spraying [14, 15], where thermal plasma is used to heat and melt dispersed material before depositing it on a surface. However, the obtained results may also be useful for current-carrying plasma, which is used, for example in PTA surfacing. Our recent study showed that for particles with a radius of up to $\sim 10^{-3}$ m, the thermal effect of plasma on the particle does not significantly depend on the plasma current but rather on its temperature, which is determined by the current.

In Refs. [20, 21], the heat flux from atmospheric-pressure plasma to a particle was studied, taking into account the thermal and ionization nonequilibrium of the plasma, the violation of quasineutrality near the particle surface, and rarefaction effects over a wide range of Knudsen numbers. However, the inverse effect of the particle on the characteristics of the surrounding plasma was not considered in these studies. Such effects were examined in our previous works [22, 23, 24].

In the present study, we used a modified boundary condition for the electron heat flux and accounted for an additional mechanism of ion heat transfer to the particle. Additionally, particles with a radius of $a = 10^{-3}$ m were considered, corresponding to the droplet size of electrode metal in GMA welding. The influence of particles of this size on plasma characteristics is expected to be more pronounced.

2. MODEL AND BASIC EQUATIONS

Atmospheric-pressure currentless argon plasma with a temperature $T_0 = 6 - 18$ kK is considered. In this temperature range, the density of multiply charged argon ions is much lower than that of singly charged ions. We study the interaction of such a plasma with a single stationary spherical particle (either metal or dielectric) of radius $a = 10^{-5} - 10^{-3}$ m placed in it. The particle surface adsorbs electrons (e) and ions (i) from plasma, which then recombine on the surface and desorb as argon atoms (a). It means that there are electron, ion and atom fluxes $\mathbf{J}_\alpha = n_\alpha \mathbf{v}_\alpha$ near the particle (n_α is the number density and \mathbf{v}_α is the velocity). Since the mobility of electrons is much higher than that of ions, the initially neutral particle gains a negative electric charge, which increases until the electron and ion fluxes become equal $\mathbf{J}_i = \mathbf{J}_e$ in the stationary state. Also, we consider plasma at rest relative to the particle, i.e. the mass-average plasma velocity is zero $m_e \mathbf{J}_e + m_i \mathbf{J}_i +$

$m_a \mathbf{J}_a = 0$ that gives $\mathbf{J}_a = -\mathbf{J}_i$. Thus, only one flux density is independent, and we will consider the ion flux density, which satisfies the following continuity equation

$$\nabla \mathbf{J}_i = \omega_i = k_i n_e n_a - k_r n_e^2 n_i. \quad (1)$$

Here ω_i is the production rate of ions due to ionization-recombination reactions, obviously $\omega_i = \omega_e = -\omega_a$; k_i and k_r are the ionization and recombination rate constants, respectively.

Desorbed atoms have a temperature equal to the temperature of the particle surface $T_s \ll T_0$. Due to efficient energy transfer between ions and atoms (heavy particles h) they share the same temperature, T_h . Since energy transfer between heavy particles and electrons is slow, T_h differs from the electron temperature T_e i.e., the plasma is not in thermal equilibrium nor, consequently, in ionization equilibrium near the particle. A spatial distribution of plasma particle density and temperature is established around the spherical particle.

The momentum equations for plasma particles have the form [25]:

$$-\nabla p_\alpha - n_\alpha Z_\alpha e \nabla \varphi + \sum_\beta \nu_{\alpha\beta} \mu_{\alpha\beta} n_\alpha n_\beta (\mathbf{v}_\beta - \mathbf{v}_\alpha) - C_\alpha^{(e)} n_\alpha k \nabla T_e = 0. \quad (2)$$

Here $\alpha, \beta = e, i, a$; $p_\alpha = n_\alpha k T_\alpha$ is the partial pressure of α plasma component, where k is the Boltzmann constant; T_α is the temperature; Z_α is the particle charge number ($Z_e = -1$, $Z_i = 1$, and $Z_a = 0$); e is the elementary charge; φ is the distribution of electric potential in plasma; $\nu_{\alpha\beta}$, $\mu_{\alpha\beta} = m_\alpha m_\beta / (m_\alpha + m_\beta)$ are the momentum transfer collision rate and the reduced mass of particle species α and β , respectively, where m_α is the mass of a particle of species α . The last term in (2) is thermal diffusion force due to electron temperature gradient, where $C_\alpha^{(e)}$ are the thermal diffusion coefficients. The thermal diffusion force due to heavy particle temperature gradient can be neglected [26].

The space charge layer (sheath) is formed around the charged particle in plasma. The thickness of the sheath l_{sh} is of the order of Debye length that is $r_D \sim 10^{-7}$ m for the considered plasma parameters [22]. The considered particle radii are much greater than the sheath thickness $a \gg l_{sh}$. Thus, we study plasma outside the sheath, where it is quasineutral $n_e = n_i$.

The sum of partial pressures of all particle species is constant and equal to atmospheric pressure p_0 , i.e. $n_e k T_e + n_i k T_h + n_a k T_h = \text{const} = p_0$. Taking into account that $n_e = n_i$, we obtain the expression for atom number density

$$n_a = \frac{p_0}{k T_h} - n_i \left(1 + \frac{T_e}{T_h} \right). \quad (3)$$

Equations (2) for electrons and ions ($\alpha = e, i$), taking into account that $\mathbf{J}_e = \mathbf{J}_i$, can be rewritten as

$$-k \nabla (n_i T_\alpha) - n_i Z_\alpha e \nabla \varphi - \gamma_\alpha \mathbf{J}_i - C_\alpha^{(e)} n_i k \nabla T_e = 0, \quad (4)$$

where $\gamma_e = \nu_{ea} \mu_{ea} (n_i + n_a)$ and $\gamma_i = \nu_{ia} \mu_{ia} (n_i + n_a)$.

By adding equations (4) we eliminate the term with $\nabla \varphi$ and obtain the expression for ion flux

$$\mathbf{J}_i = -\frac{k}{\gamma_e + \gamma_i} \left((T_e + T_h) \nabla n_i + n_i \nabla T_h + \tilde{C}_i^{(e)} n_i \nabla T_e \right), \quad (5)$$

where $\tilde{C}_i^{(e)} = 1 + C_e^{(e)} + C_i^{(e)}$. Substitution of Eq (5) and $n_e = n_i$ into continuity equation for ion flux density (1) gives the second order differential equation.

Substituting equation (5) into one of the equations (4) allows us to obtain the potential gradient distribution in the plasma near the particle.

$$\nabla \varphi = \frac{k}{e (\gamma_e + \gamma_i) n_i} \left[(\gamma_i T_e - \gamma_e T_h) \nabla n_i - \gamma_e n_i \nabla T_h + (\gamma_i + \gamma_i C_e^{(e)} - \gamma_e C_i^{(e)}) n_i \nabla T_e \right]. \quad (6)$$

The heavy particle temperature gradient in plasma leads to the appearance of heat flux $\mathbf{q}_h = -\lambda_h \nabla T_h$, which satisfies the following continuity equation [25]

$$\nabla \mathbf{q}_h = -e \mathbf{J}_i \nabla \varphi + \kappa_{eh} n_i k (T_e - T_h), \quad (7)$$

where λ_h is the thermal conductivity coefficient of heavy particles; κ_{eh} is the energy exchange frequency.

The heat flux for electrons [26] contains additional terms that describe energy transfer between electrons and heavy particles due to their relative drift.

$$\mathbf{q}_e = -\lambda_e \nabla T_e + k T_e n_e \left[A_i^{(e)} (\mathbf{v}_e - \mathbf{v}_i) + A_a^{(e)} (\mathbf{v}_e - \mathbf{v}_a) \right] = -\lambda_e \nabla T_e + k T_e A_a^{(e)} \mathbf{J}_i (1 + n_i/n_a), \quad (8)$$

where $A_\alpha^{(e)}$ are the kinetic coefficients. It was taken into account in (8) that $\mathbf{J}_a = -\mathbf{J}_i$, $\mathbf{J}_e = \mathbf{J}_i$ and $n_e = n_i$.

The continuity equation for electron heat flux is [25]

$$\nabla \left(\mathbf{q}_e + \frac{5}{2} k T_e \mathbf{J}_i \right) = e \mathbf{J}_i \nabla \varphi - \kappa_{eh} n_i k (T_e - T_h) - U_i \omega_e. \quad (9)$$

The first terms on the right-hand sides of Eqs. (7) and (9) describe the heat transfer between plasma particles and electric field, the second terms describe the energy exchange between electrons and heavy particles. The last term describes the power released in ionization-recombination processes ($U_i = 15.75$ eV is the argon ionization potential.)

The considered problem has a spherical symmetry, so it is one-dimensional in the spherical coordinate system placed in the center of the particle. All vector functions have only radial nonzero components that depend on single variable r . For instance, the electron flux takes the form $\mathbf{J}_i = (J_{ir}(r), 0, 0)$, where $J_i = J_{ir}$. We have three unknown functions of single variable $n_i(r)$, $T_h(r)$, and $T_e(r)$ along with three differential equations (1), (7) and (9). The system of equations should be supplemented with proper boundary conditions, which are discussed in the next section.

3. BOUNDARY CONDITIONS

As it was mentioned above, we consider quasineutral plasma, i.e. outside the sheath. The boundary conditions are set on the sheath outer boundary, which is denoted with letter S on the figure 1. The values of functions on this surface are denoted with subscript s , for instance $n_i|_S = n_i(a + l_{sh}) = n_{is}$.

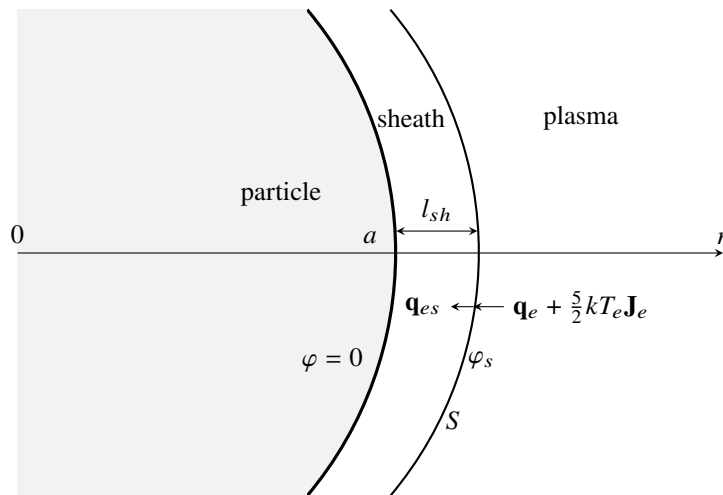


Figure 1. Scheme of the problem

The normal component of ion flux on surface S is

$$J_i(a + l_{sh}) = J_{is} = -n_{is} v_B, \quad (10)$$

where $v_B = \sqrt{k(T_{es} + T_{hs})/m_i}$ is the Bohm velocity. It has a negative sign because it is directed opposite to the r -axis. Neglecting ion collisions with atoms within the sheath and taking into account that $l_{sh} \ll a$, we can write $J_i(a + l_{sh}) = J_i(a)$.

The boundary condition for the electron flux can be derived from the electron velocity distribution function. At the sheath outer boundary, it takes the form

$$f_s(\mathbf{v}) = f_{sn}(v_n) f_{st}(\mathbf{v}_t), \quad (11)$$

where v_n is the component of velocity along the \mathbf{e}_r (normal to surface), \mathbf{v}_t is the component perpendicular to \mathbf{e}_r (tangential to surface) and

$$f_{st}(\mathbf{v}_t) = \frac{m_e}{2\pi k T_{es}} \exp\left(-\frac{m_e v_t^2}{2k T_{es}}\right), \quad (12)$$

$$f_{sn}(v_n) = \begin{cases} 0, & v_n > v_{n0}, \\ \sqrt{\frac{m_e}{2\pi k T_{es}}} \exp\left(-\frac{m_e v_n^2}{2k T_{es}}\right), & v_n < v_{n0}. \end{cases} \quad (13)$$

where $v_{n0} = \sqrt{2e\varphi_s/m_e}$ and $\varphi_s = \varphi(a + l_{sh})$. The potential of the particle surface is considered to be zero.

The electron flux density on sheath outer boundary is

$$J_e(a + l_{sh}) = J_{es} = n_{es} \int d\mathbf{v} v_n f_s(\mathbf{v}) = n_{es} \int_{-\infty}^{v_{n0}} dv_n v_n f_{sn}(v_n) \int d\mathbf{v}_t f_{st}(\mathbf{v}_t) = -\frac{n_{es} \bar{v}_{es}}{4} \exp\left(-\frac{e\varphi_s}{kT_{es}}\right), \quad (14)$$

where $\bar{v}_{es} = \sqrt{8kT_{es}/\pi m}$ is the mean thermal velocity of electrons.

Equating the currents $J_{es} = J_{is}$ we obtain from Eqs. (14) and (10) expression for the sheath potential

$$\varphi_s = -\frac{kT_{es}}{e} \ln\left(\frac{4v_B}{\bar{v}_{es}}\right). \quad (15)$$

Since $v_B \ll \bar{v}_{es}$ the value of φ_s is positive in order to decrease the electron flux $n_{es}\bar{v}_{es}/4$ to the value of ion flux.

Temperature of heavy particles is equal to the temperature of the particle surface

$$T_h(a + l_{sh}) = T_s. \quad (16)$$

There is an energy flux from plasma to the particle, thus, in general, T_s is a function of time. Since the characteristic time for plasma parameter establishment is much shorter than the time for a temperature change of the particle surface [22], we can consider the temperature of the particle surface as constant and study the stationary distribution of plasma characteristics near the particle.

The boundary condition for the electron temperature is determined by the electron heat flux. The electron heat flux from the sheath outer boundary to the particle is

$$q_{es} = n_{es} \int d\mathbf{v} v_n \frac{m_e v^2}{2} f_s(\mathbf{v}) = n_{es} \int_{-\infty}^{v_{n0}} dv_n \int d\mathbf{v}_t v_n \frac{m_e}{2} (v_n^2 + v_t^2) f_{sn}(v_n) f_{st}(\mathbf{v}_t) =$$

$$n_{es} \int_{-\infty}^{v_{n0}} dv_n f_{sn}(v_n) v_n \left(\frac{m_e v_n^2}{2} + kT_{es} \right) = J_{es} (e\varphi_s + 2kT_{es}). \quad (17)$$

It should be equal to the electron heat flux from plasma to S , that gives the boundary condition

$$\left(q_e + \frac{5}{2} J_e kT_e \right)_{r=a+l_{sh}} = J_{es} (e\varphi_s + 2kT_{es}). \quad (18)$$

Thus, we have three conditions on the sheath outer boundary: (10), (16), and (18). Another set of conditions is determined far away from the particle where plasma is unperturbed, i.e. it is in thermal equilibrium $T_h|_{r=\infty} = T_e|_{r=\infty} = T_0$ and ionization equilibrium. The ratio between ion n_{i0} and atom n_{a0} number densities in the state of ionization equilibrium for quasineutral plasma ($n_{i0} = n_{e0}$) is defined by the Saha equation

$$n_{i0}^2/n_{a0} = S(T_0) = 12 \left(\frac{2\pi m_e kT_0}{h^2} \right)^{3/2} \exp\left(-\frac{U_i}{kT_0}\right), \quad (19)$$

which together with expression (3) for atom number density gives

$$n_{i0} = S(T_0) \left(\sqrt{1 + \frac{p_0}{S(T_0)kT_0}} - 1 \right). \quad (20)$$

For numerous practical applications, it is important to know the heat flux from plasma to the particle. The heat flux density on the particle surface q_p consists of the several components. The electron component can be determined from the following reasoning.

The electron velocity distribution function on the particle surface ($r = a$) is

$$f_a(\mathbf{v}) = f_{an}(v_n) f_{at}(\mathbf{v}_t), \quad (21)$$

where

$$f_{at}(\mathbf{v}_t) = \frac{m_e}{2\pi kT_{ea}} \exp\left(-\frac{m_e v_t^2}{2kT_{ea}}\right), \quad (22)$$

$$f_{an}(v_n) = \begin{cases} 0, & v_n > 0, \\ \sqrt{\frac{m_e}{2\pi kT_{ea}}} \exp\left(-\frac{m_e v_n^2}{2kT_{ea}}\right), & v_n < 0. \end{cases} \quad (23)$$

The electron heat flux on the particle surface is

$$q_{ea} = n_{ea} \int d\mathbf{v} v_n \frac{m_e v^2}{2} f_a(\mathbf{v}) = 2J_{ea} k T_{ea}. \quad (24)$$

Since the sheath is collisionless, then $J_{ea} = J_{es} = J_{is}$ and $T_{ea} = T_{es}$. Thus electron component of the heat flux on the particle surface is given by

$$q_{pe} = -2J_{is} k T_{es}. \quad (25)$$

Since J_{is} is negative (see Eq. (10)), the minus sign was added to ensure that q_{pe} is positive.

The difference between energy fluxes (18) and (24) equals to $J_{es} e \varphi_s$ it is due to electrons energy loss in the sheath electric field. On the other hand, ions gain additional energy $-J_{is} e \varphi_s$ from electric field in the sheath. Also, on the sheath outer boundary ions have directed velocity v_B and corresponding kinetic energy $m_i v_B^2/2$. Thus, the heat flux component due to the kinetic energy of heavy particles is

$$q_{ph} = \lambda_h \nabla T_h \big|_{r=a+l_{sh}} - J_{is} \left(e \varphi_s + \frac{m_i v_B^2}{2} \right). \quad (26)$$

When an ion reaches the particle surface, it recombines and releases energy equal to the ionization potential U_i . The corresponding heat flux component is

$$q_{pi} = -J_{is} U_i. \quad (27)$$

Finally, the total heat flux on the particle surface consists of the three components

$$q_p = q_{pe} + q_{ph} + q_{pi}. \quad (28)$$

4. RESULTS AND DISCUSSION

For spatial distributions of ion number density $n_i(r)$ and temperatures $T_h(r)$ and $T_e(r)$, the system of three differential equations (1), (7), and (9) was solved numerically on the segment $[a, b]$. Since $l_{sh} \ll a$, the left boundary of the computation segment was taken equal a . The right boundary $b \gg a$ is where plasma unperturbed, i.e. $n_i(b) = n_{i0}$ and $T_h(b) = T_e(b) = T_0$. Numerical calculations were performed using the FlexPDE program (ver.7.22) in which the finite element method is realized. The transport and kinetic coefficients used in the equations can be found in the appendix of [22]. Note that there is a misprint in equation (A19) of [22] for the energy exchange frequency; the correct formula is given in equation (19) of [27]. The dependence of these coefficients on T_e , T_h , and n_i was taken into account in the calculations, meaning that a fully nonlinear problem was solved.

The temperature distribution in plasma with $T_0 = 1.4$ kK near the particle with $T_s = 1$ kK is presented in figure 2a). According to boundary condition (16) the temperature of heavy particles (dashed line) is equal T_s for $r = a$. Due to heat transfer between heavy particles and electrons, their temperature also decreases. The electron temperature on the sheath outer boundary T_{es} is considerably less than T_0 , namely $T_{es} = 13070, 11465$ and 9212 K for $a = 10^{-5}, 10^{-4}$, and 10^{-3} m,

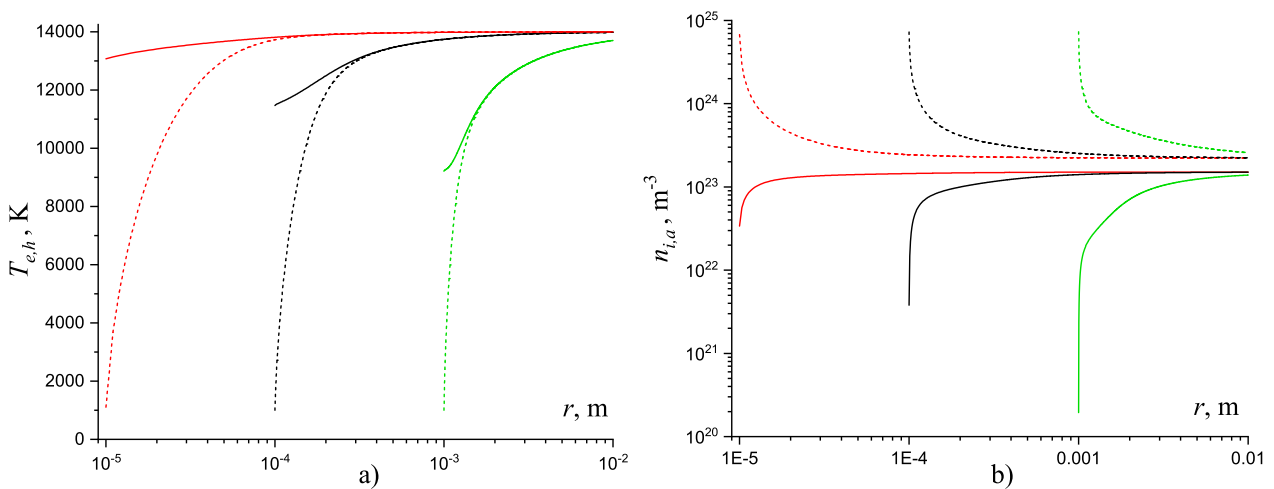


Figure 2. Spatial distributions of: a) electron temperature T_e (solid lines) and heavy particle temperature T_h (dashed lines), b) ion number density n_i (solid lines) and atom number density n_a (dashed lines), for $a = 10^{-5}, 10^{-4}$, and 10^{-3} m, $T_0 = 1.4$ kK and $T_s = 1$ kK

respectively. At some distance from the particle, plasma becomes isothermal $T_e = T_h$, however, the temperature is still less than T_0 . The decrease of electron temperature near the particle leads to the decrease of plasma ionization, i.e. to the decrease of n_i . This effect is more pronounced for larger particles (see solid lines in figure 2b). The ion number density on the sheath outer boundary is equal to $n_{is} = 3.35 \times 10^{22}$, 3.74×10^{21} and $1.92 \times 10^{20} \text{ m}^{-3}$ for $a = 10^{-5}$, 10^{-4} , and 10^{-3} m , respectively. Since the plasma pressure is constant, the decrease of n_i is compensated by the increase of atom number density n_a , see Eq. (3). The sheath potential is higher for smaller particles $\varphi_s = 5.23$, 4.58 and 3.67 V , respectively.

Table 1. Electron temperature T_{es} , ion number density n_{is} , Bohm velocity v_B , ion flux J_{is} , and potential φ_s on the sheath outer boundary S , heat fluxes from plasma to the particle surface q_p and heat power $4\pi a^2 q_p$ for various unperturbed plasma temperatures $T_0 = 6 - 18 \text{ kK}$, $a = 10^{-4} \text{ m}$, and $T_s = 1 \text{ kK}$.

T_0 (kK)	T_{es} (kK)	n_{is} (m^{-3})	v_B (m/s)	J_{is} ($\text{m}^{-2}\text{s}^{-1}$)	φ_s (V)	q_p (W/m^2)	$4\pi a^2 q_p$ (W)
6	5.920	2.34×10^{17}	1200	-2.81×10^{20}	2.35	5.04×10^6	0.634
8	7.770	1.46×10^{19}	1351	-1.98×10^{22}	3.09	8.68×10^6	1.09
10	9.300	1.89×10^{20}	1464	-2.76×10^{23}	3.71	1.55×10^7	1.95
12	10.500	1.11×10^{21}	1547	-1.72×10^{24}	4.19	3.16×10^7	3.97
14	11.470	3.74×10^{21}	1611	-6.03×10^{24}	4.58	6.40×10^7	8.04
16	12.250	7.64×10^{21}	1660	-1.27×10^{25}	4.90	1.05×10^8	13.2
18	12.980	1.12×10^{22}	1706	-1.91×10^{25}	5.19	1.43×10^8	18.0

The difference $T_0 - T_{es}$ grows with temperature of unperturbed plasma T_0 (see table 1). The ion number density on the sheath outer boundary n_{is} also grows with T_0 as well as the Bohm velocity. According to boundary condition (10) $J_{is} = -n_{is}v_{Bs}$, one can directly verify that this condition is satisfied. The ion flux density increases by five orders of magnitude as T_0 rises from 6 kK to 18 kK, while the sheath potential increases from 2.35 to 5.15 V.

The heat flux density and the heat power on the particle surface are presented in the last two columns in table 1 and in figure 3. For $T_0 \leq 10 \text{ kK}$, the total heat flux is almost entirely provided by the kinetic energy of heavy particles q_{ph} (26). For $T_0 > 10 \text{ kK}$, the heat flux due to recombination of ion on the particle surface q_{pi} becomes significant that is explained by the substantial increase of J_{is} . The electron heat flux is minor in the considered temperature range.

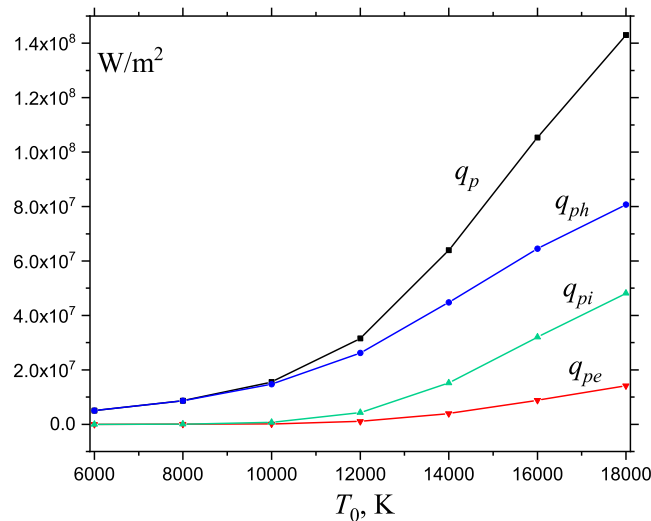


Figure 3. The heat flux on the particle surface q_p and its components q_{ph} (26), q_{pi} (27), and q_{pe} (25)

5. CONCLUSIONS

The electron heat flux at the outer boundary of the sheath, which is formed near charged spherical particle, is given by $J_{es}(2kT_{es} + e\varphi_s)$, where J_{es} is the electron flux density, T_{es} is the electron temperature, and φ_s is the sheath potential. Electrons transfer part of their energy to the electric field in the sheath and their heat flux on the particle surface becomes equal to $2J_{es}kT_{es}$ (assuming that electron flux and temperature are constant within the sheath).

The electron temperature near the particle surface is lower than the temperature of unperturbed plasma. The difference $T_0 - T_{es}$ increases with T_0 and it reaches $\approx 5 \text{ kK}$ for $a = 10^{-4} \text{ m}$ and $T_0 = 18 \text{ kK}$. In contrast, for $T_0 = 6 \text{ kK}$ $T_{es} \approx T_0$.

The heat flux from plasma to the particle surface depends non-linearly on T_0 . The increase of temperature from 6 K to 18 K leads to the increase of q_p almost in 30 times. The main contribution to the heat flux comes from the kinetic energy of heavy particles, while the contribution from electron kinetic energy reaches a maximum of approximately 10% at $T_0=18$ K. The energy released by ions during their recombination on the particle surface becomes significant for $T_0 > 10$ K accounting for up to one-third of the total heat flux at $T_0=18$ K.

Acknowledgments

This work was supported by Guangdong Academy of Sciences Project of Science and Technology Development (2020GDASYL-20200301001), The National Key Research and Development Program of China (grant number 2020YFE0205300), and Science and Technology Planning Project of Guangdong Province (2022B1212050001).

ORCID

 Shiyi Gao, <https://orcid.org/0009-0002-7627-3040>;  Andrii Momot, <https://orcid.org/0000-0001-8162-0161>
 Igor Krivtsun, <https://orcid.org/0000-0001-9818-3383>;  Danylo Antoniv, <https://orcid.org/0009-0009-4970-3616>
 Oksana Momot, <https://orcid.org/0009-0003-8528-8938>

REFERENCES




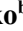


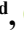

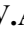
- [1] P.K. Shukla, and A.A. Mamun, *Introduction to Dusty Plasma Physics*, (CRC Press, Boca Raton, 2015). <https://doi.org/10.1201/9781420034103>
- [2] A. Melzer, *Physics of Dusty Plasmas*, (Springer, Cham, 2019). <https://doi.org/10.1007/978-3-030-20260-6>
- [3] J. Beckers, J. Berndt, D. Block, et al., *Phys. Plasmas*, **30**, 120601 (2023). <https://doi.org/10.1063/5.0168088>
- [4] M. Lampe, G. Joyce, G. Ganguli, and V. Gavrilchaka, *Phys. Plasmas*, **7**, 3851 (2000). <https://doi.org/10.1063/1.1288910>
- [5] O. Bystrenko, and A. Zagorodny, *Phys. Rev. E*, **67**, 066403 (2003). <https://doi.org/10.1103/PhysRevE.67.066403>
- [6] A.I. Momot, and A.G. Zagorodny, *Europhys. Lett.* **114**, 65004 (2016). <https://doi.org/10.1209/0295-5075/114/65004>
- [7] I.B. Denysenko, M. Mikikian, and N.A. Azarenkov, *Phys. Plasmas*, **29**, 093702 (2022). <https://doi.org/10.1063/5.0100913>
- [8] A.A. Mamun, and P.K. Shukla, *J. Plasma Phys.* **77**, 437 (2011). <https://doi.org/10.1017/S0022377810000589>
- [9] F. Verheest, *Waves in dusty space plasmas*, (Springer, Cham, 2012). <https://doi.org/10.1007/978-94-010-9945-5>
- [10] D.N. Gao, H. Zhang, J. Zhang, Z.Z. Li, and W.S. Duan, *Phys. Plasmas*, **24**, 043703 (2017). <https://doi.org/10.1063/1.4979354>
- [11] A.I. Momot, A.G. Zagorodny, and O.V. Momot, *Phys. Plasmas*, **25**, 073706 (2018). <https://doi.org/10.1063/1.5042161>
- [12] A.B. Murphy, and D. Uhrlandt, *Plasma Sources Sci. Technol.* **27**(6), 063001 (2018). <https://doi.org/10.1088/1361-6595/aabdc6>
- [13] M.I. Boulos, P.L. Fauchais, and E. Pfender, *Handbook of Thermal Plasmas*, (Springer, Cham, 2023). <https://doi.org/10.1007/978-3-030-84936-8>
- [14] A. Vardelle, C. Moreau, and J. Akedo, et al., *J. Therm. Spray Technol.* **25**, 1376 (2016). <https://doi.org/10.1007/s11666-016-0473-x>
- [15] M.I. Boulos, P.L. Fauchais, and J.V. Heberlein, *Thermal Spray Fundamentals: From Powder to Part*, (Springer, Cham, 2021). <https://doi.org/10.1007/978-3-030-70672-2>
- [16] L. Latka and P. Biskup, *Adv. Mater. Sci.* **20**, 39 (2020). <https://doi.org/10.2478/adms-2020-0009>
- [17] Z. Zhang, C. Wang, Q. Sun, S. Zhu, and W. Xia, *Plasma Chem. Plasma Process.* **42**, 939 (2022). <https://doi.org/10.1007/s11090-022-10250-6>
- [18] D. Stroganov, V. Korzhyk, Y. Jianglong, A.Y. Tunik, O. Burlachenko, and A. Alyoshyn, *The Paton Welding J.* (9), 51 (2022). <https://doi.org/10.37434/tpwj2022.09>
- [19] T. Lienert, T. Siewert, S. Babu, and V. Acoff, *Welding Fundamentals and Processes*, (ASM International, Ohio 2011). <https://doi.org/10.31399/asm.hb.v06a.9781627081740>
- [20] E. Leveroni and E. Pfender, *Int. J. Heat Mass Transfer*, **33**, 1497 (1990). [https://doi.org/10.1016/0017-9310\(90\)90046-W](https://doi.org/10.1016/0017-9310(90)90046-W)
- [21] V. Nemchinsky, *J. Phys. D*, **43**, 215201 (2010). <https://doi.org/10.1088/0022-3727/43/21/215201>
- [22] I.V. Krivtsun, A.I. Momot, D.V. Antoniv, and B. Qin, *Phys. Plasmas*, **30**, 043513 (2023). <https://doi.org/10.1063/5.0141015>
- [23] I.V. Krivtsun, A.I. Momot, D.V. Antoniv, and B. Qin, in: *Welding and Related Technologies*, edited by I.V. Krivtsun, et al., (CRC Press, London, 2025), pp. 129-135. <https://doi.org/10.1201/9781003518518-27>
- [24] I.V. Krivtsun, A.I. Momot, D.V. Antoniv, and S. Gao, *Plasma Chem. Plasma Proc.* **45**, (2025). <https://doi.org/10.1007/s11090-025-10554-3>
- [25] V.M. Zhdanov, *Transport Processes in Multicomponent Plasma*, (CRC Press, 2002).
- [26] N.A. Almeida, M.S. Benilov, and G.V. Naidis, *J. Phys. D*, **41**, 245201 (2008). <https://doi.org/10.1088/0022-3727/41/24/245201>
- [27] I.V. Krivtsun, A.I. Momot, I.B. Denysenko, O. Mokrov, R. Sharma, and U. Reisgen, *Phys. Plasmas*, **31**, 083505 (2024). <https://doi.org/10.1063/5.0216753>

**ВЗАЄМОДІЯ СФЕРИЧНОЇ ЧАСТИНКИ З БЕЗСТРУМОВОЮ АРГОНОВОЮ ПЛАЗМОЮ
АТМОСФЕРНОГО ТИСКУ****Шіі Гао^a, Андрій Момот^{b,c}, Ігор Кривцун^b, Данило Антонів^{b,c}, Оксана Момот^c**^a *Китайсько-український інститут зварювання академії наук провінції Гуандун,
вул. Чансін, 363, Тяньхе, Гуанчжоу, 510650, КНР*^b *Інститут електрозварювання ім. Є.О. Патона НАН України, вул. Казимира Малевича, 11, Київ, 03150, Україна*^c *Київський національний університет імені Тараса Шевченка, вул. Володимирська, 64/13, Київ, 01601, Україна*

Чисельно вивчалася взаємодія сферичної частинки радіусом $10^{-5} - 10^{-3}$ м з безструмовою аргоною плазмою атмосферного тиску в рамках гідродинамічного підходу. Нелінійна задача розв'язувалася з урахуванням температурної залежності транспортних і кінетичних коефіцієнтів. Використовувалася двотемпературна модель, яка враховує теплову та іонізаційну нерівноважність плазми поблизу частинки. Детально обговорюється гранична умова для теплового потоку електронів на зовнішній межі шару просторового заряду. Визначено та проаналізовано просторові розподіли характеристик плазми поблизу частинки, таких як температура та концентрація. Розраховано тепловий потік від плазми до частинки в широкому діапазоні температур однократно іонізованої аргонової плазми.

Ключові слова: *аргонова плазма атмосферного тиску; безструмова аргонова плазма; чисельне моделювання плазми; сферична частинка в плазмі; взаємодія плазма-частинка*

MULTILAYER WNbN/WNbC, WN/WC AND NbN/NbC COATINGS: VACUUM-ARC DEPOSITION STRATEGY AND MICROSTRUCTURE ASSESSMENT

 O.V. Maksakova^{a,b},  V.M. Beresnev^b,  S.V. Lytovchenko^b,  D.V. Horokh^b,  B.O. Mazilin^b,
 I.O. Afanasieva^{b,d},  M. Čaplovičová^c,  Martin Sahul^a,  V.A. Stolbovoy^d

^aInstitute of Materials Science, Slovak University of Technology in Bratislava, 25, Jána Bottu Str., 917 24 Trnava, Slovakia

^bV.N. Karazin Kharkiv National University, 4, Svobody Sq., 61000 Kharkiv, Ukraine

^cCentre for Nanodiagnostics of Materials, Slovak University of Technology in Bratislava, Vazovova 5, 812 43 Bratislava, Slovakia

^dNational Science Center «Kharkiv Institute of Physics and Technology», 1, Akademichna Str., Kharkiv, 61108, Ukraine

*Corresponding Author e-mail: s.lytovchenko@karazin.ua

Received December 19, 2024; revised January 21, 2025; accepted February 14, 2025

Abstract. Reactive gases such as nitrogen, oxygen, and carbon-based gases (e.g., acetylene) are introduced into the generated plasma flow to create coatings with chemical compounds including nitrides, oxides, and carbides. By managing the rate of gas addition, the stoichiometric composition of the material, which influences its crystal structure and range of properties, can be controlled. In light of this, the vacuum-arc PVD technique was utilised to deposit carbide/nitride multilayer coatings based on W and Nb in a dynamically changing atmosphere of nitrogen and acetylene gases. The two-channel control device – “evaporator-injector” – was employed to control the functions of vacuum-arc evaporators and the gas introduction ports in the vacuum chamber of the installation. The material of the substrates for the deposition of coatings was corrosion-resistant high-temperature steel (grade 12X18H9T). The W (99.97 wt.%) and Nb (98.2 wt.%) cathodes were produced through mechanical boring of ingots made from the respective metals obtained via electron beam re-melting. The present work reports on the deposition strategy of vacuum-arc multilayer WNbN/WNbC, WN/WC, and NbN/NbC coatings with nanometre layer thicknesses and a preliminary assessment of their microstructure. The multilayer systems presented have yet to be studied and hold considerable scientific interest regarding synthesis and experimental investigation.

Keywords: Ceramic coatings; Tungsten nitride; Tungsten carbide; Niobium nitride; Niobium carbide; Vacuum-arc; Microstructure

PACS: 68.55.Jk, 68.65.Ac

INTRODUCTION

Because of the ease of use and excellent properties, physical vapour deposition (PVD) techniques are the most preferred method for applying hard protective coatings. PVD works by atomizing or vaporizing coating atoms from a target, transporting them through a vacuum or plasma, and then condensing them onto the substrate. PVD's widespread adoption in the industry can be attributed to its energy and cost-effectiveness, eco-friendliness, lower deposition temperatures (below 500 °C), higher deposition rates (up to 10 nm/s), increased flexibility in coating design, and outstanding coating quality [1-4]. Generally, PVD is categorized based on how the coating atoms are ejected from the target, which includes evaporative and sputtering processes. The growth mechanisms of hard coatings rely significantly on deposition conditions, plasma kinetics, and the physiochemical properties of the source elements.

Figure 1 depicts the recent PVD techniques used to create hard coatings alongside the key deposition parameters that affect the coatings' characteristics and functionality. Of these, magnetron sputtering methods are the most common for hard coating fabrication, mainly because they enable precise control over stoichiometry, microstructure, mechanical properties, and the creation of highly dense, defect-free, uniform coatings by adjusting various processing parameters. These include ion energy, ion flux, sputtering power, substrate bias, gas flow rate, partial pressure, and substrate temperature [5]. Various advanced sputtering techniques, such as balanced magnetron sputtering, radio frequency sputtering, reactive sputtering, and high-power impulse magnetron sputtering, are commonly employed in fabricating hard coatings. Additionally, laser deposition (LD) methods, along with their hybrid combinations with magnetron sputtering, have gained traction for extreme environmental applications in recent years [6,7].

Nevertheless, evaporative PVD methods remain predominant in industrial coating production, owing to their higher ionisation and deposition rates, more uniform coatings, and less stringent vacuum requirements [1,2]. The PVD process based on evaporation can employ various heat sources such as resistance, induction, electron beam, and arc sources, including arc discharge, filtered cathodic vacuum arc (FCVA), electron beam PVD, and thermal evaporation. The limitations of resistance, induction, and electron beam evaporative PVD systems render arc evaporative PVD systems more appealing compared to their industrial counterparts. For instance, resistive systems face electron beam systems encounter gun deterioration and substrate geometry restrictions [8], induction systems tend to be expensive [9,10], and melting point limitations [11]. Furthermore, arc evaporation PVD systems provide increased versatility, superior ionisation, adaptable target configurations, and a high deposition rate [1,8].

Cite as: O.V. Maksakova, V.M. Beresnev, S.V. Lytovchenko, D.V. Horokh, B.O. Mazilin, I.O. Afanasieva, M. Čaplovičová, M. Sahul, V.A. Stolbovoy, East Eur. J. Phys. 1, 396 (2025), <https://doi.org/10.26565/2312-4334-2025-1-49>

© O.V. Maksakova, V.M. Beresnev, S.V. Lytovchenko, D.V. Horokh, B.O. Mazilin, I.O. Afanasieva, M. Čaplovičová, M. Sahul, V.A. Stolbovoy, 2025; CC BY 4.0 license

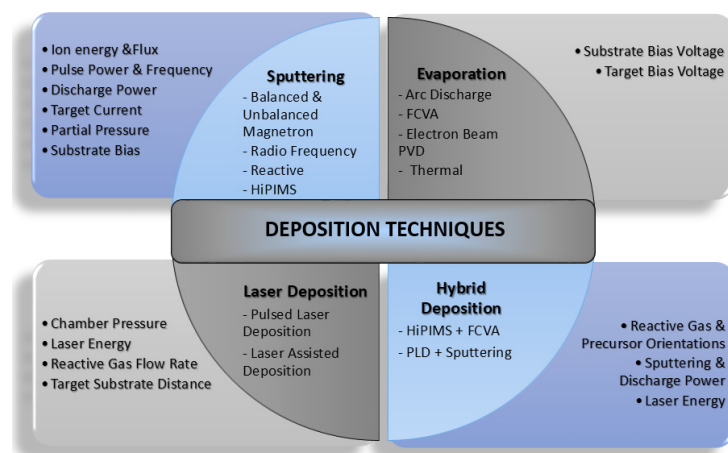


Figure 1. PVD methods to deposit hard coatings and the crucial process parameters for tuning the coating properties

Since commercialising the arc evaporation PVD technique in the early 1980s, researchers have made substantial technological advancements to enhance process efficiency and coating quality. Initial improvements focused on refining the quality and ionisation of coating materials [12]. These involved using higher-quality targets, employing high-purity reactive gases, and incorporating additional anode and plasma sources to boost the ionisation process [2,3] – subsequent enhancements centred on optimising deposition parameters. The key parameters significantly affecting defects include substrate bias, arc current, and reactive gas pressure. These studies indicated that optimising these factors is an auspicious, cost-effective, and practical approach to improving the stability and reliability of coatings suitable for large-scale industrial applications. Driven by technological advancements and increased market demand, the architecture of evaporated coatings has evolved into four distinct structures: mono, duplex, composite, functionally graded, and multilayer. These advancements have led to significant improvements in the tribological performance of coatings over time [13-15].

Numerous studies have shown that arc evaporation PVD multilayer architectures can be tailored to optimise the tribomechanical properties of coatings for complex technological applications [16-20]. Firstly, these multilayers prevent crack propagation at multiple-layer interfaces and across grain boundaries. Secondly, they combine the properties of each individual layer into a new structure with unique, enhanced characteristics. For example, one layer can have a low coefficient of friction, high hardness, and resistance to high-temperature oxidation, reducing friction and preventing cracks. In contrast, another layer provides high adhesion, plasticity, and elasticity, boosting the coating's mechanical strength. The simultaneous function of these layers gives the multilayer structure a distinctive range of properties, effectively preventing early failure of the coating. Additionally, the multilayer architecture significantly changes the wear mechanism due to transition zones between adjacent layers, which can hinder crack propagation and reduce stress. While this research area is advancing, there is an ongoing need to improve the structure and properties of these coatings. This drives the search for new protective coating compositions that can meet modern requirements, especially those that maintain the structural integrity of coated products under high mechanical stresses and temperatures, thereby extending their operational lifespan.

Despite the ongoing evolution of this research domain, there remains a continual need to improve the structure and properties of arc evaporated PVD multilayer coatings. A discernible trend has developed in the past decade towards increasingly complex compositions within the resultant coatings. The integration of novel metallic and gaseous components into vacuum arc coating, along with the addition of supplementary layers possessing unique physical and mechanical characteristics, necessitates the modernization of current equipment and the advancement of new programmable devices to expand the variety of coatings produced.

Functional Structure of the Device for Deposition of Arc Evaporated PVD Simple and Complex Composition Multilayer Coatings

Figure 2 illustrates the upgraded arc evaporated PVD system designed to synthesize multilayer coatings with simple and complex compositions. A feature of the update to the classic equipment is the addition of a two-channel control device, termed the “evaporator-injector” [21]. Channel 1 manages the operation of vacuum-arc evaporators, whereas Channel 2 governs the operation of gas starters. Consequently, operating two evaporators and two gas starters is feasible. The device comprises five blocks on separate boards: a device control unit, a relay switch circuit, a data input panel, a display panel, and a power supply. The central component of the device is a control unit built on a low-power 8-bit Atmel microcontroller. The relay switch circuit is designed to activate or deactivate each channel within a specified time frame. Setting the time parameters for the device's channels and selecting the mode and cycle of the control device's operation is accomplished manually via the control elements. Thus, the thickness of the vacuum-arc coating layers, along with the sequence of their application, can be regulated through the modes and duration of operation of the channels of the “evaporator-injector” control device.

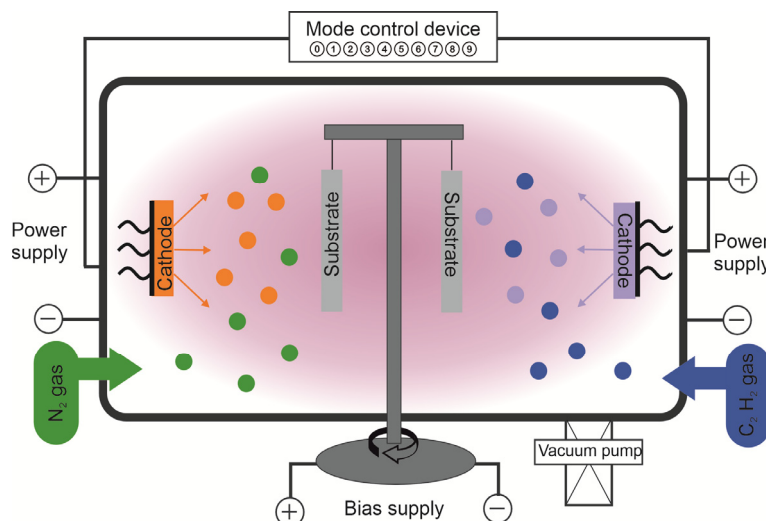


Figure 2. Schematic view of the arc evaporated PVD unit used to synthesize complex multilayer coatings

The “evaporator-injector” has 10 modes (modes 0–9). The time intervals for the operation of vacuum-arc evaporators and gas starters are set by parameters t_1 – t_4 . Here are details about the operating modes [21]:

1) Mode 0. Two vacuum-arc evaporators are activated alternately, while gas is continuously supplied to the vacuum chamber by one of the gas G injectors. The operating time of the evaporators is defined by time parameters t_1 for cathode 1 (metal 1 – Me_1) and t_2 for cathode 2 (metal 2 – Me_2). This operating mode permits the production of simple Me_1G/Me_2G -type multilayer coatings, such as TiN/ZrN or TiC/ZrC.

2) Mode 1. The first vacuum-arc evaporator operates continuously. The operating time of the second evaporator is determined by the time parameters: t_1 – the duration of the evaporator's off state, and t_2 – the duration of the evaporator's on state. Gas is continuously supplied to the vacuum chamber through one of the gas injectors. Consequently, the thickness of the Me_1G layer relies on the parameter t_1 , while the parameter t_2 governs the thickness of the Me_1Me_2G layer. This operating mode allows for the production of simple Me_1G/Me_1Me_2G type multilayer coatings, such as TiN/TiZrN or TiC/TiZrC.

3) Mode 2. Both channels (the vacuum-arc evaporator and gas injector control channels) operate synchronously. The operational duration of the evaporators and gas injectors is specified by the time parameters t_1 (cathode 1 – Me_1 , gas 1 – G_1) and t_2 (cathode 2 – Me_2 , gas 2 – G_2). This operating mode allows for producing simple Me_1G_1/Me_2G_2 -type multilayer coatings, such as TiN/ZrC or ZrN/TiC.

4) Mode 3. The first vacuum-arc evaporator (cathode 1 – Me_1) operates continuously, with gas (G_1) constantly supplied through the initial gas inlet. The operating time of the second evaporator (cathode 2 – Me_2) and the gas supply duration (G_2) through the second inlet are determined by time parameters: t_1 – duration of the off state of the vacuum-arc evaporator and inlet, t_2 – duration of the on state of the evaporator and inlet. Employing this operating mode enables the creation of simple multilayer coatings composed of compounds of the type $Me_1G_1/Me_1Me_2G_1G_2$, such as TiN/TiZrNC.

5) Mode 4. Channel 1 (cathode 1 – Me_1 and cathode 2 – Me_2) operates in mode 0, meaning the vacuum-arc evaporators are activated alternately. The duration of the evaporators is regulated by time parameters: t_1 – duration of the on state of the first evaporator, t_2 – duration of the on state of the second evaporator. Channel 2 (injector 1 – gas 1 (G_1) and injector 2 – gas 2 (G_2)) operates in mode 1, meaning gas 1 (G_1) is continuously supplied through the first gas inlet while gas 2 (G_2) is provided for the duration t_2 of the operation of the second evaporator (cathode 2 – Me_2). Using this operating mode facilitates the attainment of simple multilayer coatings composed of $Me_1G_1/Me_2G_1G_2$ type compounds, such as TiN/ZrCN.

6) Mode 5. Channel 1 (cathode 1 – Me_1 and cathode 2 – Me_2) operates in mode 1, i.e. the first vacuum arc evaporator (cathode 1 – Me_1) operates continuously, while the second vacuum arc evaporator (cathode 2 – Me_2) is activated for time t_2 . Channel 2 (injector 1 – gas 1 and injector 2 – gas 2) functions in mode 0, meaning the injectors are switched on alternately. The operational duration of each gas injector is defined by the time parameters: t_1 – the duration of the activated state of the first gas injector, and t_2 – the duration of the activated state of the second gas injector. This operating mode facilitates the production of $Me_1G_1/Me_1Me_2G_2$ -type multilayer coatings, such as TiC/TiZrN.

7) Mode 6. From this operating mode onwards, the device employs two timers: t_3 and t_4 . Both channels operate in mode 0. The duration of operation for each vacuum-arc evaporator and gas injector is governed by the following time parameters: t_1 – duration of the on-state of the first evaporator, t_2 – duration of the on-state of the second evaporator, t_3 – duration of the on-state of the first gas injector, t_4 – duration of the on-state of the second gas injector. The operational time parameters are selected as follows: $t_3 = t_1 + t_2$, $t_4 = n(t_1 + t_2) = nt_3$, where $n = 1$. Utilizing this operating mode allows for the production of complex multilayer coatings of $Me_1G_1/Me_2G_1/[Me_1G_2/Me_2G_2/Me_1G_2/Me_2G_2/...]$ -type, such as TiN/ZrN/[TiC/ZrC/TiC/ZrC/...].

8) Mode 7. Both channels operate synchronously. Channel 1 (cathode 1 – Me₁ and cathode 2 – Me₂) operates in mode 0, which means the vacuum-arc evaporators are activated alternately. The duration of the evaporators is determined by the time parameters: t_1 – the duration of the first evaporator's active state and t_2 – the duration of the second evaporator's active state. Channel 2 (injector 1 – gas 1 and injector 2 – gas 2) operates in mode 1, indicating that gas 1 is supplied continuously through the first gas injector, while the duration of the second gas injector is defined by the time parameters: t_3 – the duration of the second injector's inactive state and t_4 – the duration of the second injector's active state. Utilizing this operating mode permits the production of complex multilayer coatings from compounds of Me₁G₁/Me₂G₁/[Me₁G₁G₂/Me₂G₁G₂/Me₁G₁G₂/Me₂G₁G₂/...] -type, such as TiC/ZrC/[TiCN/ZrCN/TiCN/ZrCN/...].

9) Mode 8. Both channels operate synchronously. Channel 1 (cathode 1 – Me₁ and cathode 2 – Me₂) functions in mode 1, meaning the first vacuum-arc evaporator (cathode 1 – Me₁) operates continuously, while the operational duration of the second evaporator (cathode 2 – Me₂) is determined by the time parameters: t_1 – the duration of the second evaporator's inactive state and t_2 – the duration of its active state. Channel 2 (injector 1 – gas 1 and injector 2 – gas 2) operates in mode 0, indicating that the injectors are activated sequentially. The time parameters establish the operational duration of each gas starter: t_3 – the active state of the first injector and t_4 – the active state of the second injector. Employing this operating mode enables the acquisition of complex multilayer coatings of Me₁G₁/Me₁Me₂G₁/[Me₁G₂/Me₁Me₂G₂/Me₁G₂/Me₁Me₂G₂/...] -type, for example, TiC/TiZrC/[TiN/TiZrN/TiN/TiZrN/...].

10) Mode 9. Both channels operate synchronously in mode 1. Channel 1 (cathode 1 – Me₁ and cathode 2 – Me₂) functions in mode 1, meaning the first vacuum-arc evaporator operates continuously, while the operation duration of the second evaporator is determined by the time parameters: t_1 – duration of the off state of the second evaporator, and t_2 – duration of the on state of the second evaporator. Channel 2 (injector 1 – gas 1 and injector 2 – gas 2) also operates in mode 1, which indicates that gas 1 is supplied continuously through the first gas injector, with the operation duration of the second gas injector defined by the time parameters: t_3 – duration of the off state of the second injector, and t_4 – duration of the on state of the second injector. In this device's operating mode, various control algorithms can be implemented by setting the time parameters. Here are two of the most noticeable algorithms. The first one when $t_1 = t_3$ and $t_2 = t_4$. Employing this operational algorithm enables the production of multilayer coatings of Me₁G₁/Me₁Me₂G₁G₂ -type, such as TiC/TiZrCN. The second one is when the time parameters of the device operation are chosen as follows: $t_3 = t_1 + t_2$, $t_4 = n(t_1 + t_2) = nt_3$. Utilising this operational algorithm enables the achievement of complex multilayer coatings from compounds of this type. Me₁G₁/Me₁Me₂G₁/[Me₁G₁G₂/Me₁Me₂G₁G₂/Me₁G₁G₂/Me₁Me₂G₁G₂/...], for instance, TiC/TiZrC/[TiCN/TiZrCN/TiCN/TiZrCN/...].

The initial results from operating the developed device in the laboratory for intensive ion-plasma technology research at the National Research Centre Kharkov Institute of Physics and Technology (KIPT) of the NAS of Ukraine confirmed its technical specifications.

EXPERIMENTAL PROCEDURE

Deposition

Using a two-channel control device enabled the fabrication of multilayer vacuum-arc WNbN/WNbC, WN/WC and NbN/NbC coatings. The coatings were obtained through the vacuum-arc evaporation of two tungsten (W) and niobium (Nb) cathodes, positioned on the same horizontal level at an angle of 90 degrees to one another in an upgraded Bulat-6 type installation. The cathodes were made by mechanical boring from ingots of the corresponding metals obtained by electron beam re-melting. The starting components of re-melting were pure tungsten (W content not less than 99.97 wt.%) and technical niobium (Nb content not less than 98.2 wt.%, main impurity Zr with the content between 1-1.4 wt.%).

Table 1. Technological parameters of coating deposition.

No.	Coating composition	I _d , A	I _f , A	U _b , V	Gas	P, Pa	T, h	Notes
1	2	3	4	5	6	7	8	9
1	WNbN/WNbC	130/120	0.5/0.5	200	N/C ₂ H ₂	0.4	1.0	VR: C ₂ H ₂ -10 s, N - 50 s
2	WNbN/WNbC	150/110	0.5/0.5	200	N/C ₂ H ₂	0.4	0.8	VR: C ₂ H ₂ - 5 s, N - 55 s
3	WNbN/WNbC	150/115	0.5/0.5	120	N/C ₂ H ₂	0.4	1.0	VR: C ₂ H ₂ - 5 c, N - 90 c
4	NbN/NbC	120	1.0	220	N/C ₂ H ₂	0.4	1.0	VR: C ₂ H ₂ - 5 s, N - 55 s
5	WN/WC	170	1.0	220	N/C ₂ H ₂	0.4	1.0	VR: C ₂ H ₂ - 5 s, N - 55 s

Explanation of table columns:

1 – the number of the series of samples;

2 – the elemental composition of the coating;

3 – I_d, is the value of the cathodic arc current;

4 – I_f, is the value of the current of the focusing coils on the corresponding cathode;

5 – U_b, is the value of the negative bias voltage (potential) applied to the substrate;

6 – the composition of the reaction gas in the deposition chamber (nitrogen N or acetylene C₂H₂);

7 – P is the value of the reaction gas pressure in the deposition chamber;

8 – T is the duration of the coating deposition process (measured in hours);

9 – the notes explaining the sample rotation characteristics and exposure time near the appropriate evaporator or with the proper reaction gas in the chamber, seconds: CR – constant rotation, VR – variable rotation.

The stainless-steel plates of 12X18H9T (corrosion-resistant high-temperature steel, analogue to AISI321 (USA)) were used as substrates. The size of each sample was 15 mm × 15 mm × 2.5 mm. The surface of the substrates before coating deposition was prepared in several stages. The first stage involved mechanical grinding and polishing, executed with abrasive materials of varying grain sizes on a paper or fabric base, while employing forced cooling with water on a manual grinding and polishing device. The second stage consisted of mechanical fine polishing using diamond pastes with diamond particle dispersion ranging from 6 μm to 0.1 μm. After the mechanical processing to remove any grease and impurities, the samples were washed in isopropyl alcohol. The third sample preparation stage was plasma-electrolytic polishing in an electrolyte from an aqueous solution (3 wt.%) of ammonium sulfate (NH₄)₂SO₄. Such polishing clearly leads to a loss of sample mass, but the amount of such loss does not exceed 0.2 mg/cm². In the end, the last stage of preparing the substrate surface – ion bombarding – was applied. The vacuum chamber was evacuated to a pressure of 0.001 Pa. Then a negative bias potential of 1000 V was applied to the substrate holder, which cleaned and activated the surface of the substrates by bombarding it with metal ions emitted from the evaporator cathode. The duration of bombarding was around 5 minutes. After the cleaning operation was completed, the bias voltage was reduced to the value necessary to deposit the coating of the selected type and composition.

The vacuum chamber of the arc installation has cylindrical form, with an internal diameter of 600 mm and a height of 800 mm. This, a vacuum chamber volume is approximately 0.22 m³. As demonstrated in the experiment, the installation's pumping system efficiently reduced the working gas pressure from 0.4 Pa to a residual vacuum value of 1·10⁻³ Pa within 1 second, ensuring a swift and reliable process. The accuracy of setting the internal channel switching time of the developed two-channel control device is 1 second. The interval between deactivating one of the gas injectors and activating the other is approximately 1 second. This duration is sufficient to reduce the pressure in the vacuum chamber to the ultimate residual value of 0.001 Pa. Given these parameters, the proximity of both gases in the chamber during the coating process is unlikely. When producing a multilayer coating, the pumping speed of the chamber was monitored by observing the current pressure value using a vacuum gauge. For the formation of the carbide layer WNbC, WC, and NbC, the acetylene (C₂H₂) was introduced into the vacuum chamber and dissociated during the coating process. We maintained a strict control over the pressure of reaction gases in the vacuum chamber, ensuring stability and quality in the process.

Equipment and Procedure of Microstructure Analysis

The morphology and cross-sections of multilayer vacuum-arc WNbN/WNbC, WN/WC and NbN/NbC coatings were examined using the JEOL JSM 7600F high-resolution field emission scanning electron microscope (FE-SEM, JEOL Ltd., Tokyo, Japan) in secondary electron (SE) imaging mode. The microscope operated within an accelerating voltage range of 20-30 kV, with a magnification capability of up to 100,000 times. The maximum resolution of the raster microscope reached 2.5 nm at an accelerating voltage of 30 kV.

To obtain precise results from the SEM technique, we adhered to the author's methodology for specimen preparation. Specifically, the coatings' cross-section was prepared using a mechanical polishing method. Specimens measuring approximately 20 mm in length and 4 mm in width were cut from bulk samples employing a diamond wire-cutting machine. These specimens were then embedded in phenolic resin and ground down to #1200 using silicon carbide (SiC) abrasive grit paper. Subsequently, they were polished with diamond suspensions featuring particle sizes of 1, 3, and 6 microns, and finally rinsed with distilled water before being dried with warm air. This methodology enabled us to create mirror-like cross-sectional specimens and capture high-quality images of the coatings and the substrate. Figure 3 presents images illustrating the SEM's specimen preparation process.

The ImageJ software was utilized for the SEM image analysis. In summary, the obtained images were transferred into ImageJ and analyzed using two distinct techniques: the first employed 8 bits (designated as 8B) and the second referred to as "R G B" (Red, Green, Blue colors). These techniques were utilized to detail the features of typical structural defects (macroparticles, pores, inclusions, etc.) including their locations, quantities, and areas (maximum, minimum, and mean).

RESULTS AND DISCUSSION

Figure 3 illustrates the typical view of the surface and cross-section of multilayer vacuum-arc WNbN/WNbC coatings. Evidence of the intercolumnar fracture of the upper layer can be seen in the coating's surface. The coating exhibits a well-defined layered structure with dense growth. Light grey layers are attributed to the WNbN, whereas dark grey layers correspond to the WNbC. The subtle zigzag shape of the layers results from applying negative substrate bias during deposition, causing ion bombardment on the WNbN/WNbC layers while the added atoms advance to the substrate surface [22]. In work [23] observed that sputtered layers exhibit a cupola-like microstructure at a working pressure of 0.67 Pa without substrate bias. In contrast, work [24] reported a wave-like layer structure arising from the kinetic energy of the incident ionic species influenced by the rf-bias, which enhances the velocity and surface mobility of the ad-atoms, consequently impacting the crystalline structure. The cross-section image allows for measuring the coating's total thickness, which is 568.7 nm.

The impact of hydrogen, which emerges during the dissociation process, on the properties of vacuum-arc coatings is presently insufficiently studied due to the specificities inherent in the technology utilized for their production. Historically, nitrogen was used as the reaction gas to create vacuum-arc coatings. Exploring alternative gases – namely

oxygen and acetylene – is in its early stages. A thorough analysis of the characteristics exhibited by the produced coatings leads to the conclusion that the potential impact of hydrogen on their properties, as observed in our experiments, is relatively minimal. This conclusion is supported by the observation that the coating displays a qualitatively dense structure in cross-section.

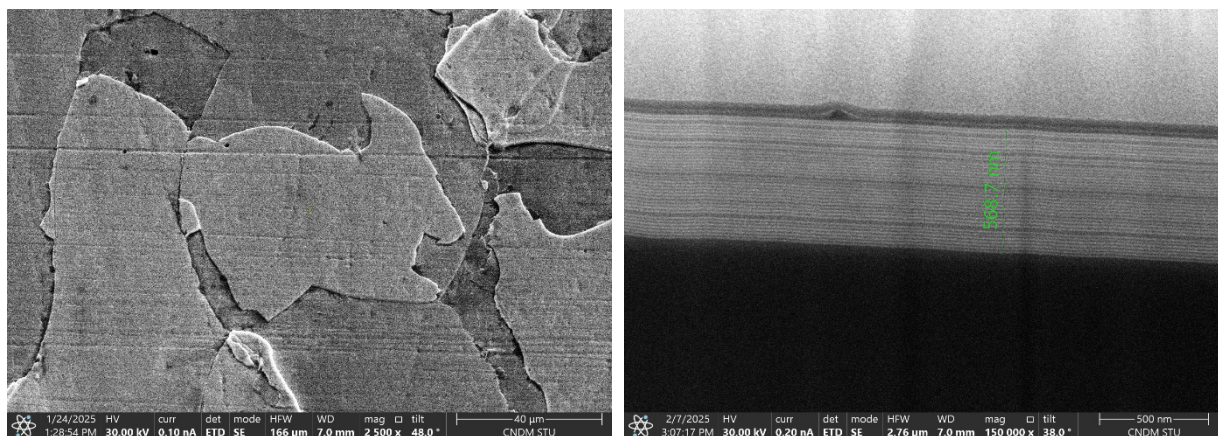


Figure 3. SEM images of the surface and cross-sections of multilayer vacuum-arc WNbN/WNbC coatings and the total coating thickness

CONCLUSIONS

To enhance the chances of synthesis of both simple and complex multilayer vacuum-arc coatings within one technological deposition cycle of arc evaporation PVD technology, a two-channel control device – “evaporator-injector” – was created to control the functions of vacuum-arc evaporators and the gas introduction ports in the vacuum chamber of the Bulat-6 installation.

This device enabled the production of multilayer vacuum-arc coatings such as WNbN/WNbC, WN/WC, and NbN/NbC, all of which feature nanometer thickness and excellent structural integrity.

Acknowledgments

This project has received funding through the EURIZON project, which is funded by the European Union under grant agreement No.871072. Additional funding was received from the EU NextGenerationEU through the Recovery and Resilience Plan for Slovakia under the project No. 09I03-03-V01-00028.

ORCID

- O.V. Maksakova, <https://orcid.org/0000-0002-0646-6704>; V.M. Beresnev, <https://orcid.org/0000-0002-4623-3243>
 S.V. Lytovchenko, <https://orcid.org/0000-0002-3292-5468>; D.V. Horokh, <https://orcid.org/0000-0002-6222-4574>
 B.O. Mazilin, <https://orcid.org/0000-0003-1576-0590>; I.O. Afanasieva, <https://orcid.org/0000-0002-9523-9780>
 M. Čaplovičová, <https://orcid.org/0000-0003-4767-8823>; M. Sahul, <https://orcid.org/0000-0001-9472-500X>
 V.A. Stolbovoy, <https://orcid.org/0000-0001-7734-0642>

REFERENCES

- [1] D.M. Mattox, *Handbook of Physical Vapor Deposition (PVD) Processing*; (Elsevier Science & Technology Books: Amsterdam, The Netherlands, 2007).
- [2] A. Baptista, F.J.G. Silva, J. Porteiro, J.L. Míguez, and G. Pinto, “Sputtering Physical Vapour Deposition (PVD) Coatings: A Critical Review on Process Improvement and Market Trend Demands,” *Coatings*, **8**, 402 (2018). <https://doi.org/10.3390/coatings8110402>
- [3] Y. Deng, W. Chen, B. Li, C. Wang, T. Kuang, and Y. Li, “Physical vapor deposition technology for coated cutting tools: A review,” *Ceram. Int.* **46**, 18373–18390 (2020). <https://doi.org/10.1016/j.ceramint.2020.04.168>
- [4] A. Pak, M. Masoudi, and H. Elmkhah, “Effect of ultrasonic peening on the surface properties of nano-layered CrN/CrAlN coating deposited by CAPVD method on D3 tool steel,” *Surf. Interfaces*, **28**, 101618 (2021). <https://doi.org/10.1016/j.surf.2021.101618>
- [5] K.S. Lim, Y.S. Kim, S.H. Hong, G. Song, and K.B. Kim, “Influence of N₂ Gas Flow Ratio and Working Pressure on Amorphous Mo–Si–N Coating during Magnetron Sputtering,” *Coatings*, **10**, 34 (2020). <https://doi.org/10.3390/coatings10010034>
- [6] M.R. Alhafian, J.B. Chemin, Y. Fleming, L. Bourgeois, M. Penoy, R. Useldinger, F. Soldera, *et al.*, “Comparison on the Structural, Mechanical and Tribological Properties of TiAlN Coatings Deposited by HiPIMS and Cathodic Arc Evaporation,” *Surf. Coat. Technol.* **423**, 127529 (2021). <https://doi.org/10.1016/j.surfcoat.2021.127529>
- [7] B.C.N.M. de Castilho, A.M. Rodrigues, P.R.T. Avila, R.C. Apolinario, T. de Souza Nossa, M. Walczak, *et al.*, “Hybrid Magnetron Sputtering of Ceramic Superlattices for Application in a next Generation of Combustion Engines,” *Sci. Rep.* **12**, 2342 (2022). <https://doi.org/10.1038/s41598-022-06131-9>
- [8] A. Jacob, *Effect of Micro-blasting on Characteristics and Machining Performance of PVD AlTiN Coated Cutting Tools*; *Master of Technology*; (National Institute of Technology: Rourkela, India, 2015).
- [9] J.Y. Sheikh-Ahmad, and T. Morita, “Tool coatings for wood machining: Problems and prospects,” *For. Prod. J.* **52**, 43–51 (2002).

- [10] S. Grundas, *Advances in Induction and Microwave Heating of Mineral and Organic Materials*, (IntechOpen, Rijeka, Croatia, 2011).
- [11] K. Holmberg, and A. Mathews, *Coatings Tribology—Properties, Mechanisms, Techniques and Application in Surface Engineering*, 2nd ed. (Elsevier: Amsterdam, The Netherlands, 2009).
- [12] I.I. Aksenov, A.A. Andreev, V.A. Belous, V.E. Strel'nitsky, and V.M. Khoroshikh, *Vacuum Arc: Plasma Sources, Coating Deposition, Surface Modification*, (Naukova Dumka, Kyiv, 2012).
- [13] X. Li, et al., "Cathodic arc evaporation for hard and decorative coatings: A review." *Surface Engineering*, **34**(8), 553-570 (2018). <https://doi.org/10.1080/02670844.2017.1397537>
- [14] J.C. Sánchez-López, et al., "A review on superhard nanocomposite coatings: Recent progress and future directions." *Materials Science and Engineering: R: Reports*, **91**, 1-46 (2015). <https://doi.org/10.1016/j.mser.2015.02.001>
- [15] D. Depla, et al., "Comparison of reactive magnetron sputtering and cathodic arc deposition for the synthesis of TiN and TiAlN thin films." *Thin Solid Films*, **519**(15), 5047-5054 (2011). <https://doi.org/10.1016/j.tsf.2010.12.122>
- [16] B.K. Rakhadilov, O.V. Maksakova, D.B. Buitkenov, M.K. Kylyshkanov, A.D. Pogrebnyak, V.P. Antypenko, Ye.V. Konoplianchenko, "Structural-phase and tribo-corrosion properties of composite Ti₃SiC₂/TiC MAX-phase coatings: an experimental approach to strengthening by thermal annealing", *Appl. Phys. A*, **128**, 145 (2022). <https://doi.org/10.1007/s00339-022-05277-7>
- [17] M. Beresnev, S.V. Lytovchenko, O.V. Maksakova, A.D. Pogrebnyak, V.A. Stolbovoy, S.A. Klymenko, and L.G. Khomenko, "Microstructure and high-hardness effect in WN-based coatings modified with TiN and (TiSi)N nanolayers before and after heat treatment: experimental investigation," *High Temperature Material Processes*, **25**(4), 61–72 (2021). <https://doi.org/10.1615/HighTempMatProc.2021041565>
- [18] O.V. Maksakova, S. Zhanyssov, S.V. Plotnikov, P. Konarski, P. Budzynski, A.D. Pogrebnyak, V.M. Beresnev, et al., "Microstructure and tribomechanical properties of multilayer TiZrN/TiSiN composite coatings with nanoscale architecture by cathodic-arc evaporation," *J. Mater. Sci.* **56**, 5067–5081 (2021). <https://doi.org/10.1007/s10853-020-05606-2>
- [19] C. Ducros, and F. Sanchette, "Multilayered and nanolayered hard nitride thin films deposited by cathodic arc evaporation. Part 2: Mechanical properties and cutting performances," *Surface and Coatings Technology*, **201**(3-4), 1045-1052 (2006). <https://doi.org/10.1016/j.surfcoat.2006.01.029>
- [20] Y.X. Ou, J. Lin, S. Tong, W.D. Sproul, and M.K. Lei, "Structure, adhesion and corrosion behavior of CrN/TiN superlattice coatings deposited by the combined deep oscillation magnetron sputtering and pulsed dc magnetron sputtering," *Surf. Coat. Technol.* **293**, 21–27 (2016). <https://doi.org/10.1016/j.surfcoat.2015.10.009>
- [21] I.V. Serdiuk, V.O. Stolbovyi, A.V. Dolomanov, and V.M. Domnich, "Modernization of Vacuum-Arc Deposition Technology of Multilayer Nanostructured Coatings," *Metallofiz. Noveishie Tekhnol.* **44**(4), 547–563 (2022). (in Ukrainian). <https://doi.org/10.15407/mfint.44.04.0547>
- [22] J. Xu, T. He, L. Chai, L. Qiao, P. Wang, and W. Liu, "Growth and characteristics of self-assembled MoS₂/Mo-S-C nanoperiod multilayers for enhanced tribological performance," *Sci. Rep.* **6**, 25378 (2016). <https://doi.org/10.1038/srep25378>
- [23] K. Järrendahl, I. Ivanov, J.-E. Sundgren, G. Radnóczy, Z. Czigany, and J.E. Greene, "Microstructure evolution in amorphous Ge/Si multilayers grown by magnetron sputter deposition," *J. Mater. Res.* **12**, 1806–1815 (1997). <https://doi.org/10.1557/JMR.1997.0249>
- [24] C. Cancellieri, E. Klyatskina, M. Chiodi, J. Janczak-Rusch, and L.P.H. Jeurgens, "The Effect of interfacial Ge and RF-bias on the microstructure and stress evolution upon annealing of Ag/AlN multilayers," *Appl. Sci.* **8**, 2403 (2018). <https://doi.org/10.3390/app8122403>

**БАГАТОШАРОВІ ПОКРИТТЯ WNbN/WNbC, WN/WC ТА NbN/NbC:
СТРАТЕГІЯ ВАКУУМНО-ДУГОВОГО ОСАДЖЕННЯ ТА ОЦІНКА МІКРОСТРУКТУРИ**
**О.В. Максакова^{a,b}, В.М. Береснев^b, С.В. Литовченко^b, Д.В. Горох^b, Б.О. Мазілін^b, І.О. Афанасьєва^{b,d},
М. Чапловичова^c, Мартин Сахул^a, В.А. Столбовой^d**

^aІнститут матеріалознавства, Словацький технологічний університет у Братиславі,
вул. Яна Ботту 25, 917 24, Трнава, Словаччина

^bХарківський національний університет імені В.Н. Каразіна, пл. Свободи, 4, 61000 Харків, Україна

^cЦентр нанодіагностики матеріалів, Словацький технологічний університет у Братиславі,
Вазовова 5, 812 43, Братислава, Словаччина

^dНаціональний науковий центр «Харківський фізико-технічний інститут», 61108, вул. Академічна 1, м. Харків, Україна

Реактивні гази, такі як азот, кисень і гази на основі вуглецю (наприклад, ацетилен), додають до згенерованого плазмового потоку для створення покриттів з хімічних сполук, включаючи нітриди, оксиди і карбіди. Керуванням швидкості додавання газу можна контролювати стехіометричний склад покриття, який впливає на його кристалічну структуру і спектр властивостей. З огляду на це для осадження багатошарових карбідних/нітридних покриттів на основі W і Nb у динамічно мінливій атмосфері газів азоту та ацетилену було використано метод вакуумно-дугового осадження (PVD). Для керування роботою вакуумно-дугових випарників і портів введення газів у вакуумній камері установки використовувався двоканальний пристрій керування «випарник-інжектор». Матеріалом підкладок для осадження покриттів була корозійностійка жароміцна сталь марки 12X18H9T. Катоди W (99,97 мас. %) і Nb (98,2 мас. %) виготовляли механічним розточуванням зливків з відповідних металів, отриманих електронно-променевим переплавом. У роботі описано стратегію осадження вакуумно-дугових багатошарових покриттів WNbN/WNbC, WN/WC і NbN/NbC з нанометровою товщиною шарів і проведено попередню оцінку їхньої мікроструктури. Представлені багатошарові системи ще не вивчені і становлять значний науковий інтерес з точки зору процесу синтезу та експериментального дослідження властивостей.

Ключові слова: керамічні покриття; нітрид вольфраму; карбід вольфраму; нітрид ніобію; карбід ніобію; вакуумно-дугова обробка; мікроструктура

INTERACTION OF HEAVY METALS WITH 7S SOYBEAN GLOBULIN: MOLECULAR DYNAMICS STUDY

O. Zhytniakivska*, U. Malovytsia, K. Vus, V. Trusova, G. Gorbenko

*Department of Medical Physics and Biomedical Nanotechnologies, V.N. Karazin Kharkiv National University
4 Svobody Sq., Kharkiv, 61022, Ukraine*

**Corresponding Author e-mail: olga.zhytniakivska@karazin.ua*

Received December 29, 2024; revised February 5, 2025; accepted February 17, 2025

Molecular dynamics (MD) simulations were performed to examine the structural and dynamic effects of Cd^{2+} and Co^{3+} binding on 7S soybean globulin. Using a 200 ns simulation at 300 K with GROMACS and the CHARMM General Force Field, key structural parameters—including root-mean-square deviation (RMSD), radius of gyration (Rg), solvent-accessible surface area (SASA), and root-mean-square fluctuations (RMSF)—were analyzed to assess protein stability, flexibility, and compactness under varying metal ion concentrations. The results of the MD simulation indicate: i) at low metal concentrations, the protein maintained structural stability with minimal deviations; ii) increasing metal ion concentrations induced distinct structural changes in the protein structure depending on the ion type; iii) lower metal concentrations primarily affected specific regions of the α -subunit, whereas higher concentrations influenced both the α - and β -subunits; iv) fluctuations in secondary structure elements— α -helices, 3_{10} -helices, and β -strands—suggested potential destabilization, particularly in systems with high metal concentrations; v) α -helical content remained stable throughout the simulation, a slight decrease in β -sheet content was observed at higher metal concentrations. This suggests that heavy metal binding may have a destabilizing effect on β -sheet structures, altering the overall conformation of 7S globulin. These insights are valuable for the development of protein-based nanomaterials for heavy metal detection and sorption.

Keywords: *Protein-metal interaction; Heavy metals; Molecular dynamics*

PACS: 87.14.Cc, 87.16.Dg

Over the past few decades, soybean proteins have gained significant attention not only for their nutritional benefits in the food industry but also for their role in developing protein-based nanomaterials for industrial and biomedical applications [1-12]. For instance, soybean proteins have been effectively utilized in the fabrication of biodegradable nanocomposite films for food packaging [1,2], thermally conductive composites [3,4], and soy protein-based coatings [5], among others. Additionally, soybean proteins have been employed in the synthesis of various nanoparticles for nutraceutical and drug encapsulation and delivery [6-8]. Teng et al. [6] developed curcumin-loaded soy protein nanoparticles with high encapsulation efficiency and a controlled biphasic release profile. Furthermore, Zare-Zardini et al. [7] proposed slow-release curcumin-containing soy protein nanoparticles as potential anticancer agents for osteosarcoma.

Recent studies indicate that soybean proteins are specifically promising for the development of nanosystems for metal detection and sorption owing to their diverse amino acid functional groups, which exhibit strong metal-binding properties [9-12]. Ju et al. [9] introduced a soybean protein fiber (SPF)-derived skeleton to regulate Li deposition and enhance Li metal battery stability. Their findings demonstrate that, during battery cycling, SPF facilitates the formation of a lithium fluoride (LiF) nanocrystal-enriched interface, which reduces interfacial impedance and enhances charge transfer kinetics. In the realm of heavy metal removal, a soy protein-based polyethylenimine hydrogel exhibited high efficiency in adsorbing Cu(II) ions from aqueous solutions, even in the presence of competing heavy metal ions such as Zn(II), Cd(II), and Pb(II) [10]. Similarly, soy protein microsponges have shown exceptional Pb(II) adsorption capabilities [11]. Yamada et al. [12] explored an inorganic composite material composed of soy protein and 3-glycidyloxypropyltrimethoxysilane for heavy metal sorption from wastewater. Their study revealed that the composite material exhibits selectivity for divalent light metal ions, based on a comparative analysis of accumulation rates for different heavy metals [12].

Although numerous studies highlight the potential of soybean proteins for the development of protein-based nanocomposites for heavy metal removal and accumulation, the underlying factors influencing nanosystem metal selectivity remain insufficiently understood and require further investigation. Specifically, detailed insights into the specific binding sites and intermolecular interactions between heavy metal ions and soybean proteins are still lacking. In our previous research, we identified the binding sites for a range of heavy metal ions (Cu^{2+} , Fe^{3+} , Mg^{2+} , Mn^{2+} , Zn^{2+} , Cd^{2+} , Fe^{2+} , Ni^{2+} , Hg^{2+} , Co^{2+} , Cu^{+} , Au^{+} , Ba^{2+} , Pb^{2+} , Pt^{2+} , Sm^{3+} , and Sr^{2+}) on two main soybean protein (7 S globulin and glycinin) and explored the nature of their interactions [13]. The present study employs molecular dynamics simulations to investigate the effects of selected heavy metal ions (Cd^{2+} and Co^{3+}) on the structure and dynamics of soybean 7S globulin.

MOLECULAR DYNAMICS SIMULATIONS

The three-dimensional X-ray crystal structure of basic 7S globulin from soybean was retrieved from the Protein Data Bank (<https://www.rcsb.org/>) using PDB ID 3AUP. Molecular dynamics (MD) simulations and trajectory analyses

were performed using GROMACS (version 5.1) with the CHARMM36m force field. For the simulations, chain A of the 7S globulin structure was selected. The input files for MD simulations were generated using the Solution Builder module within the web-based CHARMM-GUI interface [14]. The system was solvated using a TIP3P water rectangular solvation box, with a variable side length adjusted according to the protein size and heavy metal ion concentration, ensuring a minimum distance of 10 Å between the protein and the box edges. Cadmium and cobalt ions were introduced to the system at five concentrations (5, 50, 100, 500 and 550 ions, respectively). The control systems included the protein along with the necessary Na⁺ ions to neutralize its net charge were also simulated. Heavy metal ions were introduced and randomly distributed within the system. Molecular dynamics (MD) simulations and trajectory analyses were conducted using GROMACS (version 2023.3) with the CHARMM36m force field in the NPT ensemble and a 2-fs time step. Simulations were performed at 300 K, with system minimization and equilibration carried out over 50,000 and 250,000 steps, respectively. During equilibration, the Berendsen algorithm was used for temperature and pressure control, while the LINCS algorithm was applied to constrain hydrogen-containing bond lengths. The total simulation time was 200 ns. The GROMACS commands `gmx rms`, `gmx gyrate`, `gmx rmsf` were used to calculate the protein backbone root-mean-square deviation (RMSD), protein radius of gyration (R_g), root-mean-square fluctuations of the C-alpha atoms (RMSF). Visualization of the snapshots of the MD runs and analysis of the protein secondary structures and protein solvent-accessible surface area (SASA) were performed in VMD. The evolution of the secondary structure was followed using the VMD Timeline tool [15] and Tcl scripts.

RESULTS AND DISCUSSION

Representative snapshots from a 200 ns simulation of cadmium heavy metal binding to 7S globulin are presented in Figure 1.

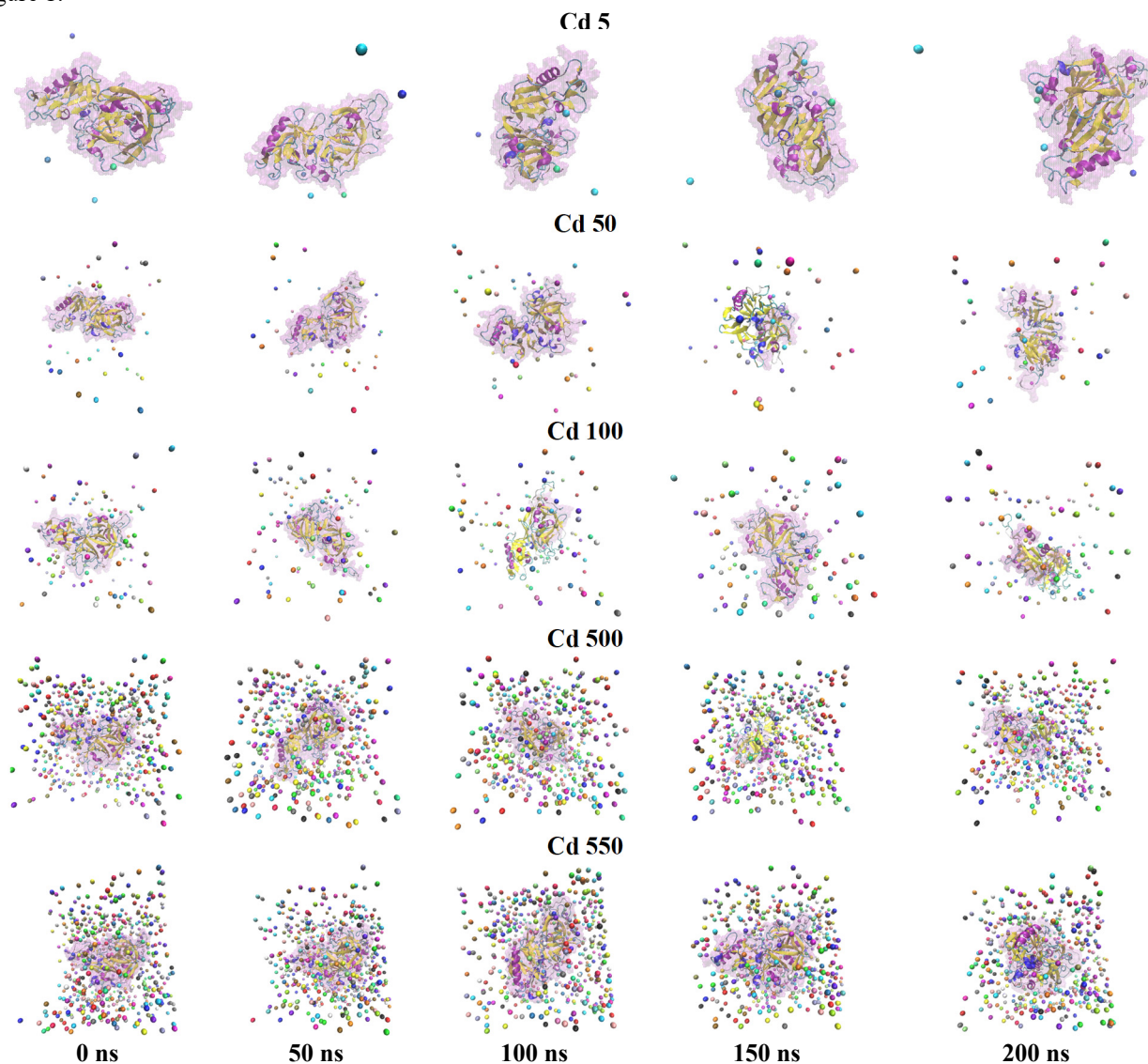


Figure 1. The snapshots of the Cd-protein complexes

In the initial phase of our study, we assessed the overall stability of the protein during the simulation by analyzing the time evolution of key structural parameters, including the backbone root-mean-square deviation (RMSD), radius of gyration (Rg), root-mean-square fluctuations (RMSF) of C-alpha atoms, and solvent-accessible surface area (SASA). Figure 2 depicts the temporal variations in the backbone RMSD, offering insights into the dynamic stability of the protein throughout the simulation period.

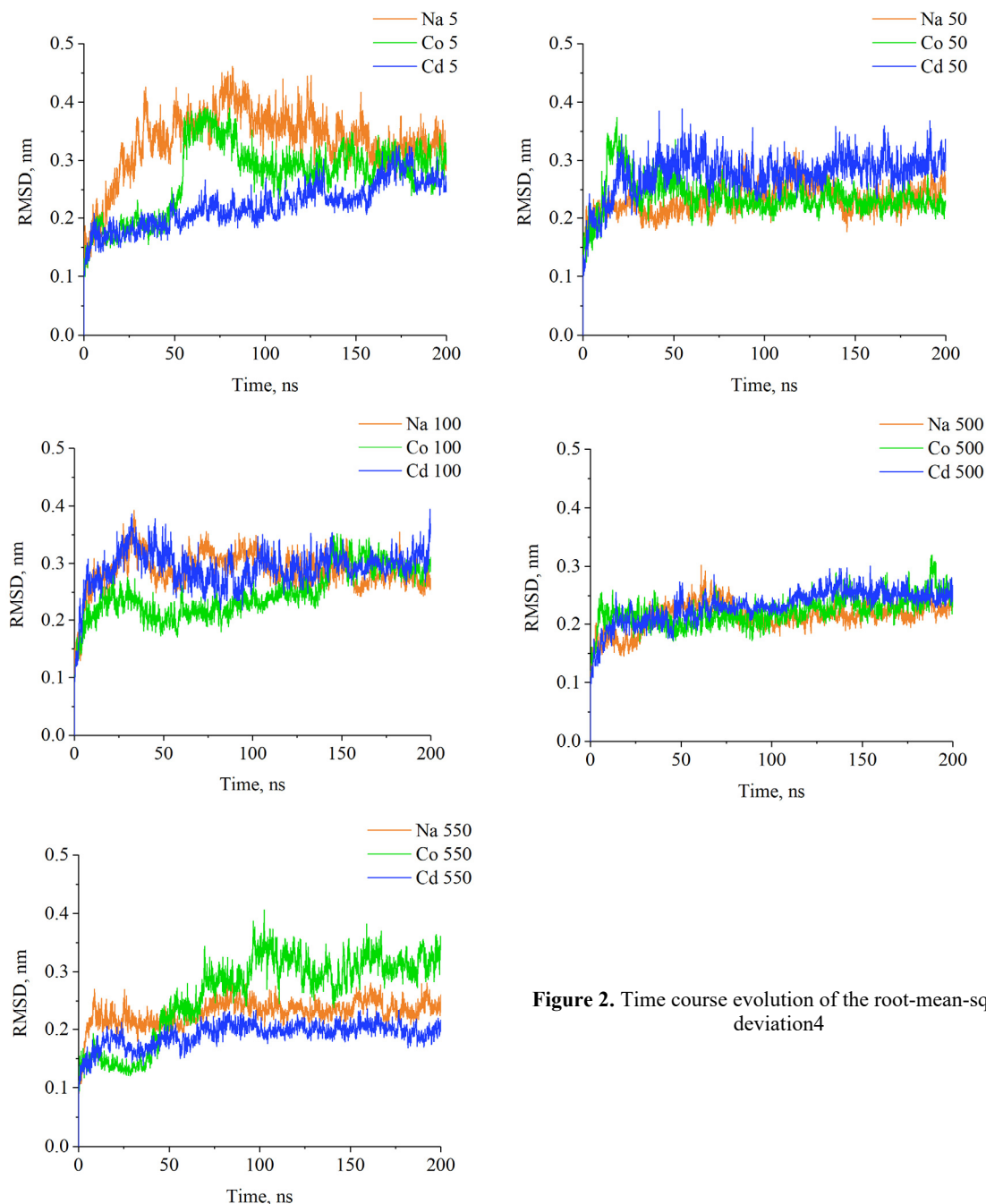


Figure 2. Time course evolution of the root-mean-square deviation4

As shown in Figure 2, the calculated RMSD values for the Cd^{2+} and Co^{3+} -containing systems do not exceed 0.4 nm, remaining below 0.25 nm for the majority of protein-metal complexes, except for brief fluctuations observed in the Cd 100/7S globulin system during the first 50 ns. The RMSD time profile for the Co5/protein system exhibits two clear stages: i) the first phase shows small fluctuations around 0.15 nm during the initial 50 ns of the simulation, indicating minimal structural deviation; ii) in the second phase, there is a sharp rise in RMSD to 0.4 nm at around 52 ns, after which the value decreases to roughly 0.2 nm. From this point, the protein's structure stabilizes and fluctuates around this value for the rest of the simulation, suggesting a stable conformation. For the Co550/protein system, a notable increase in RMSD values was observed starting from 46 ns, after which the RMSD values stabilized and fluctuated around an average of 0.33 nm for the rest of the simulation, indicating equilibration and structural stability. Therefore, it can be concluded that the molecular dynamics simulations achieved satisfactory convergence.

To determine how different concentrations of heavy metal ions affect the dynamic behavior of amino acid residues of 7S globulin, the RMSF values of the C-alpha atom were calculated (Fig. 3). The RMSF analysis revealed detailed information on the fluctuations of amino acid residues in all the heavy-metal/protein systems examined. It identified specific regions of the protein that experienced heightened spatial fluctuations, which were attributed to the binding of metal ions. The 7S globulin from soybean, also known as β -conglycinin, is a major storage protein composed of multiple subunits that adopt a compact, globular structure. Its secondary structure is predominantly composed of β -sheets, with a smaller proportion of α -helices and random coil regions [16]. A defining feature of this protein is the presence of 12 cysteine residues [36], forming five intra-chain and one inter-chain disulfide bridges [16].

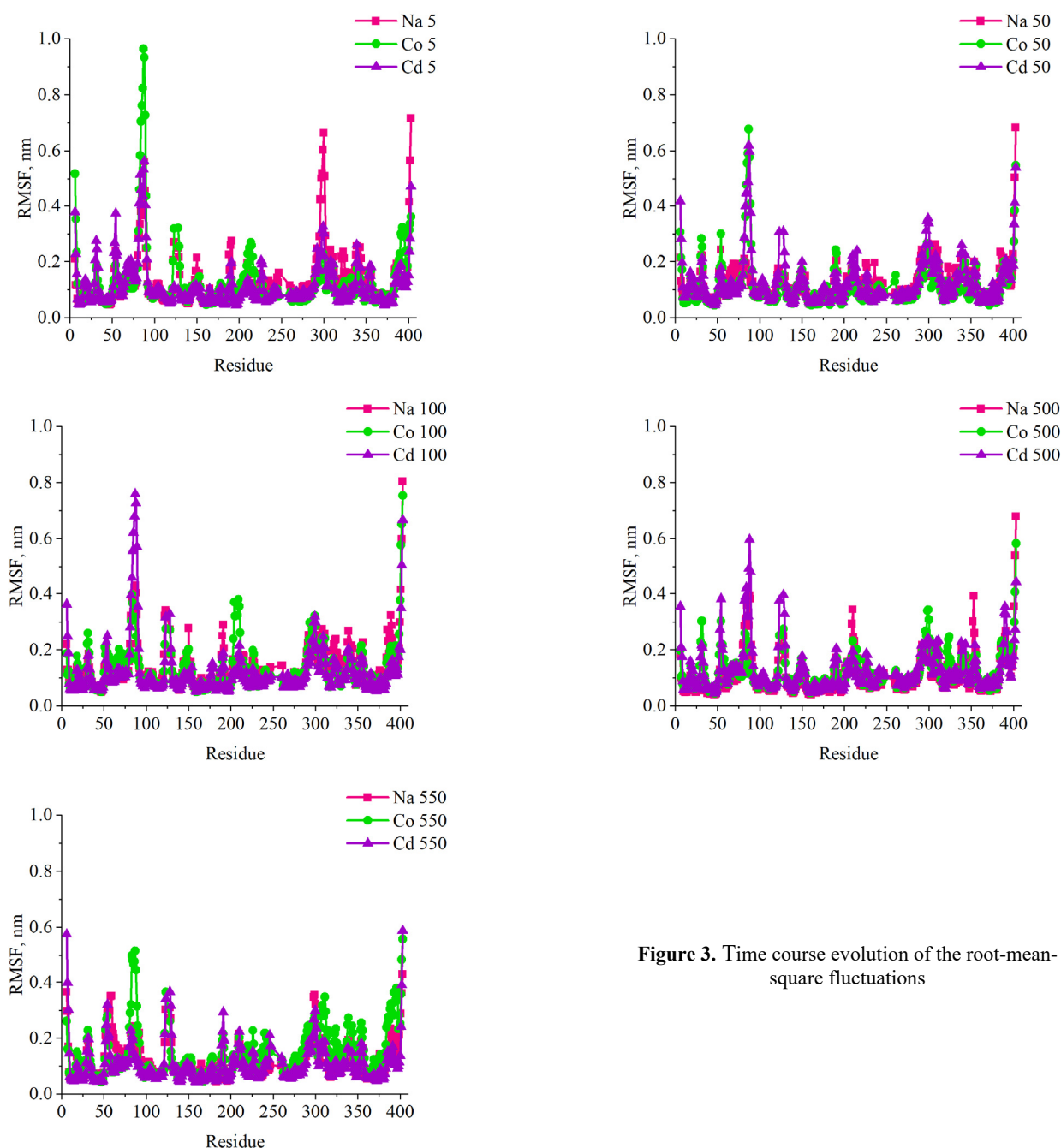


Figure 3. Time course evolution of the root-mean-square fluctuations

As shown in Figure 3, the binding of Cd^{2+} and Co^{3+} at low ion concentrations (5 and 50 ions) was associated with noticeable fluctuations in specific protein regions, particularly residues 81-92, 120-130, and 290-305. A further increase in heavy metal ion concentration led to a rise in RMSF values in the 81-92 residue region, with this effect being more pronounced in the presence of 100 and 500 cadmium ions. Moreover, in systems containing 550 heavy metal ions, the most significant RMSF increase in the 81-92 residue region was observed in the presence of cobalt ions, suggesting a stronger destabilizing effect of Co^{3+} at high concentrations. Notably, the high heavy metal ion concentrations (500 and 550 ions) lead to the fluctuation increase of all residues starting from V271 to K310. This region of 7S globulin contains the α -helix, 3_{10} -helix and β -strands, indicating the possible destabilization of the protein structure. Notably, as illustrated

in Figure 3, heavy metal binding appears to primarily affect the α -subunit (residues 25–275) in systems containing 5, 50, and 100 ions. However, at higher metal concentrations, RMSF changes were observed in both the α -subunit and the low-molecular-weight β -subunit (residues 276–427), indicating a broader impact on protein flexibility and structural dynamics.

Another parameter, reflecting the protein's structural compactness is the radius of gyration (Rg), with lower Rg values signifying a more tightly folded conformation and higher Rg values reflecting a more expanded or less compact structure. To assess how heavy metal binding influences protein structure, the Rg values for the metal/protein complexes were computed and monitored throughout the simulation. Figure 4 presents the time evolution of Rg, providing insights into changes in protein compactness throughout the simulation.

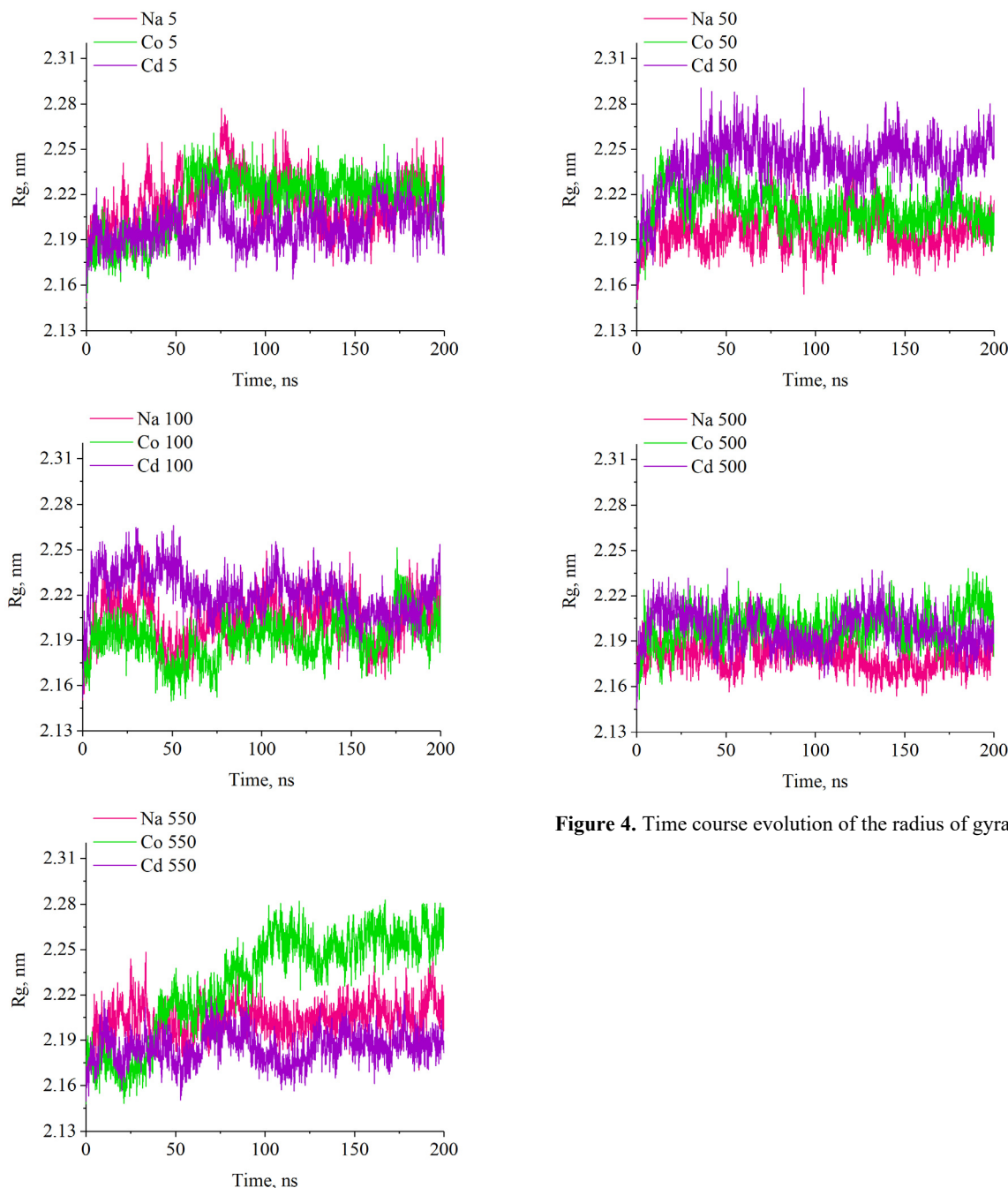


Figure 4. Time course evolution of the radius of gyration

The findings presented in Figure 4 indicate that at a low heavy metal ion concentration (5 ions), the 7S globulin structure remained highly stable throughout the simulation, with an average radius of gyration (Rg) of 2.20 nm, suggesting minimal structural perturbation. However, as cobalt concentration increased, the protein structure expanded, with the most pronounced effect observed in the Co550 protein/metal system. A linear approximation of the Rg time evolution revealed a clear increasing trend, with Rg values rising from approximately 2.16 nm at the start of the simulation to 2.27 nm at 200 ns. This suggests a spatial rearrangement of amino acid residues, potentially influencing secondary structural

elements. In contrast, for systems containing cadmium ions, the radius of gyration decreased at high metal concentrations, with the most significant reduction observed in the Cd550 system. This decrease suggests that the protein structure becomes more compact under these conditions.

To evaluate changes in the hydrophobic residue environment throughout the simulation, we analyzed the relative variations in solvent-accessible surface area (SASA) per residue (Figure 5).

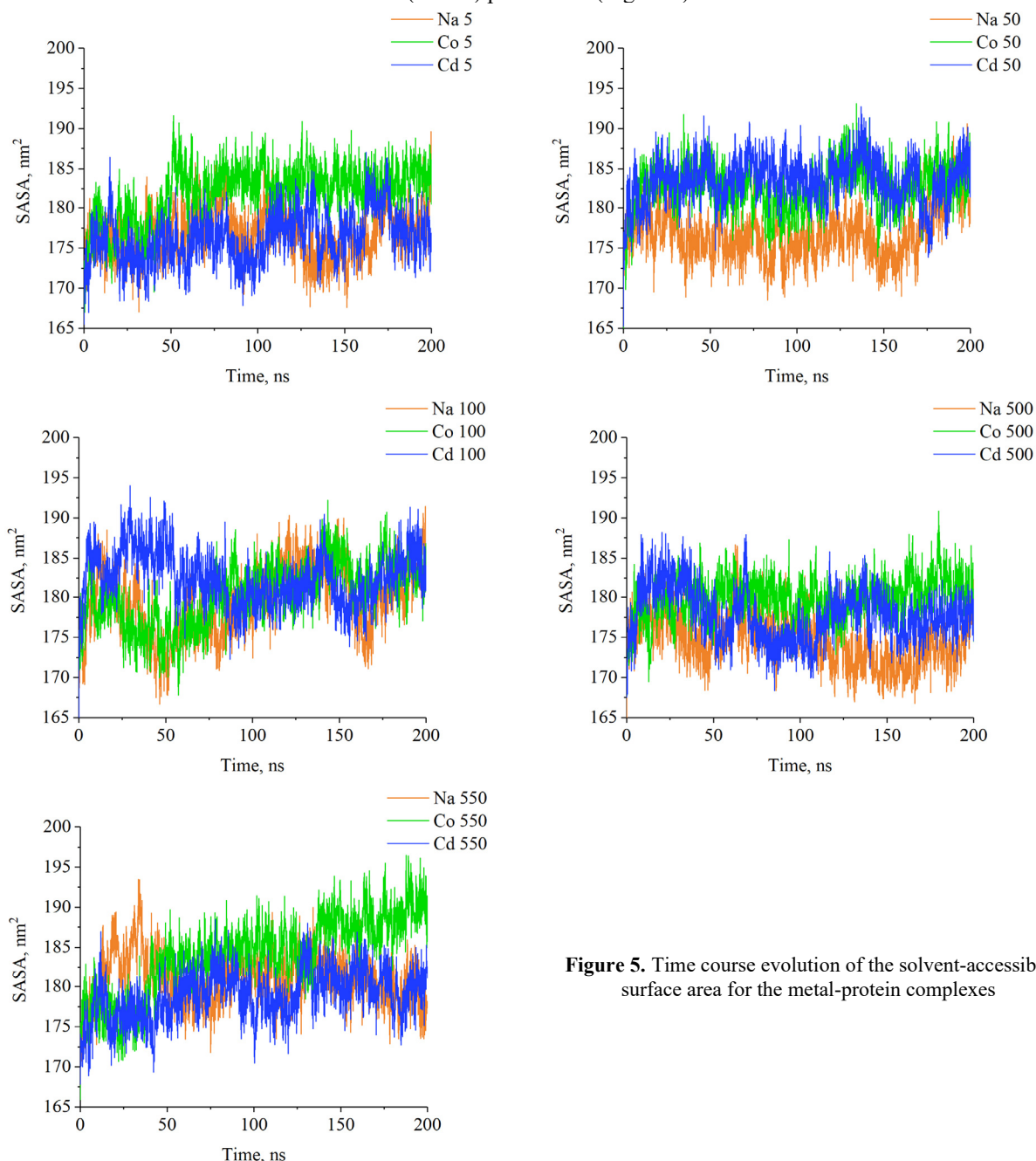


Figure 5. Time course evolution of the solvent-accessible surface area for the metal-protein complexes

The analysis showed no significant variations in SASA values across most protein-metal complexes at metal ion concentrations below 500. In the majority of studied systems, SASA remained within the range of 175–185. However, a slight increase in SASA was observed in systems containing 550 metal ions, suggesting a minor expansion of the protein's solvent-exposed surface at higher ion concentrations.

To characterize the changes in the secondary structure of 7S globulin in the presence of heavy metals during the simulation, we analyzed the time evolution of α -helices and β -sheet content (Fig. 6).

The binding of Cd^{2+} and Co^{3+} does not significantly alter the α -helical content of the protein. This finding suggests that while an increase in RMSF values was observed in the α -helical regions, it primarily reflects residue-level fluctuations rather than disruptions in the secondary structure, which remained stable throughout the simulation. Conversely, heavy metal-protein complexation resulted in a slight reduction in β -sheet content, as the proportion of residues adopting β -sheet conformations gradually decreased throughout the simulation. This effect became more pronounced at higher heavy metal concentrations, suggesting a potential destabilization of β -sheet structures in response to metal binding.

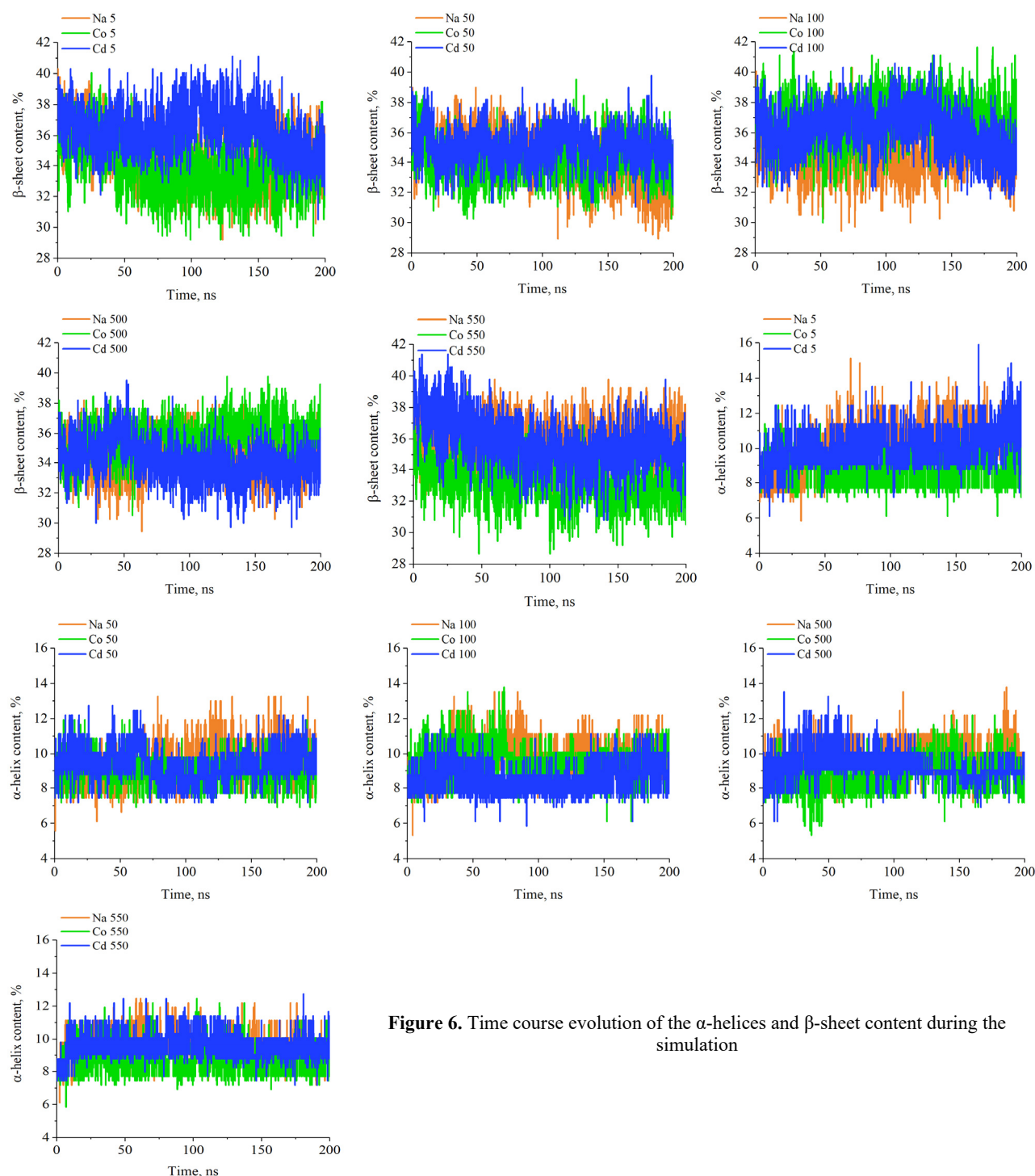


Figure 6. Time course evolution of the α -helices and β -sheet content during the simulation

CONCLUSIONS

The present study employed molecular dynamics (MD) simulations to investigate the effects of Cd^{2+} and Co^{3+} binding on the structure and dynamics of 7S globulin. Key structural parameters—including RMSD, Rg, RMSF, and SASA—were analyzed over a 200 ns MD simulation at 300 K using GROMACS and the CHARMM General Force Field to assess protein stability, flexibility, and compactness at varying metal ion concentrations. Our MD results indicate that at low metal concentrations (5 ions), the protein remained highly stable with minimal structural deviations. However, as metal concentrations increased, distinct effects were observed depending on the ion type. RMSF analysis revealed that heavy metal binding primarily affected specific regions of the α -subunit at lower concentrations, while both the α - and β -subunits were impacted at higher concentrations. Increased fluctuations in regions containing secondary structural elements (α -helices, 3_{10} -helices, and β -strands) suggest potential destabilization, particularly in systems with high metal ion concentrations (500 and 550 ions). Secondary structure analysis demonstrated that α -helical content remained stable, indicating that observed fluctuations were primarily residue-level rather than structural disruptions. In contrast, a gradual

reduction in β -sheet content was observed, particularly at high metal concentrations, suggesting a destabilizing effect of heavy metal binding on β -sheet structures.

Overall, our findings highlight the distinct structural responses of 7S globulin to cadmium and cobalt binding and contribute to a deeper understanding of protein-metal interactions. These insights may have implications for the development of protein-based nanomaterials for heavy metal detection and sorption.

Acknowledgements

This work was supported by the Ministry of Education and Science of Ukraine (the project “Development of economically affordable nanosystems for rapid identification and purification of water from heavy metal ions based on carbon nanoallotropes and amyloids from organic waste”).

ORCID

Olga Zhytniakivska, <https://orcid.org/0000-0002-2068-5823>; Uliana Malovytsia, <https://orcid.org/0000-0002-7677-0779>
Kateryna Vus, <https://orcid.org/0000-0003-4738-4016>; Valeriya Trusova, <https://orcid.org/0000-0002-7087-071X>
Galyna Gorbenko, <https://orcid.org/0000-0002-0954-5053>

REFERENCES

- [1] Y. Wei, Z. Huang, Z. Yu, C. Han, and C. Yang *Materials*, **14**, 5436 (2021). <https://doi.org/10.3390/ma14185436>
- [2] Q. Wang, Y. Duan, Y. Huang, *et al.*, *Carbohydrate Polymers*, **323**, 121410 (2023). <https://doi.org/10.1016/j.carbpol.2023.121410>
- [3] S. Zhang, C. Long, X. Zhu, *et al.*, *ACS Nano*, **17**, 18850 (2023). <https://doi.org/10.1021/acsnano.3c03782>
- [4] X. Huang, R. Li, L. Zeng, *et al.*, *Carbon*, **161**, 360 (2020). <https://doi.org/10.1016/j.carbon.2020.01.069>
- [5] X. Ren, and M. Soucek, *ACS Symposium Series*, **1178**, 207 (2014). <https://doi.org/10.1021/bk-2014-1178.fw001>
- [6] Z. Teng, Y. Luo, and Q. Wang, *J. Agric. Food Chem.* **60**, 2712 (2012). <https://doi.org/10.1021/jf205238x>
- [7] H. Zare-Zardini, H. Soltaninejad, A. Ghorani-Azam, *et al.*, *Prog Biomater*, **11**, 311 (2022). <https://doi.org/10.1007/s40204-022-00197-4>
- [8] K. Chien, E. Chung, and R. Shah. *J. Biomat. App.* **28**(7), 1085 (2014). <https://doi.org/10.1177/0885328213497413>
- [9] Z. Ju, G. Lu, O. Sheng, *et al.*, *Nano Lett.* **22**(3), 1374 (2022). <https://doi.org/10.1021/acs.nanolett.1c04775>
- [10] J. Liu, D. Su, J. Yao, Y. Huang, J. Shao, and X. Chen, *J. Mater. Chem. A*, **5**, 4163 (2017). <https://doi.org/10.1039/C6TA10814H>
- [11] S. Anselmo, T. Avola, K. Kalouta, S. Kataldo, *et al.*, *Int. J. Biol. Macromol.*, **239**, 124276, (2023). <https://doi.org/10.1016/j.ijbiomac.2023.124276>
- [12] M. Yamada, M. Ujihara, and Y. Yamada, *J. Compos. Sci.* **7**, 419 (2023). <https://doi.org/10.3390/jcs7100419>
- [13] O. Zhytniakivska, U. Tarabara, K. Vus, V. Trusova, and G. Gorbenko, *East European Journal of Physics*, (1), 497 (2024). <https://doi.org/10.26565/2312-4334-2024-1-55>
- [14] S. Jo, T. Kim, V.G. Iyer, and W. Im, *J. Comp. Chem.* **29**, 1859 (2008), <https://doi.org/10.1002/jcc.20945>
- [15] W. Humphrey, A. Dalke, and K. Schulten, *J. Mol. Graph.* **14**, 33 (1996), [https://doi.org/10.1016/0263-7855\(96\)00018-5](https://doi.org/10.1016/0263-7855(96)00018-5)
- [16] T. Hashimoto, T. Shimizu, M. Yamabe, M. Taichi, *et al.*, *FEBS Journal*, **278**, 1944 (2011). <https://doi.org/10.1111/j.1742-4658.2011.08111.x>

ВЗАЄМОДІЯ ВАЖКИХ МЕТАЛІВ З 7S ГЛОБУЛІНОМ З СОІ: ДОСЛІДЖЕННЯ МЕТОДОМ МОЛЕКУЛЯРНОЇ ДИНАМІКИ

О. Житняківська, У. Маловиця, К. Вус, В. Трусова, Г. Горбенко

Кафедра медичної фізики та біомедичних нанотехнологій, Харківський національний університет імені В.Н. Каразіна
м. Свободи 4, Харків, 61022, Україна

У цьому дослідженні були використано метод молекулярної динаміки (MD) для дослідження структурних і динамічних ефектів зв'язування Cd^{2+} і Co^{3+} з 7S соєвим глобуліном. Використовуючи 200-нс симуляцію при 300 K з GROMACS і CHARMM General Force Field, були проаналізовані ключові структурні параметри, зокрема корінь середньоквадратичного відхилення остову ланцюга (RMSD), радіус інерції (Rg), площа поверхні, доступна для розчинника (SASA), та середньоквадратичні флуктуації (RMSF), для оцінки стабільності, гнучкості та компактності білка при різних концентраціях іонів металів. Результати MD дослідження показали: i) при низьких концентраціях металів білок зберігав структурну стабільність з мінімальними відхиленнями; ii) зростання концентрацій металевих іонів викликало більш суттєві структурні зміни в структурі білку залежно від типу іону; iii) на низьких концентраціях металів зміни переважно стосувалися конкретних регіонів α -субодиниці глобуліну, в той час як на вищих концентраціях впливали як на α -, так і на β -субодиниці; iv) коливання в елементах вторинної структури — α -спіралях, 3_{10} -спіралях та β -ланцюгах — вказували на потенційну дестабілізацію, особливо в системах з високими концентраціями металів; v) вміст α -спіралей залишався стабільним протягом симуляції, однак спостерігалось незначне зменшення вмісту β -ланцюгів при високих концентраціях металів. Це свідчить, що зв'язування важких металів може мати дестабілізуючий ефект на β -ланцюгові структури та змінювати загальну конформацію 7S глобуліну. Ці результати є корисними для розробки наноматеріалів на основі білків для виявлення та сорбції важких металів.

Ключові слова: взаємодія білок-метал; важкі метали; молекулярна динаміка